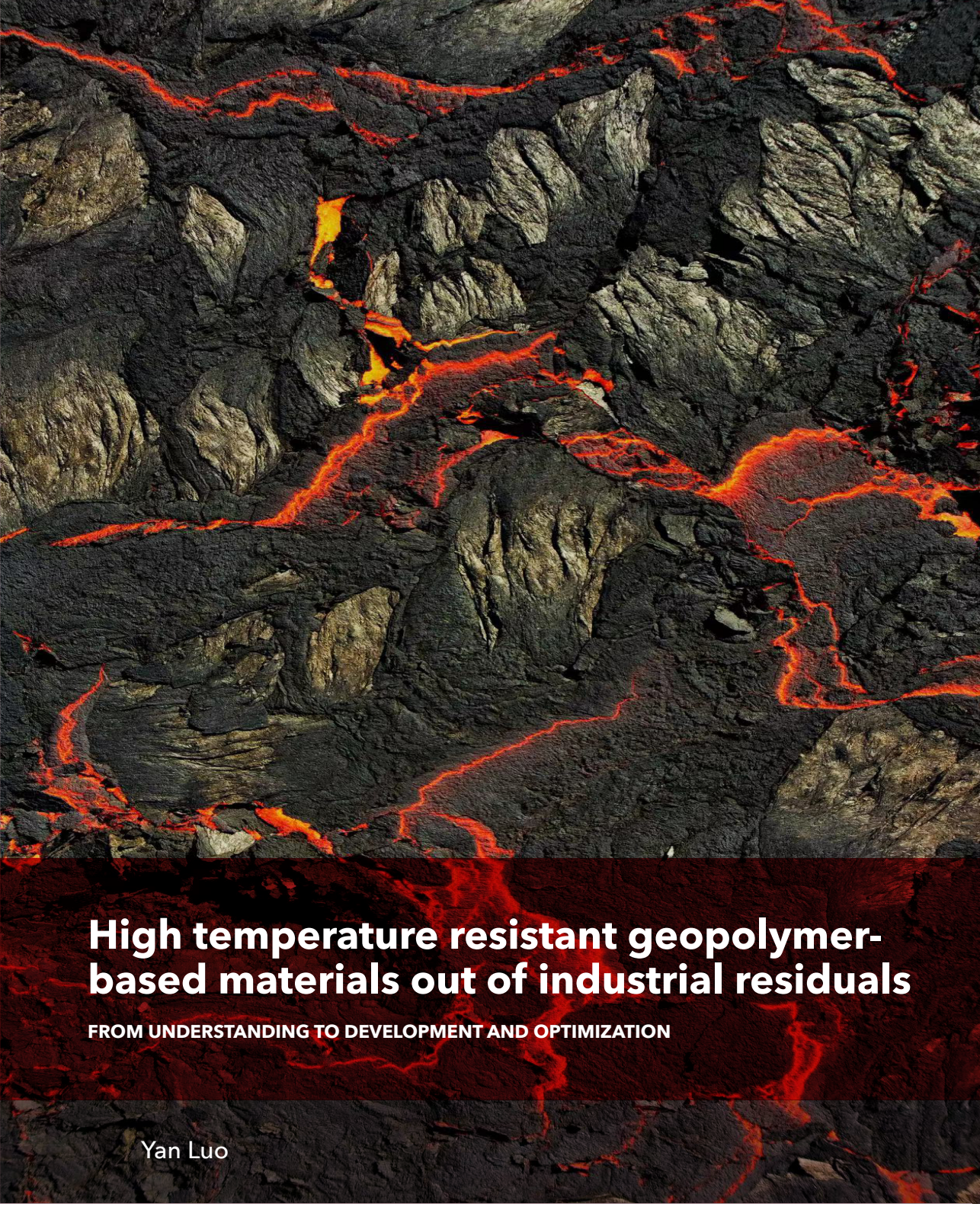

High temperature resistant geopolymer-based materials out of industrial residuals

FROM UNDERSTANDING TO DEVELOPMENT AND OPTIMIZATION

Yan Luo

Bouwstenen 376

High-temperature resistant geopolymer-based materials out of industrial residuals

From Understanding to Development and Optimization

Yan Luo

CIP-DATA LIBRARY TECHNISCHE UNIVERSITEIT EINDHOVEN
High-temperature resistant geopolymer-based materials out of industrial residuals / by Yan Luo
A catalogue record is available from the Eindhoven University of Technology Library
ISBN: 978-90-386-5926-8
Bouwstenen 376
NUR 955

Cover design: Yan Luo, Photo by Mengyuan Ma from Iceland
Ph.D. thesis, Eindhoven University of Technology, the Netherlands

High-temperature resistant geopolymer-based materials out of industrial residuals

From Understanding to Development and Optimization

PROEFSCHRIFT

ter verkrijging van de graad van doctor
aan de Technische Universiteit Eindhoven,
op gezag van de rector magnificus, prof.dr. S.K. Lenaerts,
voor een commissie aangewezen door het College voor Promoties,
in het openbaar te verdedigen op dinsdag 16 januari 2024 om 16:00 uur

door

Yan Luo

geboren te Sichuan, China

Dit proefschrift is goedgekeurd door de promotoren en de samenstelling van de promotiecommissie is als volgt:

Voorzitter:	Prof. dr. ir. T.A.M. Salet
1e Promotor:	Prof. dr. ir. H.J.H. Brouwers
2e Promotor:	Prof. dr. Q.L. Yu
Leden:	Prof. dr. W. Chen (Wuhan University of Technology)
	Prof. dr. N. De Belie (University of Ghent)
	Prof. dr. M.C. Bignozzi (Universita di Bologna)
	Prof. dr. M. Tyrer (Technological University Dublin)
	Prof. dr. Ž. Tomović

Het onderzoek of ontwerp dat in dit proefschrift wordt beschreven is uitgevoerd in overeenstemming met de TU/e Gedragscode Wetenschapsbeoefening.

Dedicated to my beloved parents

献给我亲爱的父母

Preface

FOUR YEARS LATER as I put the final words of my PhD dissertation, I was to remember the distant afternoon when I decided to embark on the journey towards a doctoral degree in the Netherlands, thousands of miles away from home, wondering what this adventure would entail. Now, I can finally say how incredible and unforgettable this journey has been!

As a starting point, I wish to extend my heartfelt gratitude to my promotors Prof. dr. ir. H.J.H (Jos) Brouwers and Prof. dr. Qingliang Yu. Thank you, Jos, for your farsighted guidance in shaping my research trajectory, for teaching me how to conduct application-oriented research, and for helping me forge a connection between academia and industry. Your broad knowledge, invaluable counsel, and trust have empowered me to venture into uncharted scientific territory fearlessly and assuredly. My warmest thanks also go to Qingliang, the one who always brought me on the right track when I found myself lost in my research or daily life. Your extensive expertise, endless patience, and enlightening guidance have motivated me to reach for greater heights, push boundaries, and continuously challenge myself. Working with both of you has been a true honor and pleasure for me, and what I've learned from you will serve as an invaluable asset in my future career.

My great gratitude goes to Prof.dr. Sieger van der Laan. I have enjoyed all the discussions with you and have been inspired by your dedication to translating research into tangible, practical solutions in the industry. I would like to extend my gratitude to Dr. Katrin Schollbach for her insightful advice in my research, especially in the area of mineralogy, as well as her patient assistance with the lab equipment. I also appreciate all the teachers in my life, especially Mr. Heli Zheng and Prof. Zhi Li. You nurtured the seeds of knowledge within me that have shaped who I am and where I stand today.

I would like to express my sincere appreciation to the committee members. Prof. dr. Wei. Chen, whose encouragement truly means a lot to a young man in his early career, as well as Prof. dr. Nele De Belie, Prof. dr. Maria Bignozzi, Prof. dr. Mark Tyrer, Prof. dr. Željko Tomović for their precious time in reviewing my thesis and providing valuable comments and suggestions to improve the quality.

The experimental work presented in this thesis would not have been achieved without the support of specialized technicians and engineers. I would like to thank the technical staff in the Laboratory of Building Physics and Services at TU/e, especially Anneke Delsing and Harrie Smulders. I am also grateful to the engineers at the Ceramic Research Center (TATA Steel), namely Paul van den Idsert, Donald Mittertreiner, Dr. Stefan Melzer, and Pieter Put. Thank you all for your kindness and willingness to help. In the meantime, words of thanks also go to my project partners, in particular Paul van Dooren (VRBZO), Louis Cleef, and Andreas Leismann (Rockwool) for their technical support and raw material supply.

In this incredible journey, marked by its mix of challenges and triumphs, I consider myself fortunate to have such amazing friends who have accompanied me on the path to reaching this point. I extend special thanks to Kinga. I can vividly recall the lab tour you gave me on my first day at TU/e. I guess none of us expected this shared PhD project would foster a friendship extending far beyond work. Luyang, a brother I can always count on. I appreciate your friendship, hospitality, unconditional support, and special sense of humor. I would like to thank you, Shaohua, for the experience and suggestions you shared at the beginning of my PhD study. Furthermore, I'll package with me all the priceless memories shared with Fan, Tao, Xuan, and Yanjie-those nights of beer and joy, cycling trips, and all the incredible travels. Alex and Leila, I've cherished the time we've spent together, and all the funny talks.

My appreciation also goes to my dear colleagues in the Building Materials group, including, but not limited to, Florent, Hoss, Anna, Peipeng, Yueye, Zixiao, Zhengyao, Gang, Yuxuan, Winnie, Jawad, Jonathan, Naomi, Ricardo, Iris, Charles, Marc, Felix, Marina, Samuel, Daoru, Zhihan, Helong, Jia, Zixing, Jingyang (thank you for the job information you shared with me), and Yanshuo, Samantha, Beatrice, Nataliya, Shashank, Ceren, Quan, Jiale, and my master's student Jody. I take immense pleasure in working alongside each and every one of you, and I've been truly fascinated by the diverse cultures you bring. I wish you all the best in the future, and I hope our friendship will endure, even if we find ourselves in different corners of the world.

Now is the moment to express my gratitude to all of my friends in China, with special mention to Hangyu Li, Peng Yuan, Hui Zhang, and Yuanyuan Jia. Despite the distance and time zones that separate us, your support and encouragement through all the good times and bad times hold immeasurable value to me.

Of utmost significance, I extend my sincerest appreciation to my mother Lingmin Dong, and father Hongwen Luo. No words can express my thanks to you two. You raise me, offer me the best you have, respect and support all my decisions, and seek nothing in return. Special thanks are given to my sister Chang Luo, brother-in-law Henk Zhang, Yige Yang, and my cute nephew, Luis. Thank you for providing me with the warmth of a home in a foreign country.

In the end, I thank myself for never giving up.

Yan Luo

Eindhoven, November 2023

Summary

Fire hazards in buildings constitute a substantial risk to both occupants and property, highlighting the significance of fire safety measures in construction practices. In recent years, the negative environmental benefits and poor thermal performance of Portland cement have spurred research efforts toward exploring new generation of thermal resistant building materials. This dissertation focuses on high temperature resistant geopolymer-based materials, spanning from understanding to development and optimization, with the goal of attaining economically and environmentally sustainable solutions.

In the **first section** (**Chapter 2**), an exploration of the thermal degradation behavior of geopolymer-based materials is conducted. The evolution of geopolymers under high temperatures is a complex process that conjuncts with chemical transformation and physical changes at the same time, which remains unclear. To systematically characterize the thermal evolution, the chemical transformation, e.g., gel and crystalline phase, is investigated and a quantitative crack assessment is developed to learn the thermally induced cracking behavior. Results reveal that, the water evaporation and gel decomposition lead to two different cracking behaviors in geopolymer-based materials at elevated temperatures. Chemically, further geopolymerization, gel decomposition, and viscous sintering emerge sequentially at various temperature stages. Notably, the ground granulated blast furnace slag addition in the hybrid geopolymer lessons the geopolymeric behavior such as further geopolymerization and viscous sintering, but further aggravates the thermal damage owing to the compact structure and unstable hybrid gel. The interaction among physico-chemical changes plays the key factor in determining the mechanical evolution of geopolymer-based materials under elevated temperatures. Accordingly, the conceptual models of plain geopolymer and hybrid geopolymer are proposed to reveal the thermal degradation mechanism of geopolymer-based materials.

In light of the revealed thermal degradation mechanism, the **second section** focuses on the modification of the geopolymer gel system by co-activation of Class F fly ash and Ladle slag. As a steel manufacturing by-product, ladle slag is largely underutilized due to its low hydraulic reactivity. On the basis of phase composition and high crystallinity, ladle slag is proposed as a calcium and aluminium source in the joint activation with Class F fly ash (**Chapter 3**). The effect of ladle slag on the geopolymer system, regarding the reaction process, hydrates assemblage, mechanical strength, and thermal behavior is investigated. The results show that the ladle slag addition has a positive influence on geopolymers, which not only enhances the mechanical strength but also retains the geopolymerization. It enables a high residual compressive strength of 64.7 MPa in the hybrid geopolymer with 25 wt.% ladle slag addition, compared to 55.2 MPa in plain geopolymers after 800 °C exposure. However, a drastic volumetric shrinkage is noticed. In continuation, to understand and optimize the hybrid gel system, the alkali activator is tailored to control the dissolution of ladle slag (**Chapter 4**). According to energy-dispersive spectroscopy (EDX) coupled with the PhAse Recognition and Characterization (PARC) analysis, the product layer wrapping around slag particles largely governs the Ca availability in the environment, enabling the development of two separated gels, namely C-(N)-A-(S)-H and N-(C)-A-S-H type gel. A dense matrix

consisting of geopolymer gel and Ca-enriched gel is achieved with 8 wt.% Na_2O while increasing silica modulus intensifies the incompatibility between the two gels. The initial properties (porosity, mechanical strength) and thermal performance (volumetric stability, residual strength) of the hybrid binder are largely influenced by the competition between different reaction mechanisms of the two gels. It reveals that, by tailoring the gel compatibility, the performance of the designed geopolymer binder at both room and high temperatures can be deliberately controlled.

Based on the optimized gel system, the **third section** moves towards structural development on geopolymer-based composites. The potential for recycling mineral wool waste in the development of fiber-reinforced geopolymer composites is examined (**Chapter 5**). The impact of mineral wool waste on geopolymerization, microstructure, durability, and thermal behavior are investigated. It is learned that the ion dissolution and dimension of mineral wool waste have a synergetic effect on the microstructural formation and performance of the designed composites. The inclusion of mineral wool waste, particularly in fine particle form, accelerates the geopolymerization process, leading to enhanced gel formation and increased Al uptake in the N-A-S-H gel. With an optimum substitution, the mineral wool fibers not only alleviate the drying shrinkage but achieve improved flexural properties. After high temperature exposure, a significant strength retention/gain with drastic thermal shrinkage is achieved in the designed composites. In addition to fiber reinforcement, a novel approach for designing high temperature resistant geopolymer mortar is introduced by applying particle size distribution theory (**Chapter 6**). The impact of aggregate packing and binder-aggregate interaction on the microstructural and thermophysical properties are systematically analysed. Based on that, a numerical simulation is carried out to explore the heat transfer pattern within the designed geopolymer composites. With the optimized aggregate packing, a counterbalance between thermal conductivity and mechanical strength is reached in lightweight geopolymer composite. The study reveals that the type and packing of aggregates significantly affect the heat transfer pattern and the subsequent thermal progression in geopolymer composites. The incorporation of lightweight aggregates results in less thermal destruction with better mechanical stability as compared to normal sand. The increased distribution modulus from 0.2 to 0.3 potentially slows down the thermal deterioration and eases the mechanical degradation in lightweight geopolymer composites up to 800 °C.

Content

CHAPTER 1

Introduction

1.1 Background and motivation

Despite the recent technological advancements and fire prevention measures, the threat of fire outbreak always lingers all over the world. According to the 2020 World Fire Statistics Report by the International Association of Fire & Rescue Services, residential building fires constituted 24.2% of all recorded fires, including vehicle fires, other structures, and forest fires. Shockingly, residential building fires accounted for 82.7% of all reported fire-related fatalities and 61.0% of injuries [1]. Fire hazards in buildings can pose much critical risk to human beings and property, emphasizing the importance of fire safeguarding in buildings.

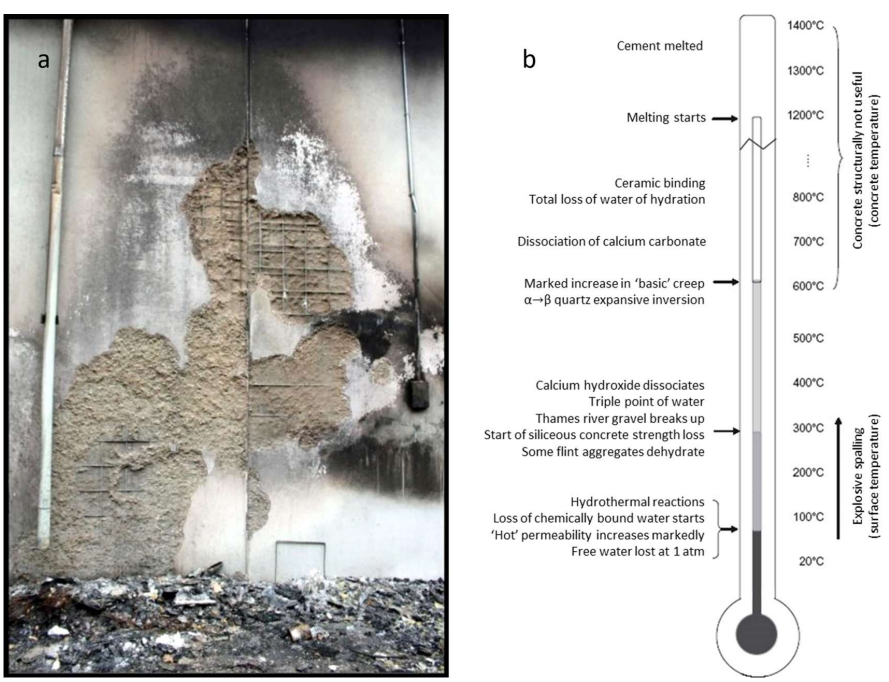

Fig. 1.1 (a) Explosive spalling [2] and (b) physicochemical transformation in Portland cement concrete during high temperature exposure [3].

Among all safety measures, passive fire protection systems, including structural and non-structural building components, should serve as the ultimate 'safety net' to guarantee structural integrity when exposed to fire. The primary objective is to provide sufficient time for firefighting and rescue operations while also minimizing property losses [4]. As the most widely used man-made building material, Ordinary Portland Cement (OPC) based materials are widely acknowledged as offering certain fire resistance, with non-combustible nature, and relatively low thermal conductivity [5]. However, as shown in **Fig. 1.1**, in cement-based materials, the rapid moisture transport and pore pressure build-up before 300 °C leads to a layer-by-layer structural loss, so-called spalling. Furthermore, the main hydration products including calcium silicate hydrate (C-S-H) and calcium hydroxide dehydrate and decompose at the range of 100-600 °C [6,7]. In consequence, the structure and mechanical properties of OPC-based materials drastically deteriorate at elevated heating conditions, which poses a serious threat to firefighting and evacuation.

Today, the development of high temperature resistant materials remains a focal research point, given their widespread utilization, such as the construction sector, ceramic and refractory industry for steel and glass production, and aerospace industry, etc. As one of the biggest markets, the consumption of high temperature resistant materials for construction reached $4.88 billion in 2023 with an annual growth rate of 11.6%, according to Fire Protection Materials for Construction Global Market Report 2023. Several thermal resistant materials have been widely used in construction applications, including high alumina cement, gypsum board, fire-resistant ceramic/glass, metal alloys, coatings, and refractory brick/castable [8]. Despite these traditional materials have demonstrated effectiveness with their unique advantages, concerns are arising amid the growing demand for sustainability in the construction industry. Firstly, some of them, such as high alumina cement, ceramics, and coatings are expensive to produce, which largely raises the cost. Secondly, the production of fire-resistant ceramic/glass, metal alloys, and refractory brick/castable always involves energy-intensive processes (pre-heating, melting, sintering), resulting in a significant carbon footprint.

In the past decades, geopolymers have received significant attention from both academia and the industrial community. The key reason behind the keen interest is their potential to serve as sustainable alternatives to traditional cementitious materials. The synthesis of geopolymers represents a cost-effective and environmentally friendly process. It involves a reaction between alkaline activator and aluminosilicate sources with low calcium, typically derived from industrial by-products or other cost-effective materials [9,10]. Besides, only 0.18 t CO_2 footprint is attributed out of 1t geopolymer, when compared with OPC (0.9t CO_2 out of 1t OPC, 8% of global emissions) [11,12]. Moreover, geopolymers possess superior mechanical stability and structural integrity over OPC under high temperature exposure. Hence, geopolymer-based materials potentially serve as a promising and sustainable solution for passive fire protection in buildings, tunnels, and other facilities where fire safety is imperative [13].

1.1.1 Geopolymer and its related materials

The technology of Alkali activated material (AAM) was first introduced with a patent awarded to Kühl in 1908 [14]. It refers to the binder systems derived from solid silicate or natural pozzolans, for instance, fly ash and ground granulated blast furnace slag (GGBS) [15]. Owing to their low or latent reactivity, alkali activation is necessitated to promote dissolution and solidification. In the 1950s, Glukhoveky developed a concept model to describe the alkali activation of materials primarily comprising reactive silica and alumina. The binder was first termed as 'soil cement', which serves as the theoretical foundation of 'Geopolymer'. In the 1970s, Davidovits [16] defined the term 'Geopolymer' as three-dimensional aluminosilicates, which is typically produced from low calcium or calcium-free aluminosilicate precursors, such as Class F fly ash and metakaolin. **Fig. 1.2** depicts the geopolymer reaction model simplified from Glukhovsky theories, involving dissolution, gelation, polymerization and hardening process. As the aluminosilicate sources dissolve in contact with alkaline solution, the dissolved silicate and aluminate species gradually interact to form three-dimensional network of aluminate and silicate tetrahedra on the atomic and nanometric scale [17,18]. Owing to the difference in the dissolution rate between aluminum and silicate, a transformation from Al-rich gel to Si-rich gel can be observed. Ultimately, a continuous sodium aluminate silicate hydrate gel (N-A-S-H) is formed using NaOH based alkali activator.

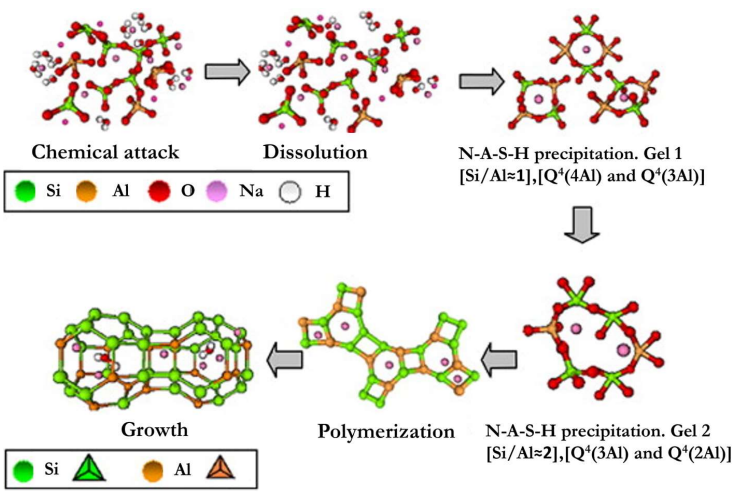

Fig. 1.2 Conceptual model of geopolymerization [18].

Due to the three-dimensional structure and gel composition, geopolymers show potential in a broad range of applications, e.g., high temperature resistance, chemical (acid) resistance, heavy metal immobilization, etc, [19–21]. However, the exclusive reliance on Class F fly ash or metakaolin as the sole precursor for geopolymer production inevitably leads to resource competition. Most importantly, major concerns have been raised from the limitation of application, such as energy-consuming high temperature curing and unsatisfied mechanical strength.

1.1.2 Thermal degradation of geopolymer-based materials

Intrinsically, the promising thermal stability of geopolymer gel (N-A-S-H) in originates from its typical structure, which is different from calcium (aluminate) silicate hydrate (C-(A)-S-H) gel in cement-based material (**Fig. 1.3**). In the 3D N-A-S-H network, the water does not present as an integral component of the gel structure, which contrasts with the C-(A)-S-H gel [22]. In addition, N-A-S-H gel contains significantly less chemical-physical sorbed waster as compared to C-(A)-S-H gel [23]. These features reduce the negative impact of thermally induced water removal, largely retaining the gel structure at elevated temperatures. Thus, N-A-S-H gel is inherently thermal stable, only exhibiting partial recrystallization at 800 °C [24].

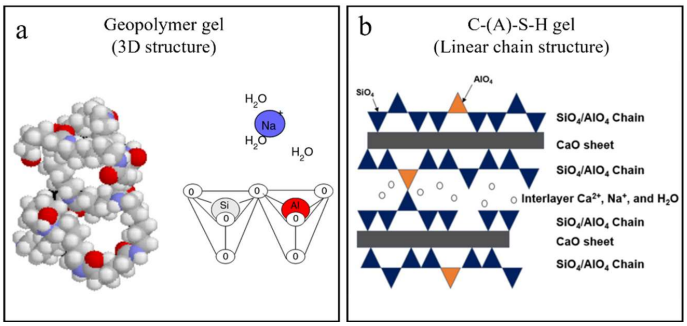

Fig. 1.3 Conceptual structure of (a) geopolymer gel [25] (b) C-(A)-S-H gel [26,27].

While the high temperature behavior of geopolymer-based material should not be solely assessed according to the gel stability at the nanometric scale. It is well acknowledged that the microstructural evolution of alkaline activated materials under high temperatures is a complex process. For instance, from a chemical perspective, further geopolymerization takes place at relatively low temperatures with new gel formation due to the presence of unreacted precursor [24]; the re-crystallization, sintering, and partial melting at elevated temperatures can alter the pore structure and impact the volumetric stability of geopolymer matrix. With respect to the physical change, the geopolymer matrix is prone to cracking due to the evaporation of physically and chemically bonded water at elevated temperatures. Moreover, the cracking behavior of geopolymers is dependent on factors such as mix design, preparation methods, and microstructure. Consequently, the occurrence of phase transformation and physical changes adds complexity to the thermal evolution of geopolymers, posing a synergetic impact on the thermal performance, including mechanical properties, and volumetric stability. To improve and optimize the thermal behavior of geopolymer-based materials, a comprehensive understanding of thermally induced physicochemical transformations is of great significance.

1.1.3 Alternative hybrid geopolymer binder (Gel development)

To address the limitations of geopolymers, a concept of 'hybrid geopolymer' has been generated and attracted keen interest over the past decade. By joint activation of additional calcium source (mostly OPC and GGBS) with aluminosilicate precursor, a calcium involved

binder, namely $CaO-Na_2O-Al_2O_3-SiO_2$ binder is obtained. The presence of ready calcium largely promotes the reaction rate, enabling improved mechanical strength with no need for high temperature curing [28,29]. In hybrid geopolymers, the calcium incorporation further influences the reaction process with the formation of a blended gel system, including N-(C)-A-S-H, C-A-S-H, C-(A)-S-H gels as calcium concentration varies. Due to the complexity of the gel system, at elevated temperatures, the hybrid geopolymers exhibit a similar mechanical evolution to both plain geopolymer and C-(A)-S-H dominated binder, such as cement-based binder and alkali activated slag. For instance, a strength gain is observed in hybrid geopolymer before 400 °C, which is resulted from further geopolymerization [24]; a drastic strength loss until 600 °C due to the vulnerability of C-(A)-S-H gel [30,31]. Therefore, it has been widely accepted that thermal performance is negatively impacted by calcium incorporation, and inevitable structure decomposition and strength deterioration take place in hybrid geopolymers on exposure to high temperatures [32,31,30].

To counterbalance the initial properties and high temperature performance of geopolymers, recent studies have extensively shifted to explore new types of precursors, especially those sources from industrial by-products and waste residuals. Several materials have been investigated as supplementary cementitious materials (SCM) in producing hybrid geopolymers for high temperature applications, including steel slag, copper slag, and waste glass, etc., [33–35]. It not only valorizes the by-products/wastes with low commercial value but also improves or entitles new functions to the resultant materials. Among them, ladle slag (LS) is a by-product of steel-making industry, and the annual production is estimated to be 1.9-2.4 million tons in Europe [36]. The reutilization of LS is largely hindered by its high degree of crystallinity and low Si/Al ratio due to the specific production procedures [37]. Up to now, nearly 80% of LS production in Europe is deposited in landfills [38]. In recent years, the joint activation of LS with aluminosilicate sources has been proposed as an alternative approach to recycling LS as SCM in producing hybrid geopolymers. For instance, Bignozzi et al. [39] and Papayianni et al. [40] investigated the performance of LS incorporated hybrid geopolymers. The results showed that an increased LS substitution refines the pore structure and enhances the mechanical strength. Via alkali activation, LS partially participated in geopolymerization, resulting in the co-existence of different types of gels. Therefore, LS potentially represents a promising co-precursor to promote the geopolymerization reaction. On the other hand, LS is rich in crystalline calcium aluminates, namely mayenite ($C_{12}A_7$), and tricalcium aluminate (C_3A). These phases and corresponding hydrates are relatively thermally stable, which transforms to more stable compounds at high temperatures [41]. Thus, it offers significant possibilities to utilize LS in producing hybrid geopolymer with improved thermal properties. Nevertheless, up to now, there are several scientific barriers and knowledge gaps ahead to effectively reutilize LS into geopolymers, regarding the reaction mechanisms, gel composition and thermal behavior.

1.1.4 Geopolymer composite (Structure optimization)

Fiber reinforced geopolymer composites

Upon exposure to high temperatures, the migration of moisture within a non-deformable

pore structure invariably results in a significant build-up of pore pressure, which constitutes the primary cause of crack formation and damage to the cementitious matrix. As widely accepted, the addition of fibers is one of the most effective strategies to ease the thermal stress and improve the thermal stability of cementitious based materials [20]. Commercially available steel fibers and synthetic fibers (polypropylene (PP) fiber and polyvinyl alcohol (PVA) fiber) are commonly reported in both cement and alkali activated materials for high temperature application [42].

As illustrated in **Fig. 1.4**, the incorporation of fibers with low melting points, such as PP fibers, alleviates the water vapor pressure during exposure to elevated temperatures by enhancing the pore interconnectivity of the matrix [43]. This, in turn, diminishes the tendency of pore collapse and cracking. On the other hand, the high stiffness of fiber poses a positive effect on the thermal stability. For example, the addition of steel fiber promotes the mechanical properties of cementitious matrix, such as flexibility, tensile strength and toughness [44]. It effectively constrains the initiation and propagation of cracks within the matrix under drastic thermal stress, thus preserving the performance of the composites at a consistent level [45,46].

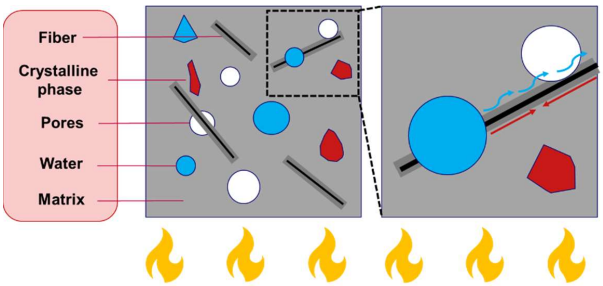

Fig. 1.4 A representation of fiber reinforcement mechanisms in cementitious materials at elevated temperatures.

Nevertheless, in the design of fiber reinforced composites, apart from the evaluation of the properties of binder and fiber independently, it is essential to thoroughly consider the interaction among fiber and matrix. For example, weak interfacial contact is always formed due to the poor interaction between fiber and geopolymer binder, especially for hydrophilic fibers with limited roughness [47]. It not only influences the initial properties but also has the potential to impact the thermal performance of the resulting composites. Hence, to enhance the thermal performance of geopolymer composites, strengthening the fiber-gel interface is of great importance. In addition, from cost-effective and eco-friendly viewpoints, it is imperative to explore the feasibility as well as effectiveness of utilizing fibers sourced from industrial by-products and wastes.

Geopolymer/aggregate composites

As the promising thermal properties of geopolymer binders have been well-established through extensive research, there is a rising interest in developing high-temperature-resistant

geopolymer composites, namely normal/lightweight mortar and concrete, for wide-ranging applications. As compared to OPC based concrete, geopolymer concrete exhibits better high temperature performance, concerning volumetric stability and mechanical strength, due to the superior thermal stability of geopolymer gel [48]. Nonetheless, in geopolymer composites, the interfacial contact between geopolymer binder and aggregates would deteriorates owing to the difference in thermal expansion with increasing temperature [49,50]. Ultimately, it leads to an unavoidable strength reduction in geopolymer composites. It is concluded that the thermal compatibility between aggregates and binders plays a crucial role in the structural and mechanical stability of geopolymer composites at elevated temperatures. However, there is very limited information regarding the interaction between geopolymer binders and aggregates at high temperatures. On the other hand, the intrinsic characteristic of aggregates, such as inert property, density, and particle size, significantly varies the microstructure as well as thermophysical parameters of the composites [50,51]. It further affects the heat transfer and thermal behavior of the designed composites on exposure to elevated temperatures. Therefore, in the design of geopolymer composites for high temperature applications, both the performance of the geopolymer binder and the selection of aggregate are vital considerations. Moreover, to improve the applicability of geopolymer composites, a design methodology that considers factors of aggregate size and packing is vital.

1.2 Scope and objective

This dissertation aims to develop thermal resistant building materials for the future sustainable construction industry. The research concept centers on improving the high temperature performance of geopolymer-based materials via binder gel tailoring and structure design, considering both economic and environmental factors. The focus can be divided into three interrelated topics.

1.2.1 Thermal degradation mechanism of geopolymer-based materials

The understanding of the degradation mechanism of geopolymer-based materials at elevated temperatures is of great importance for the thermal performance optimization, which remains unclear. With the aim to clarify the degradation behavior of geopolymers, on the one hand, the thermally induced chemical transformations, such as gel and crystalline phase variation are determined. On the other hand, physical changes, including density, pore structure, and cracking behavior under elevated temperatures are characterized. Subsequently, the interrelation between the physicochemical changes and thermal-mechanical evolution of geopolymer-based materials is revealed to elucidate the degradation mechanism.

1.2.2 Gel development by precursor tailoring

The drive to enhance the performance of geopolymer binders has spurred research efforts toward exploring new precursor formulations. In consideration of its waste nature and advantageous phase composition, ladle slag is proposed as a co-precursor in the joint alkaline activation with Class F fly ash. Firstly, the impact of ladle slag on the geopolymer system

regarding the reaction process, gel composition, microstructural formation, and mechanical properties are studied in detail. Furthermore, to optimize the gel system, the alkali activator parameters are tailored to control the Ca availability in the hybrid geopolymer system. The subsequent influence on the gel compatibility is monitored via gel phase identification and microstructural formation. The high temperature behavior of the designed binder concerning phase transformation, structural change, and residual strength is examined. Lastly, the role of gel compatibility in determining the room/high temperature behavior is clarified.

1.2.3 Structure optimization by physical design

Apart from the gel development, the incorporation of fiber and aggregate has been acknowledged as an efficient way to mitigate thermal-induced damage on geopolymer-based materials. To develop fiber reinforced geopolymer composites for high temperature applications, mineral wool waste is proposed as both co-precursor and micro-fiber reinforcement. The effect of ions dissolution and particle dimension of mineral wool waste on geopolymer system is evaluated to reveal the feasibility of recycling mineral wool waste in geopolymers. Moreover, based on particle size distribution theory, a practical design methodology is proposed for the development of high temperature resistant geopolymer composites. A comprehensive picture of the thermal progressive evolution of geopolymer composites is built for advancing high temperature resistant geopolymer composite design.

1.3 Outline of the thesis

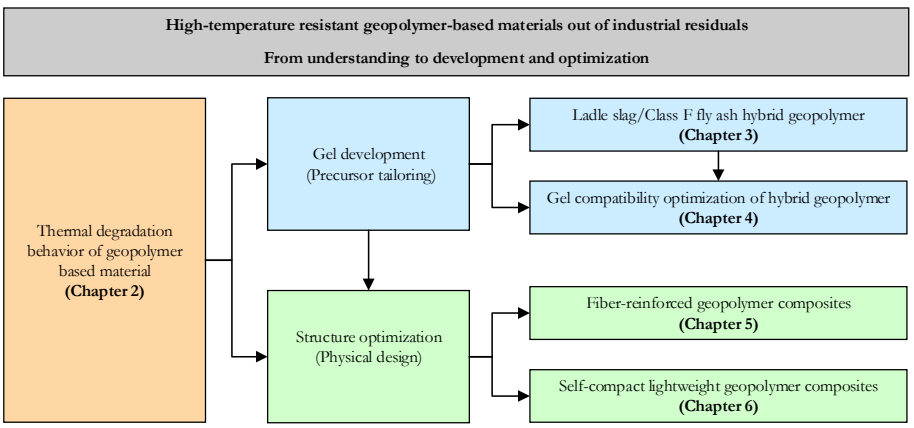

Fig. 1.5 Outline of the thesis.

The outline of this dissertation is depicted in **Fig. 1.5**.

Chapter 1 briefly discussed the research background, motivation, scope, and objective.

Chapter 2 performs a comparative study on plain Class F fly ash geopolymer and hybrid GGBS/Class F fly ash geopolymer. The physicochemical transformations up to 800 ˚C are

systematically investigated and interrelated to clarify the thermal degradation mechanism of geopolymer-based materials. Based on the mechanism understanding, methodology and strategies are proposed to develop and optimize high temperature resistant geopolymers.

Chapter 3 introduces an industrial by-product, ladle slag as co-precursor in Class F fly ash geopolymer. The effect of ladle slag on the reaction process, hydration products, durability, and thermal behavior of the hybrid geopolymer is evaluated, and the geopolymerization reaction with ladle slag incorporation is revealed.

A continuous study is presented in **Chapter 4**, where the Na_2O percentage and silica modulus in the alkali activator are tailored to control the ladle slag dissolution in the hybrid geopolymer system. The effect of Ca availability on the gel compatibility of the hybrid geopolymer system is clarified. Subsequently, the role of gel compatibility in determining the room and high temperature performance is studied in detail.

Chapter 5 aims to recycle mineral wool waste in class F fly ash geopolymer for high temperature application. The role of mineral wool waste in geopolymer system is examined with consideration of both ion dissolution and fiber dimension. The feasibility of applying mineral wool waste in geopolymers is evaluated by reaction kinetics, phase assemblage, microstructure, durability, and high temperature stability.

Chapter 6 introduces the particle size distribution theory to tailor the particle packing in geopolymer composites with normal quartz sand or lightweight aggregates. The interaction between geopolymer binder and aggregate packing is revealed by characterizing microstructural-thermophysical properties, heat transfer pattern, and thermal behavior via both experimental and modeling approaches.

Chapter 7 summarizes the major findings from the presented dissertation and provides corresponding recommendations for future research.

CHAPTER 2

Degradation mechanism of fly ash-based geopolymers exposed to elevated temperatures

As a promising alternative to alkali-activated fly ash (AAF) for high temperature application, the degradation mechanism of alkali-activated fly ash/GGBS (AAFS) under high temperature is not clear. This chapter investigates physicochemical properties of AAFS up to 800 °C and presents their synergetic influence on the thermal behavior. A quantitative assessment of the crack is developed to learn the cracking behavior. Results reveal that the crack density exhibits a linear relationship with ultrasonic pulse velocity. The crack density and compressive strength exhibit a positive correlation before 100 °C, but a negative relationship beyond 100 °C. The addition of slag into geopolymers lessons the geopolymeric behaviors such as further geopolymerization and viscous sintering, but further aggravates the thermal damage owing to the compact structure and unstable hybrid gel. The conceptual models of AAF and AAFS are proposed to explain the degradation mechanism of low slag contained geopolymers under elevated temperatures.

This chapter has been published in the following article:

Y. Luo, S.H. Li, K.M. Klima, H.J.H. Brouwers, Q.L. Yu, Degradation mechanism of hybrid fly ash/slag based geopolymers exposed to elevated temperatures, Cement and Concrete Research 151 (2022), 106649.

2.1 Introduction

Alkali-activated fly ash (AAF), also named geopolymer, exhibits significant mechanical property and structural integrity under high-temperature exposure compared to Ordinary Portland cement (OPC) binders [52–54]. For this reason, geopolymers have received the most attention in terms of fire resistance nowadays, which enables a broad range of applications including fire-resistant materials [13,55,56], thermal insulators [57–59], thermal energy storage concretes [60]. However, for AAF, the energy-consuming high-temperature curing process, as well as the unsatisfied initial strength, largely hinder the further development of its in-situ applications [61]. To counterbalance these limitations, growing attention has been paid to blended alkali-activated fly ash/GGBS binders (AAFS), which combine aluminosilicate source (fly ash or metakaolin) with calcium additives [28,62,63]. The calcium source from the substitution of slag could not only contribute to the formation of C-(A-)S-H gel, but also partially replace sodium from N-A-S-H gel to form N-C-A-S-H hybrid gel, which results in a higher degree of cross-linking [64–66]. Therefore, the AAFS blends could exhibit a good initial strength with no need of high temperature curing. In terms of high temperature application, different from AAF that exhibits strength gain after elevated temperature exposure, AAFS specimens with higher initial strength eventually exhibit more violent loss of mechanical strength [30,51,67,68]. With the increasing addition of slag, AAFS blends exhibit severer weight loss along with more cracks and deteriorations [30,68]. This strength deterioration is highly associated with the physicochemical transformation of AAFS blends. However, up to now, it remains largely unexplored regarding the thermal degradation of AAFS in comparison to that of AAF.

As well known, the evolution of alkaline activated materials under high temperature is a complex process that conjuncts with chemical transformation and physical changes at the same time. Lahito et al. [69,70] reported that, in fly ash-based system, two major mechanisms, namely, matrix densification and crack formation, determine the mechanical strengths when exposed to elevated temperatures. The matrix densification favors a strength gain, while the formation of cracks accounts for the loss of strength. However, for AAFS hybrid system, due to the coexistence of N-A-S-H, C-A-S-H or hybrid N-C-A-S-H type gels, their evolution under elevated temperature is more complicated. The mechanical properties of AAFS blends under elevated temperature are both similar to those of AAF and alkali-activated slag. For instance, Park et al. [24] reported the strength gain of AAFS blends before 400 ºC is influenced by the further geopolymerization of unreacted fly ash. Pan et al. [30] and Lee et al. [31] concluded that the strength loss of AAFS blends at elevated temperatures is associated with vulnerability of C-(A-)S-H to dehydration and re-crystallization. As a result, the interaction between chemical transformation and physical change on thermal

mechanical behavior of AAFS involves in several interactive mechanisms during high temperature exposure, such as further polymerization, dehydration and decomposition, crack formation, re-crystallization and sintering reaction. Nevertheless, very scarce work has systematically connected all the mechanisms and investigated their synergetic influence on the degradation of AAFS blends under high temperatures.

Moreover, it is well acknowledged that the physical change of the AAM matrix caused by cracking would have a direct influence on their further high-temperature performance [71,72]. But limited data are available concerning the cracking behavior of the AAFS blends under high temperatures. Çelikten et al. [67] found that the depth and number of the cracks in the AAFS mortars increase with the exposure temperature, which further has an adverse impact on their flexural and compressive strength. Dudek et al. [73] compared the cracking behavior between AAFS and AAF mortar, indicating that the AAFS shows larger crack widths and higher crack occurrence frequency as compared to the AAF system under elevated temperatures. In addition, the hybrid AAFS system has a different cracking behavior from sole alkaline activated fly ash or slag materials, which ultimately leads to a different degradation behavior under high-temperature exposure. However, the relationship between cracking behavior and mechanical strength deterioration of AAFS blends that is connected to physicochemical transformations induced by elevated temperatures has not been addressed yet. Moreover, the mechanisms of mechanical evolution of the hybrid AAFS system under elevated temperatures are not well understood either.

The objective of this chapter is to reveal the mechanism behind the mechanical evolution of AAFS blends under elevated temperatures and clarify the interaction between the concerning competing mechanisms by investigating the synergetic influence of chemical transformation and physical change. A pure fly ash-based paste is introduced as a reference to the hybrid system. To learn the chemical transformation and physical changes of binders exposed to high temperatures under different conditions (20, 100, 200, 400, 600, 800 °C), the chemical properties are evaluated by X-ray diffractometry (XRD), Fourier transform infrared (FTIR) spectroscopy and thermal gravimetric analysis (TGA) analysis. Physical properties including density, pore structure, microstructure, are detected by using pycnometry, mercury intrusion porosimetry (MIP), scanning electron microscopy (SEM) and ultrasonic pulse velocity (UPV) before and after exposure to different temperatures. In addition, to further reveal the mechanical degradation of the hybrid AAFS binder under high temperatures, a quantitative characterization of microcrack based on MATLAB is performed to study their cracking behavior and its influence on the residual strength of AAFS blends.

2.2 Materials and methods

2.2.1 Materials

The raw materials investigated in this study are Class F fly ash (FA) and ground granulated blast furnace slag (GGBS). FA is commercially purchased from the Netherlands with an average particle size (d_{50}) of 21.09 μm. GGBS with a d_{50} of approximately 19.38 μm is provided by ENCI (IJmuiden, the Netherlands). The particle size distribution of the FA and GGBS is determined by a laser particle size analyzer (Mastersizer 2000, Malvern Instruments, UK), shown in **Fig. 2.1**. The chemical composition of the FA and GGBS, as shown in **Table 2.1**, is analyzed using X-ray fluorescence spectrometry (XRF) (PANalytical Epsilon 3), and the loss on ignition has been determined from 105 ˚C to 1000 ˚C. The XRD patterns of raw FA and GGBS are shown in **Fig. 2.2**. In FA, the presence of crystalline phases quartz (SiO_2) and mullite ($Al_{1.69}Si_{1.22}O_{4.85}$), hematite ($Fe_2O_3$) and magnetite ($Fe_3O_4$) are detected. The GGBS shows several low intensity peaks that are related to anhydrite ($CaSO_4$) and calcite ($CaCO_3$), with a broad amorphous hump between 30° and 40°. Sodium hydroxide pellets (analytical level) and sodium silicate solution (27.69 wt.% SiO_2, 8.39 wt.% Na_2O, and 63.9 wt.% H_2O) are used for alkaline activator. Distilled water is used to obtain a certain water/binder ratio.

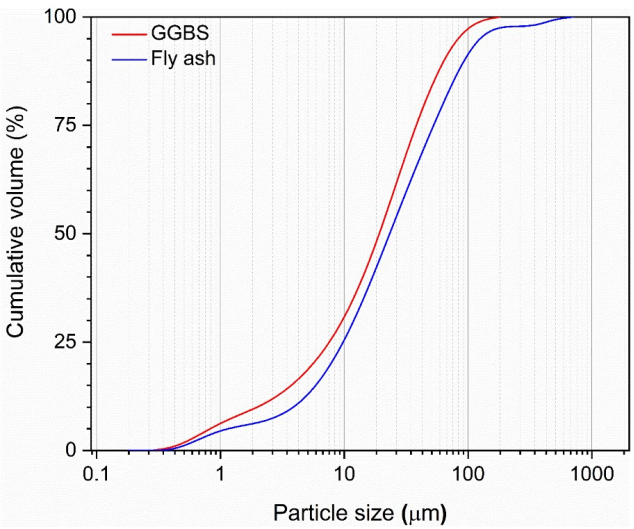

Fig. 2.1 The particle size distribution of raw materials.

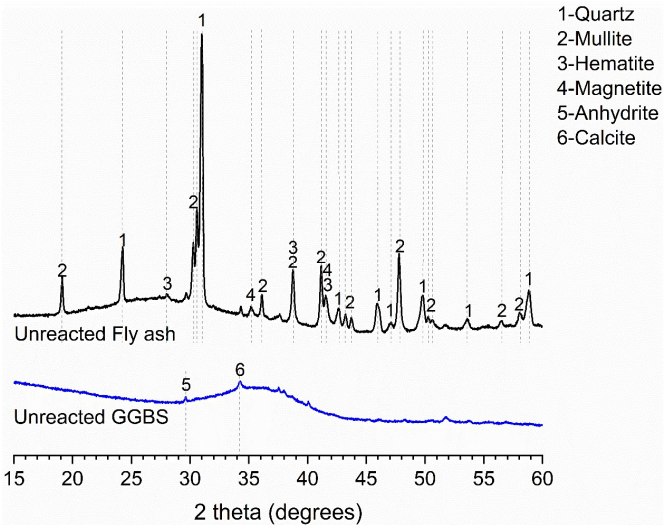

Fig. 2.2 XRD patterns of GGBS and fly ash.

Table 2.1 Chemical composition of fly ash (FA) and ground granulated blast furnace slag (GGBS).

Oxides (%)	FA	GGBS
SiO_2	53.06	29.41
Al_2O_3	25.23	13.21
CaO	5.27	41.67
MgO	1.05	8.57
Fe_2O_3	8.23	0.37
K_2O	2.01	0.42
SO_3	0.56	2.64
TiO_2	1.61	1.49
Other	0.62	1.07
LOI	2.42	1.15
Specific density (g/cm^3)	2.30	2.93
Specific surface area (m^2/g)	0.82	0.37

2.2.2 Sample preparation

The alkali-activator was synthesized by mixing sodium hydroxide pellets, sodium silicate solution, and distilled water at a certain ratio, and the blended solution was kept at ambient temperature for 1 day prior to use. For all samples, the silicate modulus (Ms) was set constant as 1.4 and the equivalent Na_2O% was kept at 5.6 wt.%, because these appeared to be optimum values [74]. The water to solid ratio by mass was 0.35 in all pastes, in which the water consists of the added distilled water as well as the water in sodium silicate solution. The chosen activator modulus, equivalent Na_2O wt.%, and water to binder ratio were determined in advance to not only reach a sufficient activation with satisfying

flowability but also obtain decent integrity after exposure to elevated temperatures for further characterization.

According to previous works [30,68] and our preliminary experiments, high slag substitution would result in an unstable matrix with drastic inner damage and microstructural change at high temperatures, making the characterization of thermal degradation, especially cracking behavior, more complex. Therefore, the blend weight ratio of FA to slag was set as 95/5 (denoted as AAFS), and a pure FA sample was prepared as reference (denoted as AAF). For the preparation of samples, dried raw materials were firstly mixed by using a 5-liter Hobart mixer. When the raw materials reached a homogeneous state, the activator solution was slowly added while stirring. The mixtures were mixed at a low speed for 30s and another 120s at a high-speed. The fresh paste was poured into prismatic molds (40 mm ×40 mm ×160 mm) and cubic molds (100 mm ×100 mm ×100 mm). Due to the poor dissolution and low reactivity of FA, a 24h of 60 °C curing was carried out on sealed AAF pastes according to [75], and AAFS pastes were sealed and kept at room temperature (20.0 ± 2.0 °C). After 24 h, all samples were demoulded and placed at room temperature in a sealed condition for 27 days before characterization.

2.2.3 Test methods

In order to investigate the chemical transformations, structural changes, and ultimately reveal their co-influence on the thermal behavior of the geopolymers, series of high-temperature exposure treatment were carried out under 100, 200, 400, 600, 800 °C. Multiple analytical methods were carried on the samples after different temperature treatments to build a picture of the physicochemical transformations as a function of temperature. X-ray diffractometry (XRD), Fourier transform infrared spectroscopy (FT-IR) and Thermogravimetry/differential scanning calorimetry (TG/DSC) were applied for evaluating chemical transformations, while density, Mercury intrusion porosimetry (MIP), scanning electron microscopy (SEM), Ultrasonic pulse velocity (UPV) for structural changes. To prepare the powder samples for XRD, FTIR, and TG-DSC analysis, the unheated samples at the age of 28 days were crushed and immersed in iso-propanol for 72 h, and then dried at 40 °C for 24 h to cease the hydration, whereas the thermal exposed samples were tested directly.

Elevated temperature exposure procedure

After 28 days of curing, the obtained pastes were exposed to different temperatures of 100, 200, 400, 600, 800 °C, in a high-temperature oven. In general, the thermal treatment for alkali activated materials remain diverse without a universally accepted protocol, and the heating rate applied in previous studies varying from 1 to 10 °C/min [24,30,31,67,68,70,76–80]. In

this work, with a guarantee of providing a decent structure integrity after elevated temperature exposure for further characterization, a heating rate of 10 °C/min was applied to make the results comparable with previous works. In order to reach a uniform temperature distribution within the specimens, the maximum exposing temperature was kept for 1 hour for all samples. The test samples were then naturally cooled down to ambient temperature by opening the vent hole of the furnace. After that, to avoid moisture immersion, all test samples were sealed with plastic film before further characterization. The thermal exposure procedure is shown in **Fig. 2.3**, and it should be noted that the cooling process is depicted in dash line representing the schematic instead of actual situation.

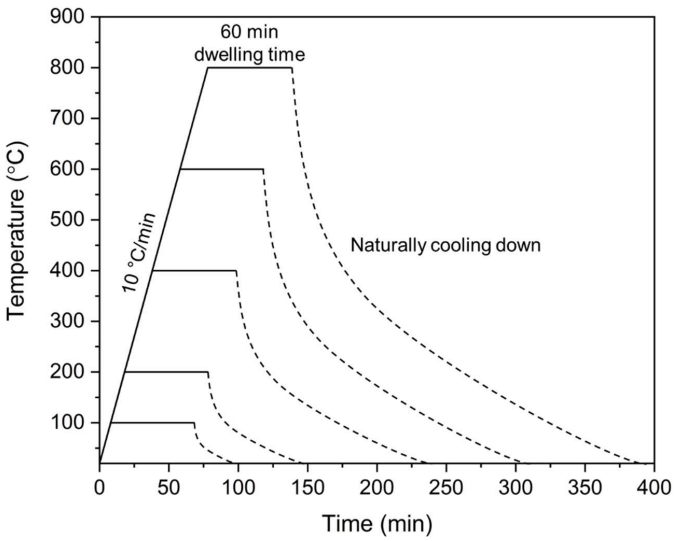

Fig. 2.3 The schematic diagram of heating curve for different target temperatures.

X-ray diffraction (XRD)

The X-ray diffraction (XRD) characterization was conducted by using a Bruker D4 PHASER for investigating the mineralogical phase changes after exposure to elevated temperatures. All samples were then crushed into powder by ball milling for the test. The parameters are set as time 0.6 s, increment 0.02, scanning range from 10° to 60°, 30 KV by Co tube (Co K α1 1.7901 Å and K α2 1.7929 Å).

Fourier transform infrared spectroscopy (FT-IR)

The Fourier transform infrared spectroscopy (FT-IR) measurement was performed in a Varian 3100 instrument with the wavenumbers ranging from 4000 to 400 cm^{-1} with a resolution of 1 cm^{-1}. The reference samples as well as heated samples were ground prior

to the FTIR analysis.

Thermogravimetry/differential scanning calorimetry (TG/DSC)

Thermogravimetry/differential scanning calorimetry (TG/DSC) analysis was conducted using a STA 449-F1 instrument with a heating rate of 10 °C/min from room temperature to 1000 °C and nitrogen as the carrier gas.

SEM with EDS analyses

To determine the changes in morphology of the specimens under different temperatures and identify their cracking behavior, scanning electron microscopy (SEM, Phenom Pro, The Netherlands) equipped with energy-dispersive spectroscopy (EDS) is applied. The test samples with a thickness of 10 mm were cut from the center of thermally treated pastes and then polished to obtain a smooth and flat surface. In order to minimize the effect of drying shrinkage on matrix, prior to the SEM analysis, the test samples were first immersed in isopropanol for 72 h and subsequent dried at 60 °C for 24 h. The dried sample were then coated with Pt or Au using Quorum 150TS plus sputter coater with a current of 40 mA for 30s. Then, the test was performed in a Backscattered electron (BSE) mode under an accelerating voltage of 15 kV. The EDS measurements were carried out on the outer surfaces of the samples. For the cracking behavior study, an image combination method described in Lahoti et al. [69] was applied, as shown in **Fig. 2.4**. A surface area of 400 μm ×400 μm at a magnification of 2000× was captured for all tested specimens.

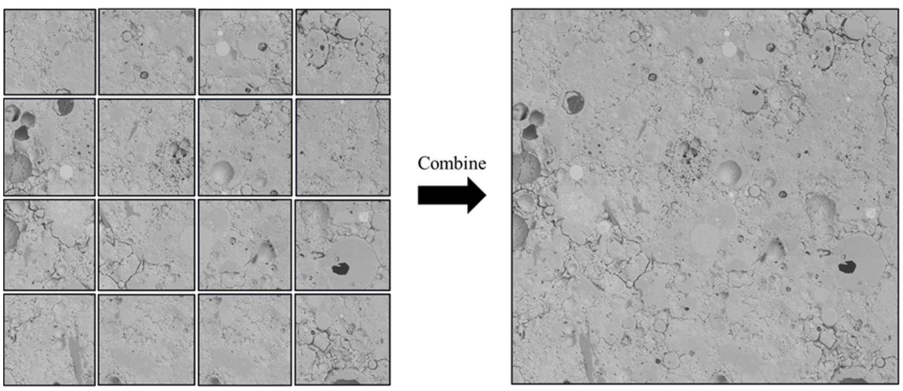

Fig. 2.4 The image combination for cracking behavior study.

Quantification of microcrack characteristics

An automatic quantification method for the characterization of microcrack length and number of microcracks was developed based on grayscale method inspired by previous

studies [81–83]. The script for the crack characterization is written in MATLAB R2019a [84]. High resolution 2D images at 2000× magnification (1024×1088 pixels) with an area of 134 μm ×134 μm obtained by SEM, were analyzed. In this process, four steps were involved, and the example of automated procedure for crack mapping is shown in **Fig. 2.5**. Firstly, a grayscale method was used to distinguish cracks from background and a binary image was created as shown in **Fig. 2.5b**. Secondly, for the calculation of crack length and crack number, the original objects in binary image were skeletonized with a single pixel in thickness, as seen from **Fig. 2.5b-c**. Thirdly, to improve the accuracy of calculation, small objects induced from pixel noise were removed in **Fig. 2.5d**. Fourthly, the microcrack length and microcrack number were automatically calculated based on the identified pixels and structs. The crack density L_A was calculated by

$$L_A = \frac{L}{A} \tag{2.1}$$

where L is the cumulative crack length, A is the size of observation area (17956 μm^2). For each sample, 10 pictures taken in different location were analyzed respectively in order to representatively calculate crack number and cumulative crack length, and the mean value was adopted. Error bars were calculated by the standard deviation from the mean microcrack length, number, and crack density. To validate the proposed automatic procedure, the results are further numerically compared to the UPV results.

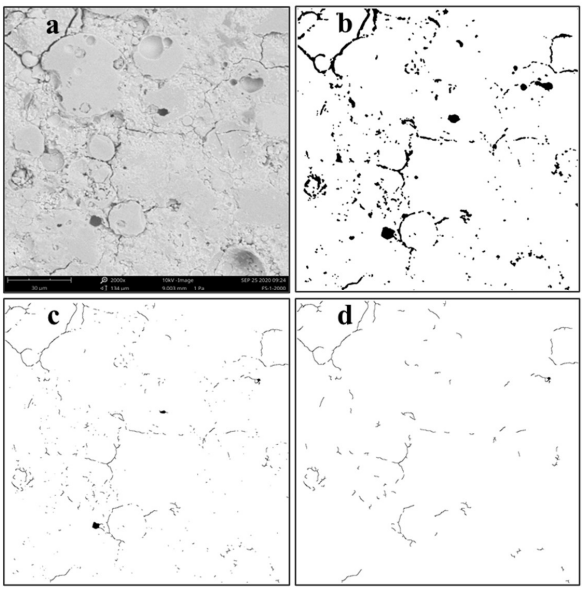

Fig. 2.5 Processing procedure for crack calculation.

Bulk density, skeleton density, and porosity

The bulk density of the obtained samples was calculated by measuring the mass and volume of cubic specimens. The skeleton density was measured using a Micromeritics AccuPyc II 1340 Pycnometer and the test samples were cut into pieces (15 mm×15 mm×25 mm) to fit in the testing chamber (diameter of 35 mm). The porosity was calculated according to

$$Porosity\% = \left(1 - \frac{\rho_b}{\rho_s}\right) \times 100\% \quad (2.2)$$

Where ρ_s represents the skeleton density, ρ_b is the bulk density.

Mercury intrusion porosimetry

To observe the pore structure of the obtained samples, mercury intrusion porosimetry (MIP) analysis was performed using a mercury porosimeter (AutoPore IV 9500, Micromeritics). Before MIP characterization, all tested samples were prepared to be cubic pieces with grain sizes between 2-4 mm. The obtained pieces from fresh paste were immersed in isopropanol for 72 h and dried at 40 ˚C for further test, while the thermally treated samples were tested directly.

Ultrasonic pulse velocity

The ultrasonic pulse velocity (UPV) was determined according to ASTM C597-16 [85]. The test was performed by a Pundit 200, Proceq (Switzerland). A constant signal of frequency 54 KHz, pulse voltage 50 V was sent from a transducer (diameter of 50 mm) to pass through cubic specimens (100 mm ×100 mm ×100 mm), and the signal was captured by another transducer. This method involved measuring the travel time over a known transmit distance of an ultrasonic wave pulse, and the pulse velocity was calculated by dividing the transmission duration from the thickness of the test specimens

$$V = \frac{d}{t} \quad (2.3)$$

Where d represents the distance and t is the transit time.

Mechanical strength test

The compressive strength was determined according to EN 196-1 [86], and paste samples were tested. Before test, the prisms were halved by applying the three-point loading method without being subjected to harmful stress. A loading rate of 2400 N/s was applied,

and the recorded strength value was obtained from the average of 3 fractured parts.

2.3 Results

2.3.1 Chemical transformation

Crystalline phase

The XRD patterns of AAF and AAFS pastes at different temperatures are shown in **Fig. 2.6**. Before thermal exposure, comparable features are identified in AAF and AAFS, with the main crystalline phases are quartz, mullite, hematite and magnetite, which are similar to raw FA. This indicates that the crystalline phase of AAFS is mainly determined by FA. Moreover, the typical slag related hydrates C-S-H is not observed in this work. This might be because, in a high NaOH concentration and low slag addition system, the Ca^{2+} content is insufficient to form crystalline C-S-H gel but replace Na^{+} in geopolymeric gel to form N-(C)-A-S-H hybrid gel [87].

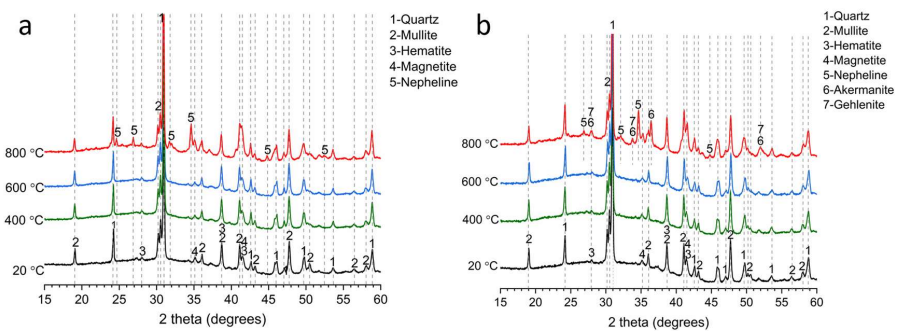

Fig. 2.6 XRD patterns of different materials (a) AAF and (b) AAFS pastes at different temperatures.

When exposed to elevated temperatures, there is no distinct change identified in AAF and AAFS pastes before 600 °C, indicating that both binders are chemically stable without the formation of new crystalline phases. While a significant change in crystalline phases is detected after exposure to 800 °C. An obvious peak of nepheline ((Na, K)$AlSiO_4$) is noticed at around 34° 2 theta in AAF, which is because of the partial crystallization of N-A-S-H gel [70]. Similarly, nepheline is observed in AAFS, confirming the presence of N-A-S-H in hybrid binder. However, a minor majority of akermanite ($Ca_2MgSi_2O_7$) and gehlenite ($Ca_2Al[AlSiO_7]$) are also detected in AAFS. This observation is highly associated with the addition of slag [88]. The crystalline phases of quartz, mullite, hematite, and magnetite can be found at all test temperatures, which are neither affected by alkali activation nor high-temperature exposure.

FTIR

FTIR test is carried out to study the chemical change under high temperatures. **Fig. 2.7a** shows the FTIR spectra of raw FA and GGBS. The main band observed at 870 cm^{-1} in GGBS as well as the band at 1040 cm^{-1} in fly ash are both attributed to the asymmetric stretching vibration of Si-O-T bonds, in which T represents Si or Al units. For fly ash, the band in the range of 670-850 cm^{-1} is associated with the stretching vibrations of Si-O-Si in quartz. In GGBS, the vibration band at 1420 cm^{-1} is due to the asymmetric stretching vibration of the O-C-O bonds, indicating the presence of calcite, as also observed in XRD (**Fig. 2.2**). And a small absorption band at 670 cm^{-1} is assigned to the asymmetric T-O stretching vibrations.

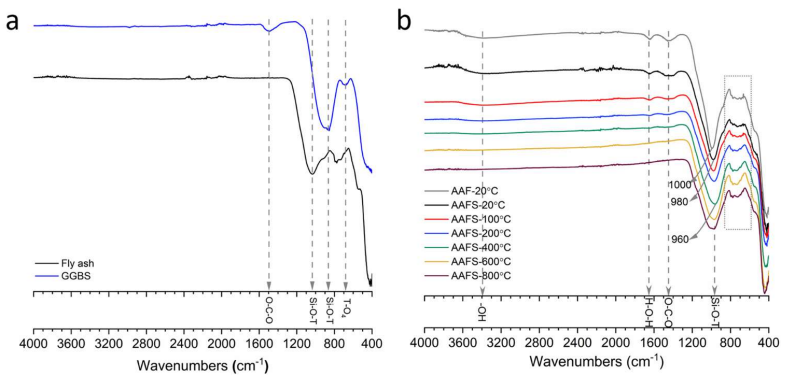

Fig. 2.7 FTIR spectra (a) solid raw materials and (b) AAF and AAFS pastes before and after elevated temperature exposure.

The infrared spectra of AAF and AAFS paste are shown in **Fig. 2.7b**. After alkaline activation, it can be observed that, as compared to raw fly ash, the typical adsorption band of the Si-O-T bridge bond undergoes an obvious shift from 1040 cm^{-1} to 1000 cm^{-1} in AAF, and further shifts to 980 cm^{-1} in AAFS, which indicates the different degree of polymerization. Other chemical bonds observed in AAF and AAFS are identical. A broad absorption band appearing at around 3400 cm^{-1} is associated with the vibration from free water, while the H-O-H bending vibration band at 1640 cm^{-1} is associated with the presence of physically and chemically bond water in the reaction product, which is not identified in the raw materials. As a consequence of thermal treatment, a further shift of the Si-O-T band from 980 cm^{-1} to 960 cm^{-1} is observed in AAFS as the exposure temperature increases from room temperature to 400 °C. It can be related to the increasing temperature favors a further polymerization and a higher degree of calcium contained cross-linking is formed [30]. After exposed from 400 °C to 800 °C, this peak position keeps

constant, but the absorption area becomes broader and wider. This sharp feature is an indicator of the structural disorder in the binder gel induced by elevated temperature [69]. In addition, it should be noted that the absorption band at 3400 cm^{-1} as well as the H-O-H bending vibration band at 1640 cm^{-1} linking to physically and chemically bond water becomes invisible at 600 °C, indicating that the loss of moisture is completed before 600 °C. The vibration band for carbonates from soluble alkali species also disappears between 400 °C and 600 °C. Moreover, there is no significant change in the quartz band between 670 cm^{-1} - 850 cm^{-1}, which is consistent with the previous XRD results, confirming that quartz phase is quite stable at all test temperatures, and only an alpha-beta transition of quartz occurs at around 600 °C [89].

Thermal analysis

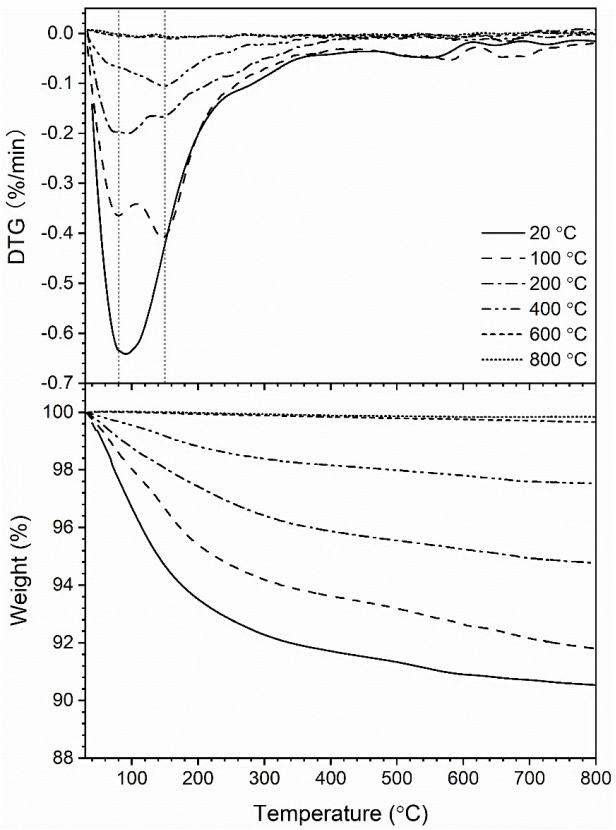

Fig. 2.8 TG-DTG analysis of AAFS blend.

The TG-DTG results of AAFS pastes treated with different temperatures are shown in **Fig. 2.8**. The results can reflect the phase change during thermal exposure test since the same heating rate as thermal exposure test is applied. For unheated specimens, the

maximum weight loss peak can be detected at around 100 ˚C, and this is associated with loss of free water. Furthermore, the weight loss peaks between 480 ˚C and 590 ˚C should be due to the decomposition of calcium carbonates of different crystallinity [90], which agrees with the FTIR results. Some insignificant weight loss peaks after 600 ˚C might be because of the re-crystallization of hydration products [91]. As for thermal treated samples, it is interesting to note that the 100 ˚C treated sample shows two peaks between 20 and 200 ˚C. It suggests that the sharp peak at around 100 ˚C observed in 20 ˚C sample should be derived from two peaks. The first peak at around 80 ˚C is mainly due to the evaporation of free water within the mixture [54], while the second peak observed at around 150 ˚C can represent the initial dehydration of hydrated aluminosilicate species [76,92]. It is possible that the extensive peak due to the loss of free water overwhelms the endothermic peak of chemically bound water loss from aluminosilicates species, thus showing a combined peak in 20 ˚C sample. After exposed to 100 ˚C, free water is partially evaporated, which further weakens the corresponding endothermic peak, and thus two endothermic peaks can be observed at 80 ˚C and 150 ˚C respectively in 100 ˚C treated sample. Here, it should be mentioned that the mass losses before 200 ˚C in low temperature treated samples (100 ˚C, 200 ˚C, 400 ˚C) are resulted from the residual physically and chemically bonded water after corresponding thermal treatment, indicating the relatively low exposing temperature might be unable to remove all evaporable water. By comparing the DTG curves of AAFS exposed to different temperatures, the intensity of the first peak keeps decreasing and could not be detected from 400 ˚C treated sample, which reveals that the free water continues to be released till 400 ˚C. Moreover, the second peak is not identified as the exposure temperature increases to 600 ˚C. It suggests that the hydrated aluminosilicate species experiences a slow and lengthy dehydration process from 150 to 600 ˚C, which is consistent with the FTIR results.

2.3.2 Structural changes

Qualitative observations

The evolution in appearance of the AAFS before and after exposure to different temperatures are shown in **Fig. 2.9**. In **Fig. 2.9a**, before exposure to high temperatures, the obtained AAFS paste exhibits a homogeneous appearance without any visible cracks. It can be observed from **Fig. 2.9b-f** that the sample morphology changes along with increasing exposure temperature, such as the formation of cracks, the changes in color and texture. Among which, the surface color gradually turns to reddish-brown from room temperature to 800 ˚C, owing to the oxidation of iron present in fly ash, which is always the case in the fly ash-based system when exposed to high temperature [93]. The crack development under elevated temperature is in accordance with the mass loss observed in

TG results. When exposed from 100 ˚C to 600 ˚C, the matrix exhibits a more severe cracking. This is mainly because, as the external temperature increases, moisture within the hybrid binder rapidly migrates to the surface and evaporates, which, in turn, causes surface-cracking and internal damage. Notably, a smooth texture with obviously fewer cracks is detected after 800 ˚C exposure, which might be attributed to the healing effect caused by viscous sintering reaction. It should be emphasized that the AAFS blends maintain the structural integrity at all tested temperatures.

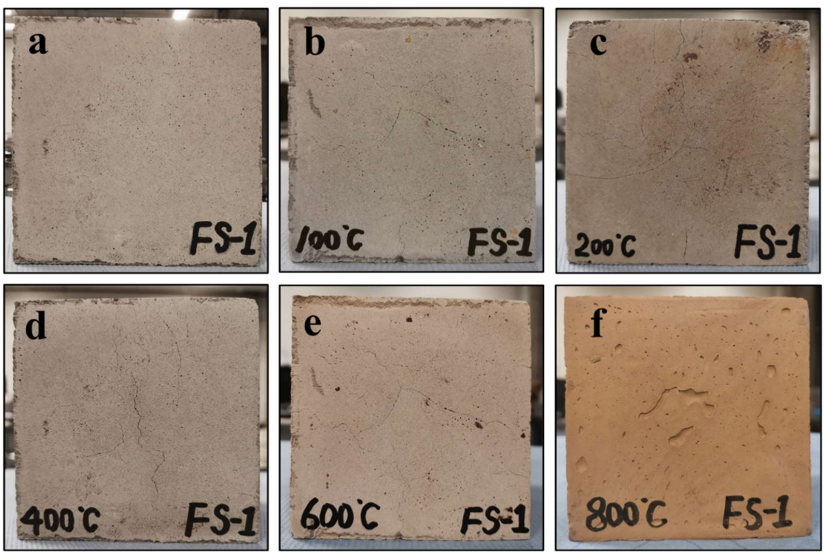

Fig. 2.9 Visual appearance of AAFS pastes at different temperatures. (a: 20 ˚C; b: 100 ˚C; c: 200 ˚C; d: 400 ˚C; e: 600 ˚C; f: 800 ˚C).

Skeleton and bulk density

The volume change of geopolymers under elevated temperatures can be reflected by density variation. Among these, the skeleton density variation trend could reflect the change of binder gel structure under high temperatures, while the change in bulk density represents not only the binder gel but also the pore structure transformation. To identify the unique structural change of AAFS geopolymers under elevated temperature, the variation of skeleton density and bulk density of AAFS is compared with AAF as shown in **Fig. 2.10**.

In **Fig. 2.10a**, it is noted that the initial skeleton density of AAF is higher than that of AAFS, indicating a denser gel skeleton is formed in AAF. Moreover, an obvious rise of skeleton density is observed in AAF from 20 to 600 ˚C, following a sharp reduction after

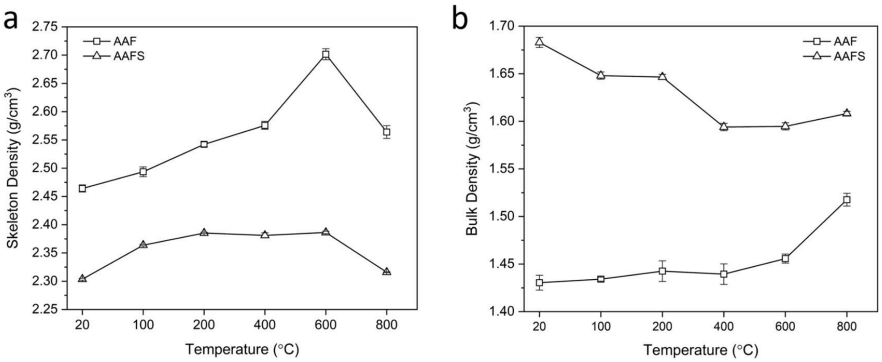

Fig. 2.10 (a) Skeleton density and (b) bulk density of pastes exposed to different temperatures.

800 ˚C exposure. In comparison, the skeleton density of AAFS undergoes a slight increase till 200 ˚C, then stabilizes at around 2.381 g/cm^3 between 200 and 600 ˚C before a drop at 800 ˚C. The rise of skeleton density up to 400 ˚C can be mainly attributed to the further polymerization of the binder as observed in FTIR, which leads to a higher degree of cross-linking. Here, in contrast to the notable densification of AAF skeleton, the insignificant variation of skeleton density in AAFS between 200 and 600 ˚C might be because a balance between the formation of additional gel and depolymerization of binder gel is reached. After exposure to 800 ˚C, the reduction of skeleton density in both matrixes could be attributed to two causes. For one thing, as learned in XRD results, porous crystalline phases such as nepheline are detected at 800 ˚C, which reduces the skeleton density [31]. As a result, more nepheline can be formed in AAF pastes owing to its rich N-A-S-H gel, leading to a more significant reduction. For another, the sintering reaction might account for the skeleton density reduction, which will be explained in subsequent sections.

As shown in **Fig. 2.10b**, the AAFS paste has a much higher bulk density as compared to AAF. When exposed to elevated temperature, the bulk density of AAF almost remains unchanged before 400 ˚C whereafter largely increases up to 800 ˚C, while that of AAFS keeps falling before 400 ˚C, and then a slight increase is detected in the range of 400 to 800 ˚C. The decrease of bulk density before 400 ˚C in AAFS is mainly associated with the drastic mass loss as observed in TG, in which the evaporation of free water and chemically bound water leads to crack formation and looser matrix. In contrast, the loose matrix with a lower bulk density in AAF facilitates the water migration, which remains stable under high temperatures. After 600 ˚C, the viscous sintering of unreacted FA leads to the densification of the matrix [54]. Thus, the bulk density increases in both mixtures, and a larger increase is noticed in AAF.

Pore structure

Fig. 2.11 displays the pore size distribution in AAF and AAFS pastes at different temperatures observed by MIP. It is known that the intrusion data used in MIP analysis are measured by pore throat size instead of pore radii [94], which only serves as comparative indices for the connectivity and pore capacity [94,95]. Due to the fact that cracking has a strong influence on pore throat size as well as pore connectivity [96], the MIP is capable to reflect the inner structure change including inherent pore structure and the formation of cracks. But, it should be mentioned that, due to the threshold effect during MIP measuring, large pores with small pore throat size might be identified as smaller pores, which results in the test intruded value and porosity relatively lower than the actual value [97].

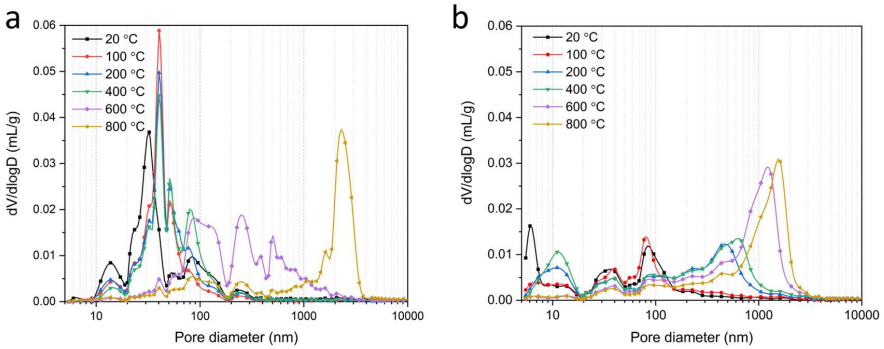

Fig. 2.11 The pore size distribution of pastes subjected to different temperatures, a) AAF, b) AAFS.

Clearly, the AAF and AAFS pastes exhibit different pore size distribution at room temperature. The pore size distribution of AAF sample is mostly below 300 nm with the highest peak centered at around 30 nm, and AAFS has the similar pore size range, but the pores of 5-10 nm is observed to be the highest fraction. Therefore, it can be deduced that AAFS exhibits a higher degree of reaction since the pore size may reflect the reaction degree, and the well-reacted sample exhibits a higher proportion of gel pores (<10 nm) [98]. In addition, different evolution patterns of pore size distribution are observed between AAF and AAFS under high temperature exposure. The pore size distribution of AAF shows an insignificant change with the majority of pores remains below 300 nm before 600 °C. The pore fraction centered at 15 nm is reduced, and the main pore fraction of 30 nm shifts to 40 nm with a higher fraction at 100 °C and keep decreasing from 100 to 400 °C. In accordance with the skeleton density variation, the reduction of pore fraction can be attributed to the further geopolymerization and contraction of geopolymer gel, while the shift of pore fraction to a larger size should be induced by cracking. The pore size distribution transfers to a wider range at 600 °C and then becomes narrower with the main fraction of pore diameter around 2500 nm at 800 °C, which might be because the sintering

reaction fills up small pores, but big voids are formed. As compared to AAF, the pore size distribution of AAFS is relatively stable at 100 ˚C, except the main fraction of pores from 5 nm to 10 nm disappears. However, from 100 to 400 ˚C, the fraction of pore diameter around 10 nm increases, and the pore fraction between 20 nm and 50 nm shifts to a larger diameter from 200 nm to 1000 nm. According to the density change in **Fig. 2.10**, it is possibly due to the dehydration and decomposition of hydrated aluminosilicate species damage the matrix and enlarge the original cracks, contributing to a shift of pore fraction to larger sizes. After exposure to 600 ˚C, the pore size distribution is narrowed with the main fraction of pore diameter around 1000 nm, and no significant change in the pore distribution occurs at 800 ˚C.

To further learn the pore structure evolution under elevated temperature, the porosity of AAF and AAFS at different temperatures are compared in **Fig. 2.12**. Here, to determine the effect of threshold on MIP results, the intrudable porosity from MIP is further compared with calculated porosity. The tested results are relatively lower than calculated porosity for both pastes. By comparison, obvious discrepancy is noticed in AAFS, especially at 100 ˚C, indicating that the threshold effect is more predominant in a dense matrix with low porosity. Here, it is likely that the further geopolymerization occurred at 100 ˚C plays a dominant role in AAFS matrix which narrows the pore throat and largely intensifies the threshold effect, resulting in an underestimate on pore fraction. With increasing exposure temperature, the tested value is getting more approximate to the numerically calculated value in AAFS due to the thermal induced cracking increases the porosity and pore connectivity, hence weakening the threshold effect. In general, there is no significant difference between the porosity from MIP and calculation, and a comparable trend is observed.

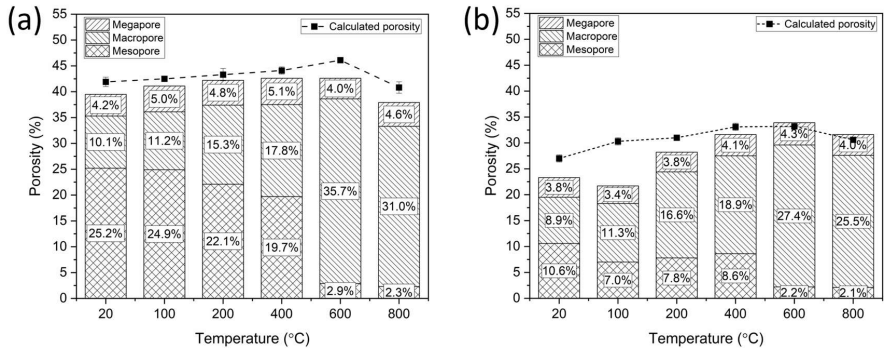

Fig. 2.12 The porosity of pastes at different temperatures from MIP, (a) AAF, (b) AAFS.

As shown in **Fig. 2.12**, it is clear that AAFS paste exhibits a lower initial porosity of 23.3% comparing to AAF of 39.5%. From 100 to 600 ˚C, the porosity of AAFS undergoes an

obvious rise from 21.7% to 33.9%, while that of AAF is stabilized between 41.1% and 42.6%. Reduction of porosity is detected in both samples at 800 ˚C due to sintering reaction, in which a larger reduction of porosity observed in AAF indicates a more drastic viscous sintering occurred in pure FA based geopolymer. In order to identify the thermally induced structural change in different scale, the pore fraction are further divided into three categories: mesopore (2-50 nm), macropore (50-7500 nm), and megapore (>7500 nm) [99]. In AAF, the mesopores keep reducing while the macropore is increased before 400 ˚C. This is because, on the one hand, the further geopolymerization refines the pore structure and reduces the fraction of mesopores. On the other hand, the contraction of geopolymer gel might transform mesopores to macropores. At 600 ˚C, the severe shrinkage of binder gel as observed in **Fig. 2.10a** remarkably contributes to the transformation of mesopores to macropores. By comparison, a similar reduction of mesopores is noticed in AAFS at 100 ˚C due to further geopolymerization. While the mesopores and macropores are observed to increase since 100 ˚C, confirming that the dehydration of matrix and decomposition of binder gel take place simultaneously, which not only introduces microcracks but enlarges intrinsic pores or cracks at the same time. After 600 ˚C, the further degradation of hybrid binder largely increases macropores, resulting in the highest porosity. Accordingly, the thermal-induced pore structure change in AAFS pastes could be divided into 3 stages: i) At 100 ˚C, the formation of additional gel due to the further geopolymerization densifies the pore structure. ii) between 100 ˚C and 600 ˚C, due to the removal of free water and severe decomposition of binder gel further destroy the matrix, the pore interconnection as well as porosity increases continuously. It should be emphasized that before 400 ˚C, the fraction of pores in all size range increases slowly, while a sharp increase of macropore is observed at 600 ˚C, indicating that the matrix undergoes a violent deterioration from 400 ˚C to 600 ˚C. iii) upon 600 ˚C, the viscous sintering starts to dominate the decomposition of binder gel, which densifies the matrix. As a result, the fraction of meso pores largely decreases and a reduction in porosity is observed.

2.3.3 SEM and EDS analysis

The gel transformation at different temperatures is verified by SEM and EDS analysis in **Fig. 2.13a-h**. It should be noted that observable pores around 5-10 μm present in both pastes, which is inconsistent with MIP results. This is likely caused by dropping out of fly ash particles during polishing and/or the threshold effect in MIP measurement. Before exposure to high temperatures, AAF exhibits a loose matrix, consisting of N-A-S-H gel and abundant unreacted fly ash (**Fig. 2.13a**). As for AAFS, a compact matrix with less unreacted fly ash but obvious microcracks is observed in **Fig. 2.13e**. Here, the formation of microcracks is mainly attributed to the autogenous and drying shrinkage during curing

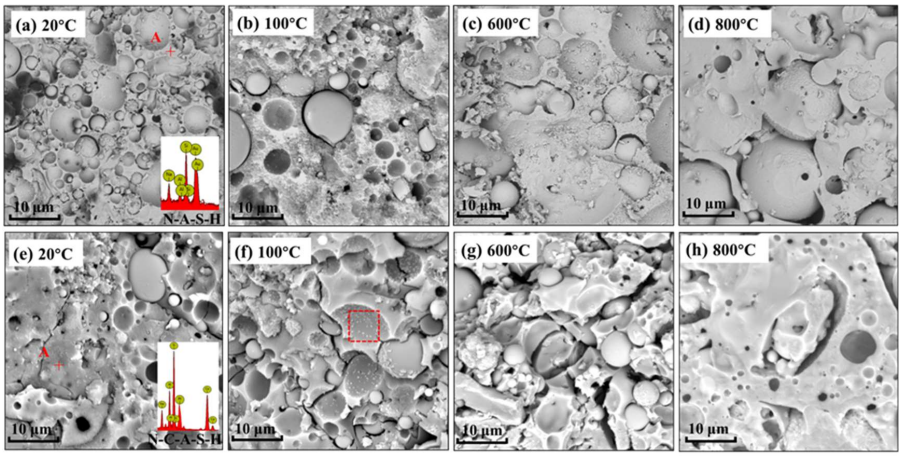

Fig. 2.13 SEM micrographs with EDS results of samples at different temperatures, AAF: (a), (b), (c), (d); AAFS: (e), (f), (g), (h).

because of the synergetic effect of factors such as slag addition, w/b ratio, curing condition [100–102]. Meanwhile, due to the dense matrix, slight number of cracks might be induced during drying process before SEM. In contrast to AAF, the matrix of AAFS is dominated by a hybrid N-C-A-S-H gel, which is consistent with previous studies on blended systems with low slag addition [30,64]. In **Fig. 2.13b** and **f**, a coarser texture with additional grains is detected in both samples at 100 °C. These dispersed grains could be due to the further geopolymerization as also noticed in FTIR and MIP results. As the exposure temperature increases to 600 °C, the binder phase of AAF exhibits a good stability except the unreacted fly ash particles begin to combine owing to sintering, while AAFS binder gel experiences an obvious degradation with wider cracks. It can be explained by the drastic depolymerization of hybrid gel up to 600 °C. After exposure to 800 °C, the AAF and AAFS pastes exhibit an identical transformation to smoother texture in **Fig. 2.13d** and **h**. This, on the one hand, can be attributed to the sintering reaction of unreacted fly ash that contributes to a better inner particle bonding [103]. On the other hand, partial melting of aluminosilicate gel might occur at 800 °C within the system rich in sodium [79], which fixes small cracks and voids. Here, the sintering reaction and partial melting results in a large number of closed spherical pores/voids which is indetectable in MIP analysis, accounting for the reduction in skeleton density and porosity at 800 °C.

2.3.4 Cracking and degradation behavior

The cracks and damage incurred to AAF and AAFS blends prior and subsequent to elevated temperatures are compared in **Fig. 2.14** and **Fig. 2.15**. Before elevated temperature exposure, a loose matrix with numerous unreacted FA particles is detected in

AAF paste. When exposed to elevated temperatures, regardless minor cracks are observed in AAF at 100 ˚C due to water evaporation, the binder is overall stable and getting increasingly denser before 400 ˚C, which can be mainly attributed to further geopolymerization. In accordance with the density variation in **Fig. 2.10**, the binder gel shrinks after 400 ˚C exposure, resulting in the formation of voids and widened interfacial transition zone (ITZ) between the hydration products and unreacted FA particles (See **Fig. 2.14h, j**). At the same time, small holes on the surface of these particles are detected, indicating that the sintering reaction of residual FA initiates at around 600 ˚C. Up to 800 ˚C, a remarkable transition to smoother structure is observed due to the sintering and partial melting.

In comparison, as shown in **Fig. 2.15a**, AAFS initially shows a dense matrix with microcracks occurring in the ITZ. As explained above, microcracks are formed by the shrinkage during curing or drying before SEM analysis. When exposed to 100 ˚C, it is evident that cracks begin to connect through ITZ, and longer cracks are formed. It is because, in a condensed matrix with low ductility, typical long and thin cracks are induced by the evaporation of free water, thereafter, leading to the propagation of cracks through the weak interface. Meanwhile, in the enlarged micrograph in **Fig. 2.15d**, tiny microcracks are less visible after 100 ˚C exposure. Here, the intrinsic cracks are likely to be filled up by the formation of additional hybrid gel at that temperature. However, compared to AAF, the effect of further geopolymerization is lessened in AAFS after 100 ˚C. The matrix deteriorates with two different crack growth patterns (long and narrow crack, tiny and widened crack) observed from 200 ˚C to 600 ˚C in **Fig. 2.15e-i**. During this process, on the one hand, severer thermal stress is generated within the matrix due to the higher exposure temperature, which lengthens and widens the original cracks. On the other hand, the binder gel is observed to be more disordered with evenly distributed small, widened cracks formed after 200 ˚C, and getting looser with a coarser texture up to 600 ˚C in **Fig. 2.15i**. This is mainly because the decomposition of hybrid gel that severely impacts the compactness of the matrix, allowing for the aggregation of cracks and the formation of voids, which could explain the enlargement of porosity in the MIP results. After exposure to 800 ˚C, the matrix exhibits a denser texture without any visible microcracks. The viscous sintering as well as partial melting heal small cracks and fill voids, which is consistent with the rise of bulk density at 800 ˚C in **Fig. 2.10**.

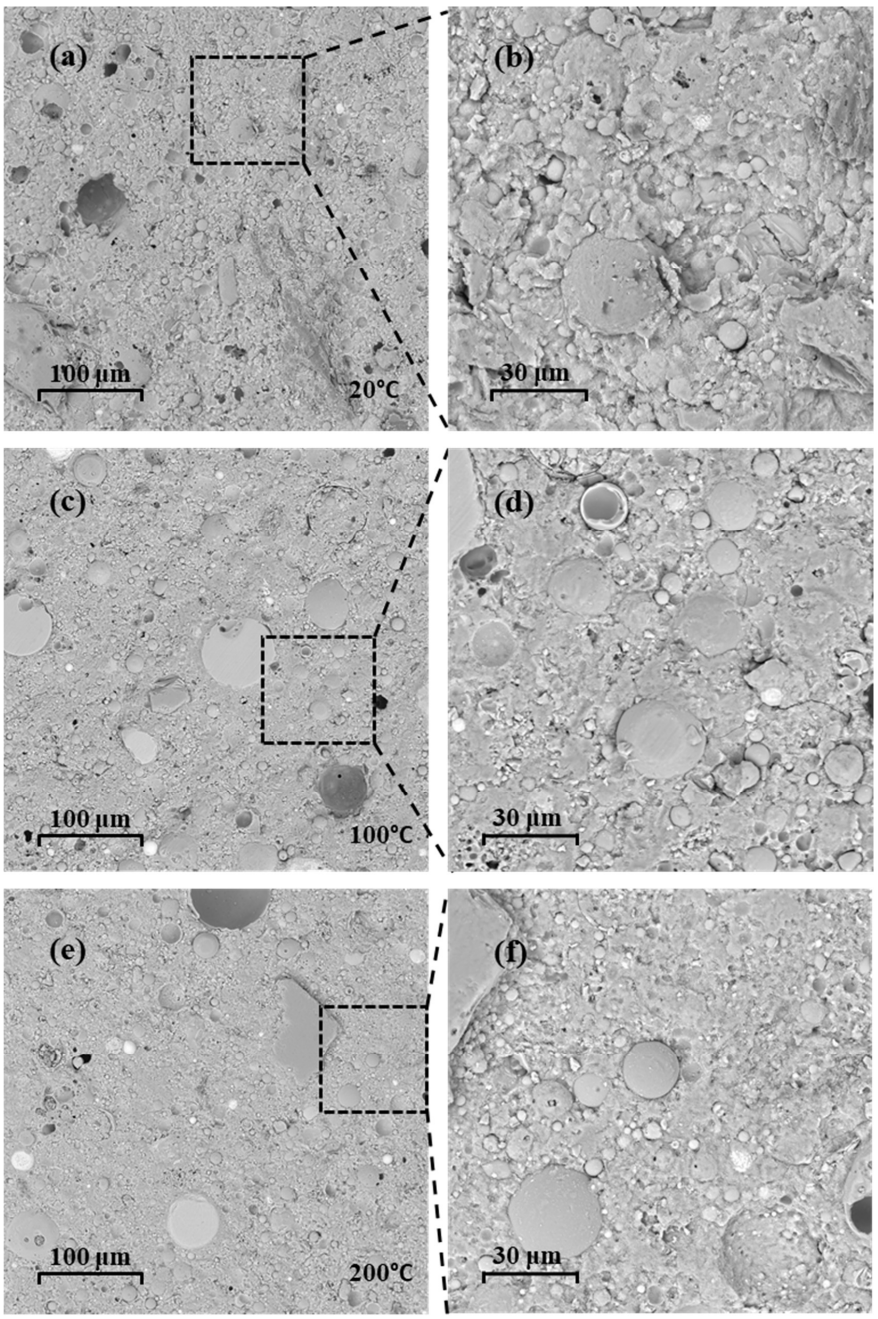

Fig. 2.14 The microstructure of AAF pastes at different temperatures. (a) drying shrinkage and (b) mass loss of miscanthus mortar.

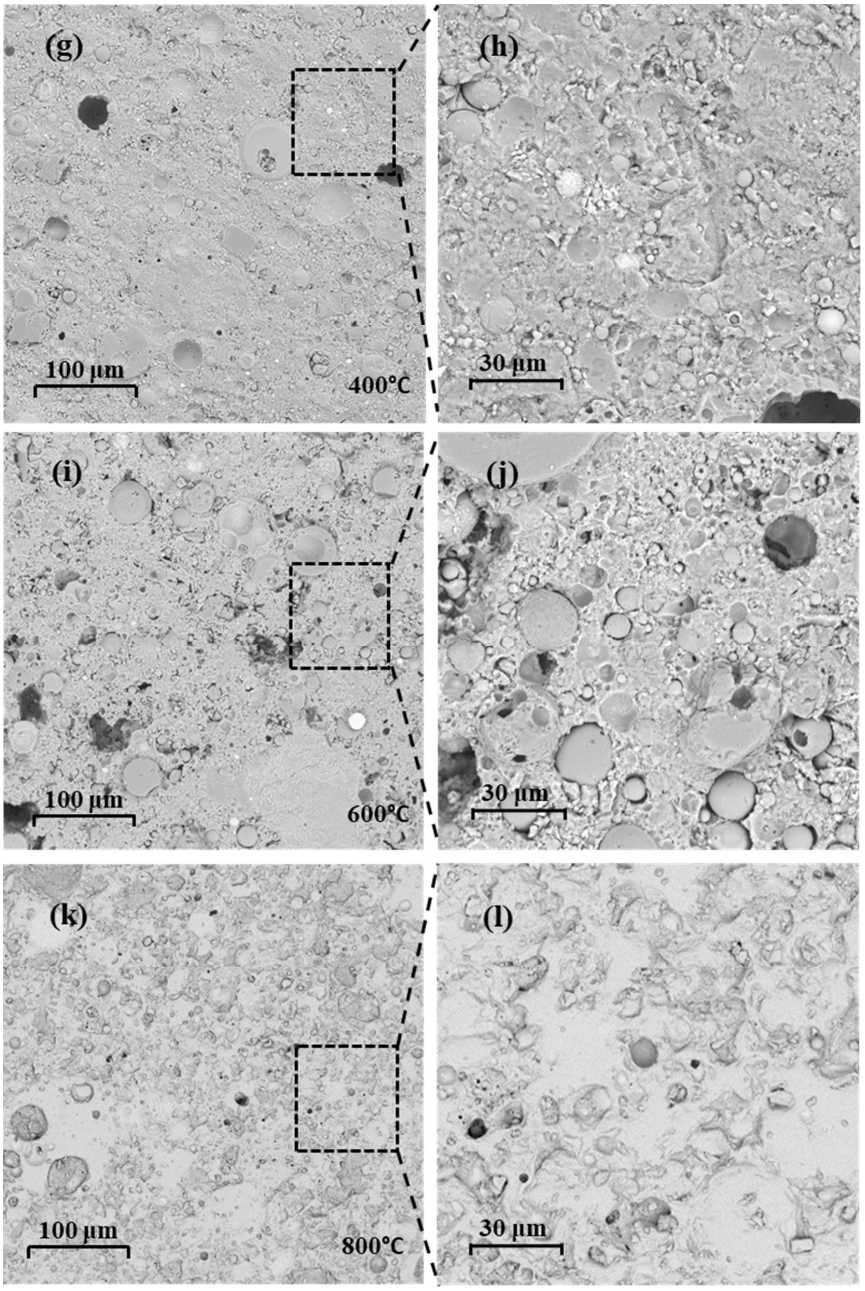

Fig. 2.14 (continued).

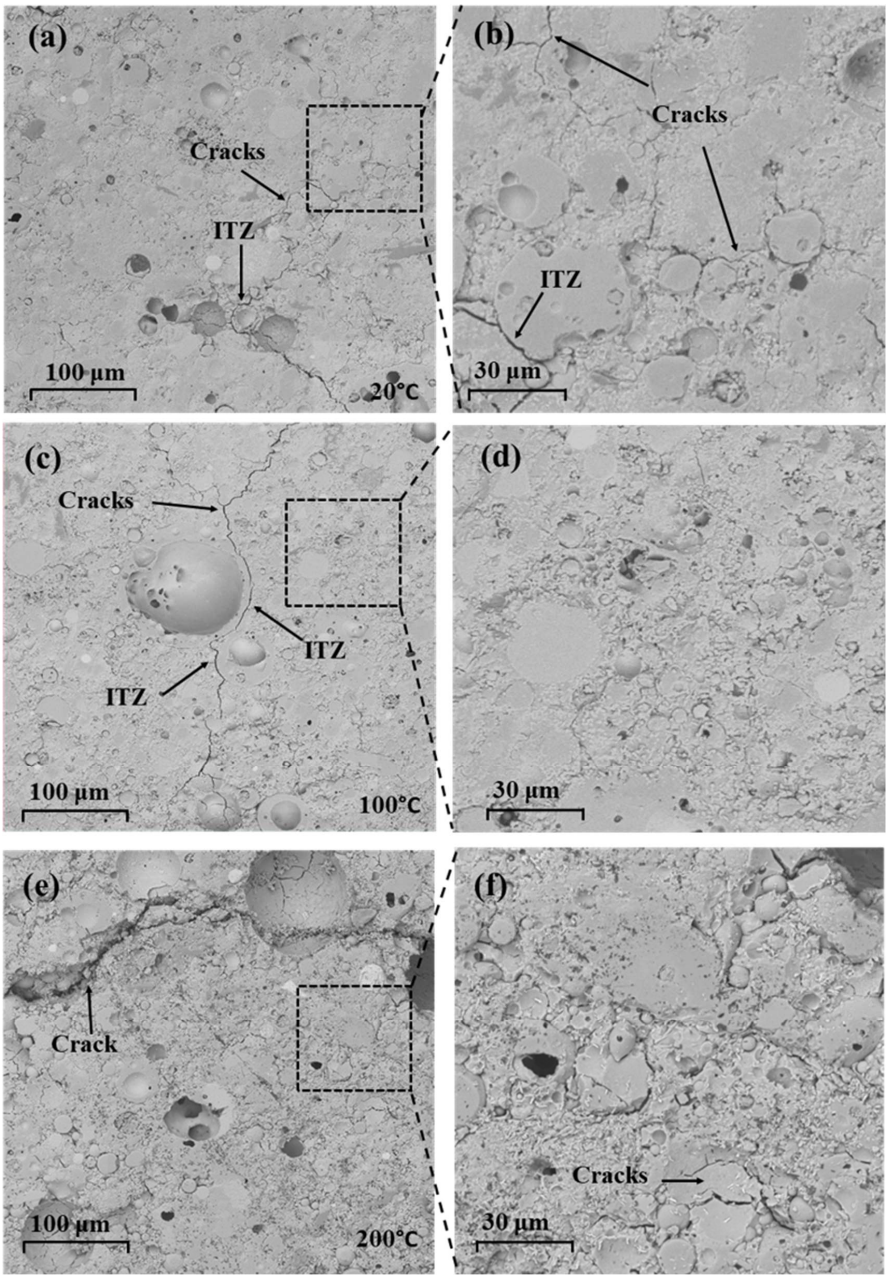

Fig. 2.15 The microstructure of AAFS pastes at different temperatures.

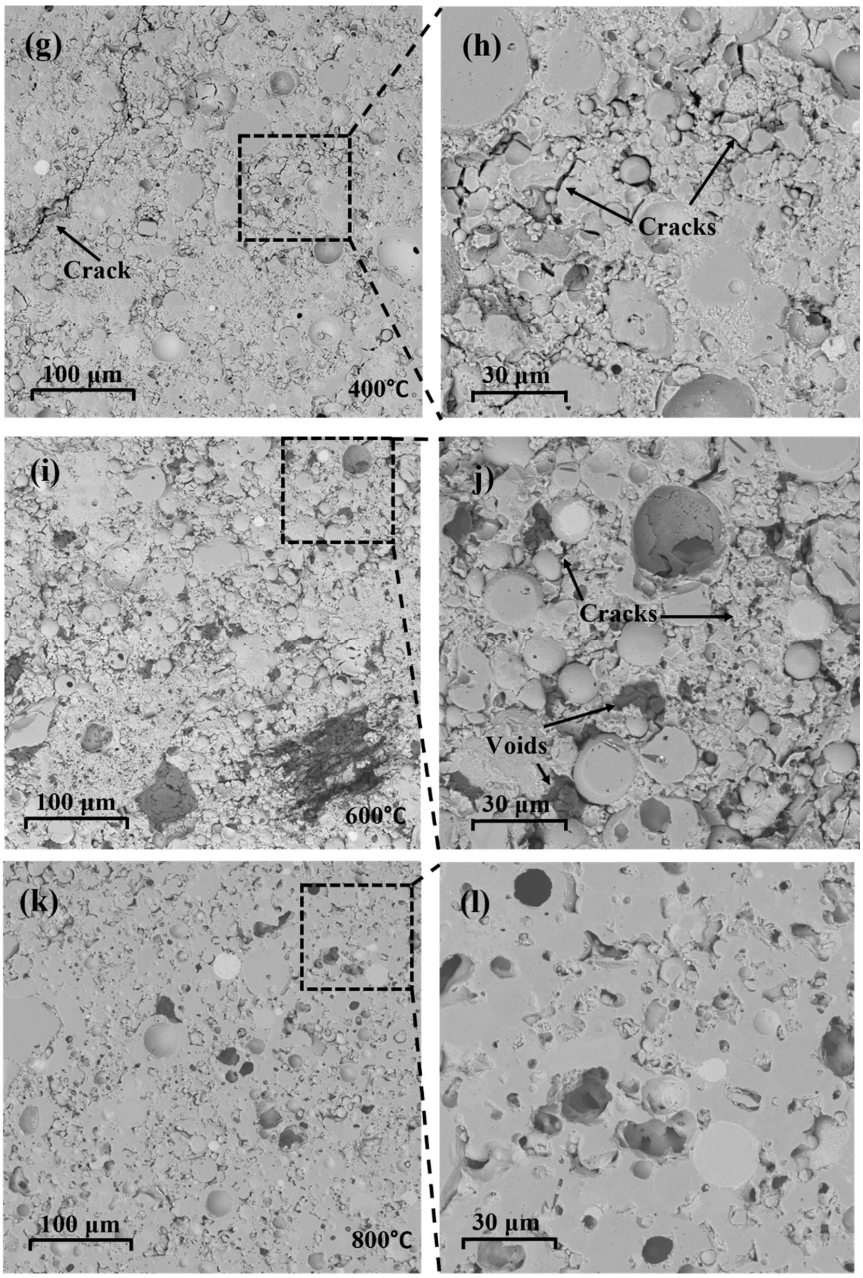

Fig. 2.15 (continued).

In order to understand the cracking behavior, a quantitative characterization of microcrack based on MATLAB is performed on AAF and AAFS, and the evolution of crack number, cumulative crack length and crack density as a function of elevated temperature are summarized in **Table 2.2**. To provide representative results, 10 pictures were analysed for each mixture. The mean value and standard deviation was adopted.

Table 2.2 The observed crack number, crack length and the calculated value of crack length per unit area in AAF and AAFS under different temperature exposure.

Temperature (˚C)	AAF					
	Number of cracks	St dev	Cumulative crack length (μm)	St dev	Crack density (μm/μm²)	St dev
20	32	2	165.6	24.1	0.009	0.001
100	37	3	253.1	36.0	0.014	0.002
200	13	2	117.7	14.8	0.006	0.001
400	39	2	425.4	24.8	0.023	0.001
600	40	2	467.9	50.4	0.026	0.003
800	19	2	249.0	17.6	0.013	0.001
Temperature (˚C)	AAFS					
	Number of cracks	St dev	Cumulative crack length (μm)	St dev	Crack density (μm/μm²)	St dev
20	82	3	775.9	40.7	0.043	0.002
100	95	28	1098.5	66.0	0.061	0.003
200	164	29	1432.3	76.5	0.080	0.004
400	281	51	1637.7	129.3	0.092	0.007
600	103	14	1773.3	82.7	0.099	0.004
800	71	12	895.3	92.1	0.050	0.005

The AAF is relatively stable with few cracks and low cumulative crack length at the investigated temperatures. Reduction in crack number and cumulative crack length is observed at 200 ˚C owing to further geopolymerization, then the binder gel shrinkage with enlarged ITZ that gives rise to the crack number and length at 400 ˚C. By comparison, it is clear that AAFS sample shows a much higher crack number than AAF at the investigated temperatures. The further geopolymerization has a limited effect on against cracking in AAFS, in which the crack number keeps growing from 82 to 281 with an increasing crack growth rate from 100 ˚C to 400 ˚C. Here, the growth of cracks mainly results from the strong inner thermal stress and the decomposition of hybrid gel, and the cracks grow faster as the cumulative thermal stress increases with higher temperature. After 600 ˚C, the number of cracks largely decreases in both pastes. The reduction of cracks after 600 ˚C could be explained from two aspects. For one thing, as exposed to a higher temperature, small cracks begin to converge into large cracks due to thermal stress. For another, microcracks are partially healed by the sintering reaction. In addition, as compared to AAF,

the cumulative crack length in AAFS sharply increases from 799.2 μm to 1623.3 μm up to 600 °C, and interestingly, the growth rate of crack length slows down at higher temperature. This is because, in AAFS matrix, the free water evaporation at a lower temperature (before 200 °C) results in the formation of long cracks and largely increases the cumulative crack length. However, as free water is almost evaporated, small cracks are formed owing to the dehydration and decomposition of binder gel, and thus, the increase of cumulative crack length slows down at a higher temperature (after 200 °C), but the crack number grows faster at this stage. The variation of crack density is similar to that of cumulative crack length in both AAF and AAFS samples.

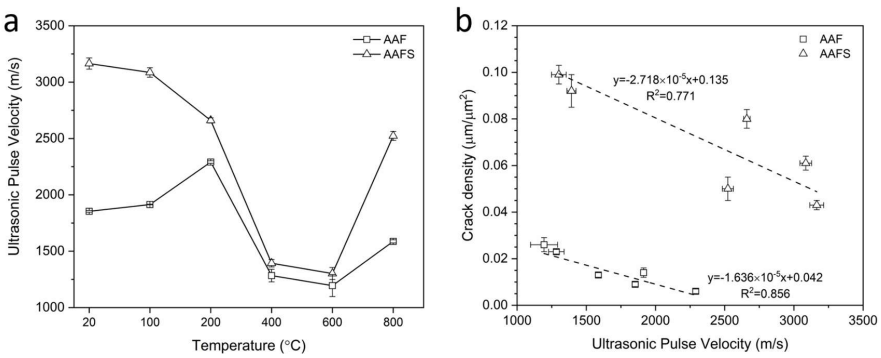

Fig. 2.16 The relation of crack density and ultrasonic pulse velocity of geopolymers under high temperatures.

As a non-destructive characterization for assessing the quality of structural concrete, the capability of UPV on estimating the thermal damage of geopolymers is not yet determined. In this work, UPV is performed on AAF and AAFS before and after exposed to elevated temperatures. In **Fig. 2.16a**, an opposite trend is observed between AAF and AAFS from 20 to 200 °C, the UPV value of AAF is increased, while that of hybrid AAFS is decreased. After 200 °C, the variation of UPV in AAF and AAFS is similar, which reduces from 200 to 600 °C then increases up to 800 °C. Comparable results are reported by Çelikten et al [67] that the UPV value of alkali activated slag/fly ash mortar (slag/fly ash mass ratio: 50/50) kept reducing with temperature rise to 800 °C. Here, the reduction in UPV value is mainly attributed to the formation of cracks or binder shrinkage, which result in more internal flaws and voids. While the increase of UPV is induced by matrix densification because of further geopolymerization or sintering reaction. It can be deduced that with increasing slag addition, the binder deterioration gradually weakens the positive effect of geopolymeric behaviors such as further geopolymerization or sintering, resulting in a continuous reduction in UPV.

To further set up the correlation between the UPV and crack behavior, the variation of

crack density with UPV is plotted in **Fig. 2.16b**. Clearly, a linear relationship is seen, and the UPV is negatively related to the crack density in both mixtures. Moreover, it is interesting to note that the correlation between UPV and crack density in AAF and AAFS is fitted into different linear equations with the slope slightly varies. This might be due to the different initial structural properties in AAF and AAFS, such as porosity and density, etc. In general, the result indicates that the UPV can be applied to effectively evaluate the crack evolution or matrix deterioration during high temperature exposure.

2.3.5 Compressive strength

The strength evolution of AAF and AAFS blends at elevated temperatures are compared in **Fig. 2.17**. Before high temperature exposure, the AAFS paste exhibits a compressive strength of 47.1 MPa, which is promising as compared to sole fly ash-based pastes of 18.1 MPa. It is because the addition of slag leads to a higher provision of Ca and Si than sole fly ash-based system [64,87], and thus, more hydration products are formed in hybrid system. When exposed to elevated temperatures, the compressive strength of AAF shows a sharp rise before 200 ˚C, and then largely maintains the strength gain effect from 200 to 800 ˚C with a 150.3% improvement recorded after 800 ˚C exposure, which is consistent with Kong et al [80]. In terms of AAFS, the compressive strength slightly increases at 100 ˚C, then continuously drops as the exposure temperature increases from 100 ˚C to 600 ˚C, reaching the minimum compressive strength of 26.9 MPa at 600 ˚C. After exposure to 800 ˚C, a slight increase in residual strength is observed.

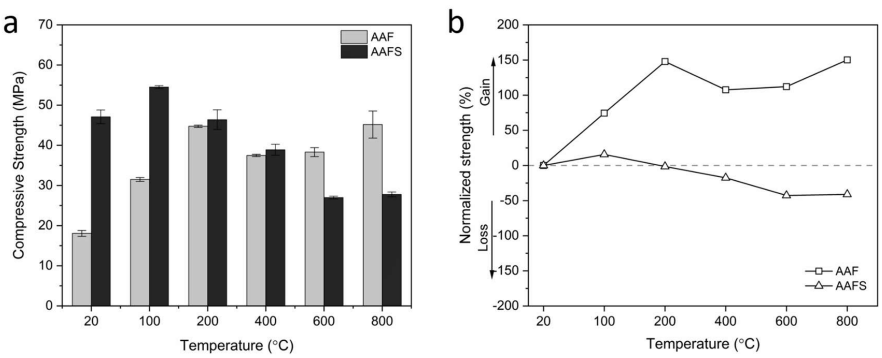

Fig. 2.17 Compressive strength (a) and normalized strength (b) of AAF and AAFS at different temperatures.

At a low temperature exposure, as learned from the corresponding MIP and density results, further geopolymerization refines the pore structure and strengthens the skeleton, which has a positive effect on the compressive strength. However, when compared to AAF, the

higher degree of activation in AAFS in turn hinders the positive effect of further geopolymerization, which only exhibits a slight strength gain up to 100 ˚C. At intermediate temperatures (100-600 ˚C), different from the AAF that exhibits a good binder stability, a severer decomposition occurred in AAFS hybrid binder as shown in **Fig. 2.13** and **Fig. 2.15**. The increasingly crack formation in different scale could be the main reason for the strength deterioration in AAFS. At 800 ˚C, as a result of viscous sintering, a denser matrix with a stronger ceramic bond is obtained, contributing to a higher compressive strength in both matrixes. Here, the insignificant strength gain in AAFS compared to AAF might be attributed to more drastic crystallization occurs in AAFS at 800 ˚C as learned in XRD.

2.4 Discussion

2.4.1 Degradation mechanisms at high temperatures

As exposed to elevated temperature, AAMs experience a series of chemical transformation and physical change at the same time, which has a synergetic influence on its mechanical strength. It is reported that two competing mechanisms, namely, matrix densification and crack formation, determine the residual strengths of sole fly ash-based system on exposure to elevated temperatures [69,70]. However, in terms of AAFS hybrid system, the mechanism of strength evolution under high temperature is more complicated since the AAFS blends exhibit a thermal behavior that is influenced not only by FA but also by GGBS [24]. In order to clarify the fundamental role of slag in the high temperature performance of geopolymers, the typical physicochemical transformation and the related competing influence on thermal behavior of AAF and AAFS blends is compared. The conceptual models of AAF and AAFS are proposed in **Fig. 2.18** to explain the degradation mechanism of AAFS blends under elevated temperatures.

Before exposed to higher temperatures, the AAF sample exhibits a porous structure with abundant unreacted fly ash particles and residual water. By comparison, a dense matrix with low porosity, fewer unreacted fly ash but obvious microcracks are observed in AAFS blends. This is mainly attributed to the addition of slag largely promotes the activation process, leading to a compact matrix with a relatively low ductility. When exposed to 100 ˚C, with increasing inner thermal stress, the porous structure of AAF facilitates the release of water and in consequence, the matrix is largely retained with minor microcracks. In contrast, due to its dense structure with lower pore connectivity, the existing microcracks in AAFS grow longer and wider, and independent cracks begin to connect through the ITZ as observed in SEM (**Fig. 2.15a-d**). On the other hand, the increased temperature favors the further geopolymerization both in AAF and AAFS, which is confirmed by FTIR

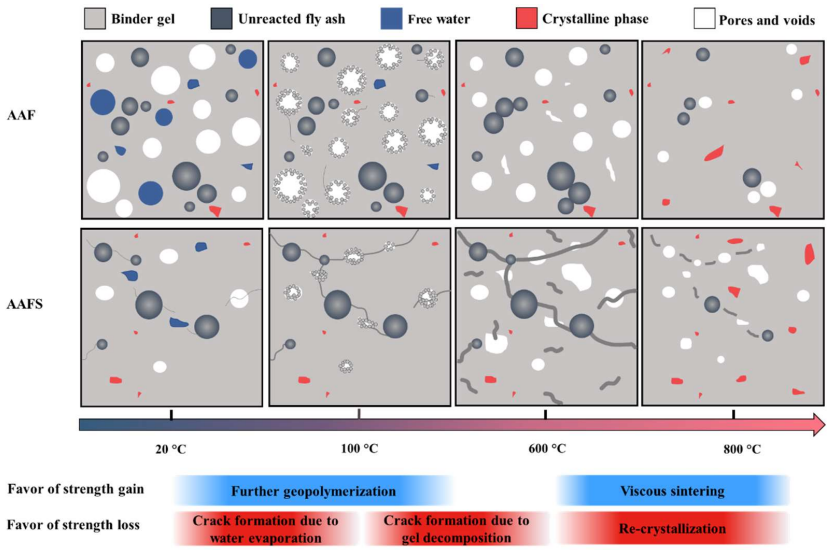

Fig. 2.18 The conceptual model of the degradation mechanism of AAF and AAFS blends under elevated temperatures.

and density results. It is believed that the further geopolymerization plays a key role in geopolymeric matrix to avoid spalling as always experienced by OPC binders under elevated temperature. For one thing, the further geopolymerization consumes part of free water, and thus reduces the inner thermal stress to some extent. For another, the further formation of geopolymer gel would fill in the existing cracks, pores or voids, as noted by a reduction in porosity in **Fig. 2.12**, thereafter strengthening the matrix. Thus, the further geopolymerization at this temperature compensates for the crack formation induced by free water evaporation. As a result, a strength gain is observed.

In the exposure temperature range between 100 and 600 ˚C, the geopolymeric binder of AAF still exhibits a good stability and the further geopolymerization keeps playing a predominant role on AAF up to 400 ˚C. Moreover, the binder phase is detected to rearrange to form macropores due to the binder shrinkage and sintering at 600 ˚C, but no decomposition of the binder gel is observed. In terms of AAFS, the dehydration and decomposition of hybrid gel shows a dominating effect on the matrix. This is because, with the addition of slag, the sodium in N-A-S-H gel can be substituted by calcium to form hybrid N-C-A-S-H gel, thus decreasing its thermal stability [30]. During this period, on the one hand, moisture within the matrix is completely evaporated along with more severe inner thermal stress, which further widens and prolongs the preexisting cracks (**Fig. 2.15e-j**). On the other hand, numerous evenly distributed tiny and widened cracks are formed because of the depolymerization of hybrid gel. The number of cracks rapidly increases

during this stage, which brings more micro defects into the AAFS matrix. Big voids are also formed because of the decomposition of binder. These mechanisms give rise to the increase in macropore and megapore fraction as well as the pore interconnection, as evidenced by the MIP results. Consequently, the AAFS blends undergo a drastic strength loss in this temperature range. It reveals that the formation of cracks is the main cause that induces the strength deterioration of AAFS under elevated temperature. From 600 °C to 800 °C, the mechanisms of re-crystallization and viscous sintering take place simultaneously in AAF and AAFS. New crystalline phases, such as nepheline, akermanite, gehlenite, appear according to the XRD in **Fig. 2.6**. It should be noted that the newly formed porous crystalline phases, such as nepheline, can adversely affects the compactness, leading to a weakened gel skeleton as evidenced by the large decrease in skeleton density in **Fig. 2.10**. At the same time, the viscous sintering consumes remaining fly ash to fill small pores and tiny cracks, resulting in an obvious transformation from rough texture to smooth texture. However, as compared to AAF, a portion of big voids and cracks is remained in AAFS due to the drastic matrix deterioration (see **Fig. 2.15k, l**). A reduction in porosity from MIP results further proves this transformation. Ultimately, the viscous sintering diminishes the adverse impact of crack formation as well as re-crystallization, and the mechanical strength is retained.

In overall, it should be mentioned that the proposed degradation model and mechanism for AAFS is only valid for low slag contained geopolymer (or N-C-A-S-H gel dominated) system. The thermal degradation behavior may vary with higher slag addition since increasing slag addition could alter the resulted phase composition and microstructure, which deserves further investigation.

2.4.2 The relationship between cracking behavior and mechanical strength deterioration

As exposed to high temperature, the mechanical property of geopolymers is mainly influenced by thermal induced physicochemical changes. Different from the sole FA based geopolymer that exhibits a good structural stability under elevated temperature exposure, it is notable that AAFS blends inevitably undergo a drastic matrix cracking. As learned from this work, such a discrepancy can be explained from two aspects. From the perspective of microstructure, the hybrid AAFS geopolymers exhibit a denser matrix with higher initial strength but lower ductility as compared to AAF pastes (See **Fig. 2.10** and **Fig. 2.17**). During high temperature exposure, higher thermal stress can arise from water evaporation due to the compact structure. Meanwhile, the brittleness of the matrix weakens its compatibility for thermal stress during high temperature exposure, which further aggravates the thermal damage (**Table 2.2**). From the point view of binder gel,

owing to the slag addition as a source of calcium, the thermal stability of AAFS hybrid gel (N-C-A-S-H gel) is negatively impacted by the Na/Ca exchange. As evidenced by the crack characterization, small cracks grow rapidly at high temperatures because of the decomposition of hybrid gel, which introduces more defects into the matrix.

As reported in previous works on AAMs [67,76,92,104], it is believed that under elevated temperature, the growth of crack number and size is always accompanied with mechanical strength deterioration. Nevertheless, in the geopolymer system as learned in this study, a more complex relationship between crack behavior and mechanical strength evolution is observed.

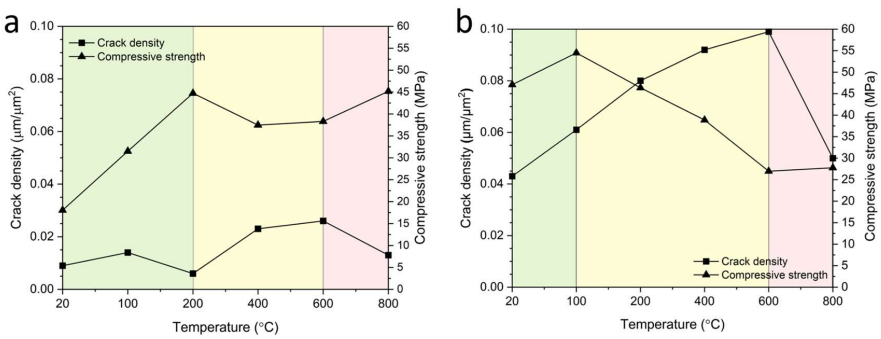

Fig. 2.19 Comparison of crack density and compressive strength under different temperatures, (a) AAF, (b) AAFS.

The variation of crack density and compressive strength at different temperatures in AAF and AAFS are depicted in **Fig. 2.19**. Before 100 °C, the crack density and compressive strength show a positive correlation in AAF and AAFS, the compressive strength increases despite the crack density rises with higher temperatures. While after 100 °C, a negative relationship between the compressive strength and the crack density is observed in both mixtures. Among which, the increase of crack density accompanies with strength deterioration, and the reduction of crack density is associated with strength gain. The observed erratic variation is because in geopolymer system, the mechanical property is not only influenced by cracking behavior but also chemical transformation.

As for AAF, owing to the further geopolymerization, the crack propagation is inapparent at a low temperature, and the crack density is further decreased at 200 °C along with a continuous strength gain. When it comes to AAFS, it is clear that the effect of further geopolymerization is lessened, which could not prevent the increase of crack number and length with exposure temperature. Nevertheless, the further formation of geopolymer gel contributes to a higher degree of cross linking, in that case, strengthening the matrix as

well as avoiding spalling during such a violent cracking process. With the exposure temperature keeps increasing, the cracking behavior starts to have a direct influence on the mechanical property of AAFS as the decline of further geopolymerization, which brings more flaws and voids to the matrix and results in a mechanical degradation. In order to hinder/postpone the adverse impact of thermal induced cracking and improve the thermal performance of hybrid geopolymers, effort can be made to enhance the effect of further geopolymerization by tailoring the molecular silicate modulus or water content.

2.5 Conclusions

This chapter aims to understand the underlying mechanism of the mechanical evolution of hybrid geopolymeric binder when exposed to elevated temperatures (up to 800 °C). With a pure fly ash based geopolymer (AAF) as the reference, the synergetic influence of physicochemical transformation on thermal degradation of alkali-activated FA/GGBS (AAFS) blends is revealed by investigating the physicochemical properties such as the stability of crystalline phase and binder gel, skeleton and bulk density, pore structure, cracking behavior and mechanical strength at different temperatures. The following conclusions can be drawn:

(1) AAFS undergoes a severer thermal deterioration as compared to AAF. The hybrid geopolymer has a denser matrix with high initial strength but lower ductility that creates a high thermal stress during the water vapor evaporation. The brittleness of the matrix weakens its compatibility for thermal stress, which further aggravates the thermal damage. Moreover, the thermal stability of geopolymeric gel is negatively impacted by the slag addition, and small cracks grow rapidly at high temperatures because of the decomposition of hybrid gel.

(2) Two different cracking patterns are detected in the AAFS hybrid matrix under elevated temperatures: a) Long and narrow cracks are formed through the interfacial transition zone (ITZ) because of the inner thermal stress induced by the release of free water. b) Evenly distributed and widened cracks result from the dehydration and decomposition of hybrid gel under elevated temperatures. Among these, long, narrow cracks are observed in the early stage, leading to a rapid increase in the cumulative crack length. While a robust growth of widened cracks is observed in the later stage that largely increases the crack number and brings more defects to the matrix.

(3) Within the investigated temperature region, the crack number, cumulative crack length and crack density keep growing in AAFS until the viscous sintering takes place. The crack density exhibits a linear relationship with UPV, which indicates that the UPV is capable of

estimating the thermal damage or crack evolution of geopolymers under elevated temperatures. The crack density and compressive strength are not always negatively related as a positive correlation between the two is observed before 100 ˚C. It is because the thermal-mechanical property of AAFS is not only influenced by cracking but also chemical transformation. At a low temperature, the further formation of geopolymer gel could compensate for the thermally induced cracks and result in a strength gain.

(4) As compared to AAF, the effect of geopolymeric behaviors such as further geopolymerization and viscous sintering is lessened in AAFS. The further geopolymerization in AAFS consumes part of free water and strengthens the gel skeleton, which largely contributes to the matrix for avoiding spalling as violent water evaporation occurs before 200 ˚C. From 200 to 600 ˚C, the development of cracks due to the severe dehydration and decomposition of hybrid gel gradually dominates the further geopolymerization, accounting for the main inducer of strength deterioration. After 600 ˚C, the sintering reaction not only partially heals the micro/meso pores/cracks but also diminishes the adverse impact of re-crystallization on the gel skeleton, thus the mechanical strength is retained.

CHAPTER 3

Effects of ladle slag on reaction mechanism and high temperature behavior of Class F fly ash geopolymer

Due to its low hydraulic reactivity, ladle slag is currently underutilized with nearly 80% of annual generation is either landfilled or dumped. This chapter investigates the joint activation of LS with Class F fly ash, and the impact of ladle slag on fly ash geopolymer with the focus on activation, hydrates assemblage, conversion process, and thermal behavior. Results reveal that the unique reaction process of ladle slag in alkali activation system shows a positive influence on fly ash geopolymers. Within an alkaline system rich in soluble Si, the initially hydrated CAH phases transform into C-A-S-H, which not only hinders the conversion and enhances the mechanical strength but also retains the geopolymerization. The hybrid geopolymer system exhibits superior thermal performance to pure fly ash geopolymers, especially under high temperature exposure. With increasing ladle slag substitution, more stable crystalline phases are formed at high temperatures. After 800 °C exposure, a high residual compressive strength of 64.7 MPa is achieved with 25 wt.% ladle slag addition compared to 55.2 MPa in pure fly ash geopolymers.

This chapter has been published in the following article:

Y. Luo, K.M. Klima, H.J.H. Brouwers, Q.L. Yu, Effects of ladle slag on Class F fly ash geopolymer: Reaction mechanism and high temperature behavior, Cement and Concrete Composites 129 (2022), 104468.

3.1 Introduction

Fire breakout remains a threat to building structures regardless the decades of improvement on passive fire prevention. As the most widely used construction material, Ordinary Portland Cement (OPC) is prone to structural distortion and mechanical deterioration at high temperatures owing to the thermal decomposition of calcium silicate hydrate and portlandite [6,105]. In the last decades, geopolymer has emerged as a promising fire-resistant binder over OPC. In general, the formation of geopolymer is involved in the reaction of alkali activators with aluminosilicate sources, such as fly ash (FA) and metakaolin [13]. With its typical three-dimensional aluminosilicate networks, geopolymer exhibits superior mechanical performance and structural integrity under high temperatures [22]. Nevertheless, in order to break through limitations such as energy-consuming high temperature curing and unsatisfied mechanical strength, attention has been increasingly drawn into blended alkaline systems for geopolymer nowadays. By incorporating a calcium source, mostly, granulated blast furnace slag (GGBS), into aluminosilicates, a hybrid gel system can be obtained with modified characteristics [28,74,106]. The presence of soluble calcium leads to the formation of C-(A)-S-H gel and thus the mechanical strength can be largely improved. However, the thermal stability of alkali activated FA/GGBS blends is relatively low compared to sole alkali activated FA, and inevitable decomposition and strength deterioration take place after exposure to high temperature [30,31,32].

As a by-product from the steelmaking industry, ladle slag (LS) represents about one-third of the total amount of slag produced in an electric arc furnace [107], and the annual production is estimated to be about 1.9-2.4 million tons annually in Europe [36]. Unfortunately, LS has attracted less attention as compared to its counterparts such as GGBS and basic oxygen furnace slag (BOFS). It is reported that about 80% of LS production in Europe is either landfilled or in store yard [38], and the valorization of LS is extremely low. The further application of LS is largely hindered by its high degree of crystallinity and low Si/Al ratio due to the high basicity and slow cooling procedures in the furnace [37]. Thus, the joint activation of LS with aluminosilicate sources is proposed as an alternative approach to recycle LS as sustainable building materials. For instance, Bignozzi et al. [39] observed that LS partially participated in gel formation when substituting metakaolin, resulting in the coexistence of different types of gels and un-soluble crystalline phases dispersed in the matrix. However, one drawback of utilizing LS as cementitious material is the conversion reaction of calcium aluminate hydrate. The initially formed calcium aluminate hydrates such as CAH_{10}, C_2AH_8, are known to be metastable and will convert into a more stable phase C_3AH_6, which is accompanied by volume shrinkage and strength loss during the engineering application [108,109]. Therefore, to recycle LS as a

supplementary cementitious material (SCM) in geopolymer system for the in-situ application, the conversion reaction must be controlled. Nevertheless, information related to the hydration reaction of LS within alkaline environment is still very limited, and the mechanism behind the conversion process of LS based geopolymers remains unknown.

From the perspective of phase composition and hydration process, LS is comparable to calcium aluminate cement (CAC). As the most important hydraulic binder used for refractory castable and concretes, CAC and its hydration products contain thermally stable crystalline phases at ambient conditions and form more stable compounds at high temperatures [41,110], which equips CAC with superior thermal stability over OPC. But, owing to its low annual production, CAC is considerably four or five times more expensive than OPC that largely raises its application cost [111]. Here, the similarities between LS and CAC in mineralogy and hydration reaction offer great potential for LS to replace CAC and therefore provide a sustainable and cost-efficient way to recycle LS for high temperature applications. However, the information concerning the thermal behavior of alkali activated LS is very limited. Adesanya et al. [112] reported that alkali activated LS based mortar shows comparable thermal performance to CAC under high temperatures, and their thermal behavior such as cracking, volume change, and residual strength is mainly influenced by the hydrated gels. Murri et al. [33] further investigated the thermal behavior of LS blended geopolymer in early-age (7 days) and revealed that the high calcium content and the presence of crystalline phase in LS has a strong influence on the final products after calcination. However, up to now, the long-term influence of LS, especially its typical composition in crystalline phases as well as the conversion reaction between calcium aluminate hydrates, on hydrate assemblage within hybrid geopolymer system is unclear. Moreover, how the resultant hydrate assemblage affects the thermal behavior of hybrid geopolymer deserves further investigation.

The main objective of this chapter is to investigate the reaction and conversion mechanisms of LS within a hybrid geopolymer system and the possibility of utilizing LS as SCM in FA based geopolymers for high temperature applications. The applied slag is directly collected from slag yard and the reactivity of the weathered LS is determined by an alkaline reactivity test. The LS substitution is ranged from 0 wt.% to 25 wt.% based on the preliminary investigation, and the related influence on the reaction kinetics, phase assemblage, conversion mechanism, microstructural and mechanical properties are investigated by a multiple analytical approach, applying calorimetric measurements, quantitative X-ray diffractometry (XRD), thermalgravimetric analysis (TGA), Fourier transform infrared spectroscopy (FT-IR), porosimetry (MIP), micro-computed tomography (micro-CT) and mechanical strength testing. Moreover, high temperature exposure tests (400 and 800 °C) are performed to investigate the phase transformation,

structural change, and mechanical strength evolution under high temperatures.

3.2 Experimental design

3.2.1 Materials

Low calcium (Class F) fly ash (FA) and ladle slag (LS) was used as raw materials in this work. FA was commercially purchased from Vliegasunie, The Netherlands. LS was provided by TATA Steel, The Netherlands, and the slag was collected directly from stockpiles. The received LS was processed using a disk mill to achieve the desired particle size. The particle size distribution of raw materials was determined by a laser particle size analyzer (Mastersizer 2000, Malvern Instruments, UK), as shown in **Fig. 3.1**. The average particle size (d_{50}) of FA and LS were approximately 21.48 μm and 15.22 μm, respectively. The chemical composition was analyzed by X-ray fluorescence spectrometry (XRF) (PANalytical Epsilon 3) and the loss on ignition was determined by the mass difference from 105 ˚C to 1000 ˚C. The detailed chemical composition and the loss on ignition of FA and LS are given in **Table 3.1**. Sodium hydroxide pellets (analytical level of 99 wt.%) and commercial sodium silicate solution (27.69 wt.% SiO_2, 8.39 wt.% Na_2O, 63.9 wt.% H_2O) were applied to prepare alkali activating solution. Distilled water was used to obtain a certain water/binder ratio.

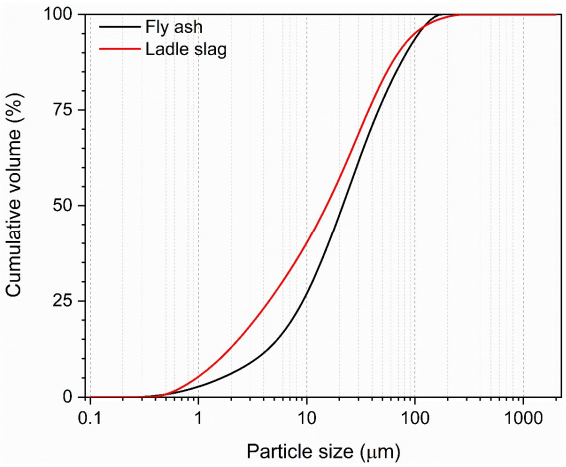

Fig. 3.1 The particle size distribution of raw materials.

Table 3.1 Chemical composition (wt.%) and loss on ignition of ladle slag and Class F fly ash.

Oxide	SiO_2	Al_2O_3	CaO	Fe_2O_3	MgO	SO_3	K_2O	Others	LOI (1000 °C)
Ladle slag	2.46	28.83	51.86	2.60	3.34	0.89	-	0.85	9.17
Fly ash	52.47	26.22	5.42	7.83	1.09	0.38	1.49	2.54	2.56

3.2.2 Sample preparation

Alkali activator with desired silicate modulus (Ms, SiO_2/Na_2O molecular ratio) and equivalent Na_2O wt.% was prepared by mixing a specific amount of sodium hydroxide pellets, sodium silicate solution, and distilled water. The pH value of the alkaline solution was about 13.15 ± 0.30. The obtained solution was kept at room temperature for 24 h prior to being used for geopolymer preparation. The detailed mix proportions are listed in **Table 3.2**. The added LS relative to binder (LS and FA) of 5, 15, and 25 wt.% in mass were used (denoted by FL5, FL15, FL25, respectively) and a control sample without LS was also prepared (denoted by Ref.). In order to study the influence of LS addition on blended system individually, the silicate modulus, as well as the equivalent Na_2O wt.%, were set constant as 1.5 and 6 wt.% respectively for all samples. The mass ratio of water to binder was 0.35 in all pastes, in which the calculated water content consists of the added distilled water and the water in sodium silicate solution. In particular, the applied activator modulus, equivalent Na_2O wt.%, and water to binder ratio were determined preliminarily to provide sufficient alkalinity with acceptable flowability, as well as to ensure good structural integrity after high temperature exposure for further characterization.

All paste specimens were prepared in a 5-liter Hobart mixer. At first, dried precursors with a specific mass ratio were mixed in the mixer to reach a homogeneous state. Then, the alkali activator was slowly added while stirring. The mixture was stirred for 30 s at a low speed and another 60 s at a high speed. Afterward, the slurry pastes were immediately cast into molds in size of 40×40×160 mm^3 and slightly vibrated for 1 min. All the specimens were cured at 20 °C under sealed condition for 24 h, followed by a 60 °C curing for another 24 h. After that, paste samples were demolded and sealed for 26 days at room temperature (20 °C) until further characterization.

Table 3.2 Mix proportions and flowability of the investigated samples.

Sample code	LS/(FA+LS) (wt.%)	Ms	Na (wt.%)	w/b	Flowability (mm)
Ref.	0	1.5	6	0.35	308
FL5	5	1.5	6	0.35	293
FL15	15	1.5	6	0.35	268
FL25	25	1.5	6	0.35	212

3.2.3 Methodology

Flowability

The flowability of the pastes was evaluated using the flow table tests according to EN 1015-3 [113]. A Hägermann cone (base diameter: 100 mm, top diameter: 70 mm, height: 50 mm) was applied for the slump flow test. The fresh pastes were transferred into the cone and then allowed to spread freely for 5 min. Two perpendicular diameters of each spread were measured, and the average value was adopted (**Table 3.2**).

Reactivity test

The reactivity test was performed on dry ladle slag. To provide a feasible environmental alkalinity, an 8 M NaOH solution was applied according to prior studies [114,115]. The applied ladle slag powder was mixed with NaOH solution at a liquid-to-solid ratio of 50 in polyethylene bottles. Then, the sealed bottle was shaken by using a liner reciprocating universal shaker (SM-30, Edmund Bühler) for 24 h at a constant rate of 250 rpm. The residual was filtered with 0.45 μm paper and dried at 40 °C for 24 h before XRD test.

Isothermal calorimetry

The isothermal calorimetry analysis was performed applying an isothermal calorimeter (TAM Air, Thermometric), and the heat release was determined under a constant temperature of 20 °C. About 9.5 grams of pastes were mixed in the ampoule for 1 min to reach a homogenous state and then loaded into the calorimetry immediately. For each mixture, the tests were conducted for 7 days, and the results were normalized by the mass of the solids.

TG-DSC, FT-IR and XRD

The thermogravimetry/differential scanning calorimetry (TG/DSC) analysis, Fourier transform infrared spectroscopy (FT-IR) spectrum, and X-ray diffraction (XRD) characterization were conducted according to the procedures described in **Section 2.2.3**. The tested samples at certain ages (7, 28, and 56 days) were crushed and immersed in isopropanol for 72 h to cease hydration, and then dried at 40 °C for 24 h prior to further characterization. Afterward, the dried samples were ground into powder, followed by passing through an 80 μm sieve. The collected samples were then stored in sealed bags in a desiccator in avoiding water immersion or carbonation before analysis. While samples after high temperature exposure were ground/cut and tested directly.

Rietveld method was applied for the XRD quantitative study. Silicon of 10 wt.% was used

as an internal standard, and the test samples were milled in an XRD-Mill McMrone for 15 min. The data analyses were performed applying TOPAS Academic software v5.0. The crystal structural data used for the qualitative and quantitative XRD analysis are provided in **Table 3.3**.

Mercury intrusion porosimetry (MIP)

The mercury intrusion porosimetry (MIP) analysis was performed according to the procedure described in **Section 2.2.3**. For the tested samples at the age of 28 days, the hydration was stopped before test, while the thermally treated samples were tested directly.

Micro computed tomography (Micro-CT)

Micro-CT 100 (Scanco Medical AG, Switzerland) was used for the tomographic scan. The tested pieces (10×10×40 mm^3) were cut from the center of the specimens to fit into the chamber (Ø 19 mm × H 84 mm). The X-rays energy was set as 70 kV, 200 mA, and an aluminium filter of 0.5 mm was applied, and the pixel resolution for all samples was 10 μm. Tomographic reconstruction was performed using a stack of 205 slices to obtain a 3D visualization. With a 2048×2048 picture resolution, a software for 3D-image processing was employed for pore segmentation and internal structure visualization.

Mechanical strength

The compressive strength of obtained specimens at 7, 28, and 56 days were determined according to EN 196-1 [86], and the procedure was provided in **Section 2.2.3**.

High temperature exposure test

According to the domain factors (dehydration, recrystallization, sintering) that govern the high temperature behavior of fly ash based AAMs, two target temperatures, i.e., 400 and 800 °C were chosen to investigate the thermal behavior of the obtained specimens. The heating procedure was briefly described in **Section 2.2.3**. In avoiding moisture immersion, the thermally treated samples were sealed with plastic foil before further characterization.

The mass loss of samples under high temperature was determined by comparing the mass of the prismatic sample before and after the designed temperature exposure. The volume change was recorded based on the measurement of the three-dimensional size of prismatic samples before and after elevated temperature exposure. The bulk density was calculated according to the measured mass and volume of the specific specimen. Among these, the reported volume, mass, and density values were recorded as the average of three specimens. The residual compressive strength was determined following the same procedure

mentioned above.

Table 3.3 Structural data of the phases used for XRD analysis.

Mineral compound	#PDF-reference	ICSD
Tricalcium aluminate (C_3A)	00-038-1429	1841
Mayenite ($C_{12}A_7$)	00-048-1882	62040
Dicalcium silicate (C_2S)	00-036-0642	81097
Katoite (C_3AH_6)	00-024-0217	9272
Nordstrandite ($Al(OH)_3$)	00-018-0050	34393
Hydrotalcite ($Mg_{0.667}Al_{0.333}$) $(OH)_2(CO_3)_{0.167}(H_2O)_{0.5}$	01-089-0460	81963
Periclase (MgO)	01-071-1176	64928
Calcite ($CaCO_3$)	01-077-2376	40544
Portlandite ($Ca(OH)_2$)	01-087-0673	15471
Magnetite (Fe_3O_4)	01-089-0951	31156
Hematite (Fe_2O_3)	01-089-2810	22505
Quartz (SiO_2)	01-083-0539	83849
Mullite ($Al_{1.69}Si_{1.22}O_{4.85}$)	01-089-2813	43297
Nepheline ($(Na, K)AlSiO_4$)	01-085-1487	26007
Wollastonite ($CaSiO_3$)	01-076-0186	23567
Gehlenite ($Ca_2Al_2SiO_7$)	01-089-1489	67687
Akermanite ($Al_{0.41}Ca_{1.53}Fe_{0.16}Mg_{0.39}Na_{0.51}O_7Si_2$)	01-072-2127	20391
Calcium sodium cyclo-hexaaluminate ($Ca_{8.5}NaAl_6O_{18}$)	00-026-0958	1880

3.3 Results

3.3.1 Characterization of raw materials

Ladle slag (LS) is produced in the final stage of steelmaking, in which the liquid steel is poured into a ladle furnace where it is deoxidized and desulphured under the protection of basic slag. In this stage, aluminium is used as the deoxidation agent, leading to the formation of calcium aluminates. It is known that calcium aluminates, especially mayenite ($C_{12}A_7$), are highly hydraulic, which would react with moisture [37]. The hydration products of calcium aluminates can be varied due to the nature of phases, according to the following equations [116,117]:

$$C_{12}A_7 + 51H \rightarrow 6C_2AH_8 + AH_3 \quad (3.1)$$

$$2C_3A + 21H \rightarrow C_4AH_{13} + C_2AH_8 \quad (3.2)$$

However, these initially formed calcium aluminate hydrates are known to be metastable and will convert into more stable phase C_3AH_6 through the endothermic reactions [108,118]:

$$3C_2AH_8 \rightarrow 2C_3AH_6 + AH_3 + 9H \quad (3.3)$$

$$C_4AH_{13} + C_2AH_8 \rightarrow 2C_3AH_6 + 9H \quad (3.4)$$

During the slag manufacturing in steel plant, a mist spray process is always adopted to either cool down the slag or dedusting, afterwards, the slag is piled up in slag yard, waiting for further landfill disposal. After this process, the above reactions would have highly possibly occurred during weathering, which makes the composition of applied LS very complex.

Table 3.4 The mineralogical composition of ladle slag acquired with Rietveld refinement.

Mineral compound	Chemical formula	Content (wt.%)
Tricalcium aluminate (C_3A)	$Ca_3Al_2O_6$	34.2 ± 0.4
Mayenite ($C_{12}A_7$)	$Ca_{12}Al_{14}O_{33}$	7.8 ± 0.2
Dicalcium silicate (C_2S)	Ca_2SiO_4	6.6 ± 0.4
Katoite-hydrogarnet (C_3AH_6)	$Ca_3Al_2(O_4H_4)_3$	18.5 ± 0.2
Nordstrandite ($Al(OH)_3$)	$Al(OH)_3$	0.6 ± 0.2
Hydrotalcite	$(Mg_{0.667}Al_{0.333})(OH)_2(CO_3)_{0.167}(H_2O)_{0.5}$	0.7 ± 0.1
Periclase (MgO)	MgO	2.5 ± 0.1
Portlandite ($Ca(OH)_2$)	$Ca(OH)_2$	1.3 ± 0.1
Metallic iron (Fe)	Fe	0.4 ± 0.1
Amorphous	-	27.3 ± 0.9

According to XRD Rietveld results presented in **Table 3.4**, apart from the intrinsic phases of $C_{12}A_7$ (7.8 wt.%), C_3A (34.2 wt.%), and C_2S (6.6 wt.%), abundant C_3AH_6 (18.5 wt.%) is also observed. This confirms the hypothesis that the applied LS would react upon contacting with moisture, following Eqs. (3.1-3.4) [119]. Moreover, small traces of periclase, portlandite, hydrotalcite, and metallic iron are identified.

To determine the reactivity of weathered LS under alkaline environment, a reactivity test is carried out on as-received raw LS, as the LS powder is dissolved in alkaline solution for 24 h. The presence of hydrated calcium aluminates in raw LS and residue is compared by TG-DTG analysis, as shown in **Fig. 3.2**. For the raw LS, the slight mass loss peak at around 150 °C is associated with the dehydration of unconverted metastable phases such as CAH_{10}, C_2AH_8 [120,121], while the main weight loss peak shown at around 300 °C is attributed to the dehydration of C_3AH_6 [121–123]. It therefore can be concluded that, during weathering, most

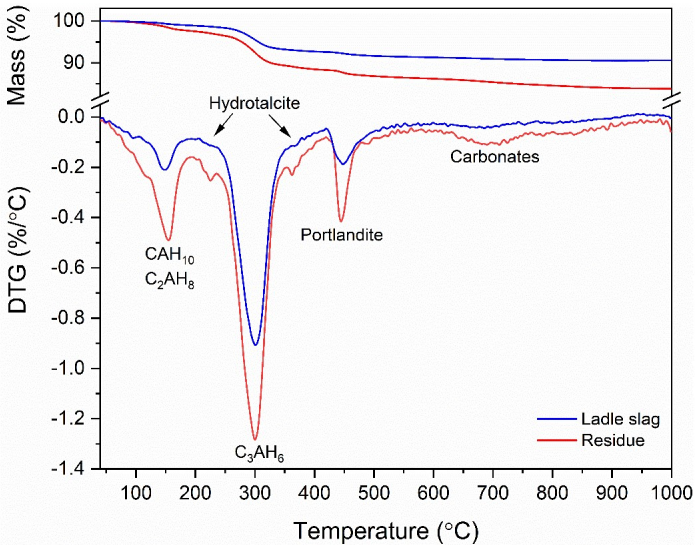

Fig. 3.2 TG-DTG analysis of raw ladle slag.

metastable hydrates such as CAH_{10}, C_2AH_8 in LS are converted into stable phase C_3AH_6 following Eqs. 3.3 and 3.4. The small shoulders observed in 224 ˚C and 370 ˚C could be the decomposition of hydrotalcite [124,125]. The mass loss peak centered at around 450 ˚C corresponds to the decomposition of portlandite. In addition, insignificant weight loss peaks at approximately 680 ˚C and 800 ˚C should be assigned to the decomposition of carbonates and dehydration of $C_{12}A_7H$, respectively [119]. By contrast, a higher mass loss is detected for the residue LS after 8 M NaOH treatment. It is interesting to note that both the mass loss peak intensity of metastable and stable phases are increased. However, since part of metastable phases would transform into C_3AH_6 at around 150 ˚C, resulting in the increase of C_3AH_6 peak intensity [126], which makes it difficult to identify the formation of C_3AH_6.

In **Fig. 3.3**, the XRD results of the residual LS are compared with the raw LS. The crystalline patterns present in the residue LS remain the same as compared to the raw LS, while the intensity of typical phases varies. The calcium aluminates in LS, namely, $C_{12}A_7$ and C_3A, are largely dissolved after NaOH treatment, and the intensity of C_3AH_6 appear to increase in the residue LS. Nevertheless, no metastable phases such as CAH_{10} and C_2AH_8 are observed in XRD, which might be due to their low content or poor crystallinity. Thus, it is confirmed by combining the discussion above that the co-existence of metastable and stable phases in alkali-treated LS. This is in line with previous studies on CAC system that during the hydration of calcium aluminates, the conversion between metastable hydrates to stable C_3AH_6 is expedited under a moderately alkaline environment (usually the alkali

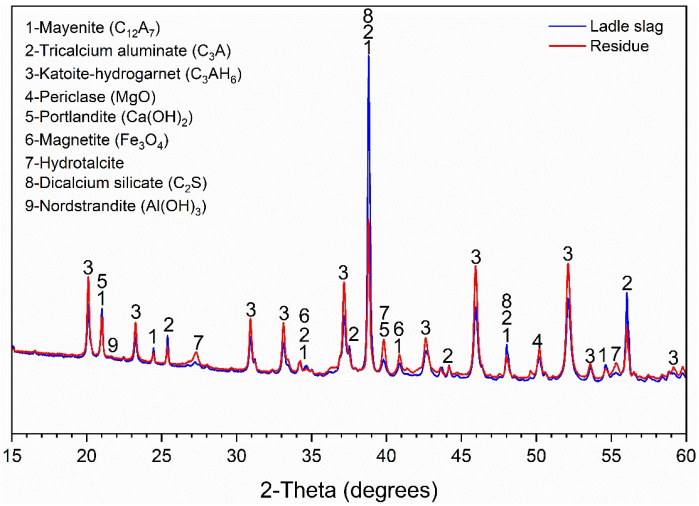

Fig. 3.3 XRD patterns of raw ladle slag and residue ladle slag after 8 M NaOH treatment (Legend: 1-Mayenite, 2-Tricalcium aluminate, 3-Katoite-hydrogarnet, 4-Periclase, 5-Portlandite, 6-Magnetite, 7-Hydrotalcite, 8-Dicalcium silicate, 9-Nordstrandite).

concentration around 8 M) [127,128]. It can be concluded that the conversion reaction of LS occurs within 24 h in an 8 M NaOH environment. Moreover, the observed crystalline phases transformation from calcium aluminates to C_3AH_6 after alkaline treatment indicates that the applied LS still shows a certain degree of reactivity in the alkaline environment even after weathering.

3.3.2 Reaction kinetics

The influence of LS substitution on the reaction kinetics of hybrid system at the early stage is characterized by isothermal calorimetric analysis. In **Fig. 3.4a**, only one exothermic peak is detected at the early stage, which is ascribed to the dissolution of solid raw material, as well as the formation of the initial dissolved silicate units and their complexation with calcium and sodium [129]. During the test period, no other visible heat peak can be detected even with a higher dosage of LS. Such sole peak phenomenon has widely been reported for sole fly ash-based alkali activated materials [130,131]. It can be deduced that, in the hybrid system, the sole exothermic peak is the combined effects of two phenomena: the late reaction of FA and the high reactivity of calcium aluminates in LS. On the one hand, as the main body of the mixture, the relatively slow dissolution of FA can result in a slow transformation of dissolved species into gels. As can be observed from **Fig. 3.4b**, the cumulative heat of all samples keeps increasing after the extensive exothermic heat flow, indicating the continuous dissolution and geopolymerization process, which is, however, not detectable in the heat flow curve. On the other hand, as suggested by Adolfsson et al.

[37] that the dissolution and hydration of C_3A and $C_{12}A_7$ occur within 1 h, and therefore, the existence of sole peak might also be caused by the overlapping of solids dissolution and rapid hydration of LS.

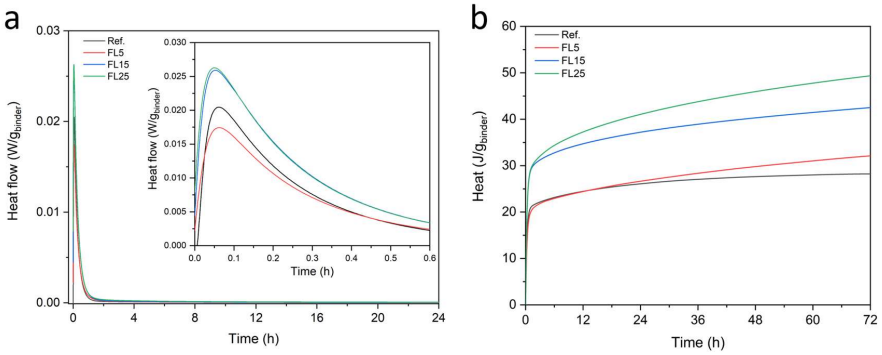

Fig. 3.4 Isothermal calorimetric response of FA/LS based geopolymer pastes at 20 ˚C a) normalized heat flow, and b) normalized cumulative heat.

In addition, by comparing the heat evolution curve of the sample with different LS substitutions, the hydration reaction is in general positively affected by LS addition. The higher the LS substitution, the larger the heat flow and cumulative heat. Here, one can conclude that a higher amount of LS promotes the dissolution process, which leads to an increase in heat flow peak intensity as well as cumulative heat release. Nevertheless, a very slight retardation effect is observed in the sample with the lowest LS addition. This can be due to the small amount of LS is insufficient to promote the reaction but further reduces the environment pH by releasing metal ions in the dissolution process. Furthermore, as widely accepted by other researchers [132], the flowability of AAMs is dependent on the dissolution and polymerization of precursors. As presented in **Table 3.2**, the flowability of mixtures in this work is strongly affected by LS addition that reduces with the increased amount of LS, which further confirms the influence of LS on reaction kinetics.

3.3.3 Hydrates assemblage

Fig. 3.5 compares the XRD patterns of all samples at the age of 28 days. As for the Ref., crystalline phases including quartz, mullite, Fe_xO_y (magnetite and hematite), periclase, and calcite are observed. In XRD patterns of LS substituted samples, besides the phases observed in the Ref., traces of C_3A and C_3AH_6 are also detected. Meanwhile, with the increased addition of LS, the intensity of peaks ascribing to C_3A and C_3AH_6 are noticeably increased. As one of the main phases in LS, the increase in C_3A with more LS indicates C_3A cannot be fully consumed after 28 days of curing. While C_3AH_6 may not only be

introduced by the applied weathered LS but also hydrated from $C_{12}A_7$ and C_3A. The Rietveld refinement results as shown in **Fig. 3.12** will be discussed later.

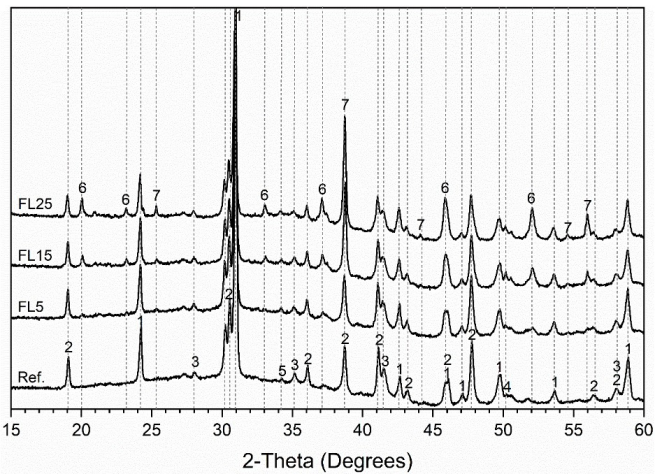

Fig. 3.5 XRD patterns of pastes prepared with different LS addition (Legend: 1-Quartz, 2-Mullite, 3-Iron oxides (Fe_xO_y), 4-Periclase (MgO), 5-Calcite ($CaCO_3$), 6-Hydrogarnet (C_3AH_6), 7-Tricalcium aluminate (C_3A)).

FTIR is performed on raw material powder and hybrid pastes with different LS content. In **Fig. 3.6a**, three adsorption peaks are observed for raw FA, where the major band at around 1046 cm^{-1} corresponds to the asymmetric stretching vibration of Si-O-T bonds (T represents Si or Al units) [133], the broad peak at 670-850 cm^{-1} represents the stretching vibrations of Si-O-Si in quartz and the weak peak at 1450 cm^{-1} attributed to the stretching vibrations of O-C-O bonds might result from incomplete combustion of carbon. For raw LS, the sharp adsorption at approximately 3654 cm^{-1} is due to the O-H stretching vibrations of portlandite [119,134]. The intensive peak at 1415 cm^{-1} is related to O-C-O bonds of carbonates as also observed in TG (**Fig. 3.2**) [129]. The adsorption peak of 510 cm^{-1} corresponds to the vibrational peak in symmetric Al-O-Al and the adsorptions of 741, 798, 903 cm^{-1} are assigned to the stretching and bending vibrations of the Al-O bonds [135–137], indicating the presence of different calcium aluminates.

The infrared spectra for samples with different LS additions are shown in **Fig. 3.6b**. The broad adsorption band appearing at around 3415 cm^{-1} and the adsorption at around 1645 cm^{-1} are associated with the stretching vibrations of O-H bonds and bending vibrations of physically and chemically bond water. The adsorption peak of O-C-O bonds at 1452 cm^{-1} is observed in all spectrums, which could be associated with carbonates and the residual carbon in raw FA as noticed in **Fig. 3.6a**. The typical absorption band of the Si-O-T bridge bond in the Ref. shifts to a lower wavenumber as compared to pure FA due to the

polymerization. Furthermore, it is interesting to note that, with more LS addition, the Si-O-T bond adsorption peak shifts from 990 cm^{-1} to 965 cm^{-1}, indicating the increased substitution of Al in Si-O-T tetrahedral within geopolymer gel [138,139]. In conclusion, with increasing LS substitution, more Al is introduced into geopolymeric gel.

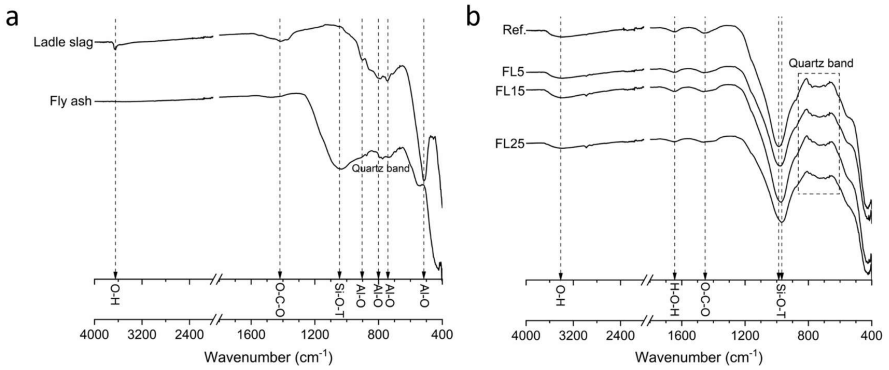

Fig. 3.6 FTIR spectra of (a) ladle slag and fly ash, (b) FL blends.

The difference in hydration products with varying LS addition is further reflected with thermogravimetric analysis, as shown in **Fig. 3.7**. In the Ref., the main mass loss peak below 120 ˚C is mainly due to the release of physically bound water [140]. A broad mass loss peak observed in the temperature range between 450 ˚C and 650 ˚C is associated with the carbonates [141]. Furthermore, an insignificant weight loss peak that occurs after 800 ˚C is mainly induced by the re-crystallization reaction [62]. For the LS substituted sample, an additional weight loss peak that appears at around 300 ˚C can be assigned to the dehydration of C_3AH_6. In accordance with the XRD results, the C_3AH_6 typical peak is intensified as a higher dosage of LS is applied, indicating that more C_3AH_6 is introduced. The decomposition of carbonates in different crystallinity is also observed between 500 and 750 ˚C.

Moreover, it should be noted that, as the LS addition increases, the main mass loss peak is intensified and the corresponding peak shifts towards higher temperatures. This might be attributed to the higher amount of hydration gel with more tightly bound water and/or smaller pores are formed in the hybrid system [64]. On the one hand, with LS substitution, additional calcium aluminate hydrates are formed as discussed above. On the other hand, as evidenced by Fernández-Jiménez et al. [142] on calcium aluminate cement (CAC) system with the presence of silica, Si can be taken in CAH phases into C-A-S-H phase. In this work, the soluble silica provided by fly ash as well as sodium silicate can promote the formation of C-A-S-H phase. Here, metastable phases from LS dehydrate at a range from

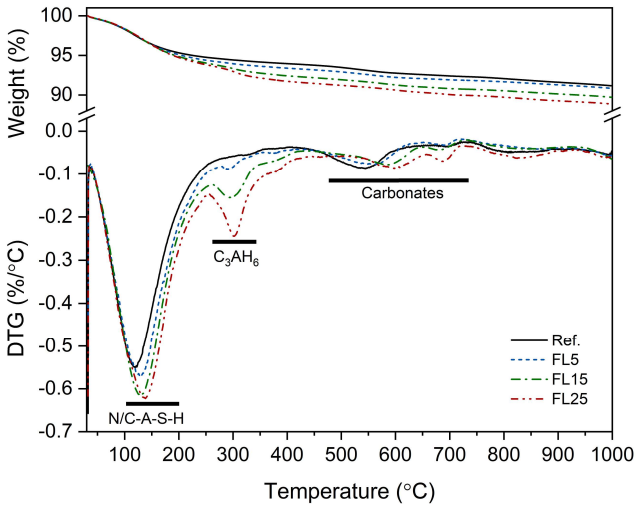

Fig. 3.7 Thermal analysis of pastes with different LS addition.

120 to 195 °C [122], and C-A-S-H gradually dehydrates at about 160 °C [74], hence the dehydration of these hydration products occurs within a similar range between 100 °C and 200 °C, which overlaps the main weight loss peak, making the change in C-A-S-H content not observable on the DTG curves. Nevertheless, a clear difference in peak intensity and corresponding temperature can be observed, indicating more aluminosilicate species are introduced with higher LS substitutions.

3.3.4 Microstructural properties

The pore structure of 28 days pastes with different substitutions of LS is investigated via Mercury intrusion porosimetry (MIP) as depicted in **Fig. 3.8**. The detailed characteristic pore parameters are summarized in **Table 3.5**, including mesopores (2-50 nm), macropores (>50 nm), open porosity, median/average pore diameter, and intrusion volume of mercury. In **Fig. 3.8a**, for all tested samples, most of pores are concentrated in the range of 5 to 1000 nm, while a very small fraction of pore larger than 100 μm is also detected, which reflects the presence of entrained air voids and pre-existing microcracks.

In terms of total porosity, it must be noted that, with LS substituting up to 25 wt.%, the porosity remains almost unchanged and only slightly varies between 38.9% and 40.4% are observed. This indicates that LS has a very limited influence on porosity within the present substitution level. According to the pore type, the pores are further classified into 3 types: gel pores (≤10 nm), capillary pores (10-50 nm), and macropores (>50 nm) [143], and the fractions of pores are shown in **Fig. 3.8b**. In agreement with previous works [33,39], the LS dosage strongly influences the pore size distribution of the blended system. In this work, a clear trend is observed that the fraction of gel pores, as well as macropores, increase

while that of capillary pores decreases with the LS addition rise from 0 to 25 wt.%. It is widely accepted that the pore size reflects the reaction degree, and the well-reacted sample may exhibit the highest proportion of gel pores. Here, the increased fraction of gel pores further confirms the promotion of hydration by LS. While the higher macropores fraction with more LS addition should be partially attributed to the poor workability that entraps more air bubbles/voids in the matrix. On the other hand, as revealed by Choi et al. [144], the typical continuous plate-shape geometry of calcium aluminate hydrates would have a direct influence on the process of unreacted particle in contact with water, in consequence, macropore is more favourable to be formed.

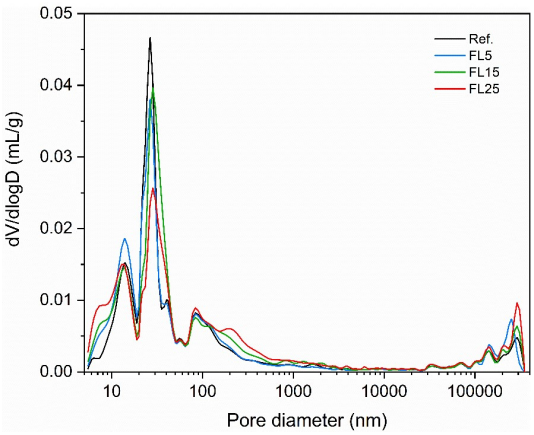

(a)

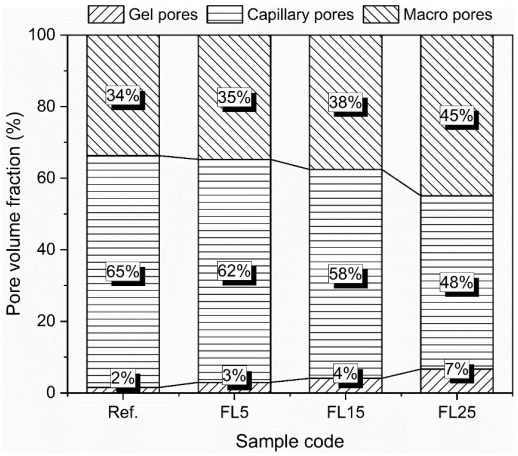

(b)

Fig. 3.8 MIP results of pastes after 28 days of hydration, a) pore size distributions, and b) pore volume fractions.

Table 3.5 Characteristic pore parameters of samples under different temperatures as measured by MIP.

Exposure temperature (°C)	Sample code	Porosity			Median pore diameter (nm)	Average pore diameter (nm)	Total intrusion volume (mL/g)
		Mesopores (2-50 nm)	Macropores (>50 nm)	Total			
20	Ref.	25.8	13.1	38.9	29.30	30.34	0.27
	FL5	26.4	14.0	40.4	28.88	28.28	0.28
	FL15	24.4	14.6	39.0	34.95	29.96	0.28
	FL25	21.5	17.4	38.9	39.88	28.73	0.27
400	Ref.	22.9	18.2	41.1	46.62	46.12	0.29
	FL5	25.9	14.9	40.8	39.11	40.66	0.28
	FL15	22.7	18.1	40.8	47.02	46.28	0.32
	FL25	20.4	21.1	41.5	51.19	49.25	0.27
800	Ref.	2.2	34.2	36.4	2161.88	208.14	0.24
	FL5	2.1	34.1	36.2	1914.17	211.63	0.23
	FL15	2.0	34.6	36.6	2506.22	237.13	0.24
	FL25	2.0	35.2	37.2	2720.18	276.50	0.24

3.3.5 Mechanical properties

The compressive strength of the samples with the substitution of LS varying from 0 to 25 wt.% at different curing ages are evaluated and presented in **Fig. 3.9**. The compressive strength increases with LS substitution from 0 to 15 wt.%, and then slightly declines. Here, as discussed in **Section 3.3**, the enhancement in compressive strength can be attributed to a higher degree of hydration with more LS substitution, which strengthens the matrix with higher content of hydrated gel. However, the slight strength reduction in FL25 might be induced by the change in the pore structure. It is suggested by Mehta et al. [145] that the mechanical strength is controlled by micropores, while macro pores larger than 50 nm would have an adverse effect on strength of the matrix. As learned by pore size distribution in **Fig. 3.8**, FL25 has the highest macropore fraction, which will negatively impact the compressive strength.

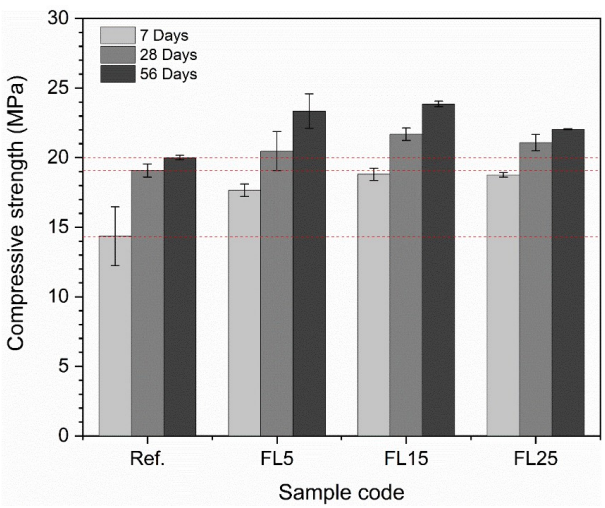

Fig. 3.9 Compressive strength of pastes with different LS dosage after 7, 28, and 56 days of hydration.

Regarding the strength evolution of mixtures at different curing ages, all mixtures gain strength during the 56 days of curing, contradicting sole LS based materials, which are prone to lose strength between 7 and 28 days due to conversion reaction [37,120,146]. In this study, the strength enhancement during the tested curing ages, on the one hand, can be ascribed to the further hydration of unreacted raw materials. On the other hand, in accordance with the conversion mechanism revealed above, calcium aluminate hydrates that convert into stronger C-A-S-H gel with the available soluble silica source. Moreover, it is interesting to note that the strength development rate from 7 days to 56 days is decreased gradually with LS substituted from 5 wt.% to 25 wt.%. This observation indicates that since the environmental silica content is consumed or insufficient, the

increasing C_3AH_6 content with a higher LS substitution would further have an adverse impact on strength gain during curing. From the point of view of utilizing LS as SCM, the incorporation of LS into hybrid alkaline system not only avoids strength loss, but also improves the mechanical strength as compared to sole FA based samples by forming C-A-S-H type gel. Moreover, the best mechanical performance is observed for the mixture with 15 wt.% LS substitution.

3.3.6 Thermal behavior

Owing to the similarity in mineralogy and reaction mechanism, LS can be compared with CAC which is mainly applied in refractory castable/concrete and linings due to its outstanding thermal performance. In this study, the thermal behavior of LS as a SCM in geopolymer system is evaluated by applying high temperature exposure tests.

Structural change

The variations of structural properties of samples treated at different temperatures are given in **Table 3.6**. The main mass loss is observed before 400 °C in all samples, which is caused by the release of physically and chemically bound water. As a result, the density of all samples decreases due to the increased content of empty pores. At the same time, the loss of water leads to a range of capillary strain and shrinkage of pores, resulting in a volume shrinkage in all samples. In the temperature range between 400 °C and 800 °C, the slight mass loss is mainly associated with the decomposition of portlandite and carbonates of different crystallinity [147]. While the increase in density and volume shrinkage for all samples from 400 °C to 800 °C is owing to the viscous sintering that occurs at around 600 °C which leads to structural densification [70]. Regarding the influence of LS substitution on structural change, the densities of all samples are similar at the tested temperatures, whereas the higher the LS substitution, the severer the mass loss and higher volume shrinkage are detected at high temperatures. As evidenced by TG-DSC analysis (**Fig. 3.7**), the intensified mass loss with higher LS contents can be ascribed to the growth of hydration products. Further, it is noted that the increased volume shrinkage is not only induced by the greater water release but also the severer re-crystallization detected in LS substituted sample.

The pore structure evolution of samples upon high temperatures is characterized by MIP, as summarized in **Table 3.5**. The porosity in all samples is found to increase after exposure to 400 °C. Meanwhile, the fraction of mesopores is reduced while macropores are detected to increase. This can be explained by the pore collapse and cracking induced by the migration of both physical and chemical water towards the surface, which results in the formation of larger pores with increased pore interconnectivity. In the temperature range

Table 3.6 Structural characteristics of samples at different temperatures.

Sample code	Mass loss (%)			Bulk density (g/cm^3)			Volume shrinkage (%)		
	20 ˚C	400 ˚C	800 ˚C	20 ˚C	400 ˚C	800 ˚C	20 ˚C	400 ˚C	800 ˚C
Ref.	-	19.82	21.84	1.72	1.47	1.56	-	6.17	13.25
FL5	-	20.19	22.66	1.68	1.43	1.53	-	6.58	15.03
FL15	-	21.16	23.37	1.68	1.43	1.53	-	7.38	15.55
FL25	-	22.41	24.05	1.71	1.43	1.55	-	7.61	15.80

400 ˚C to 800 ˚C, the porosity is slightly decreased, among which, a remarkable reduction is detected in the fraction of mesopores, while macro pores fraction is largely increased. Here, the sintering reaction leads to the healing of micropores/cracks, which results in the decline of small pores [69]. In the meantime, more large cracks are formed due to the dehydration and decomposition of the matrix, which is detected as macropores in MIP.

It is known that MIP only measures connected open pores that are smaller than 350 μm. In order to visualize the pore structure and characterize the variation of pores in a larger coverage, Micro-CT analysis is carried out. To determine the effect of LS, FL15 with optimum hardened and thermal performance is selected as representative sample to compare with Ref. for Micro-CT analysis. The pore structures are extracted and denoted in different colors according to pore size as shown in **Fig. 3.10**.

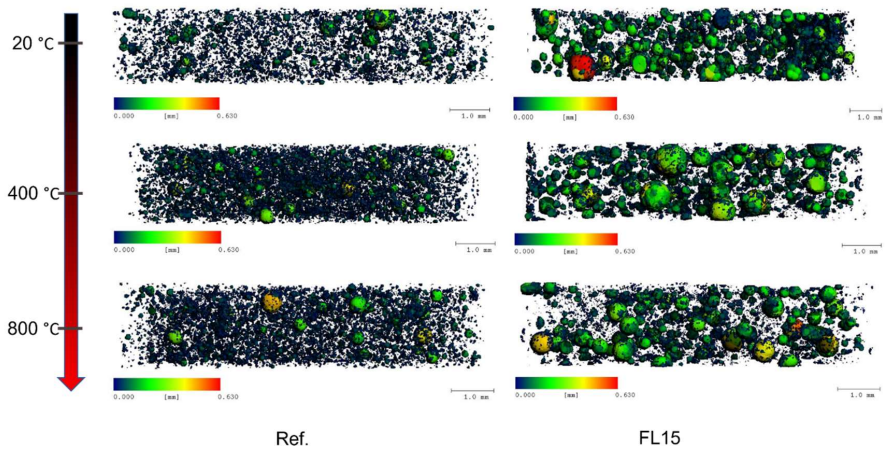

Fig. 3.10 Micro-CT images of the Ref. and FL15 at different temperatures.

By comparing the images of the Ref. and FL15, obviously, the substitution of LS introduces more big pores as compared to the Ref. at all temperatures. In addition, the detailed pore size distribution of samples upon high temperatures is presented in **Fig. 3.11**. It can be learned that the samples with and without LS substitution show a different pattern of pore size distribution. In **Fig. 3.11a** and **d**, the Ref. exhibits a narrow pore size

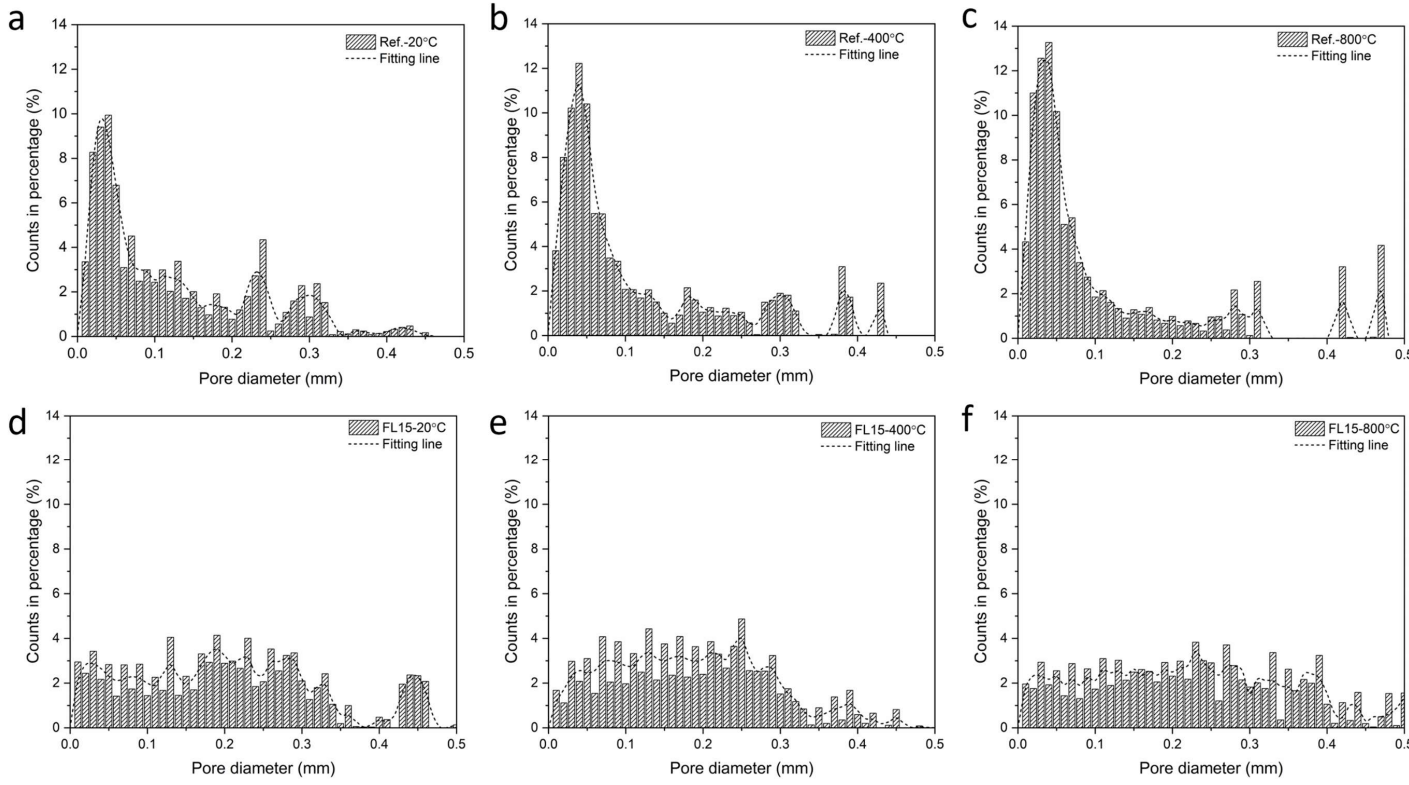

Fig. 3.11 Pore size distribution at different temperatures from Micro-CT: (a), (c), (e) Ref., (b), (d), (f) FL15.

distribution below 0.3 mm with a main peak centered around 0.05 mm, while a wide and even pore size distribution is observed in LS substituted sample. With the exposure temperature increasing from 20 ˚C to 800 ˚C, in the Ref., the fraction of pores between 0 and 0.1 mm is largely increased, and bigger pores ranging from 0.4 to 0.5 mm are detected. Nevertheless, for LS substituted sample in **Fig. 3.11b**, **d**, and **f**, the pores below 0.3 mm are relatively stable at elevated temperatures, except more big pores at around 0.5 mm are detected. This can be explained by the wide and even distribution of pore size in the LS substituted sample that facilitates the release of inner water or gas vapour at elevated temperatures that reduces the internal damage induced by pore pressure. While the narrower pore size distribution with the main fraction range from 0 to 0.1 mm for the Ref. tends to generate higher pore pressure, leading to severe pore collapse and crack extension with the increased porosity. But relatively large cracks from 0.4 to 0.5 mm can be detected in both mixtures due to severe shrinkage. In conclusion, samples with LS substitution exhibit a better inner structural stability under elevated temperatures owing to the wide and even pore size distribution. This is believed to contribute to retain a large degree of strength under elevated temperature.

Phase transformation

The phase transformation of samples at different temperatures is compared in **Fig. 3.12**. The loss of bound water (amorphous) due to high temperature exposure is excluded according to TG results. Because the contents of some crystalline phases such as periclase, rutile, etc., are relatively low and similar in different mixtures, which are not of comparison, they are classified as other phases (the detailed results from XRD-Rietveld are provided in **Appendix A Table A1**).

It is clear that the crystalline phases in the Ref. are thermally stable at 400 ˚C, while the amorphous content decreases and a minor trace of nepheline appears up to 800 ˚C. This can be explained by the release of bound water and partial recrystallization of amorphous aluminosilicates, which has been reported in sole fly ash based geopolymer [22]. Regarding the sample with the addition of LS, obvious transformation can be observed at elevated temperatures. In accordance with TG results, hydrogarnet disappears after 400 ˚C exposure, and then, mayenite starts to appear. Moreover, the content of C_3A and mayenite increases with higher LS substitutions. It is worth noting that the phase change among LS substituted samples at 400 ˚C is mainly induced by the dehydration of hydrogarnet into calcium aluminates, and the total crystalline content almost remains unchanged, indicating that the hybrid gel system is relatively stable at 400 ˚C. After 800 ˚C exposure, it is obvious that the amorphous content decreases whereas the crystalline phase content increases with higher LS substitutions. New phases such as wollastonite, akermanite, and gehlenite are

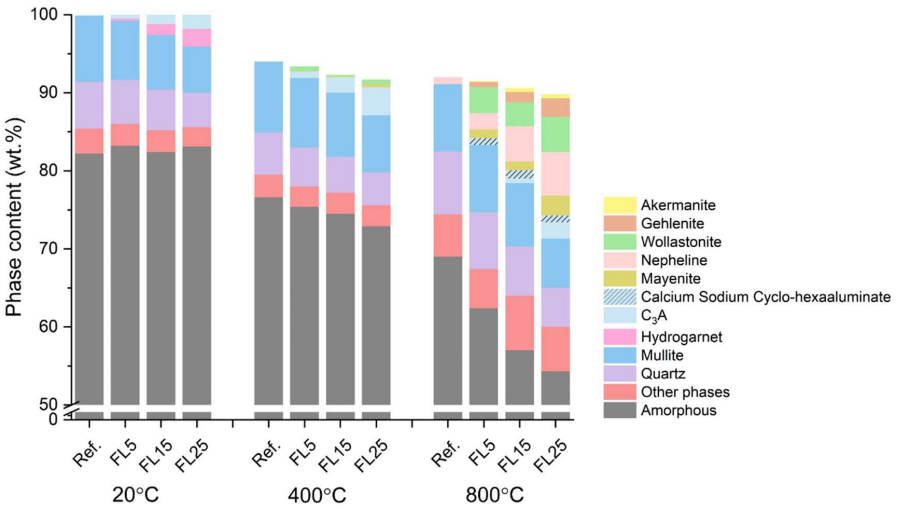

Fig. 3.12 Phase compositions of samples at different temperatures.

detected, and clearly, their contents are increased with more LS substitutions. Among these, it is known that wollastonite is highly associated with LS. Akermanite and gehlenite are formed by the crystallization of C-A-S-H gel [148], which correlates well with the phase assemblage discussed above that substitution of LS can promote the formation of C-A-S-H type gels in the hybrid system. Owing to the fact that Ca^{2+} could be replaced by Na^{+} in C_3A structure within a Na rich system, two structures including C_3A and Na^{+} substituted C_3A (Calcium Sodium Cyclo-hexaaluminate, $Ca_{8.5}NaAl_6O_{18}$) are adopted for the refinement, and their total content is similar to that of 400 °C. The increase in nepheline with more LS addition can be partially caused by the increasing Al ion from LS is taken up to form more sodium based aluminosilicate species [115]. In addition, the increasing C-A-S-H phase due to the introduction of additional calcium from LS promotes the formation crystalline phases such as akermanite and gehlenite at 800 °C [149]. Thus, a higher crystalline phase content is detected with higher LS substitutions.

Thermal mechanical properties

Here, the changes in the porosity do not reflect the evolution of the mechanical strength of samples at high temperatures. This is because the thermal mechanical evolution of geopolymer-based material is not only influenced by physical change but also chemical transformation during thermal exposure. As presented in **Fig. 3.13**, it is remarkable that the substitution of LS does not lead to strength deterioration at high temperatures as always experienced in other FA/slag systems and a continuous strength gain is observed. At 400 °C, the strength gain is mainly induced by further geopolymerization of unreacted

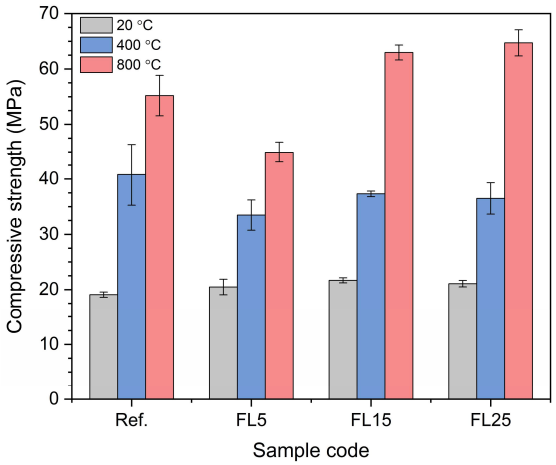

Fig. 3.13 Compressive strength of pastes exposed to different temperatures.

fly ash. In this regard, the pure fly ash paste exhibits the highest compressive strength and strength gain among LS substituted samples before 400 ˚C. After being exposed to 800 ˚C, the strength gain observed in the sole fly ash sample is widely accepted to be caused by the sintering reaction of unreacted fly ash that heals the small cracks and densifies the matrix as learned above. While it should be noted that the residual strength at 800 ˚C is improved by LS substitution. The compressive strength, as well as the rate of strength gain increase with the LS substitution, rising from 15 wt.% to 25 wt.% compared to the Ref., and FL25 exhibits the highest compressive strength of 64.72 MPa after 800 ˚C exposure. Here, as observed in **Table 3.6**, the severer shrinkage and densification with more LS substitution can be considered as one of the contributing factors. On the other hand, it is revealed by Murri et al. [33] and Dombrowski et al. [149] that high temperature induced crystalline phases with different thermal stability can influence the thermal behavior of the matrix. In this work, as evidenced by Rietveld refinement, the crystalline phase content at 800 ˚C is increased with more LS substitution, among which, more stable phases including gehlenite, akermanite, C_3A, and mayenite are formed. It is therefore likely that these phases could act as stable aggregates that strengthen the matrix at high temperatures.

3.4 Discussion

3.4.1 The hydration mechanism of ladle slag within hybrid system

It is widely accepted that within an aqueous system, the hydration process of LS can be divided into two stages: a) the hydration of LS with the initial metastable hydrates, dicalcium aluminate (C_2AH_8) before 7 days, b) the conversion from metastable phases into stable tricalcium aluminate hexahydrate (C_3AH_6) between 7 and 28 days, which is always

accompanied with the increased porosity and reduced strength [120]. However, the hydration of calcium aluminates proceeds differently in an alkaline system. In KOH/Na_2SiO_4 activated LS system, Adesanya et al. [146] observed a clear reduction in compressive strength between 7 and 28 days, indicating the presence of conversion reaction in an alkaline system. However, in Wang et al. [150], the strength loss induced by conversion after 7 days is not detected with either cured in saturated limewater or higher alkali content (4% to 8%). Similarly, Fernández-Carrasco et al. [127] and Pastor et al. [128] studied the hydration of CAC in a high alkaline environment and reported that the alkali media favours the conversion between calcium aluminate hydrates. As observed in the present study, the conversion reaction of LS occurs within 24 h with 8 M NaOH activation (**Fig. 3.2**, **Fig. 3.3**). It can be concluded that the conversion rate of calcium aluminate hydrates is largely depending on the alkaline concentration and content, since a higher alkaline content results in a faster conversion reaction. In this case, the strength reduction phenomenon may occur earlier or even not be detectable with the presence of an alkali media.

The hydration reaction of LS is governed by different mechanisms with the presence of silica or pozzolan in the starting materials. For instance, it is suggested that in alkali activated LS with abundant soluble silica, the following reaction may take place [146]:

$$C_{12}A_7 + 51H + 6S \rightarrow 6C_2ASH_8(strátlingite) + AH_3 \quad (3.5)$$

Similar results are also observed on alkali activation of CAC with a high content of reactive silica and/or low alkali content, the conversion is retarded since the metastable phases would transform into strätlingite instead of C_3AH_6 following the reactions [151,152]:

$$2CAH_{10} + S \rightarrow C_2ASH_8 + AH_3 + 9H \quad (3.6)$$

$$C_2AH_8 + S \rightarrow C_2ASH_8 \quad (3.7)$$

However, this is inconsistent with this work that no strätlingite is observed even with the highest LS substitution. Another case is reported by Fernández-Jiménez et al. [142] and Rivas Mercury et al. [153] on CAC system that with high alkali content and relatively low Si content or high temperature curing, a Si substituted calcium aluminate silicate hydrate (C-A-S-H) instead of strätlingite is detected:

$$CA \xrightarrow{High\ OH^-} C_3AH_6 \quad (3.8)$$

$$C_3AH_6 \xrightarrow{Silicate} C_3AS_nH_m + C-A-S-H\ (Amorphous\ and\ crystalline) \quad (3.9)$$

Table 3.7 The variation of calcium aluminates and hydrates content in FL15 determined by XRD-Rietveld method (wt.%).

Phase	LS	St dev	7 d	St dev	28 d	St dev
C_3A	5.1	0.4	3.4	0.1	1.3	0.1
$C_{12}A_7$	1.2	0.2	0	0	0	0
C_3AH_6	2.8	0.2	2.6	0.2	1.4	0.1

The results in the present work are more likely in accordance with the later situation. As shown in **Table 3.7**, the calcium aluminates and hydrates content in FL15 is determined by Rietveld analysis, in which 5.1 wt.% of C_3A, 1.2 wt.% of $C_{12}A_7$ and 2.8 wt.% of C_3AH_6 are introduced by the raw LS, respectively. It is observed that C_3A decreases to 1.3 wt.% at 28 d, and $C_{12}A_7$ is fully consumed after activation, indicating different degree of reactivity. While the stable hydrate of C_3AH_6 keeps decreasing from 2.8 wt.% to 1.4 wt.% after 28 d curing. The possible mechanism behind is, on the one hand, the high alkalinity with high temperature curing applied in the present work largely promotes the hydration of LS as well as the conversion reaction with the formation of C_3AH_6 at very early age. On the other hand, with the presence of silica provided by activator and fly ash, OH^- in C_3AH_6 is replaced by Si to form C-A-S-H phase following Eqs. 3.8 and 3.9. Thus, in this work, strätlingite is not detected while C_3AH_6 is observed to decrease during the studied period. As a result, a continuous strength gain from 7 to 56 days is observed in all LS substituted pastes owing to the expedited conversion and formation of C-A-S-H phase. According to the discussion, the alkali activation of LS is similar to CAC and the reaction process is highly dependent on alkalinity, Si content and curing condition. A moderate alkalinity or high temperature curing can largely accelerate the conversion of metastable phase into stable phase, while the presence of Si can retard or prevent the conversion, and ultimately these conditions can avoid the strength reduction of LS incorporated pastes at later age.

3.4.2 The influence of ladle slag on high temperature behavior of geopolymers

As for blended Na_2O-CaO-Al_2O_3-SiO_2 system, with a sodium-based alkali as the activator, Class F fly ash or metakaolin are often applied as the aluminosilicate source, while various secondary calcium sources can be found in previous works, for instance, cement, metallurgical slag, and lignite bottom ash [154–156]. The properties of secondary sources such as elemental composition, mineralogy, physical properties play a vital role on the performance of the resulting hybrid system [87,149,157,158]. Among these, GGBS contains more than 40 wt.% of calcium oxide and 30 wt.% of silicon oxide in the reactive glass phase, which is the most commonly applied secondary source. Within an alkaline system, joint activation of FA and GGBS results in formation of hybrid N-C-A-S-H gel, and typical slag-based C-(A)-S-H products can be formed with higher dissolved Ca and Si concentrations. The formation of slag-based products predominates the

geopolymerization which not only largely accelerates the hydration degree but also impedes the formation of geopolymeric gel (N-A-S-H) [75]. Thus, a dense matrix is obtained with the coexistence of N-C-A-S-H and C-(A)-S-H products, and a relatively high initial mechanical strength can be achieved. However, as learned by Chapter 2, GGBS has a negative impact on geopolymer-based materials in terms of high temperature behavior. Firstly, the exchange of Na/Ca in aluminosilicate gel reduces the thermal stability of geopolymeric gel. Secondly, slag-based products such as C-S-H gel are highly unstable at elevated temperatures. Lastly, the compact matrix with low ductility is prone to failure under elevated temperatures due to thermal-induced stress. As a result, severe cracking, decomposition, and strength deterioration are always resulted after exposure to high temperatures.

LS contains similar chemical composition, especially calcium oxide content, in comparison to commonly used GGBS. Nevertheless, it is found in this study that LS with high crystalline calcium and aluminium content exhibits a unique reaction process with the presence of alkali media and soluble Si, which shows a distinct influence on the hydration assemblage and microstructure of the hybrid geopolymer system. Owing to the prior weathering process, free lime is undetectable in LS (**Table. 3.4**), and the majority of calcium and aluminium in LS is present in crystalline phases, namely tricalcium aluminate (C_3A) and mayenite ($C_{12}A_7$). In alkaline environment, the hydration and conversion of calcium aluminates is largely promoted to form calcium aluminate hydrates. With the continuous dissolution of Si from FA, the CAH phases convert into more stable C-A-S-H phase. In this case, the hydration is not significantly accelerated by adding LS, as evidenced by reaction heat release curve (**Fig. 3.4**). Moreover, the formation of C-A-S-H gel might be unable or insufficient to alter the microstructure, and a loose matrix with a similar total porosity to sole FA based geopolymer is observed from MIP analysis (**Table. 3.5**). In terms of aluminium content, it is learned from FT-IR (**Fig. 3.6**) that with a higher LS dosage, increased Al ions are introduced into Si-O-T tetrahedral within geopolymer gel, which contributes to the increased aluminosilicate species. The above results suggest that LS would not interfere geopolymerization process in contrast to GGBS and has a limited influence on the microstructural transformation within the studied substitution range.

The distinct influence of LS on the hydration of hybrid geopolymer system results in a different high temperature behavior from other blended geopolymers. A continuous strength gain at high temperatures is observed in this work (**Fig. 3.13**). This could be attributed to the synergistic effect of several characteristics such as microstructure and phase composition. For one thing, the loose matrix with homogenous pore size distribution in blended geopolymers helps to release the thermally induced water or gas vapour. Therefore, the inner thermal stress is reduced, and consequently, the inner pore

structure is largely protected (see **Table 3.5**, **Fig. 3.10**, **Fig. 3.11**). For another, the addition of LS does not destroy the structure of thermally stable geopolymeric gel but contributes to a higher content of aluminosilicate species with the coexistence of N-A-S-H and C-A-S-H type gel. In this regard, the thermal stability of the hybrid binder gel is largely retained. Moreover, as learned from XRD Rietveld analysis in **Fig. 3.12**, more drastic recrystallization with the formation of thermally stable crystalline phases is observed at elevated temperatures with the increased LS substitution, which is likely to be another reason for the increased residual strength [149]. Here, it should be noted that the typical phase of nepheline that recrystallizes from N-A-S-H is increased with a higher LS substitution [24], which further proves that the incorporation of LS into geopolymer promotes the formation of geopolymeric gel, hence increases the thermal stability of binder gel.

3.5 Conclusions

This chapter investigates the hydration reaction and conversion process within the hybrid geopolymer system and verifies the possibility of utilizing ladle slag as a supplementary cementitious material in alkali activated material for high temperature applications. The impact of ladle slag (up to 25 wt.%) on the reaction kinetics, hydration products, microstructure, mechanical properties, and thermal behavior of hybrid geopolymer pastes is investigated. The following conclusions can be drawn:

(1) The dissolution, as well as polymerization within the hybrid system, is positively influenced by LS, as evidenced by a higher reaction heat intensity and cumulative heat release. The main hydration products within the hybrid system are C_3AH_6, C-A-S-H, and N-A-S-H type gels. The addition of LS promotes the hydration reaction, resulting in more hydration products, especially aluminosilicate gel, enabling a higher compressive strength.

(2) The strength deterioration of LS contained material at long term is avoided in hybrid geopolymer system. In an alkaline environment, the conversion reaction between metastable phases and stable C_3AH_6 is strongly expedited. With the presence of soluble silica, calcium aluminate hydrates absorb Si to form more stable C-A-S-H gel, which contributes to a continuous gain of compressive strength up to 56 days of curing. Nevertheless, the strength gain effect is lessened with more LS addition because of the limited provision of environmental silica, in addition to the adverse impact caused by the increased C_3AH_6 content.

(3) LS has no significant influence on the porosity of hybrid pastes within the present substitution level (i.e., 25 wt.%). Nevertheless, the addition of LS results in a wide and even pore size distribution pattern, which facilitates the release of inner water or gas

vapour at elevated temperatures and thus contributes to better pore structural stability. However, increasing the LS substitution leads to a higher mass loss and volume shrinkage due to severer dehydration and recrystallization at high temperatures.

(4) The unique nature of LS with high crystalline calcium and aluminium content plays a vital role on high temperature behavior of hybrid geopolymer. The initially hydrated CAH phases in weathered LS transform into C-A-S-H, which protects the geopolymerization. As a result, the thermal stability of hybrid geopolymer is largely retained, enabling a continuous gain of compressive strength up to 800 °C. With more LS substitution, the residual strength, as well as strength gain rate after 800 °C, is increased thanks to the formation of thermally stable crystalline phases.

CHAPTER 4

The optimization of gel compatibility and thermal behavior of hybrid ladle slag/Class F fly ash geopolymer

The gel compatibility in calcium incorporated geopolymers remains a controversial topic. This chapter aims to investigate the role of Ca availability in determining the geopolymerization of alkali-activated ladle slag/Class F fly ash blends. The results show that the product layer wrapping around ladle slag particles largely governs the Ca diffusion into the environment, enabling the development of two separated gels, namely C-(N)-A-(S)-H and N-(C)-A-S-H type gel. A dense matrix consisting of geopolymer gel and Ca-enriched gel is achieved with 8 wt.% of Na_2O while increasing Ms intensifies the incompatibility between two gels, leading to microcrack formation and lowered mechanical strength. The competition between different reaction mechanisms of the two gels predominates the initial properties and thermal performance of the hybrid binder. A thermal degradation model of hybrid geopolymer co-existing geopolymeric gel and Ca-enriched gel is proposed to describe the influence of gel compatibility on the thermal behavior of Ca incorporated geopolymer.

This chapter has been published in the following article:

Y. Luo, H.J.H. Brouwers, Q.L. Yu, Understanding the gel compatibility and thermal behavior of alkali activated Class F fly ash/ladle slag: the underlying role of Ca availability, Cement and Concrete Research 170 (2023), 107198.

4.1 Introduction

Geopolymer binder has attracted keen scientific interest as a potential environmentally-friendly alternative to Ordinary Portland cement (OPC) [13,159,160]. Resulting from alkaline activating industrial wastes, such as fly ash (FA), incineration bottom ash, and slag, this binder material enables a significantly low CO_2 emission [12,159,161]. With its typical three-dimensional aluminosilicate framework, geopolymers offer several advantages, for instance, low autogenous shrinkage, high temperature and acid resistance, and high immobilization capacity of toxic metals [19,22,160,162]. However, some major concerns for sole FA-based geopolymer such as relatively low early age mechanical strength and energy-consuming curing process stimulate growing interest in calcium-incorporated hybrid geopolymer binder. The incorporation of calcium sources such as OPC and ground granulated blast furnace slag (GGBS) into aluminosilicates can alter the gel composition with promoted characteristics. In this case, the phase assemblage becomes complicated in a blended Na_2O-CaO-Al_2O_3-SiO_2 system. Various studies regarding the Ca content in the blended geopolymer system have been performed, but the gel composition is still under disputation, including N-A-S-H, N-(C)-A-S-H, C-A-S-H, C-(A)-S-H as Ca concentration varies [87,163–165]. Furthermore, the binder gel compatibility in calcium incorporated geopolymer system is seen as another controversial topic, regarding whether the system develops two separated gel phases as C-A-S-H and N-A-S-H or an interacted N-C-A-S-H gel phase [24,64,87,164,166]. The compatibility study is of great importance, because the way hybrid gels coexist, as well as the discrepant characteristics of two gels, such as different gel structures, reaction kinetics, and drying shrinkage, can pose an adverse effect on the long-term durability of blended systems [167].

In general, the incorporation of calcium in the geopolymer system further complicates the reaction process, since the content of calcium, its presence in glassy or crystalline, and its availability (release rate) have a significant influence in determining the reaction pathway and gel composition/structure. Yip et al. [87,166] compared the role of calcium in geopolymerization by applying calcium silicates in form of amorphous and crystalline as a co-precursor with FA or metakaolin. Their results suggested that the alkalinity and extent of Ca dissolved from varied calcium silicate sources impacts the relative amount of Al substituted C-S-H gel and geopolymeric gel, which further influences the gel composition and mechanical strength. García-Lodeiro et al. [167] directly added soluble Ca into geopolymer gel, and a N-A-S-H gel containing Ca with preserved 3D structure was obtained. This reported phenomenon is discrepant from other works that observed the formation of chain-like C-(A)-S-H phases with the addition of initially activated Ca sources and aluminosilicates [163]. The studies discussed above revealed that the Ca release

rate/degree relative to geopolymerization reaction also plays a vital role in determining the binder gel composition, which may help to understand the gel compatibility in a hybrid geopolymer system. However, scarce attempts have been devoted to disclosing the reaction mechanism of Ca involved geopolymer system from the viewpoint of Ca availability. There is still a lack of understanding on the impact of Ca availability on the reaction mechanism and gel composition of hybrid geopolymers.

On the other hand, it has been revealed that Ca has a profound influence on the thermal behavior of the geopolymer system. Recent studies have been extensively carried out on the thermal resistance of hybrid geopolymers containing calcium sources (i.e., slag, calcium hydroxide, etc.) and aluminosilicate source (i.e., fly ash, metakaolin) [24,30,31,168,169]. The major conclusion is that the incorporation of Ca degrades the structural integrity and mechanical properties under high temperatures due to the interruption of geopolymerization and formation of C-(A)-S-H phases that are prone to dehydration/decomposition under high temperatures. Here, given the controversial and complex phase assemblage of hybrid geopolymers, very rare studies take gel compatibility into consideration to explore the thermal degradation mechanism of hybrid geopolymers. As known, N-A-S-H and C-A-S-H gel exhibit distinct thermal behavior under high temperatures. In this case, the relative content of each phase, how they bond together, and their interaction would have a significant influence on the thermal performance of the blended system. But a thorough understanding of the possible influence of gel compatibility on the thermal performance of Ca incorporated geopolymer system is not yet available.

As mentioned in the previous chapter, ladle slag (LS) is a by-product of the steel manufacturing process that continues to be extremely underutilized. Because of the particular secondary refinery process and the applied cooling technique, LS shows a high crystallinity, with calcium aluminates (CAs), namely mayenite ($C_{12}A_7$), and tricalcium aluminate (C_3A) as the main mineral phases [170]. Despite the fact that CAs, especially $C_{12}A_7$, are known to be highly hydraulic and react quickly with water, their content and reaction rate in LS varies between steel plants and production processes, resulting in varied reactivity with water [171,172]. To improve LS reaction efficiency and degree, there is a growing interest in alkali activation on LS, which turns out to be a promising pathway for reutilizing LS as a source of calcium and aluminium. The dissolution, as well as the reaction of crystalline calcium aluminates, is closely dependent on the alkaline content and SiO_2/Na_2O ratio [115,128,173]. It provides the possibility to utilize LS as a controllable calcium source by tailoring alkaline activator composition. In Chapter 3, with a moderate alkali environment, LS shows a positive effect on the geopolymer system attributed to its unique reaction process. Nevertheless, the fundamental mechanism of the dissolution and reaction of LS under alkaline activation is still not clear.

In light of the above knowledge gaps, this chapter aims to clarify the role of Ca availability in determining the gel composition of alkali-activated FA/LS (AAFL) and reveal the underlying mechanism. LS is used as a Ca source, and the alkali activator with tailored Na_2O percentage and silica modulus is applied as a tool to control its dissolution and reaction. The physicochemical properties of the obtained hybrid geopolymer are investigated by monitoring the workability, reaction products assemblage and compatibility, microstructure, and mechanical strength. High temperature exposure tests are carried out to investigate the influences of gel compatibility on the thermal behavior of hybrid binders. The results provide new insights into the gel compatibility of blended geopolymer systems and reveal the underlying reaction mechanism of the AAFL system. Additionally, a thermal degradation model of geopolymeric gel and Ca-enriched gel co-existing binder is proposed.

4.2 Experimental design

4.2.1 Materials

In this work, the precursors, ladle furnace slag (LS) and class F fly ash (FA) are obtained from the same provider as mentioned in **Section 2.2.1**. The received FA was directly used, and LS was collected from stockpiles in Tata Steel, following the pre-treatment described in **Section 4.2.3**. As shown in **Fig. 4.1**, a similar particle size distribution (PSD) was achieved with the average particle size (d_{50}) of 13.99 μm and 13.96 μm for FA and LS respectively, determined by the laser particle size analyzer (Mastersizer 2000, UK). One can observe that the obtained PSD of LS is slightly different from the previous chapter (**Fig. 3.1)**, which should be due to the material variability from different batches. As observed by the scanning electron microscope (SEM) in **Fig. 4.2**, FA and LS have different shapes. As presented in **Table 4.1**, the chemical composition of LS and FA were determined by X-ray fluorescence (XRF, PANalytical Epsilon 3), the specific density was measured via the helium pycnometer (AccuPyc II 1340, Micromeritics), and the specific surface area was determined by the laser particle size analyser.

The crystalline phase assemblage was characterized by X-ray diffractometry (XRD, Bruker D4 PHASER), as shown in **Fig. 4.3**. FA exhibits a hump between 15 and 35° owing to the presence of amorphous phases, with traces of quartz (SiO_2), mullite ($Al_{1.69}Si_{1.22}O_{4.85}$), hematite ($Fe_2O_3$), magnetite ($Fe_3O_4$). LS shows a high crystallinity. Hydrated phases such as Hydrogarnet (C_3AH_6) and Hydrotalcite ($Mg_{0.667}Al_{0.333}$) $(OH)_2(CO_3)_{0.167}(H_2O)_{0.5}$ are detected due to the weathering of slag when disposing in stockpiles. Apart from that, calcium aluminates including Mayenite ($C_{12}A_7$), and Tricalcium aluminate (C_3A) are observed as major phases, indicating the presence of reactive phases even after weathering.

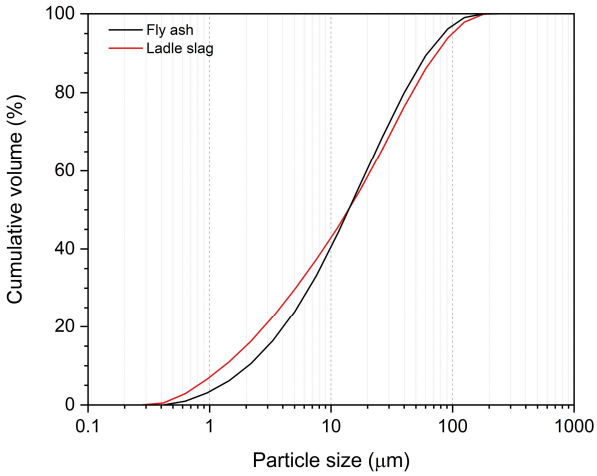

Fig. 4.1 Particle size distribution of raw materials.

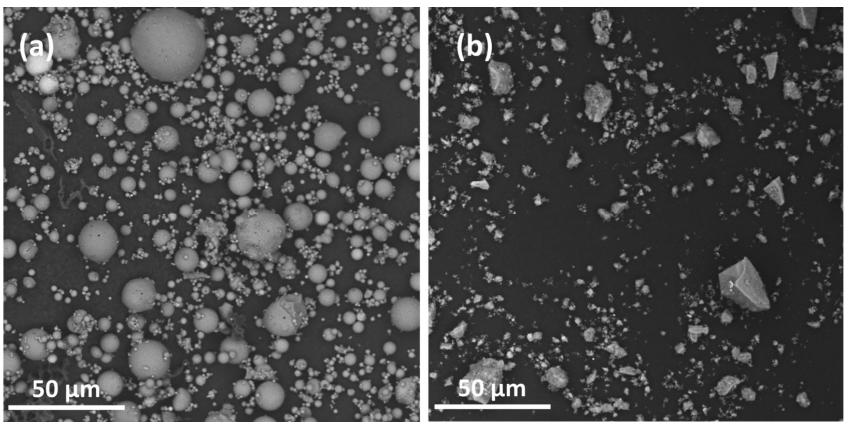

Fig. 4.2 SEM images of (a) FA and (b) LS powder.

Table 4.1 The chemical composition (wt.%) and loss on ignition of Class F fly ash and ladle slag.

Oxides	Fly ash	Ladle slag
SiO_2	54.57	2.32
Al_2O_3	21.60	23.19
CaO	6.12	55.11
Fe_2O_3	9.04	4.44
MgO	1.17	2.21
SO_3	0.41	0.61
K_2O	2.85	-
Others	2.13	1.31
LOI (1000 ˚C)	2.11	10.81
Specific density (g/cm^3)	2.14	2.65
Specific surface area (m^2/g)	1.10	1.53

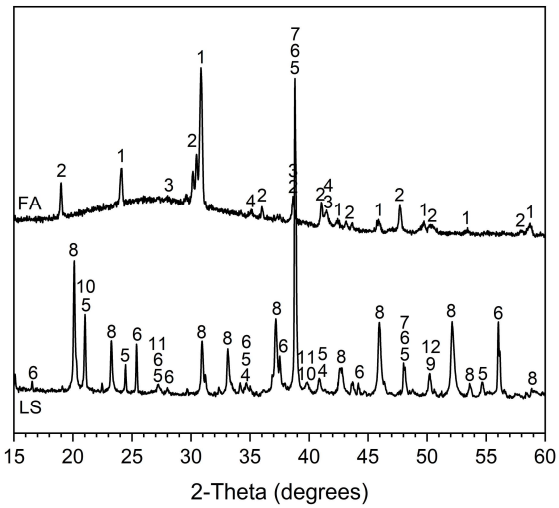

Fig. 4.3 XRD patterns of raw materials.

1-Quartz, 2-Mullite, 3-Hematite, 4-Magnetite, 5-Mayenite, 6-Tricalcium aluminate, 7-Dicalcium silicate (C_2S), 8-Hydrogarnet, 9-Periclase, 10-Portlandite, 11-Hydrotalcite, 12-Iron

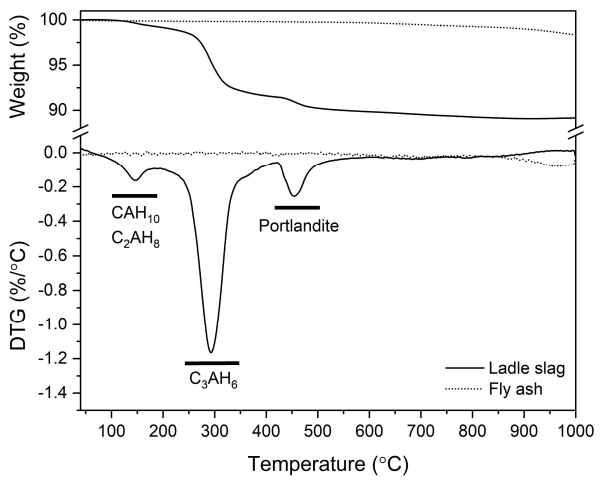

Fig. 4.4 TG-DTG analysis of raw materials.

To determine the weathering degree of the applied LS, thermogravimetry/differential scanning calorimetry (TG/DSC) analysis was carried out, and the result is compared with FA in **Fig. 4.4**. A total mass loss of 10.81 wt.% is observed until 1000 ˚C. The main weight loss peak at around 300 ˚C is attributed to C_3AH_6 [126], and slight mass losses at around 150 and 450 ˚C are associated with metastable calcium aluminate hydrates (CAH_{10}, C_2AH_8) [120,126] and portlandite, respectively. Notably, owing to the complexity of LS disposal, for

instance, the season, weather, stacking age, etc., it is very challenging to control the slag weathering degree. According to the variability among raw LS (See **Appendix B Fig. B1**), the reactivity of raw LS may vary due to different weathering degrees, nevertheless, the mineralogy compositions of LS from different batches are identical as the slag production follows the same protocol. Thus, the applied LS demonstrates sufficient robustness for further investigation. As for the alkali activator, the analytical level of sodium hydroxide pellets (99 wt.%) and sodium silicate solution (27.69 wt.% SiO_2, 8.39 wt.% Na_2O, 63.9 wt.% H_2O) were applied. Distilled water was used to control the water to binder ratio.

4.2.2 Mix design and sample preparation

In terms of mix design, two levels of equivalent sodium percentage (6 wt.% and 8 wt.%, denoted by N6, N8) were applied to tailor the alkaline environment, and three Si moduli (Ms=1.0, 1.4, 1.8, denoted by S1.0, S1.4, S1.8) were investigated at each alkali level. The activator composition is listed in **Table 4.2**. The desired activators were synthesized by mixing a specific amount of NaOH, water glass, and distilled water, thereafter, cooled for 24 h to room temperature before use. According to the previous work [174], the LS addition has a significant influence on the workability, and a high LS substitution always results in poor workability, hence the blend mass ratio of LS to FA was set as a constant of 20/80 and the mass ratio of water to binder was 0.35 in all samples. The mix proportion is shown in **Table 4.3**.

Table 4.2 Chemical composition of working solutions.

Activator	Na_2O (wt.%)	SiO_2/Na_2O modulus (Ms, mol.%)	Oxide composition (wt.%)			pH
			Na_2O	SiO_2	H_2O	
N6S1.0	6	1	12.5%	12.1%	75.4%	13.6
N6S1.4	6	1.4	12.0%	16.2%	71.8%	13.6
N6S1.8	6	1.8	11.5%	20.0%	68.5%	13.6
N8S1.0	8	1	15.3%	14.8%	69.9%	13.5
N8S1.4	8	1.4	14.5%	19.7%	65.9%	13.6
N8S1.8	8	1.8	13.8%	24.0%	62.2%	13.5

Table 4.3 Mix proportion of investigated samples.

Sample code	Ladle slag	Fly ash	NaOH	Waterglass	Water	w/c*
N6S1.0	200	800	54.7	210.0	215.8	0.35
N6S1.4	200	800	45.6	294.0	162.2	0.35
N6S1.8	200	800	36.5	378.0	108.5	0.35
N8S1.0	200	800	72.9	280.0	171.1	0.35
N8S1.4	200	800	60.8	392.0	99.5	0.35
N8S1.8	200	800	48.7	503.9	28.0	0.35

*The total water content consists of the added distilled water and the water in water glass solution.

A 5 L Hobart mixer was applied for making the paste specimens. Firstly, dry precursors were mixed until a homogeneous state was reached, followed by the addition of a certain amount of activator while slowly stirring. The slurry was stirred at a low speed for 30 s and at a high speed for another 30 s. Subsequently, the mixture was cast into plastic molds ($40 \times 40 \times 160$ mm^3) and vibrated for 1 min. The paste specimens were firstly cured at ambient temperature (20 °C) in the sealed molds for 24 h before another 24 h of 60 °C curing. Afterward, the hardened specimens were demolded and cured at ambient temperature under a sealed condition until a certain age of characterization.

4.2.3 Methodology

Raw material treatment and characterization

After being collected from stockpiles, the weathered LS was dried in the oven at 105 °C for 24 h to remove free water. Then, by applying a disc mill (Retsch, RS 300), 600 g dried slag (material feed size <20 mm) was added into a 2000 mL grinding jar and milled for 5 min to obtain the desired particle sizes.

The particle size distribution and specific surface area were determined by a laser particle size analyzer (Mastersizer 2000, UK). The sample was added into the dispersant (2-propanol), dispersed by high-speed mechanical mixing coupled with ultrasound for 1 min to de-agglomerate the particles and eliminate air bubbles before characterization.

The specific density was measured on the powdered/crushed sample via the helium pycnometer (AccuPyc II 1340, Micromeritics).

Workability

The flowability of the slurry was determined by the flow table test following EN 1015-3 [113], which is described in **Section 3.2.3**. The setting times of mixtures were determined according to EN 196-3:2016 [175] by applying a Vicat needle apparatus under an ambient environment (20 °C, 60 % of RH). The moment of adding the activator into the dry precursor was set as zero time. The time at which the needle sinks no more than 0.5 mm is collected as the final setting time.

Reaction kinetics

The reaction kinetics of mixtures were investigated by using an isothermal calorimeter (TAM Air, Thermometric), following the procedure mentioned in **Section 3.2.3**. For different mixtures, the content of dry precursors and activator were set proportionally following the mix composition shown in **Table 4.3**. As the change of working temperature

during the measurement would largely impact the precision of calorimetric measurements, a constant temperature of 20 °C was applied.

Microstructure characterization

The bulk density, skeleton density, porosity, mercury intrusion porosimetry (MIP) and microtomography (Micro-CT) analysis were determined following the same procedure mentioned in **Section 2.2.3 and 3.2.3.** For Micro-CT, the prismatic specimens (1×1×4 cm^3) were collected from the core part of the samples and tested with a pixel resolution of 6.6 μm. 634 image slices from a 4.18 mm thickness of sample were obtained with a picture resolution of 2048×2048, and the data were then gathered to reconstruct and visualize a 3D internal structure. Three sections of each sample were measured for representative results. Materials with varied densities exhibit different absorption tendencies under X-rays, therefore, the components can be identified and separated.

Phase assemblage

For Thermogravimetry/differential scanning calorimetry (TG/DSC), Fourier transform infrared spectroscopy (FT-IR), and X-ray diffraction (XRD) characterization, the tested samples were collected, treated, and tested following the same protocol mentioned in **Section 2.2.3 and 3.2.3**. The samples for SEM were kept in their original shape. The collected samples were then stored in sealed bags in a desiccator in avoiding water immersion or carbonation before analysis. While samples after high temperature exposure were ground/cut and tested directly. For XRD quantification, the XRD file numbers and ICSD codes for the applied crystal structures are provided in **Table 4.4**.

In order to determine the unreacted phases as well as reaction products, the PhAse Recognition and Characterization (PARC) software [176] was applied based on energy-dispersive spectroscopy (EDS) mapping. The tested samples were cut from the centre of the pastes at the age of 28 days. After stopping the hydration, the dried samples were impregnated with epoxy resin and polished to obtain a smooth and flat surface. Then the polished samples were coated with Pt by using a Quorum 150TS plus sputter coater with a current of 40 mA. The spectral image with EDS data was obtained via a JEOL (JSM-7001F) equipped with two 30 mm^2 SDD detectors. An accelerating voltage of 15 kV with a beam current of 6.2 nA was applied, and the step size (resolution) was 1 μm, with the region comprising of 512×384 pixels. The obtained EDS mapping data were further processed with PARC software according to the chemical composition of each point and grouped into phases. An erosion filter was used to exclude the data from the phase boundaries for obtaining representative chemical compositions. Afterwards, pixels surrounded by no less than 8 pixels with the same chemical composition were adopted for

Table 4.4 Structural data of the phases used for XRD analysis.

Phase	#PDF-reference	ICSD
Quartz (SiO_2)	01-083-0539	83849
Mullite ($Al_{1.69}Si_{1.22}O_{4.85}$)	01-089-2813	43297
Magnetite (Fe_3O_4)	01-089-0951	31156
Hematite (Fe_2O_3)	01-089-2810	22505
Metallic iron (Fe)	01-085-1410	11146
Tricalcium aluminate (C_3A)	00-038-1429	1841
Mayenite ($C_{12}A_7$)	00-048-1882	62040
Dicalcium silicate (C_2S)	00-036-0642	81097
Gibbsite ($Al(OH)_3$)	00-007-0324	34393
Hydrogarnet (C_3AH_6)	00-024-0217	9272
Hydrotalcite ($Mg_{0.667}Al_{0.333}$) $(OH)_2(CO_3)_{0.167}(H_2O)_{0.5}$	01-089-0460	81963
Periclase (MgO)	01-071-1176	64928
Calcite ($CaCO_3$)	01-077-2376	40544
Portlandite ($Ca(OH)_2$)	01-087-0673	15471
Ca-Faujasite ($Ca_{40}Al_{80}Si_{112}O_{384}$ $(H_2O)_{116}$)	01-071-0936	176465
Nepheline ($(Na, K)AlSiO_4$)	01-085-1487	-
Wollastonite ($CaSiO_3$)	01-076-0186	-
Akermanite-Gehlenite ($Ca_2(Mg0.5Al0.5(Si1.5Al0.5O7)$)	01-079-2423	-

analysis. To selectively characterize the phase composition of hydration products, a Phenom Pro (The Netherlands) equipped with EDS was used. The same SEM samples were tested as mentioned above. The measurements were conducted in a Backscattered electron (BSE) mode under an accelerating voltage of 15 kV with 4000× magnification, with a working distance between 8-10 mm. The EDS measurements were carried out on the outer surfaces of the samples with the region comprising of 512×512 pixels. More specifically, at least 60 points out of 10 regions are taken from each sample, in which points are carefully selected within the binder region and kept a sufficient distance away from unreacted precursors, following [164,177].

Mechanical property

The compressive strength test was performed on samples at the age of 7 and 28 days, following the same protocol mentioned in **Section 2.2.3**. The prism samples were halved by applying the three-point loading method without being subject to harmful stresses. Four replicates for each mixture were tested at the loading rate of 2400 N/s, and the average value was taken.

High-temperature properties

A similar thermal exposure procedure was selected according to **Section 2.2.3**. The tests were carried out on samples at the age of 28 days. The tested samples were then loaded into a muffle furnace and heated from room temperature to target temperature with a heating rate of 10 °C/min and kept at 800 °C for 1 h to reach the thermal equilibrium state. Afterward, the samples were naturally cooled down to room temperature inside the furnace and then sealed with plastic foil to avoid moisture immersion. For each mixture, three samples were tested under the same condition.

The thermally induced linear shrinkage of samples was determined by comparing the length of the prismatic samples before and after high temperature exposure. Three samples were measured for each mixture, and the average data were taken.

The residual mechanical strength test was carried out on cooled halves of the prismatic samples after high temperature exposure, following the same protocol as mentioned above. The average value of six replicate measurements was adopted as the residual strength value.

4.3 Results

4.3.1 Workability and reaction kinetics

It has been previously reported that geopolymer with the addition of LS always suffers from low flowability and fast setting problems [170]. As shown in **Fig. 4.5a**, a higher Na_2O content of 8 wt.% increases the flowability. Moreover, with a 6 wt.% Na_2O, the flowability increases with a higher Ms while an insignificant reduction of flowability with increasing Ms is observed in 8 wt.% of Na_2O sample. The workability of the mixture is mainly determined by the early age dissolution and polycondensation of raw materials, which is synergistically influenced by the nature of the precursor (fineness, composition) and activator (type, concentration, modulus) [178]. Here, the dissolution of precursors conducts at a relatively slow pace with a low Na_2O content. The higher Ms increases the thickening of the activator which promotes the dispersion of the precursor particles as an effect of lubrication [154,179]. Thus, a higher flowability is detected with the increased Ms at 6 wt.% of Na_2O. While at a higher Na_2O level, more environmental OH^- accelerates the dissolution process, and further increases flowability. The slight variation of flowability with increased Ms is expected to be the co-effect of dispersion and dissolution. The setting time of samples is depicted in **Fig. 4.5b**. As compared to the setting of sole FA based geopolymer (more than 24 hour at room temperature) [180], LS plays a dominant role in the observed setting behavior. This is because the C_3A and $C_{12}A_7$ react very quickly with water that easily

causes flash setting. At a low Na_2O content, due to the limited content as well as weathering process of LS, the flash setting is avoided but still, the setting of hybrid geopolymer is largely shortened to less than 1 h. With increasing Ms, abundant soluble Si could attract more environmental ions that accelerate the formation of hydration products. While a higher Na_2O content is noticed to prolong the setting time, and the setting is further increased with rising Ms. The reason for this observation is not entirely clear, but it is possibly related to the dissolution kinetics that a higher alkalinity slows down the Ca dissolution rate at initial phase according to solubility constant principle [181].

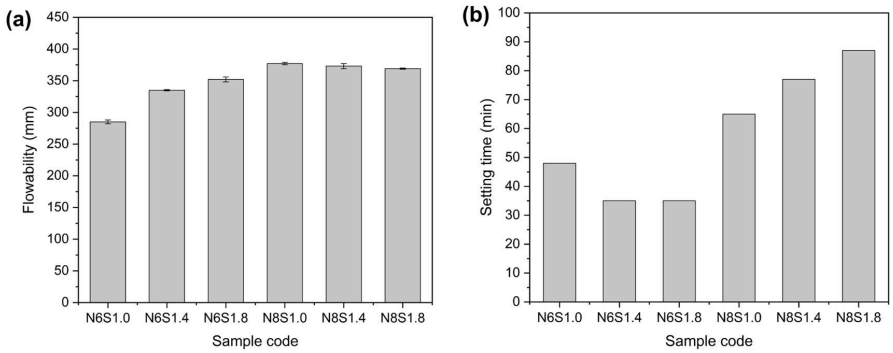

Fig. 4.5 Flowability and setting time of pastes prepared with different Na_2O wt.% and activator modulus.

The observed phenomenon clarifies that the alkali activator parameters have a significant influence on the workability of the LS/FA binder. With the 20% substitution of LS, the setting time is significantly shortened to a range between 35 to 87 min by tailoring Na_2O wt.% and Ms, indicating the setting of FA-based geopolymer can be controlled/accelerated by introducing LS with a tailored activator.

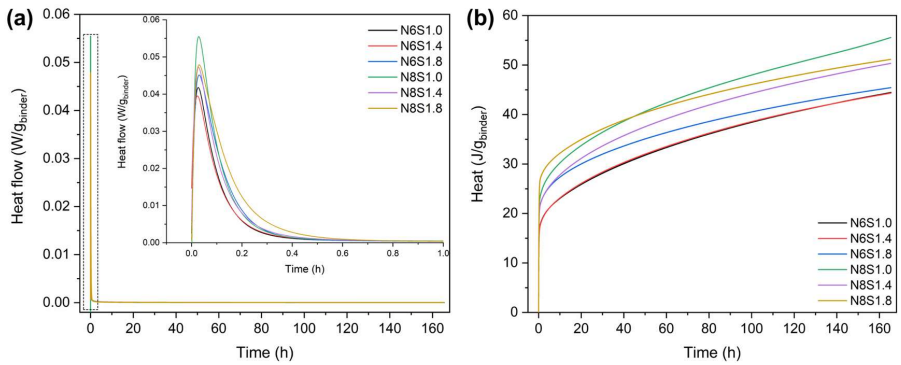

Fig. 4.6 Isothermal calorimetric response of samples, a) normalized heat flow, b) normalized cumulative heat.

The fresh property is further revealed by the reaction kinetics from isothermal calorimetry shown in **Fig. 4.6**. It should be mentioned that, as compared to the realistic curing process, the exclusion of 24 h 60 °C curing in the calorimetric test might results in relatively lower reaction heats than the actual value. But the results can still be used as a general index reflecting and comparing the trend of reaction rate among different mixtures. **Fig. 4.6a** depicts the heat evolution of mixtures for the initial 7 days. It should be mentioned that a single exothermic peak is detected during the measuring period for all mixtures. Such a sole peak phenomenon has been previously reported in FA geopolymer as well as LS/FA hybrid geopolymer [130,182], which is related to the dissolution of precursor, the initial formation of silicate and aluminate species, and their complexation with the sodium and calcium ions [183]. At a low Na_2O wt.% of 6, an increasing heat flow intensity combined with a larger cumulative heat release is observed with raising Ms, indicating its contribution to the dissolution of solid raw materials as well as the early reactivity. This is in agreement with the shortened setting time and better flowability presented in **Fig. 4.5**. Accordingly, a higher Na_2O content largely promotes the reaction degree, with the highest heat flow peak intensity and largest cumulative heat release achieved with Ms of 1.0.

4.3.2 Reaction products

The thermogravimetric (TG) and differential thermogravimetry (DTG) curves of samples are presented in **Fig. 4.7**. The samples with a high Na_2O content of 8 wt.% exhibit a larger weight loss after 1000 °C. As shown in **Fig. 4.7b**, the main mass loss peak in the range of 100-300 °C is associated with the loss of bound water from the main hydration products, namely, N-A-S-H and C-A-(S)-H gel [184]. The second peak is assigned to the dehydroxylation of $Al(OH)_3$ (AH_3, around 260 °C) [185] and hydrogarnet (C_3AH_6) [174]. Additionally, a broad weight loss in temperature ranging from 500-800 °C mainly arises from the presence of $CaCO_3$ in different crystallinity [186]. The poorly crystallized calcite and amorphous $CaCO_3$ decompose at 500-600 °C, while the well-crystallized $CaCO_3$ decomposes at a later stage around 700 °C [187].

In general, the peak intensity of the main reaction products and AH_3 vary significantly as a function of Na_2O wt.% and Ms, meaning that the activator has a significant influence on the reaction of both FA and LS. It is noted that at a Na_2O wt.% of 6 with increasing Ms, the main weight loss peak is not only intensified but slightly shifted to a higher temperature from 126 to 131 °C. Here, the higher amount of readily available silicates in the environment contributes to a higher degree of reaction with more gel phase and tightly bound water [188], intensifying the main mass loss peak. Accordingly, in samples with 8 wt.% of Na_2O, a larger mass loss with the peak temperature shifting to 135 °C is detected. Nevertheless, the difference in the main mass loss peak among samples with different Ms

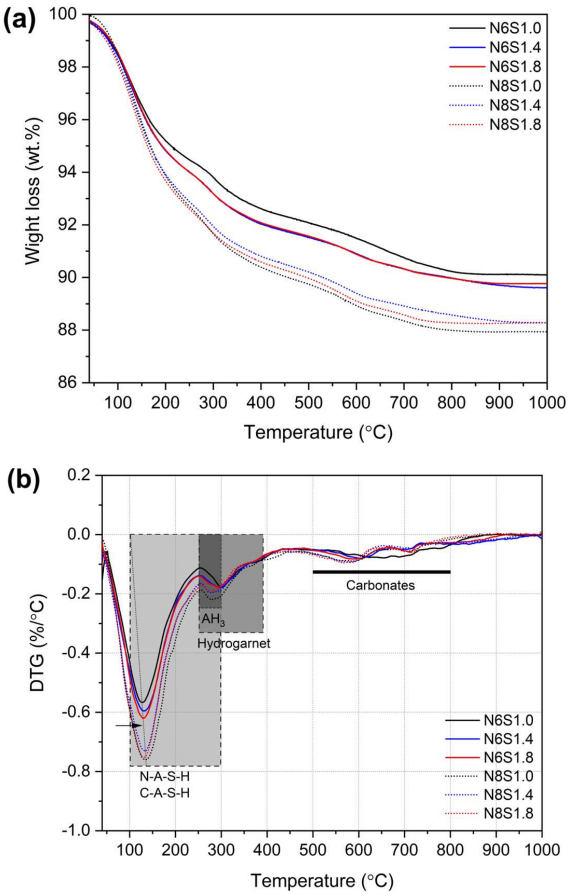

Fig. 4.7 Thermal analysis of pastes with different Na_2O wt.% and Ms at 28 days, (a) TG curves; (b) DTG curves.

is insignificant, and the highest main mass loss peak is achieved with the lowest Ms of 1.0, which is in accordance with reaction kinetics. As for AH_3, the corresponding mass loss peak is indetectable in samples with a lower Na_2O content due to its low content. While at a higher Na_2O wt.%, the AH_3 peak is intensified as consistent with the previous discussion that a high alkali content promotes the dissolution of aluminosilicate species from the precursors. But the AH_3 peak intensity is decreased with the increased Ms. It can be hypothesized that AH_3 tends to participate in the formation of aluminosilicate gels since more soluble silicates are introduced.

The infrared spectra of samples with different Na_2O wt.% and Ms are compared in **Fig. 4.8a**. The band in the range of 670-850 cm^{-1} is corresponding to the stretching vibrations of Si–O–Si, attributed to crystalline quartz introduced by FA. The typical adsorption band of the Si-O-T (where T represents Si or Al species) is observed at around 980 cm^{-1} in all

samples, resulting from the phase overlapping from precursors and aluminosilicate phases. The adsorption of 1643 cm^{-1} and 3418 cm^{-1} are identified as the bending vibrations of physically and chemically bound water and stretching vibrations of O–H bonds respectively. Series of spectra at 1463 cm^{-1} and 1404 cm^{-1} are both assigned to the different vibration modes of CO_3^{2-} [189], confirming the presence of carbonates, which is in line with the calcite detected in TG results. Additionally, the peak ascribed to periclase at 3750 cm^{-1} [190] is insignificant, indicating the relatively low presence of periclase.

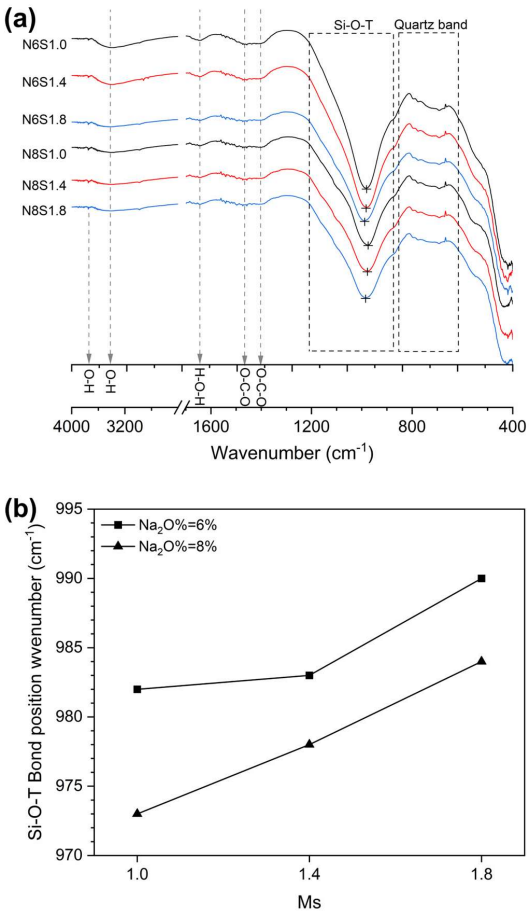

Fig. 4.8 a) FTIR spectra of pastes with different Na_2O wt.% and Ms, b) Si-O-T bond wavenumber variation of samples as a function of Na_2O wt.% and Ms.

It is known that the typical absorption band of the Si-O-T bridge bond reflects the polymerization process within a hybrid system. Here, its position change as a function of Na_2O wt.% and Ms is presented in **Fig. 4.8b**. At a lower Na_2O content of 6 wt.%, the main band shifts to lower wavenumbers with the increased Ms. This is related to more

readily available silicates in the environment that contributes to a higher polymerization degree with more silica-rich cross-linking [191]. While it is noticed that at a higher Na_2O content, the Si-O-T bond is decreased to a lower wavenumber. Because more $Al(OH)_4^-$ is released from precursors, and incorporated into gels as evidenced by TG results, consequently resulting in the shift of Si-O-T band to a lower position [139]. Nevertheless, the Si-O-T band shifts back to a higher wavenumber with a higher Ms. This is because the Si species are directly available in the solution from the activator in case of a higher Ms, while the dissolution of $Al(OH)_4^-$ from precursors is slower as compared to $Si(OH)_4$, hence a higher level of silica cross-linking is promoted in geopolymeric gel. Another feature should be highlighted is that the shape of the Si-O-T bond transforms from a narrowed to a broad shape with a lower intensity since the Na_2O wt.% and Ms increase respectively. This variation should be associated with the formation of either hybrid N,C-A-S-H gel or separated C-A-S-H and N-A-S-H gel, because the variation of gel composition/structure or relative content may alter the shape of the Si-O-T bond [192,193].

The crystalline phases of samples with different Na_2O wt.% and Ms are presented in **Fig. 4.9**. In general, the typical phases such as quartz, mullite, iron oxides, periclase, calcite, and hydrogarnet are introduced by raw precursors as observed in **Fig. 4.3**. There is no new crystalline phase observed in most samples except for N8S1.0. The remanent C_3A and $C_{12}A_7$ indicate the limited reaction degree of calcium aluminates. This is due to, despite the calcium aluminates can react with water rapidly, the hydration product manifests as a continuous plate-shape, progressively enveloping the unhydrated particles and impeding further hydration [144].

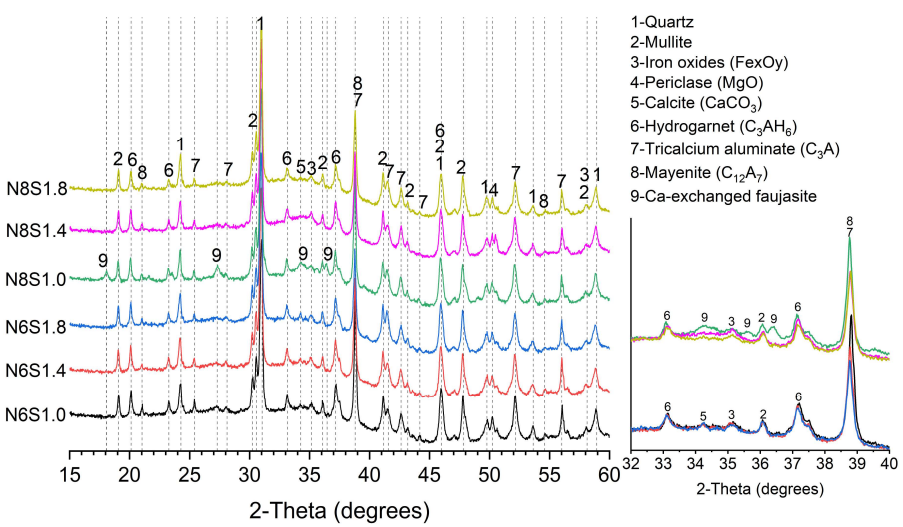

Fig. 4.9 XRD patterns of pastes at the age of 28 days.

Table 4.5 The mineral compound of the mixtures in comparison to raw ladle slag in wt.% as determined by XRD-Rietveld analysis.

Mineral compound	LS	Mixtures					
		N6S1.0	N6S1.4	N6S1.8	N8S1.0	N8S1.4	N8S1.8
Tricalcium aluminate (C_3A)	22.9 (4.6)	4.0	3.6	3.6	3.3	3.0	2.8
Mayenite ($C_{12}A_7$)	4.4 (0.9)	0.7	0.6	0.5	0.6	0.6	0.6
Hydrogarnet (C_3AH_6)	27.5 (5.5)	4.8	4.7	4.6	4.4	4.1	3.8
Dicalcium silicate (C_2S)	2.2 (0.4)	-	-	-	-	-	-
Nordstrandite ($Al(OH)_3$)	1.1 (0.2)	-	-	-	-	-	-
Hydrotalcite ($Mg_{0.667}Al_{0.333}$)($OH)_2(CO_3)_{0.167}(H_2O)_{0.5}$	0.5 (0.1)	-	-	-	-	-	-
Periclase (MgO)	2.8 (0.6)	1.1	0.9	0.8	1.0	0.9	0.8
Portlandite ($Ca(OH)_2$)	1.3 (0.3)	-	-	-	-	-	-
Metallic iron (Fe)	0.4 (0.1)	-	-	-	-	-	-
Ca-Faujasite ($Ca_{40}Al_{80}Si_{112}O_{384}$ $(H_2O)_{116}$)	-	-	-	-	1.3	-	-
Quartz (SiO_2)	-	4.4	4.2	4.3	4.0	4.0	4.1
Mullite ($Al_{1.69}Si_{1.22}O_{4.85}$)	-	5.4	5.3	5.3	4.9	4.9	4.9
Hematite (Fe_2O_3)	-	0.4	0.4	0.5	0.4	0.4	0.4
Magnetite (Fe_3O_4)	-	0.7	0.8	0.8	0.8	0.8	0.7
Calcite ($CaCO_3$)	-	0.6	0.6	0.6	0.8	0.7	0.6
Amorphous	36.9 (7.4)	77.9	78.9	79.0	78.5	80.6	81.3

( ) Content of mineral phases introduced by 20 wt.% addition of LS is calculated.

To quantitatively determine both the crystalline and amorphous phases variation as a change of alkali percentage and Ms, the Rietveld analysis is carried out as summarized in **Table 4.5**. The results reveal that crystalline phases from FA such as quartz, mullite, hematite, and magnetite remain unchanged or slightly decreased, and the reactive phase in FA is mainly amorphous, which is undetectable via XRD. Thus, FA is not included in the comparison. It is further proved that the activator can influence the dissolution of LS, in which the amount of C_3A, $C_{12}A_7$, and C_3AH_6 (hydrogarnet) are increasingly lessened with a higher Na_2O wt.% and Ms, and the reduction of the calcium aluminates is more sensitive to Na_2O content. As discussed in previous works on both calcium aluminate cement [173] and LS [174], calcium aluminate phases and the hydrated C_3AH_6 under a highly alkaline environment with the presence of silicate can react into siliceous hydrogarnet and calcium aluminosilicate hydrate gel, which might be crystallized into zeolitic phases, following the routes:

$$CA \xrightarrow{OH^-} C_3AH_6 \tag{4.1}$$

$$C_3AH_6 \xrightarrow{Silicate} C_3AS_nH_m + C-A-S-H\ (Amorphous\ and\ crystalline) \quad (4.2)$$

This is consistent with the present work. Given the conversion of the amorphous phase in FA to aluminosilicate gel should not impact the total amorphous content, the observed amorphous content variation is mainly ascribed to the dissolution of LS. Here, a larger content of calcium aluminates and hydrogarnet are consumed with increasing Na_2O wt.% and Ms, giving rise to an increase in aluminosilicate gel as evidenced by the higher amorphous content from 77.9% to 81.3%. In addition, a 1.3 wt.% of Ca exchanged Faujasite phase is detected in the high Na_2O content sample, which should be crystallized from (N, C)-A-S-H gel followed by Eq. (4.2). As Ms keeps increasing, this phase tends to disappear. It can be concluded that the Na_2O wt.% promotes the crystallization of calcium exchanged zeolite, while it is more favourable to form N,C-A-S-H gel when there is a low Ca/Si under the circumstance of low Na_2O wt.%, or high Na_2O wt.% with high Ms.

Nevertheless, despite the comprehensive characterizations carried out above, the compatibility between geopolymeric gel and Ca-enriched gel in FA/LS system is still not clear since it is difficult to precisely differentiate them from the TG, FT-IR, and XRD results.

4.3.3 Gel phase identification

Due to the metallic iron introduced by LS, it is impossible to utilize Nuclear Magnetic Resonance (NMR) to characterize the gel properties. As learned in XRD-Rietveld analysis, the reaction products are mostly amorphous and can be easily identified with SEM, which makes the EDS a reliable indicator for selective analysis of gel composition. As shown in **Fig. 4.10**, a representative AAFL sample is evaluated with the PhAse Recognition and Characterization (PARC) analysis (the calculated average chemical compositions of different phases are presented in **Appendix B Table. B1**). In contrast to XRD-Rietveld analysis, PARC analysis is capable of identifying different phases in either crystalline or amorphous forms.

In **Fig. 4.10**, combining the SEM image and phase map generated by PARC software, the unreacted FA (denoted as point A) can be easily distinguished since it exhibits a spheric shape, as also proved by a mix of quartz and mullite in PARC analysis. Moreover, clusters of LS (denoted as point B) are preferably formed, which is evidenced by the mix of calcium aluminates, calcium aluminate hydrates, C_2S, and periclase. Note that it could lead to the lubrication problem that partially explains the poor workability when utilizing LS as a co-binder in geopolymers. In addition, it is interesting to notice that two types of gel are

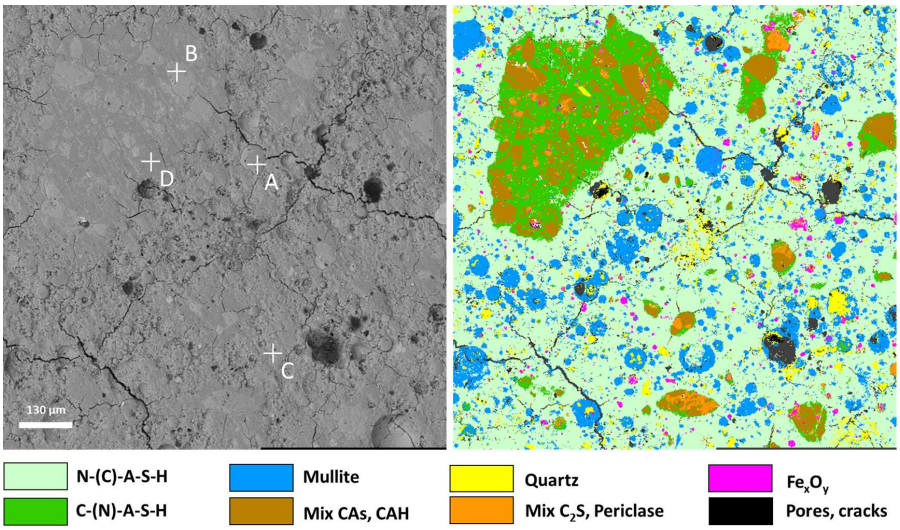

Fig. 4.10 SEM image of representative AAFL sample (left) and phase clustering generated with PARC software based on EDS (right).

differentiated in both SEM and the phase map. A rough and porous binder phase is observed as geopolymeric gel (point C, denoted as N-(C)-A-S-H in light green in phase map), in which the small portion of calcium should be resulted from the uptake of sodium in geopolymeric gel by environmental calcium as discussed above. Apart from that, a smooth and dense binder phase formed around LS particles is ascribed to calcium enriched aluminosilicate gel (point D, denoted as C-(N)-A-S-H in dark green in phase map) with high calcium, aluminium, and silicon, but low Na content.

To further learn the binder gel composition in different samples, selective EDS analysis is conducted on gel phases and the results are plotted in CaO-SiO_2-Al_2O_3 ternary diagrams as shown in **Fig. 4.11**. Interestingly, the binder gel phase distribution patterns are significantly varied in samples with different Na_2O content. Here, for the sample with a Na_2O wt.% of 6% in **Fig. 4.11 a**, the majority reaction product is geopolymeric gel with low calcium (N-(C)-A-S-H). The points are distributed in a larger area in samples with lower Ms, in which minor calcium enriched gel is also obtained. With increasing Ms, the cluster region is largely narrowed from Al-rich N-A-S-H gel to Si-rich N-A-S-H gel, in agreement with the FT-IR results. In terms of high Na_2O content samples, as shown in **Fig. 4.11 b**, unlike the concentrated clusters in lower Na_2O wt.% sample, two separated clustered regions vertically lay on the ternary diagram can be distinguished: i) a low calcium substituted geopolymer gel, ii) a C-(N)-A-S-H gel with low sodium content. The ion proportion of gels varies significantly as a function of Ms with a clear trend. The change

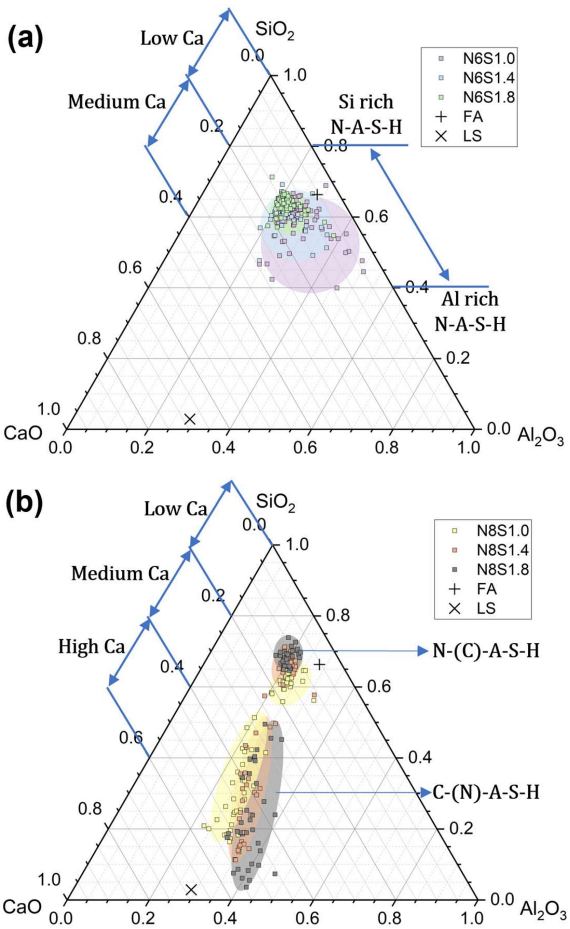

Fig. 4.11 Composition ternary diagram in CaO-SiO_2-Al_2O_3 of EDS analysis (normalized as 1) for the reaction products in samples at 28 days. Approximate regions of C-(N)-A-S-H determined from [64,194] and N-(C)-A-S-H determined from [164,167,195].

in geopolymer gel along with Ms is similar to that of low Na_2O wt.% samples. In the compositional cluster of C-(N)-A-S-H type gel, the calcium content is positively related to aluminium but negatively to silicon, inferring that the phase composition is closely related to the reaction of LS to form C-A-H, as well as its ability of incorporating Si to form C-A-S-H. With the increased Ms, the clustered region increasingly approaches raw LS, which is in accordance well with the XRD results that a higher Ms promotes the dissolution and hydration of calcium aluminates. Furthermore, the gel phase composition is largely enriched with a higher Ms since the C-A-H absorbs silicon to C-A-S-H, thus showing an enlarged cluster region, in which the silicon proportion varies approximately from 0 to 0.5.

At last, it should be emphasized that a balance of ion proportion is reached between those

two gels, namely lower Ca, Al, and higher Na, Si in geopolymer gel; but higher Ca, Al, and lower Na, Si in calcium enriched gel with increasing Ms. This phenomenon indicates a continuous ion exchange process among the two gels with changing of Ms and dissolving of raw precursors. As a result, a co-existence of two independent gels, namely N-(C)-A-S-H and C-(N)-A-S-H arising from FA and LS respectively, is obtained in the hybrid geopolymer system, especially for high Na_2O wt.% samples.

4.3.4 Microstructure and mechanical properties

Fig. 4.12 depicts the microstructure of AAFL specimens with different Na_2O content and Ms at the age of 28 days. Two distinct morphologies are identified in samples with different Na_2O wt.%. With a low Na_2O content, the samples exhibit a loose structure with abundant unreacted precursor particles. This is mainly resulted from the relatively low reaction degree. Apart from that, increasing air voids are entrained, especially for sample N6S1.8, which should be resulted from the fast setting, as observed in **Fig. 4.5**. In contrast, a clearly denser structure with fewer remanent precursors is detected in samples with a higher Na_2O content. Here, the higher Na_2O wt.% promotes the workability as well as the dissolution of the precursor, consequently resulting in a denser structure with more hydration products. The densely clustered phase formed around LS particles are observed in high Na sample but almost indetectable in low Na samples, which can be attributed to either the low reaction degree or the weak matrix that cannot protect the clustered structure during polishing. Moreover, visible microcracks originate along the boundary between the two different types of gels, which should be caused by gel incompatibility, for instance, the differences in autogenous shrinkage degree and gel formation kinetics [147,196]. Moreover, the microcracks are noticed to be increasingly visible in samples with higher Ms. It can be concluded that the increasing Ms further intensifies the incompatibility between the two different gel phases, resulting in the formation of more microcracks.

To learn the distribution of LS based clusters in the matrix, Micro-CT scanning is carried out on sample N8S1.4. In **Fig. 4.12g**, the dense clusters are differentiated from the loose geopolymeric binder and highlighted as light green in contrast to dark green geopolymer binder, the microtomography of plain FA geopolymer and LS/FA hybrid geopolymer are given in **Appendix B** (**Fig. B2**). According to the reconstructed 3D structure, as shown in **Fig. 4.12h**, the LS based clusters (represented as green particles) are scattered in the whole matrix, which further proves the separate existence of LS based gel and geopolymeric gel. Moreover, the identified clusters present in a wide size range, indicating the inhomogeneity of the hybrid binder.

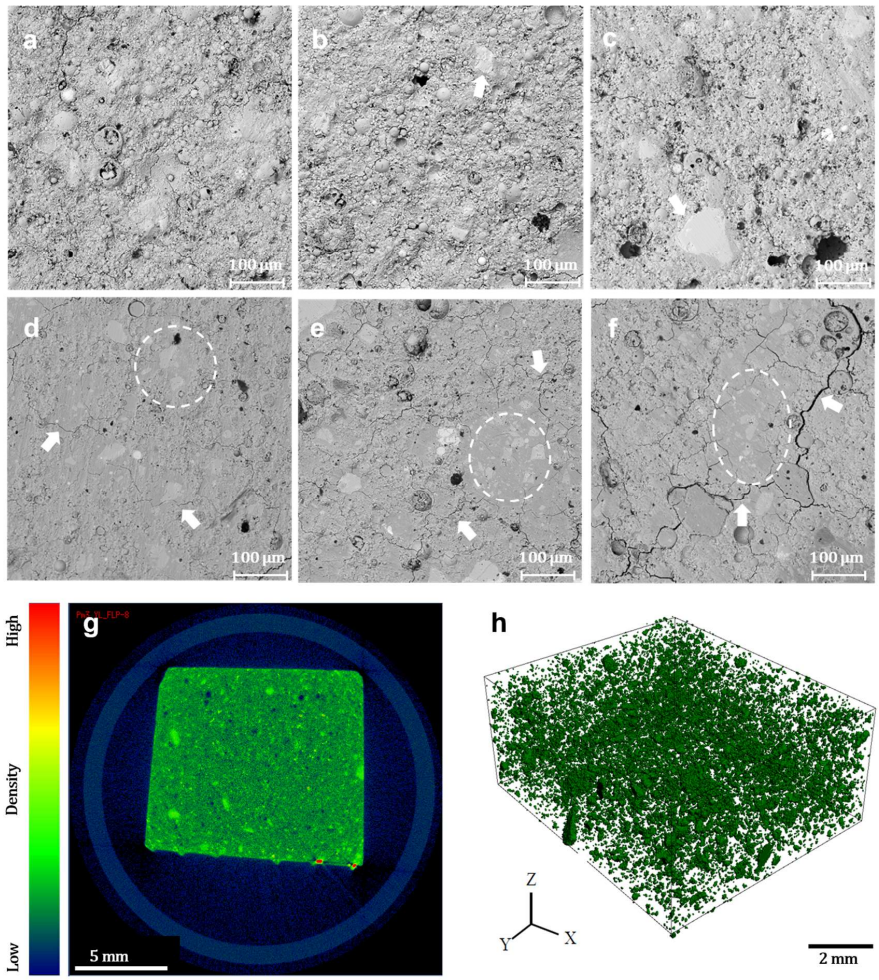

Fig. 4.12 SEM micrographs of AAFL specimens (a) N6S1.0, (b) N6S1.4, (c) N6S1.8, (d) N8S1.0, (e) N8S1.4, (f) N8S1.8; Micro-CT of N8S1.4 (g) 2D, (h) 3D image.

The measured porosity in **Fig. 4.13a** is in good agreement with the SEM observation that poor reaction in 6 wt.% Na_2O samples results in a high porosity as compared to the high Na_2O wt.% samples. There is no obvious trend in the change of porosity as Ms increases from 1.0 to 1.8. But in terms of 8 wt.% Na_2O addition, an increase of porosity along with Ms is detected, which might be related to the server cracking that is noticed in SEM micrographs (**Fig. 4.13d-f**). This is further verified by the pore size distribution obtained from MIP results. As shown in **Fig. 4.13b**, the pores are classified as gel pores ($\leq$10 nm), capillary pores (10-50 nm), and macropores ($>$50 nm) [143]. Under a low Na_2O content of 6 wt.%, with a higher Ms, the pore size distribution follows a trend that the majority of pores transform from macropores to capillary/gel pores. As suggested by Duxson et al. [197] and

Zheng et al. [198], with the binder Si/Al ratio increasing, the pores are refined thanks to the increased gel formation. Accordingly, in 8 wt.% Na_2O samples, the gel pores are largely increased with lowered macropores, which has been linked to the promoted gel formation. However, contrary to 6 wt.% Na_2O samples, a lower capillary but higher macropore is noticed with higher Ms. This is in accordance with the SEM analysis that severer incompatibility of two types of gel leads to cracking and enlarges the thin capillaries to macropores/defects.

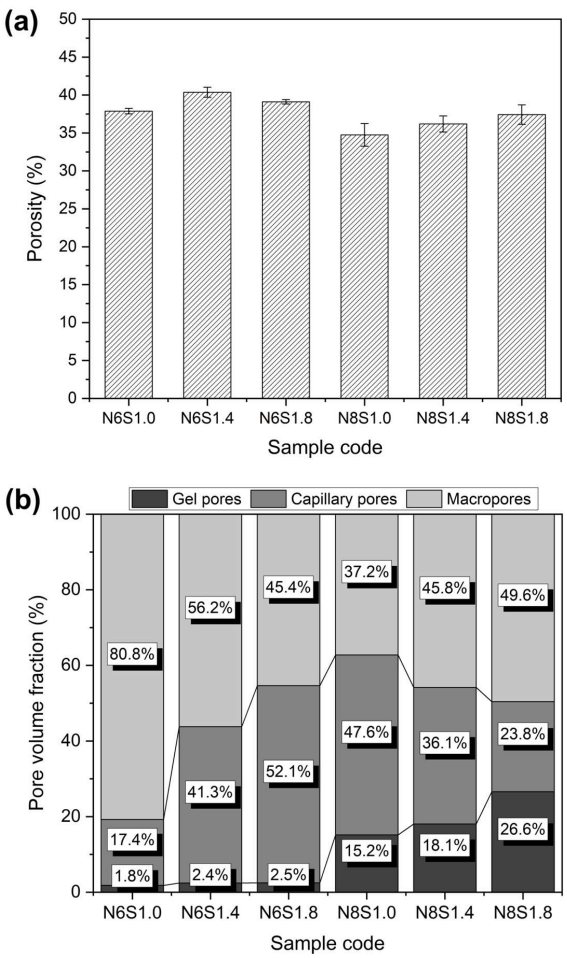

Fig. 4.13 The pore structure of samples with varied Na_2O wt.% and Ms, (a) measured porosity, and (b) pore volume fraction obtained from MIP.

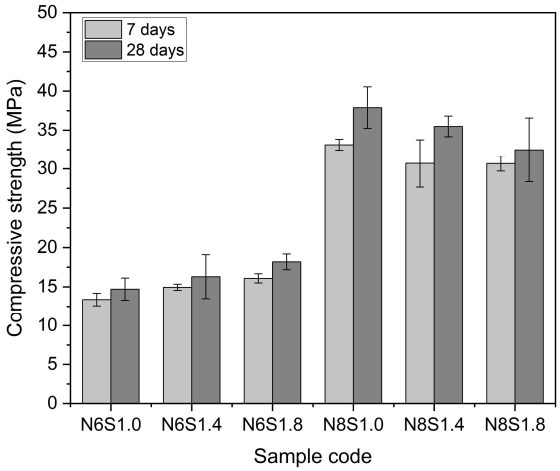

Fig. 4.14 Compressive strength and growth rate of samples between 7 and 28 days, with different Na_2O wt.% and activator modulus.

The compressive strength of the samples at the age of 7 and 28 days are depicted in **Fig. 4.14**. It is clear that Na content plays an important role in the compressive strength of AAFL, which increases significantly with a higher Na_2O content, and N8S1.0 exhibits the highest compressive strength of 37.89 MPa. This is in good agreement with the isothermal calorimetric, TG, and XRD results that a higher content of OH^- promotes the hydration reaction by increasing the dissolution of precursors, hence resulting in higher mechanical strength. At different Na_2O percentages, an opposite trend is detected in compressive strength evolution from 7 to 28 days as a function of Ms. With 6 wt.% of Na_2O, a higher Ms leads to increased compressive strength that is in line with the results presented in reaction kinetics. On the contrary, at a higher Na_2O percentage of 8 wt.%, the compressive strength at 7 and 28 days decreases with a higher Ms. Two possible causes should be noted here: i) The main reason lies in the incompatibility of two types of gel. According to XRD-Rietveld and SEM-EDS results, a higher Ms further stimulates the dissolution of LS for calcium-enriched phases formation, hence intensifying the incompatibility between geopolymeric gel and calcium enriched gel, resulting in more crack formation, as evidenced by SEM and MIP results. ii) Chemically, the highest cumulative heat release and thermalgravimetric mass loss are observed with the lowest Ms. This is suggested to arise from, at a higher Na_2O percentage, the excessive SiO_2 species from both precursors and activator could transform to polymerized SiO_4 that eventually precipitate, which in turn hinder the formation of geopolymeric gels [199]. The N8S1.0 sample possibly reaches a balance between the erosion of OH^- and absorption of soluble silicates, thus achieving the highest reaction degree and compressive strength. As a result, the compressive strength is decreased with a higher Ms at 8 wt.% of Na_2O. Notably, the strength variation is insignificant from 7 to 28 days when taking the error bar into the consideration. According

to Chapter 3, the possible conversion reaction between calcium aluminate hydrates is largely hindered within the geopolymer system. Thus, the observed strength evolution is most likely to be related to the gel incompatibility mentioned above and/or micro-cracking due to drying shrinkage within alkaline activated binder.

4.3.5 High temperature behavior

After the systematic study of initial properties, the high temperature behavior of samples, including crystalline phase transformation as well as physical change of samples exposed to 800 ˚C, are investigated, and their synergetic influence on mechanical performance is assessed.

The XRD patterns of different mixtures after 800 ˚C are characterized and shown in **Fig. 4.15**. It can be observed that, as compared to the XRD patterns in **Fig. 4.9**, the initial mineralogical phase hydrogarnet disappears in all samples upon exposure to 800 ˚C, attributed to its dehydroxylation at around 300 ˚C, as evidenced by TG results. The amorphous hump centred around 30°-40° 2θ is becoming insignificant after 800 ˚C exposure. In addition, new crystalline phases including Akermanite-gehlenite ($Ca_2(Mg_{0.5}Al_{0.5})(Si_{1.5}Al_{0.5}O_7)$), Nepheline ($Na_{6.65}Al_{6.24}Si_{9.76}O_{32}$) and wollastonite-2M ($CaSiO_3$) are noticed in all samples. Here, as triggered by high temperature, calcium enriched aluminosilicate gel (C-(N)-A-S-H) is decomposed and recrystallized into akermanite-gehlenite, and sodium enriched aluminosilicate gels (N-(C)-A-S-H) partially undergoes recrystallization, forming nepheline [24], while wollastonite-2M is thermally formed from amorphous calcium silicates [200], which further explains the weakening of the amorphous hump. The presence of akermanite-gehlenite and nepheline phases correlates well with the results in gel compatibility characterization, further revealing the co-existence of geopolymeric gel and calcium enriched aluminosilicate gel (C-(N)-A-S-H).

When comparing the peaks of newly formed crystalline phases in the zoomed XRD diffractogram, intensified peaks of akermanite-gehlenite, nepheline, and wollastonite-2M are noticed with higher Na_2O wt.%. This indicates that Na content promotes the degree of thermal crystallization. Moreover, interestingly, for both samples with 6 wt.% and 8 wt.% of Na_2O, a higher Ms has a negative influence on the thermal crystallization of akermanite-gehlenite and nepheline, especially for the sample with a higher Na_2O wt.%. Here, the re-crystallization degree of geopolymers at elevated temperatures is highly related to the chemical composition of gel phases. Klima et al. [201] and Pan et al. [202] reported that Na dosage can lower the onset melting temperature of the amorphous phase, which has a direct influence on the re-crystallization degree. However, as for silicon, a similar phenomenon has been reported in sole fly ash based geopolymer [203,204] that the intensity of the nepheline phase is reduced with increasing silica modulus. In this study, it can be

deduced that Si content has a negative influence on both sodium- and calcium-enriched crystalline phase formation at elevated temperatures. As a result, the detected thermal induced re-crystallization would inevitably vary the high temperature performance of geopolymers.

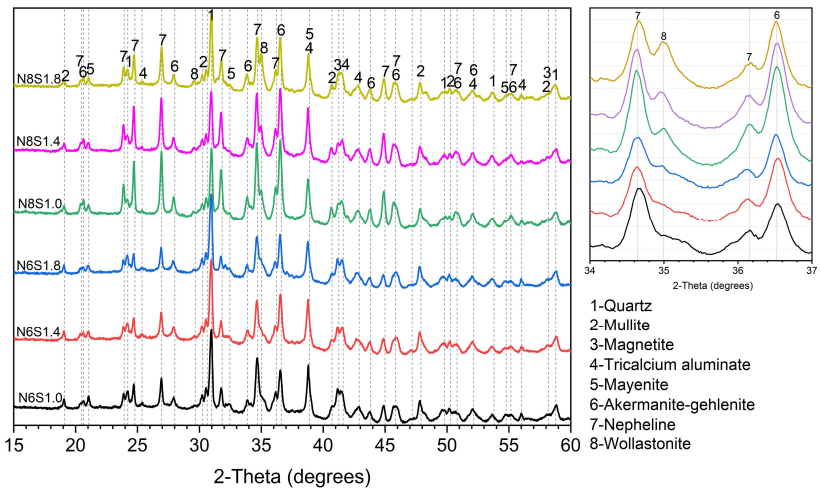

Fig. 4.15 XRD patterns of samples after high temperature exposure.

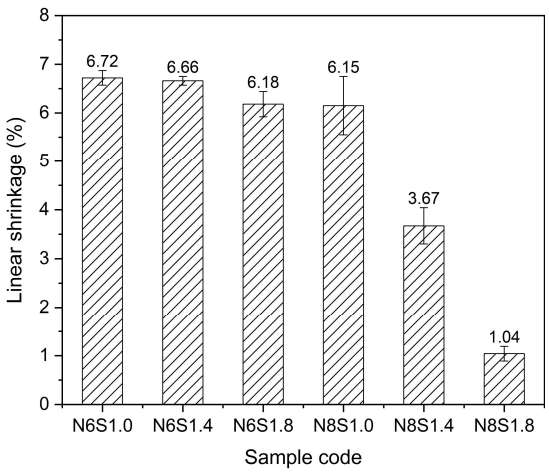

Fig. 4.16 The linear shrinkage of samples after high temperature exposure.

As shown in **Fig. 4.16**, the linear shrinkage of samples after 800 °C exposure is determined. A clear trend is detected that the thermally induced linear shrinkage is reduced with increasing Ms as well as Na_2O wt.%. And Ms has a predominant influence on the high Na content sample, where increasing Ms significantly lowers the linear shrinkage with the lowest shrinkage of 1.04% achieved in the N8S1.8 sample. In general, the thermally

induced volumetric change of hybrid geopolymers is mainly influenced by water evaporation (pore collapse), further geopolymerization (matrix densification), thermal incompatibility between different gels and their deterioration (cracking), crystallization and sintering, from room temperature to 800 °C [205]. Two linear shrinkage behaviours are differentiated in 6 wt.% and 8 wt.% Na_2O samples:

i) At a low Na_2O wt.%, the matrix exhibits a typical geopolymeric behavior at elevated temperatures. This is because, under this situation, the reaction degree of the precursor is relatively low, hence the further geopolymerization as well as the vicious sintering play a leading role, which increases the matrix densification and thermal shrinkage. In this case, a higher Ms promotes the reaction degree as evidenced by the increased mechanical strength, thereafter, weakening the further geopolymerization of remanent FA, resulting in a smaller thermal shrinkage.

ii) At a high Na_2O wt.% of 8, the thermal behavior is impacted not only by geopolymeric gel but also Ca-enriched gel. The lower shrinkage in 8 wt.% of Na_2O samples is suggested to partially arise from the high stiffness matrix owing to the promoted reactivity. Moreover, the highly dispersed dense Ca enrich gel and its re-crystalline phases at 800 °C can act as reinforcing backbone/aggregate to offer a certain degree of resistance to the thermally induced deformation [33]. In this case, the significant reduction in thermal shrinkage with increasing Ms is highly related to the stimulated Ca-enriched gel formation. Simultaneously, as aforementioned, with a higher Ms, the microcracks formed due to the incompatibility between different gels facilitate water evaporation at high temperatures, contributing to reduced thermal deformation.

More detailed information on microstructural change due to high temperature is disclosed by MIP. The pore size distribution before and after high temperature exposure is compared in **Fig. 4.17**. For samples with 6 wt.% of Na_2O, as compared to room temperature, the main peak below 500 nm transforms to a larger size fraction after 800 °C. This transformation is because of the healing of small pores and defects by further geopolymerization and sintering, as well as the crack formation induced by the thermal degradation of gels. When increasing Ms, the peak of the main pore fraction is stably centred at around 2000-3000 nm with a higher intensity. Here, the intensified peak with increasing Ms indicates the declined geopolymeric behavior as discussed above. A similar transformation of the main pore size fraction is also observed in samples with higher Na_2O percentage, which however shifts to a larger pore size diameter. But there is no obvious trend in main peak intensity variation, except the main pore fraction peak shifts from 5000 nm to 8000 nm with a higher Ms. Here, the enlarged pore size should be a result of either the discrepant expansion behavior between geopolymer gel and Ca-enriched gel

or the severe thermal degradation of hydrated products, mainly Ca-enriched gels. In addition, it is worth noting that N8S1.0 has the highest fraction of pores larger than 100 μm after high temperature exposure as an indicator of increased macrocracks.

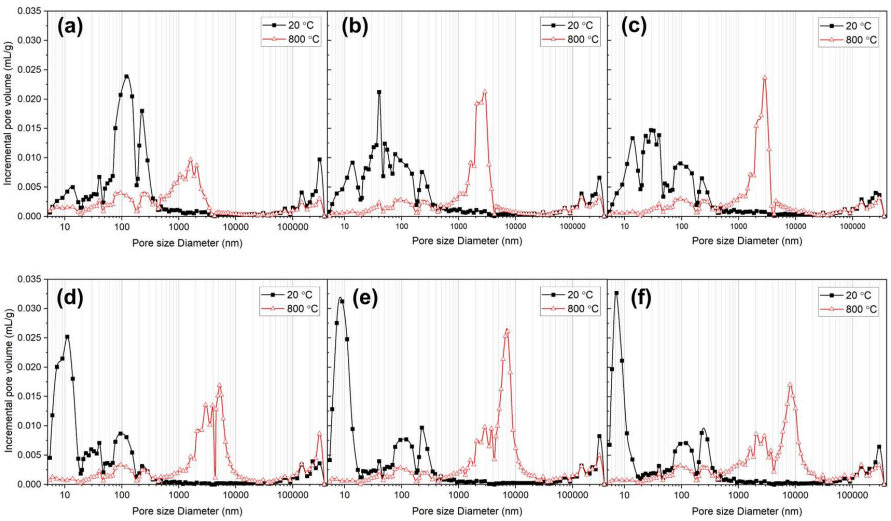

Fig. 4.17 The pore structural transformation of samples before and after high temperature exposure, (a) - (f) represent N6S1.0, N6S1.4, N6S1.8, N8S1.0, N8S1.4, N8S1.8 respectively.

The residual compressive strength of samples after 800 ˚C is compared with the initial strength in **Fig. 4.18a** and the strength change ratio is calculated. As discussed above, the distinctly different thermal evolution phenomenon observed in samples with varied Na_2O wt.% has posed a direct influence on mechanical strength evolution under high temperatures. Among these, the samples with low Na_2O content undergo an obvious strength gain at a rate from 212% to 441%, as compared to the strength gain up to 20% in the samples with high Na_2O content after elevated temperature exposure. Here the mechanical strength evolution patterns can be classified into:

(1) Geopolymer pattern (Low Na_2O content)

Geopolymer dominated pattern exhibited a typical thermal behavior of geopolymer binder, with the most distinctive feature of large strength gain upon exposure to high temperatures. A lower Na_2O wt.% leads to a higher proportion of geopolymeric gel compared to Ca-enriched gel, resulting from the low reaction degree. Hence, further geopolymerization and vicious sintering play the leading role at elevated temperatures. It leads to high thermal shrinkage with large strength gain. Whilst the increasing Ms is proved to lower the thermally induced matrix densification, thereafter, resulting in a reduction of strength gain ratio.

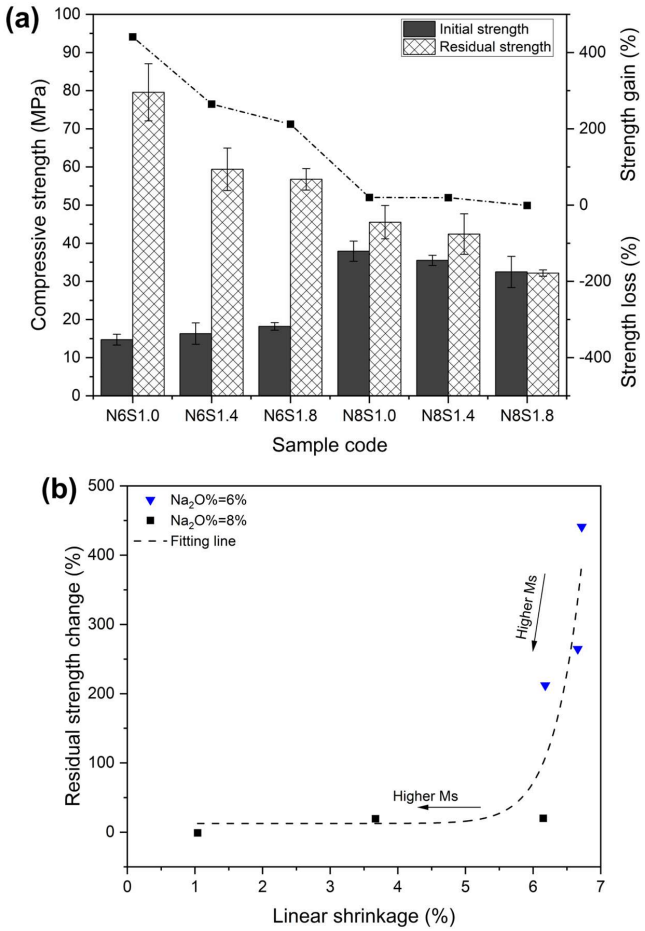

Fig. 4.18 (a) The compressive strength of samples before and after thermal exposure, (b) The relationship between linear shrinkage and residual strength

(2) Hybrid gel pattern (High Na_2O content)

This thermal strength evolution pattern in the hybrid gel system is either differentiated from geopolymeric binder or Ca-dominated binder, which exhibits good mechanical stability with slight strength gain/loss and a tolerable shrinking percentage after high temperature exposure. Here, the further reaction of geopolymer gel and degradation of Ca-enriched gel simultaneously govern the thermal mechanical evolution. On the one hand, the boosted activation degree results in a high stiffness matrix with reduced capacity to accommodate thermal incompatibilities, thus weakening the strength gain at high temperatures [202,206]. On the other hand, it is known that, as compared to geopolymeric gel with superior thermal stability, C-A-S-H gel decomposes from 400 ˚C to 600 ˚C and fully crystallizes at 800 ˚C [31,205], inevitably leading to matrix deterioration. Under the coupling

effect of two gels, a relatively small strength gain is observed at high temperatures.

The strength evolution and linear shrinkage under high temperature is further correlated in **Fig. 4.18b**. The linear shrinkage is decreasing with the residual strength gain ratio. But it is worth noting that the change of strength gain ratio also follows two different trends. At a low Na_2O wt.%, the residual strength change ratio responds rapidly from 212.1% to 441.0% as linear shrinkage increases from 6.1% to 6.7%, while at a higher Na_2O wt.%, the change ratio slowly increases from -1.0% to 20.1% when linear shrinkage increases from 1.0% to 6.2%. It indicates the thermal strength evolution is not fully predominated by matrix densification/shrinkage, especially for hybrid gel systems. In a hybrid gel system, increasing Ms promotes the reaction of LS to form C-A-(S)-H gel, which causes a tendency of cracking at high temperatures, thus weakening the densification effect raised from geopolymeric gel. With the highest Ms of 1.8, it is believed that the thermal responses of two gels reach a balance, hence a minor shrinkage with small strength variation is achieved.

4.4 Discussion

4.4.1 The calcium availability in determining geopolymer gel composition and reaction mechanism

In this chapter, the highly crystalline LS is incorporated as a Ca source in the hybrid geopolymer system. An alkali activator with a specific Na_2O content and silica modulus is applied. The results testify that Na_2O wt.% has a more significant influence on the reaction mechanism as compared to Ms, as reflected in raw materials dissolution, reaction kinetics, and binder gel assemblage. The above characterization and results are combined to provide a mechanistic understanding on the case of low Ca availability in determining hybrid geopolymer gel composition, as shown in **Fig. 4.19**.

For the initial stage in **Fig. 4.19a**, the rapid hydration of $C_{12}A_7$ and C_3A in LS surpasses FA, and initiates a quick polycondensation, resulting in a significantly shortened setting and lower flowability as compared to sole FA-based geopolymer. With continuous dissolution and reaction of LS, a layer of calcium aluminate hydrates is preferentially formed on the surface of unreacted LS grain as observed by SEM (See **Figs. 4.10, 4.12**), which has been previously reported in LS and calcium aluminate-based systems [144,207–210]. This is similar to OPC system, but the higher content of calcium aluminates (C_3A and $C_{12}A_7$) presented in LS initiates more rapid initial hydration. Thus, the Ca in LS is largely consumed as soon as it contacts with water to form the calcium aluminate hydrates layer, and the formed layer further restricts the mutual diffusion of environmental reactant species (alkali activator) as well as the dissolved ions [210], resulting in a low environmental

Ca availability. This limited ion diffusion phenomenon through the product layer is verified by the ion proportion balance among the two gels discussed in **Section 4.3.3**.

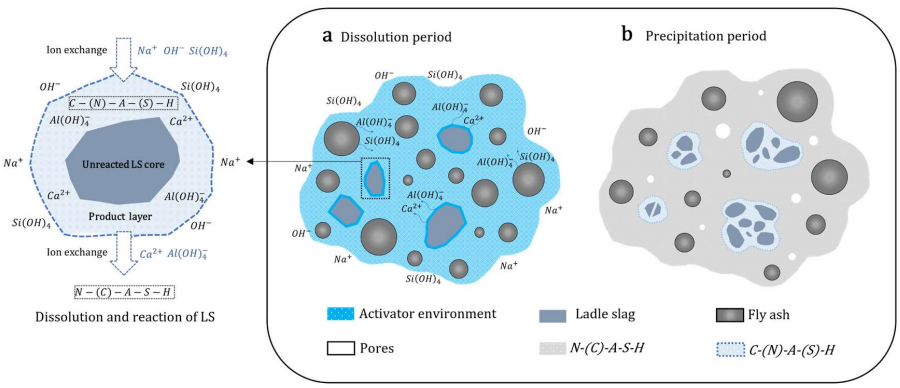

Fig. 4.19 Schematic representation of reaction mechanism between LS and FA under alkali-activation.

Owing to that, the slow Ca^{2+} diffusion into the environment results in a minor substitution of Na^{+} in N-A-S-H gels by Ca^{2+} rather than geopolymerization interruption, hence resulting in a N-(C)-A-S-H phase as observed in **Fig. 4.11**. Notably, in this case, the 3D aluminosilicate framework is retained, which can be distinguished from the 2D C-A-S-H gel as reported by García-Lodeiro et al. [167,195]. Hence the resultant geopolymeric binder shows certain thermal stability. Simultaneously, the environmental species such as Na^{+}, $Si(OH)_4$ can in turn, diffuse into the layer to be absorbed into calcium aluminate hydrates. Thus, a Na and Si substituted calcium aluminate hydrate (C-(N)-A-(S)-H) is characterized in SEM/EDS results. It is worth noting that, since the thickness of product layers keeps increasing and the continuous consumption of alkali, the ion diffusion as well as the reaction of LS are eventually restricted or hindered, resulting in the clustered areas consisting of unreacted LS and hydrated C-(N)-A-(S)-H type gel. As a result, a hybrid binder with clustered Ca-enriched gel (C-(N)-A-(S)-H) wrapping around geopolymeric gel (N-(C)-A-S-H) is observed. Among these, a higher Na_2O wt.% or Ms can promote the reaction of LS, thus governing the co-existence of two gels, which will be discussed in the following section.

In conclusion, calcium availability, including calcium release rate and release degree, plays a prevalent role in determining geopolymer gel composition. The commonly used secondary Ca precursor in geopolymers, for instance, GGBS, and OPC, leads to rapid/high amorphous Ca supply, which largely accelerates the hydration degree but also impedes the formation of geopolymeric gel (N-A-S-H), resulting in a Ca dominated binder [28,29]. While for precursors with limited Ca availability, such as LS, the limitation on the Ca diffusion

under alkali activation results in a unique reaction pathway, where a low Ca release rate into the environment relative to the geopolymeric reaction would not interfere with either the formation or the microstructure of N-A-S-H gel. With a partial ion exchange between Na^{+} and Ca^{2+}, a hybrid binder consisting of isolated C-(N)-A-(S)-H type gel and N-(C)-A-S-H type gel is resulted.

4.4.2 The compatibility between N-A-S-H and C-A-S-H gel

This chapter provides new insights into the phase compatibility in alkali activated slag/FA blends and its influence on room-high temperature behavior. A conceptual model is proposed based on the present results, as shown in **Fig. 4.20**.

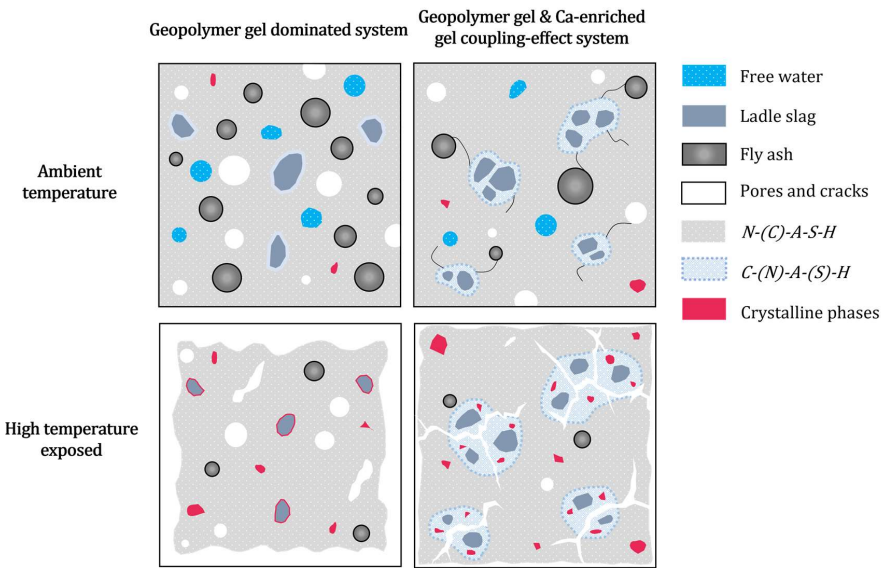

Fig. 4.20 Comparative conceptual model of the geopolymer gel dominated system, and geopolymer gel & Ca-enriched gel co-effect system, and the thermal degradation up to 800 °C.

At a low Na_2O wt.%, the limited dissolution and reaction degree results in a loose matrix with abundant unreacted precursor particles. Moreover, with a relatively low alkaline concentration, only a thin hydrated layer formed on the surface of LS particles due to its low dissolution and reaction degree. Hence the sample is dominated by a geopolymer gel, exhibiting a high porosity and low mechanical strength. Under the condition with high Na_2O wt.%, the increased alkaline concentration promotes the dissolution of precursors, leading to better workability. On the one hand, more FA particles are reacted for geopolymer gel formation. On the other hand, with an enhanced dissolution, the product shell of LS keeps growing until the cessation of LS reaction and ion exchange. As a result,

two hydrated gels, namely C-(N)-A-(S)-H type gel and N-(C)-A-S-H type gel develop simultaneously in a relatively dense matrix, achieving a low porosity and high mechanical strength as compared to geopolymer gel dominated binder. In addition, according to the XRD and SEM-EDS results, increasing Ms further promotes the dissolution as well as the reaction degree of precursors. It intensifies the incompatibility between geopolymer gel and Ca-enriched gel, giving rise to microcrack formation along the boundary between two gels, as evidenced by the SEM and MIP analyses. Therefore, a lower mechanical strength is obtained along with the increasing Ms. The discrepancy between the geopolymer gel dominated system and geopolymer gel & Ca-enriched gel coupling-effect system presents interesting characteristics under high temperatures, which are discussed below:

(a) Geopolymer gel dominated system

As presented in **Fig. 4.20**, upon 800 ˚C exposure, most remanent FA particles are further reacted to form geopolymer gel, and the free water is evaporated. The viscous sintering of geopolymer gel at around 800 ˚C fills small pores and heals microcracks. Moreover, the Ca-enriched gel is prone to dehydrate/decompose at intermediate temperature and fully recrystallize at 800 ˚C, which leads to strength deterioration and crack formation. However, in our previous study [174], the low content of C-A-S-H gel due to the low reaction degree has a limited adverse effect on high temperature behavior. Meanwhile, the calcium induced crystalline phases, such as akermanite and gehlenite further strengthen the matrix [202, 203]. These phenomena predominate in the thermal behavior, which contributes to matrix densification with high shrinkage. As a result, a large strength gain is observed in the geopolymer dominated system.

(b) Geopolymer gel & Ca-enriched gel coupled system

The proposed reaction mechanism results in the co-existence of two separate gels within the matrix, enabling a coupling effect of geopolymer gel and Ca-enriched gel under high temperatures. On the one hand, as mentioned above, the further geopolymerization along with viscous sintering leads to the densification of the matrix by healing small pores and cracks, while posing a tendency for shrinking. On the other hand, the dense Ca-enriched gel and its thermally induced crystalline phases show certain resistance to thermal shrinkage with crack formation as observed in MIP results. In addition, the crack formation because of gel incompatibility is believed to ease thermal stress by acting as a transport channel for water evaporation. Above all, the different thermal behavior between geopolymeric gel and Ca-enriched gel have a combined effect in determining the thermal performance of the resultant binder. This explains the insignificant linear shrinkage and compressive strength change observed in the sample with high Na_2O wt.% and Ms after high temperature exposure (See **Fig. 4.19**). According to the proposed model, it is possible

to design a hybrid geopolymer with desired volumetric and mechanical stability under elevated temperatures by tailoring the two competing mechanisms. Nevertheless, to achieve optimum thermal stability, a relatively high alkali content is applied in this work. Further investigation is necessary to explore alternative solutions that utilize low/non-alkali activators to realize eco-friendly applications for high temperature resistant geopolymers.

4.5 Conclusions

In this chapter, the role of Ca availability in determining the gel compatibility of calcium incorporated geopolymers is revealed. Ladle slag and Class F fly ash in a blended ratio of 2:8 is subjected to the alkali activator with different compositions. The reaction mechanism and gel compatibility are investigated, and their further influence on physicochemical properties and thermal behavior is determined. The experimental results lead to the following conclusions:

(1) The activator composition of Na_2O wt.% and silica modulus (Ms) has a direct influence on the dissolution and hydration of LS. Among these, sodium dosage has a more significant impact on hybrid binder over Ms, reflected by precursors dissolution, workability, reaction kinetics, and binder gel assemblage. A higher Na_2O content contributes to better workability and promotes the dissolution of raw precursors. Increased Ms stimulates the dissolution and hydration of calcium aluminate phases and leads to a higher level of silica cross-linking in aluminosilicate gel.

(2) The availability of environmental Ca plays a vital role in determining the gel composition of AAFL blends. With continuous dissolution and the reaction of LS, a product layer is formed on the surface of slag particles due to the hydration of calcium aluminates, which strongly limits the further Ca dissolution and diffusion into the environment. The limited Ca availability (small amount and/or slow Ca diffusion rate) retains the geopolymerization, with the formation of a partial Ca uptake N-A-S-H gel, preserving the 3D framework of geopolymer. As a result, two hydrated gels, namely C-(N)-A-S-H type gel and N-(C)-A-S-H type gel, are developed separately in a hybrid binder.

(3) For the alkali activated FA/LS system, the incompatibility between two gels is insignificant at a relatively low Na dosage, which remains to be a geopolymer gel dominated system. However, with a promoted reaction degree at higher Na_2O wt.%, a structure with clustered Ca-enriched gel (C-(N)-A-(S)-H) wrapping around geopolymeric gel (N-(C)-A-S-H) is obtained, achieving a dense matrix with low porosity and high mechanical strength as compared to geopolymer gel dominated binder. Moreover, at this condition, a higher

Ms intensifies the incompatibility between geopolymer gel and Ca-enriched gel, giving rise to microcrack formation along the boundary between the two gels. Therefore, increased porosity and decreased mechanical strength have resulted.

(4) A new thermal behavior pattern ruled by the simultaneous effect of geopolymeric gel and Ca-enriched gel is uncovered. At high temperatures, there is a combined phenomenon among the different thermal behavior between geopolymeric gel and Ca-enriched gel in determining the thermal performance of the resultant matrix. This finding helps to design hybrid geopolymers with desired volumetric and mechanical stability at elevated temperatures by tailoring the relative intensity between the two competing mechanisms.

CHAPTER 5

Valorization of mineral wool waste in Class F fly ash geopolymer

The tension between the non-recyclable nature of mineral wool waste (MWW) and the scarcity of landfill space emphasizes the imperative to explore sustainable ways to valorize these wastes. In this chapter, the potential of utilizing MWW as both co-precursor and fiber reinforcement in Class F fly ash geopolymer is investigated. The phase composition and microstructure are systematically learned by multiscale physicochemical analysis, followed by the determination of macro properties and high temperature behavior. Results indicate that the ion dissolution and dimension of MWW have a synergetic effect on the microstructural formation and macro performance of the hybrid geopolymer. The inclusion of MWW, particularly in fine particle form, accelerates the geopolymerization process, leading to enhanced gel formation and increased Al uptake in the N-A-S-H gel. With increasing MWW content (0 to 12 wt.%), a denser gel forms, but greater macropore formation increases porosity, subsequently reducing compressive strength. The desired pore structure with optimal MWW substitution significantly reduces drying shrinkage and enhances flexural properties. At elevated temperatures, MWW poses a healing effect on the matrix, achieving a 98.5% increase in compressive strength with fine MWW incorporation. While a drastic thermal shrinkage arises from the substantial mass loss and partial melting of MWW.

This chapter has been published in the following article:

Y. Luo, Q.L. Yu, Valorization of mineral wool waste in Class F fly ash geopolymer: geopolymerization, macro properties, and high temperature behavior, Cement and Concrete Composites 145 (2024), 105318.

5.1 Introduction

Alkali activation of industrial by-products and recycled aluminosilicates, such as blast furnace slag, phosphorous slag, glass waste, or construction and demolition (C&D) waste to produce alternative cementitious binders has demonstrated its potential in being environmentally sustainable and economically lucrative in the construction industry [15,212]. Compared to Ordinary Portland cement (OPC) counterparts, alkali-activated materials (AAM) not only reduce CO_2 emission by up to 80% but also enable a comparable or even better performance [213]. Among AAMs, geopolymer binders have attracted keen scientific interest owing to their unique characteristics, which are specifically derived by alkali activation on Class F fly ash (FA) or metakaolin, containing little or no Ca [10,13]. Due to its typical three-dimensional aluminosilicate framework, geopolymer possesses numerous properties found in cement, ceramics, and polymers, including controllable setting and hardening [214], high-temperature stability/resistance [201], and chemical (acid) resistance [19], etc. Nevertheless, some major concerns have been raised concerning its energy-consuming curing process, brittleness, and high shrinkage than OPC. Moreover, the exclusive reliance on FA or metakaolin as the sole precursor for geopolymer production inevitably leads to resource competition. The drive to counterbalance the limitations of geopolymer binders has spurred research and development efforts toward exploring new types of precursors for hybrid geopolymer formulations.

As the most commonly used insulating material in the world, mineral wool waste (MWW) generated from the C&D industry or manufacturing lines in Europe was estimated to reach over 2.5 Mt in 2020 and this figure continues to grow [215]. Unfortunately, MWW, including stone wool (SW) and glass wool (GW), is often considered unrecyclable with extremely low valorization, which represents the largest single waste source found in landfills on a volumetric basis regarding its fibrous nature and low density [216]. To date, MWW is mostly reutilized in the concrete industry as supplementary cementitious material and filler/fiber reinforcement [217–219]. However, owing to its fibrous nature and low hydration reactivity, issues related to workability and performance compromises largely hinder its utilization. For the last decade, there has been a growing interest in introducing MWW to the AAMs production. Owing to its advantageous chemical and mineralogical composition, particularly its high content of Si and Al, coupled with a high specific surface area, MWW demonstrates substantial potential as a precursor for alkali activation [220]. Yliniemi et al. [221] proposed an alkali-activated binder with pulverized MWW as the sole precursor and achieved a 28-day compressive strength of up to 49 MPa with heat curing. As reported by the same authors [220], by applying sodium-based alkali activator, MWW particles can be partially dissolved with the main reaction product as amorphous sodium/calcium aluminosilicate hydrate (N,C-A-

S-H). Lemougna et al. [222] and Pavlin et al. [223] further clarified the possibility of improving the alkali activity via effective milling or suitable heat curing. More recently, Ramaswamy et al. [224] investigated the dissolution kinetics of MWW under alkaline conditions and found that high pH can accelerate the dissolution of Si and Al on the MWW surface, where these dissolved species precipitate/recondense into aluminosilicate gel at certain liquid to solid ratios. It is widely accepted that during geopolymerization, the reactive Si and Al contents play a vital role in determining the cross-linking formation, microstructure, and long-term performance [197,203,225]. Thus, it is deduced that MWW holds potential as a co-precursor for geopolymerization, which serves as additional sources of Si and Al and potentially impacts the polymerization process. However, to the best knowledge of the authors, research on joint activation of MWW with aluminosilicate precursors is very limited.

Kinnunen et al. [226] initially prepared a hybrid geopolymer by co-activating FA and MWW with a fixed MWW content. The results testified that MWW has a certain influence on geopolymerization and hydration products, with the formation of N,C-A-S-H gel. Mastali et al. [227] introduced a combined mineral wool (SW and GW) into the joint activation with metakaolin. It further stated that the part-dissolved fibrous nature of mineral wool is affected by alkali parameters, which further impacts the microstructure and mechanical properties. Based on the aforementioned studies, it can be concluded that the MWW incorporation has a certain effect on both reaction products and the microstructure of hybrid geopolymer. Nevertheless, to thoroughly understand the role of MWW in hybrid geopolymer, the dissolution properties and morphology of MWW as well as its substitution content should be further considered and investigated. More specifically, the influence of these factors on the chemical composition and microstructural formation, and how they subsequently affect the performance of hybrid geopolymer remains unclear and urgently deserves further investigation.

At the same time, the drawback of MWW in alkali-activated materials lies in its fibrous nature, which leads to agglomeration, workability problems, and consequently low mechanical strength [216,221]. Hence, a pulverization process on MWW is often reported to alter the fibrous nature and ease the adverse impact. However, reutilizing MWW in hybrid geopolymers can be an alternative way to not only simplify the recycling process but also make use of its fibrous characteristic. On the one hand, the advantage of applying a binary system originates from the fact that FA particles can serve as grinding media that helps the fiber dispersion. On the other hand, alkali-activated materials, including geopolymers, are known to display high brittleness and drying shrinkage [184,228]. Due to its fibrous nature, recycled MWW holds the potential to be used as micro-fiber reinforcement in hybrid geopolymers to improve toughness and mitigate drying shrinkage [229]. Additionally, despite geopolymer has superior thermal resistance performance to OPC counterpart, it inevitably

suffers from cracking and mechanical deterioration at elevated temperatures, especially loss of flexural strength. As widely accepted, fiber incorporation is an efficient strategy to mitigate thermally induced structural deterioration by enhancing pore connectivity and constraining the initiation and propagation of cracks [20]. In this regard, as a heat-insulating material with a high melting point, there is a possibility that MWW can act as a thermal resistant filler/fiber in hybrid geopolymers and promote structural stability. Nevertheless, the impact of MWW's morphological characteristics on the long-term performance of geopolymers, under both ambient and elevated temperatures, remains uncertain.

In light of the above knowledge gaps, this chapter aims to clarify the influence of the dissolution and dimension of MWW on the geopolymer system. By performing different pre-treatments (sieving and milling), two MWWs with distinct dimensions are investigated. The potential geopolymerization reactivity of treated MWW is determined by employing a NaOH dissolution test. With a varying MWW substitution (0 to 12 wt.%), the influence of MWW on the geopolymer is investigated by monitoring the reaction kinetics, phase assemblage, gel composition, and pore structure. The observed features are further correlated with the drying shrinkage behavior and mechanical properties. Lastly, through a high-temperature exposure test, the potential of MWW as a thermal resistant reinforcement on geopolymers is explored. The methodology flowchart is presented in **Fig. 5.1**.

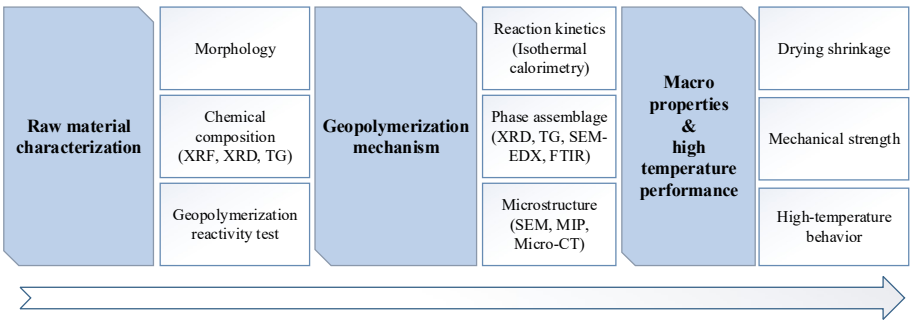

Fig. 5.1 Flowchart of the presented study

5.2 Experimental program

5.2.1 Materials

In this study, low calcium (Class F) fly ash and mineral wool waste (MWW) were applied as source materials. Commercially available FA was purchased from Vliegasunie B.V. (The Netherlands) and was used directly. MWW was provided by ROCKWOOL B.V. (Germany), generated from the cutting and fine processing of final mineral wool products. The as-

received MWW was first dried in the oven at 105 ˚C for 24 h to remove free water. Then, the MWW was classified via different pre-treatments. The dried MWW was directly sieved below 300 μm, denoted as MWW-s. The dried MWW was ground via a disc mill (Retsch, RS 300) for 10 min and then sieved with a 40 μm-sized mesh, denoted as MWW-m.

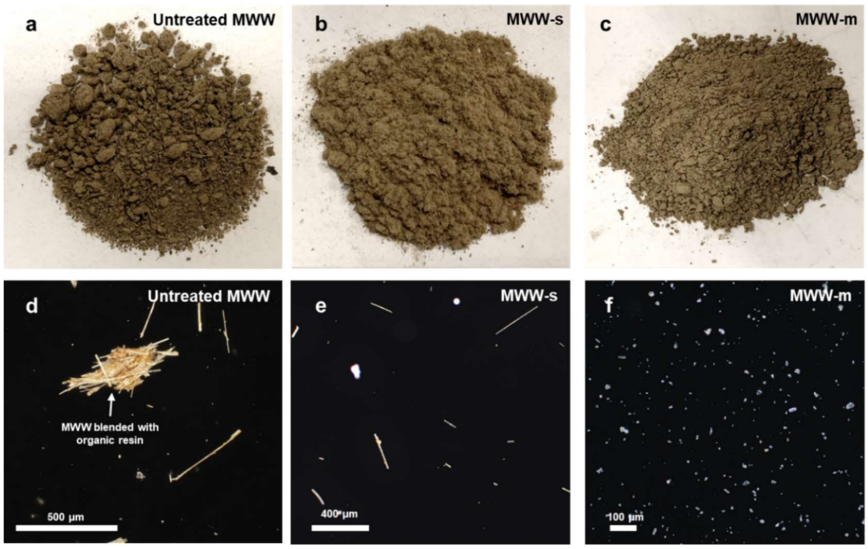

Fig. 5.2 Appearance and morphology of MWW before and after treatment.

The appearance of MWW before and after treatment are shown in **Fig. 5.2**, and the morphology is observed by an optical microscope (Carl Zeiss, Göttingen, Germany). Notably, the untreated MWW consists of crushed mineral wool fiber with cured organic resin. After different pre-treatments, MWW-m has a particle shape while MWW-s mostly remains as microfiber. The particle size distributions of FA and MWW-m were characterized by using a laser particle size analyzer (Mastersizer 2000, Malvern Instruments, UK) in **Fig. 5.3a**, the average particle size (d_{50}) of FA and MWW-m are approximately 16.28 μm and 11.17 μm respectively. Due to the fiber-like morphology, the fiber length distribution of MWW-s was evaluated via an image processing procedure according to Ref [216]. By applying the optical microscope (resolution close to 5 μm) with ImageJ analysis software, more than 1000 individual particles/fibers were evaluated. As shown in **Fig. 5.3b**, the fiber length of MWW-s ranges from 5 to 500 μm with a mean length (L_{50}) of 50.6 μm. In addition, MWW exhibits a relatively uniform fiber diameter of approximately 9.77 ± 1.46 μm, indicating a large aspect ratio.

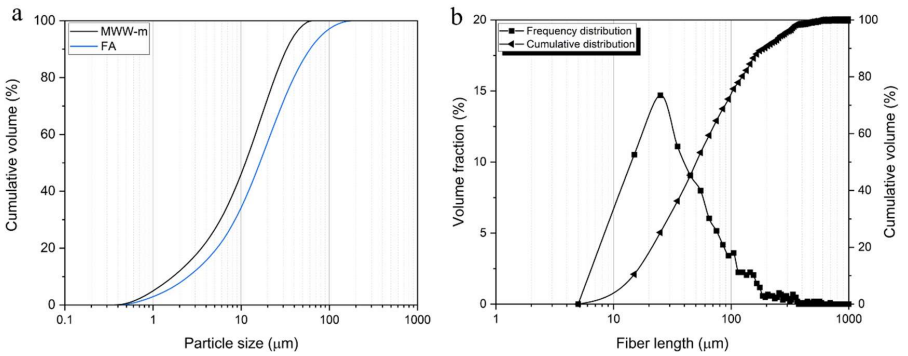

Fig. 5.3 MWW dimension analysis, (a) the particle size distribution of FA and MWW-m, (b) the fiber length distribution of MWW-s.

Table 5.1 The chemical composition (wt.%), loss on ignition (to 1000 ˚C) of class F fly ash and mineral wool waste.

	FA	MWW
Chemical composition		
SiO_2	54.57	38.53
Al_2O_3	21.6	19.39
CaO	6.12	16.97
Fe_2O_3	9.04	8.21
MgO	1.17	8.70
K_2O	2.85	0.95
SO_3	0.41	0.40
TiO_2	1.31	1.60
V_2O_5	0.04	0.04
Cr_2O_3	0.02	0.17
MnO	0.09	0.19
Others	0.67	0.37
LOI (1000 ˚C)	2.11	4.48
Physical properties		
Specific density (g/cm^3)	2.14	2.79
BET specific surface area (m^2/g)	0.79	1.81 (MWW-s) 2.39 (MWW-m)

The chemical composition of FA and MWW was analyzed by X-ray fluorescence, and the loss on ignition was determined after firing at 1000 ˚C, as shown in **Table 5.1**. FA and MWW show a similar specific density of 2.14 and 2.79 g/cm^3 respectively as characterized by Pycnometer (Micromeritics, AccuPyc II 1340). The specific surface area of FA is about 0.79 m^2/g as measured with the Brunauer-Emmett-Teller (BET) method (Micromeritics, TriStar Ⅱ 3020). In comparison, MWW-s and MWW-m show a higher specific surface area of 1.81

and 2.39 m^2/g respectively. The major mineralogical compositions of raw materials were determined by X-ray diffraction. In **Fig. 5.4**, Quartz (SiO_2, PDF# 01-089-8937), mullite ($Al_{1.69}Si_{1.22}O_{4.85}$, PDF# 01-089-2813), hematite (Fe_2O_3, PDF# 00-024-0072), and magnetite (Fe_3O_4, PDF# 01-075-1609) are detected in FA. MWW shows the presence of quartz, hematite, calcite ($CaCO_3$, PDF# 01-086-2339), pyrope ($Mg_3Al_2(SiO_4)_3$, PDF# 01-070-3332), Iron (Fe, PDF# 01-087-0721), Rutile (TiO_2, PDF# 01-082-0514) with a broad amorphous hump range from 25° to 40°. The thermogravimetry results of FA and MWW are compared in **Fig. 5.5**. FA is relatively stable during the entire test, except for a minor mass loss after 900 °C due to viscous sintering. In comparison, a total mass loss of 4.48 wt.% is noticed in MWW up to 1000 °C. The weight loss at around 100 °C is ascribed to the absorbed water release. The main mass loss peak approaching 250 °C is associated with the burning of the organic binder [222], and the peak between 650 and 700 °C corresponds to the decomposition of carbonates [124]. The slight DTG peak at approximately 900 °C corresponds to the partial crystallization of the glass phase. Following reference [216], the organic resin content is determined by the loss on ignition from 105 to 525 °C, yielding 3.57 % and 4.01 % for MWW-s and MWW-m respectively. Analytical sodium hydroxide pellets (Solids, 99 wt.%), and sodium silicate solution (27.69 wt.% SiO_2, 8.39 wt.% Na_2O, 63.9 wt.% H_2O) were applied as alkaline sources. Deionized water was used to achieve the desired water-to-binder ratio.

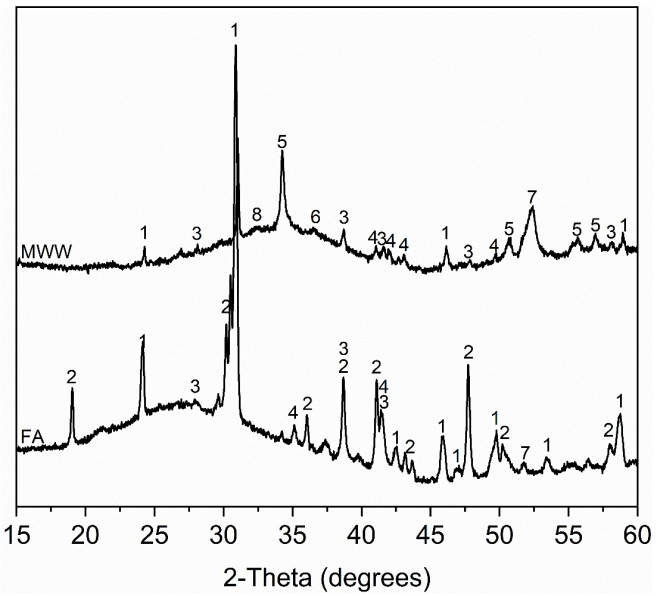

Fig. 5.4 XRD patterns of raw materials (1-Quartz, 2-Mullite, 3-Hematite, 4-Magnetite, 5-Calcite, 6-Pyrope, 7-Iron, 8-Rutile).

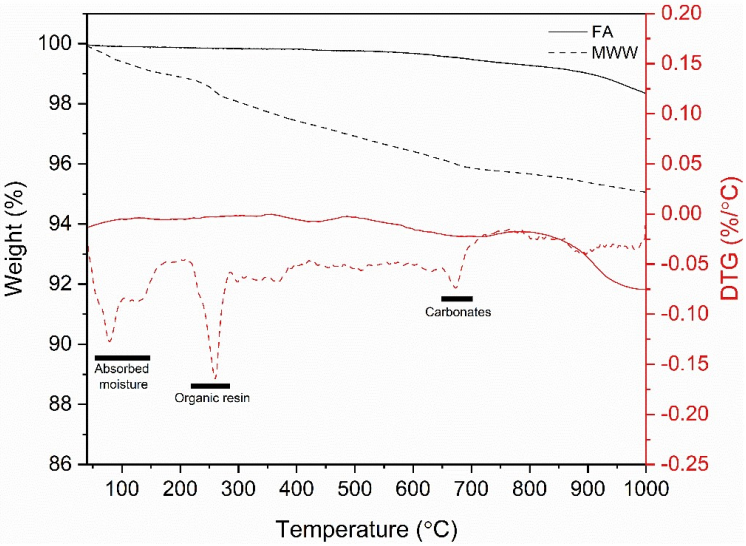

Fig. 5.5 TG-DTG curves of raw materials.

5.2.2 Mixture proportion and sample preparation

The designed mixture proportion in this study is presented in **Table 5.2**. Two pre-treated MWW with different morphologies, MWW-s, and MWW-m, were used to replace FA in the production of hybrid geopolymer binder, denoted as FS and FM. Based on the preliminary experiments, a mass-based replacement of MWW ranging from 4% to 12% was applied, with careful consideration of workability and matrix homogeneity. Accordingly, the volume fraction of MWW was varied from 5% to 18%. A control sample containing 100% FA was also prepared and labelled as Ref. For all samples, the equivalent sodium percentage (Na_2O%) and silicate modulus (Ms) were kept constant at 6 and 1.5, respectively. A water-to-binder mass ratio of 0.32 was applied to all mixtures. The activator parameters were preliminarily chosen according to our previous work [174], to reach a sufficient activation with decent performance.

The alkaline activator was prepared by mixing a specific amount of NaOH pellets, sodium silicate solution, and deionized water, and was allowed to cool down to ambient temperature (20 ± 1 °C) in a sealed container 24 h before being used in sample preparation. All mixtures were prepared using a 5 L Hobart mixer. For Ref and FM specimens, dried powders of FA and MWW-m with a specific mass ratio were directly mixed. In the case of FS specimens, MWW-s were added through a 300 μm sieve to minimize fiber agglomeration. A certain amount of MWW-s was added at a time, with a 1 min string in between additions. Then, the alkaline activator was slowly added while stirring. The mixtures were mixed at a low speed

for 30 s, followed by high-speed mixing for 60 s. The fresh slurry was cast into prismatic molds (40×40×160 mm^3) and cylindrical molds (Ø 45 mm×H 50 mm), and then sealed with plastic film. The specimens were cured at ambient temperature for 24 h, followed by another 60 ˚C curing for 24 h. All specimens were then demolded and cured at ambient temperature for 26 days under sealed conditions until further characterization.

Table 5.2 Mix proportions of the investigated geopolymer pastes.

Mixture	Mass fraction (wt.%)			Na_2O% (wt.%)	Ms*	w/b**	l/b***
	FA	MWW-s	MWW-m				
Ref	100	-	-	6	1.5	0.32	0.48
FS4	96	4	-	6	1.5	0.32	0.48
FS8	92	8	-	6	1.5	0.32	0.48
FS12	88	12	-	6	1.5	0.32	0.48
FM4	96	-	4	6	1.5	0.32	0.48
FM8	92	-	8	6	1.5	0.32	0.48
FM12	88	-	12	6	1.5	0.32	0.48

* Ms is the mol ratio of SiO_2 to Na_2O in alkaline activator

** w/b is the mass ratio between water in the alkali activator and binder, in which the water consists of deionized water and the water in the sodium silicate solution

*** l/b is the mass ratio between the alkali activator solution and binder

5.2.3 Methodology

Potential geopolymerization reactivity test

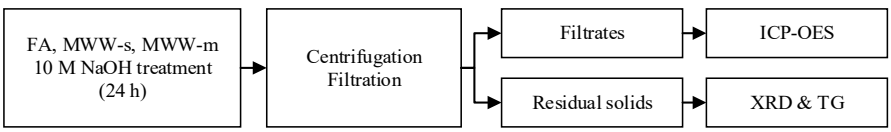

Fig. 5.6 Procedures of reactivity test

As shown in **Fig. 5.6**, the reactivity test was designed according to [224,230]. The experiments were performed at room temperature (20 ± 1 ˚C). The NaOH solution was prepared by dissolving NaOH pellets in distilled water, yielding a molarity of 10. 7.5 g of dried raw powder was added into 200 ml of NaOH solution within the 250 ml polypropylene bottle. The sealed bottles were shaken for 24 h by a liner reciprocating universal shaker (SM-30, Edmund Bühler) at 250 rpm. After stirring, a centrifuge (MULTIFUGE ×3, Thermo) was applied to obtain the suspension, following a vacuum filtration process using 5-13 μm pore diameter filter paper. The filtered solutions were diluted 100 times with deionized water, and

then acidified with concentrated HNO_3 to prevent the precipitation. The obtained solutions were analyzed by Inductively coupled plasma-optical emission spectrometry (ICP-OES, SPECTROBLUE) to determine the concentrations of the dissolved ions. The residual solids were washed with isopropanol to avoid further dissolution, and dried in the vacuum oven for 48 h. The dried samples were weighed and kept in a desiccator until XRD and TG analysis. The dissolution degree D_i (mg/g_{raw}) and the normalized dissolution extent E_i (%) were calculated according to [224,231]:

$$D_i = \frac{C_i \cdot V}{m_{raw}} \tag{5.1}$$

$$E_i = \frac{C_i \cdot V}{m_{raw} \cdot X_i} \tag{5.2}$$

Where C_i represents the concentration of the element i released (mg/L) as determined by ICP analysis, V is the volume of the alkali solution (L), m_{raw} is the mass of the raw material (g), X_i is the mass fraction of element i in the raw material according to XRF analysis. The reactive Si/Al ratio is the dissolution degree of Si to Al.

Reaction kinetics

The reaction kinetics of investigated mixtures were determined by using an isothermal calorimeter (TAM Air, Thermometric) as described in **Section 3.2.3**. The mixes were prepared according to **Table 5.2**. Besides, to compare the reaction kinetics among different raw materials, two additional mixtures using plain MWW-s and MWW-m were investigated. The tests were conducted for 7 days to evaluate the cumulative heat, and the results were normalized by the mass of the solids.

Phase assemblage

For phase assemblage characterization, the samples for XRD, TGA, and FTIR were collected at the age of 28 days or after high temperature exposure. The samples were treated and tested according to the same procedure mentioned in **Sections 2.2.3** and **3.2.3**.

Bulk properties and microstructure

The bulk density, skeleton density and porosity were calculated according to the same method mentioned in **Section 2.2.3**.

The microstructure as well as the gel composition of the hydrated samples were investigated by applying a Phenom ProX scanning electron microscope (SEM) equipped with energy-dispersive spectroscopy (EDS). The sample treatment and equipments were used as given

in **Section 2.2.3**. The microstructures were recorded at 300× magnification while EDS was conducted at 1500× magnification with a working distance between 8-10 mm. The EDS analysis was carried out on a region comprising 512 × 512 pixels. The analyzed points were carefully selected in the binder region with a sufficient distance from unreacted materials. For each specimen, at least 40 points were adopted from 8 regions.

The mercury intrusion porosimetry (MIP) as well as microtomography (Micro-CT) were performed following the procedure described in **Section 2.2.3** and **4.2.3** respectively.

Dry shrinkage and mass loss

The samples with the dimension of 40 × 40 × 160 mm^3 were tested for drying shrinkage and mass loss. The test was carried out in the curing room with a temperature of 20 °C and relative humidity of 60%. The linear dimension variation of samples along the longitudinal axis was measured by using a digital length comparator (± 0.001 mm), and the weight change was collected at the same time. The length change $L(\%)$ was calculated according to:

$$L(\%) = \frac{L_0 - L_n}{L_i} \times 100\% \quad (5.3)$$

where L_0 is the initial length after demolding, L_n is the length at specific ages, and L_i represents the effective initial length of 160 mm.

Mechanical strength

The mechanical strength tests were carried out following EN 196-1 [86]. Prismatic samples (40 × 40 × 160 mm^3) at the age of 28 days were adopted for the three-point bending tests. A universal testing machine (Instron 5967) was applied with a displacement rate of 1 mm/min. Three replicates of each mixture were measured, and the average value was taken. Afterward, the flexural energy is determined geometrically by calculating the area beneath the flexural load-displacement curve according to [232]. In terms of the compressive strength test, six halves of the prismatic specimens obtained from three-point bending tests were measured by a compression testing machine (CONTROLS, AUTOMAX 5) with a loading rate of 2400 N/s, and the average was recorded.

High-temperature behavior

The high-temperature exposure test was designed according to **Section 2.2.3** to achieve comparable results. The tests were performed on 28 days of cured cylindrical (Ø 45 mm × H 50 mm) and prismatic (40 × 40 × 160 mm^3) samples. For each mixture, 3 cylindrical samples and 3 prisms were tested. After high temperature exposure, cylindrical samples were

used to assess the thermally induced shrinkage by comparing the length change along the longitudinal axis before and after elevated temperature exposure. The mass of cylindrical samples was recorded before and after heat treatment to calculate the mass loss. The average value of 3 samples was adopted. To determine the residual mechanical strength after high-temperature exposure, an identical protocol was conducted on cooled prismatic samples as mentioned above. The average of 3 and 6 replicates were taken for flexural strength and compressive strength respectively.

5.3 Results

5.3.1 Potential geopolymerization reactivity

The available Si and Al contents play a vital role during geopolymerization [197]. To learn the potential reactivity of MWW for geopolymerization, a NaOH dissolution test is conducted to determine the available Si and Al released from MWW as compared with FA. As shown in **Table 5.3**, MWW is observed to have a larger mass loss after NaOH treatment than FA, among which the milled MWW exhibits the highest mass loss of 18.0 wt.%. In line with the mass loss, despite FA inherently having higher Si and Al content (see **Table 5.1**), the dissolution degree (D_i) as well as normalized dissolution extent (E_i) of Si and Al from MWW are almost 2 to 3 times higher than FA. Thus, the reactive Si/Al ratio is increased from 1.74 to 1.76 and 1.98 for MWW-s and MWW-m, respectively, which indicates that MWW potentially provides more available Si and Al for geopolymerization as compared to FA. Interestingly, despite the D_{Al} being lower than D_{Si} in all samples, E_{Al} is higher than E_{Si}. It reveals that Al dissolves faster than Si since Al-O bonds are weaker than Si-O [233].

Table. 5.3 The mass loss, elemental release of different materials after NaOH dissolution, and the calculated reactive Si/Al ratio.

Raw material	Mass loss (wt.%)	Dissolved concentration (mg/L)		Dissolution degree (mg/g_{raw})		Normalized dissolution extent (%)		Reactive Si/Al ratio
		Si	Al	Si	Al	Si	Al	
FA	7.8	279.3	160.3	7.4	4.3	1.8	4.0	1.74
MWW-s	10.3	541.0	308.0	14.4	8.2	5.8	9.8	1.76
MWW-m	18.0	856.9	433.1	22.9	11.5	9.1	13.8	1.98

Nevertheless, alkali activation is known to be a heterogeneous process, in which several stages including dissolution, speciation equilibrium, gelation, and polymerization occur simultaneously [161]. During the NaOH dissolution test, reactive elements would not only dissolve into the environment but also precipitate and form new phases, which inevitably affect the precision of the elemental dissolution degree and extent. Taking this into

consideration, XRD and TG analyses are further performed on NaOH-treated MWW residuals. The XRD patterns of MWW-s and MWW-m residuals after NaOH dissolution are presented in **Fig. 5.7**. As compared to the raw MWW in **Fig. 5.4**, the calcite observed in raw MWW is indetectable in treated MWW residuals. Moreover, new crystalline phases, including hydrogarnet ($Ca_3Al_2(O_4H_4)_3$, PDF# 01-084-1354) and hydrotalcite ($Mg_6Al_2CO_3(OH)_{16}\cdot 4H_2O$, PDF# 00-014-0191) are observed after NaOH treatment. Notably, the intensities of these newly formed phases are largely promoted in MWW-m residual.

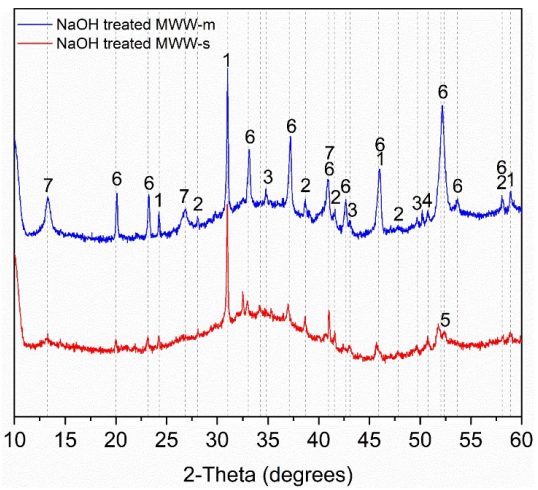

Fig. 5.7 XRD patterns of MWW-s and MWW-m after NaOH treatment (1-Quartz, 2- Hematite, 3-Magnetite, 4-Calcite, 5-Iron, 6-Hydrogarnet, 7-Hydrotalcite).

In **Fig. 5.8**, the TG-DTG results correlate well with XRD patterns. As compared to the raw MWW in **Fig. 5.5**, the organic resin is dissolved during the NaOH treatment, hence the corresponding weight loss peak at 250 ˚C is not observed. In addition, the peaks appearing at around 200 ˚C and 350 ˚C are assigned to the removal of interlayer water and decomposition of structural hydroxyl groups in hydrotalcite, respectively. The mass loss peak range from 200 to 300 ˚C can be ascribed to the dehydration of hydrogarnet [174]. Apart from that, the mass losses that arise from the decomposition of portlandite at around 450 ˚C and decarbonization of carbonates at around 710 ˚C are noticed in both NaOH-treated MWW. In agreement with the XRD results, higher peak intensities in hydrotalcite and hydrogarnet are observed in the NaOH-treated MWW-m as compared to MWW-s, indicating a promoted reaction degree.

In summation, MWW shows certain reactivity in the alkaline environment. A significant amount of Si and Al are released from MWW as stimulated by the alkali environment, and a higher reactive Si/Al ratio is obtained as compared to FA. Subsequently, new hydrates such

as hydrogarnet and hydrotalcite are formed. Furthermore, the milled MWW exhibits the highest reactivity with more released reactive content and hydration products, attributed to its finer particle size and larger surface area.

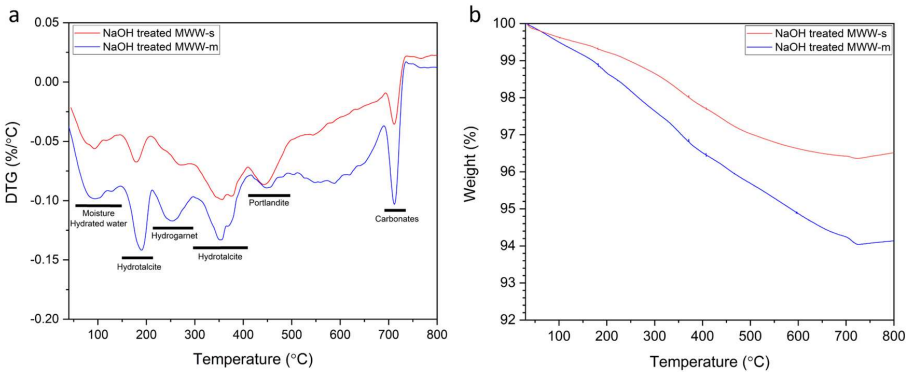

Fig. 5.8 TG-DTG results of MWW-s and MWW-m after NaOH treatment.

5.3.2 Reaction kinetics

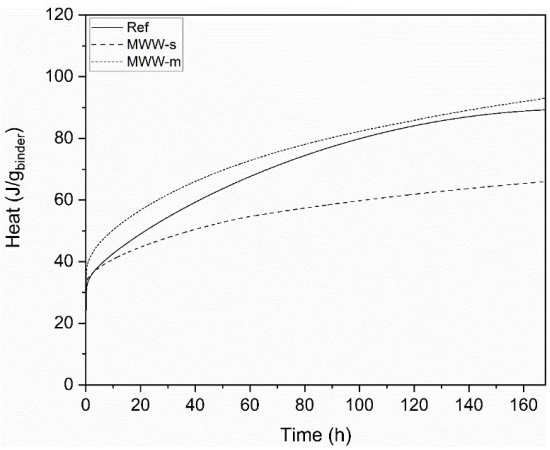

Fig. 5.9 The cumulative heat release of different raw materials.

To learn the effect of MWW incorporation on the hydration degree of geopolymers, the early age hydration kinetics is investigated with isothermal calorimetry. At first, as shown in **Fig. 5.9**, plain MWW-s and MWW-m based pastes with the same activator parameters as Ref are prepared for comparison. Notably, during the measurement, it is challenging to achieve sufficiently homogeneous mixing of MWW in the ampoule due to their poor workability, especially for MWW-s. Thus, the real MWW content that participated in

hydration is lower than the theoretical values. Despite that, the MWW-m binder exhibits a higher cumulative heat than the FA binder for up to 7 days, indicating its higher reactivity. While the cumulative heat in the MWW-s binder is largely reduced.

Accordingly, in **Fig. 5.10a** and **b**, the incorporation of both types of MWW into the geopolymer system shows a promotive effect on the total heat release. It indicates that the hybrid binder reaches a relatively homogeneous distribution of MWW since the FA particles act as dispersion aids during the mixing. The cumulative heat of FS and FM pastes with 12 wt.% MWW substitution reach 107.80 and 105.70 J/g_{binder} respectively at 168 h, which is much higher than that of Ref paste (89.20 J/g_{binder}). As consistent with the results in **Fig. 5.9**, the relatively high total heat release observed in FM can be attributed to its superior reactivity under the alkaline environment and the nucleation effect of finer particles. It is noted that with the MWW-s substitution from 4 to 12 wt.%, FS pastes exhibit a similar cumulative heat, representing 105.4, 105.1, and 105.7 J/g_{binder}, respectively. The MWW-s with long fiber lengths have high water absorbing capacity, which in turn increases the environmental alkalinity and promotes the reaction with a low MWW-s substitution. While the limited heat release enhancement with increasing MWW-s replacement should be not only related to the relatively low reactivity of MWW-s but also the poor mixing mentioned above. In FM, the heat release is largely increased with the highest MWW-m content, meaning that MWW with finer particles has a higher reactivity and improved mixing homogeneity. Nevertheless, the trend is not consistent between 4 and 8 wt.% due to the small substitution intervals. Despite this, the obtained results still robustly demonstrate the contribution of MWW to the geopolymerization process.

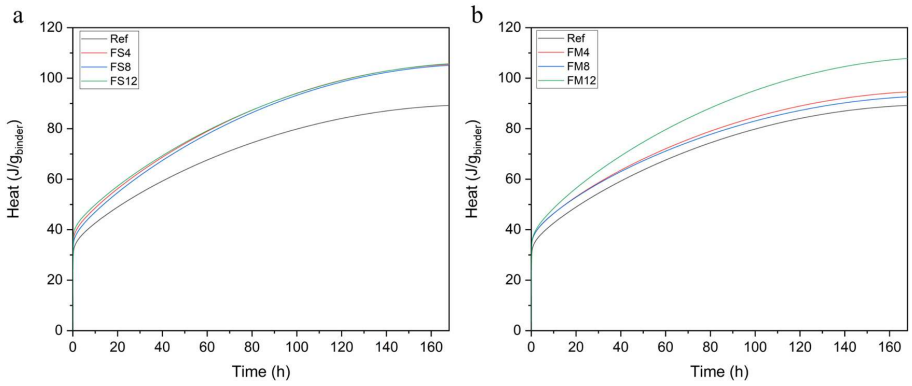

Fig. 5.10 The cumulative heat release during the sample hydration (a) the influence of MWW-s, (b) the influence of MWW-m.

5.3.3 Phase assemblage

To compare the mineralogy of the investigated samples, XRD results are presented in **Fig. 5.11**. Due to the insignificant difference among samples, the FS and FM with the highest MWW substitution (12 wt.%) are presented, and the XRD patterns of all samples are provided in **Appendix C** (**Fig. C1**). The crystalline phases in plain FA geopolymer are identical to raw FA, consisting of quartz, mullite, hematite, magnetite, and iron. With the incorporation of MWW, a noticeable trace of calcium silicate hydrate ($Ca_{1.5}SiO_{3.5}\cdot xH_2O$, PDF# 00-033-0306) is observed, particularly in FM12. Since in the structure of C-S-H, Al can take up a bridge position in the silica chain with abundant soluble Al, the detected C-S-H is more likely in the form of C-(A)-S-H. It further implies that MWW has an additional influence on the gel structure and composition of the hybrid geopolymer. Besides, an insignificant peak of rutile is identified as introduced by MWW. In comparison with NaOH-treated MWW, no hydrogarnet or hydrotalcite phase is observed in the resultant hybrid geopolymer. It should be due to the minor quantity and/or the low crystallinity of these phases.

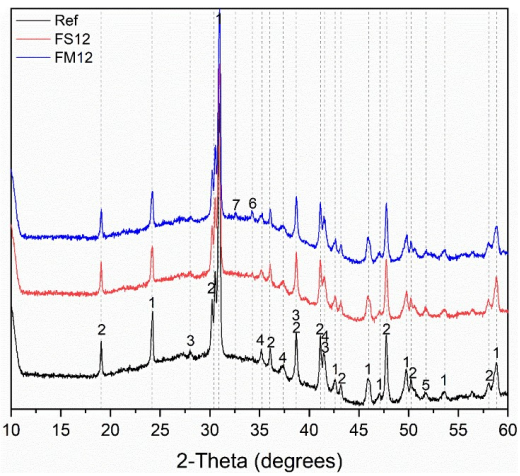

Fig. 5.11 XRD patterns of the investigated pastes at 28 days (1-Quartz, 2-Mullite, 3-Hematite, 4-Magnetite, 5-Iron, 6-C-S-H, 7-Rutile).

To learn the phase assemblage and gel composition, TG-DTG analysis is presented in **Fig. 5.12**. Here, the main mass loss peak from 100 to 300 °C is related to the release of bound water from the main reaction products, N-(C)-A-S-H gel, hydrogarnet and hydrotalcite [234]. A broad mass loss peak between 450 and 650 °C is associated with the presence of carbonates [186]. For both FS and FM samples, a clear trend is observed that a higher MWW addition leads to a widened and intensified main mass loss peak, accompanied by a shift towards higher temperatures. This phenomenon is more significant in FM samples. It

indicates the MWW incorporation either contributes to a higher gel content with more bonded water or leads to the formation of smaller gel pores [64]. Consistent with the reactivity test and reaction kinetics, MWW-m with a higher dissolution rate further promotes the hydration reaction with increased gel formation as compared to MWW-s. A more intensive carbonate-related mass loss is observed in the Ref sample, which explains the inconstant trend in the total mass loss up to 1000 °C. Nevertheless, a steady increase in total mass loss is observed with increasing MWW substitution from 4 to 12 wt.%.

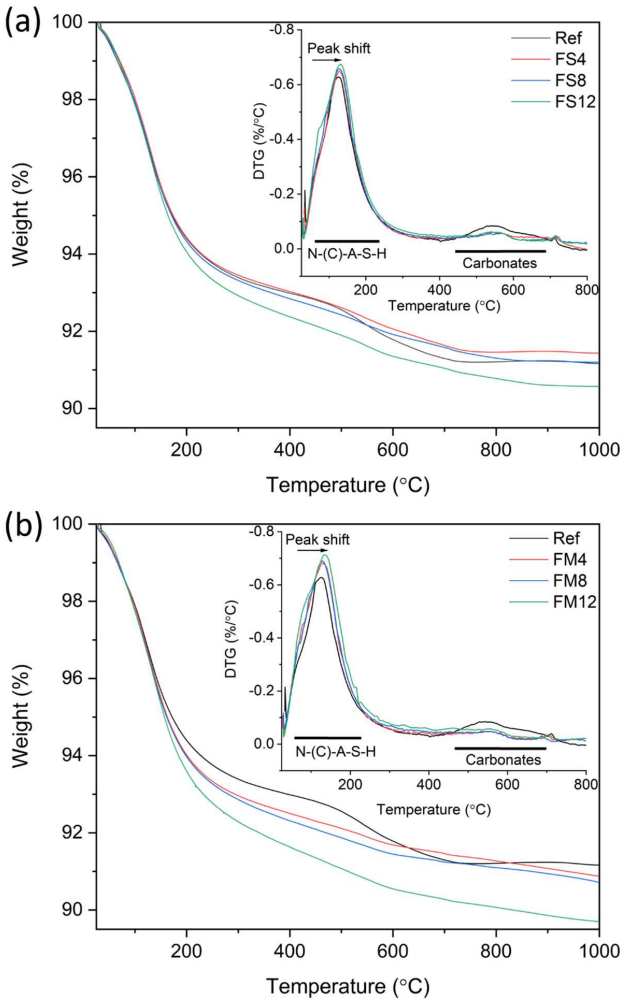

Fig. 5.12 TG-DTG results of the geopolymers with varied (a) MWW-s and (b) MWW-m substitutions.

The EDS analysis is applied to selectively characterize the binder composition. To representatively reflect the influence of MWW dissolution on gel composition, the hybrid

geopolymers with the highest MWW substitution (12 wt.%) are selected to compare with plain geopolymer paste. As shown in **Fig. 5.13a**, all mixtures consist of geopolymeric (N-A-S-H) gel characterized by low Ca, which can be introduced by either FA or MWW under an alkaline environment. Furthermore, there is a noticeable tendency that with the incorporation of MWW, the N-A-S-H gel clusters are shifted to a region with lower Si and higher Al while the Na proportion almost stays constant. More specifically, this trend is more significant in geopolymer with MWW-m than that with MWW-s.

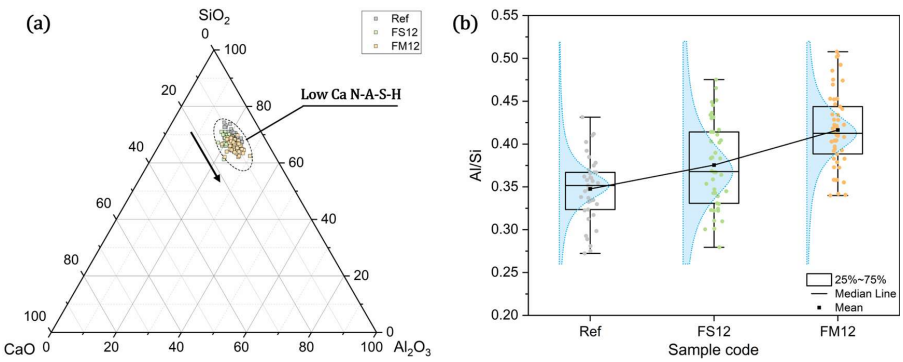

Fig. 5.13 EDS spot analysis (a) Ternary diagram of Na_2O-SiO_2-Al_2O_3 (as normalized to 100%) and (b) Box plot of Al/Si ratio of the binder gel for Ref, FS12, and FM12. Compositional regions of low Ca N-A-S-H gel are determined from [64,164].

To quantitatively clarify the Al and Si ion variation in the investigated samples, the Al/Si ratio is further calculated according to EDS analysis, and the obtained Al/Si ratio is fitted using the simple Gaussian curve in Origin Software. According to the histograms given in **Fig. 5.13b**, the data show a high variability of the Al/Si ratio. This is mainly due to the heterogeneous ion dissolution-diffusion process and/or the intermixing of different phases in reaction products [184]. In this case, it is reasonable to apply the mean value and median value to approximately reflect the gel composition. A clear trend is observed in the box plots that, as compared to Ref, the mean value of the Al/Si ratio is increased from 0.347 to 0.376 and 0.416 in FS12 and FM12 respectively. This trend partially contradicts the potential geopolymerization reactivity test. The dissolution test shows that Si and Al dissolve from MWW at a rate 2-3 times higher than from FA, with D_{Si} larger than D_{Al}. Consequently, substituting FA with MWW should yield a lower Al/Si ratio, but an opposite trend is observed. This phenomenon is likely due to that the activator provides abundant/excessive readily environmental Si, while the Al is only provided by precursors, in which the dissolved Al has a direct influence on the Al/Si ratio by taking up the bridge position in silica chains. It further explains the highest Al/Si ratio observed in FM12 due to the dissolution rate of MWW-m. In addition, it is noteworthy that the Al/Si ratio cluster in FS12 sample shows a

broader box plot of confidence interval from 25% to 75% as compared to FM12, indicating a more heterogeneous ion dissolution and diffusion in FS12. This should be related to the fibrous nature as well as the poor dissolution of MWW-s.

To verify the quantitative observation in EDS results, the infrared spectra of the investigated pastes with different MWW incorporation are compared in **Fig. 5.14**, and the assignments of absorption bands are summarized in **Table 5.4**. In general, the hybrid geopolymers have similar chemical bonds to plain geopolymers. The major band centered around 980 cm^{-1} is associated with asymmetric stretching of Si-O-T, where T represents Si or Al units. A typical band in the region 670-850 cm^{-1} is identified as the stretching vibrations of Si-O-Si of quartz from FA. The humps at 1400 cm^{-1} and 1463 cm^{-1} are related to the presence of different carbonates. Besides, the adsorption peaks at 1643 cm^{-1} and 3418 cm^{-1} are due to the stretching vibrations of O–H bonds and bending vibrations of physically and chemically bonded water respectively.

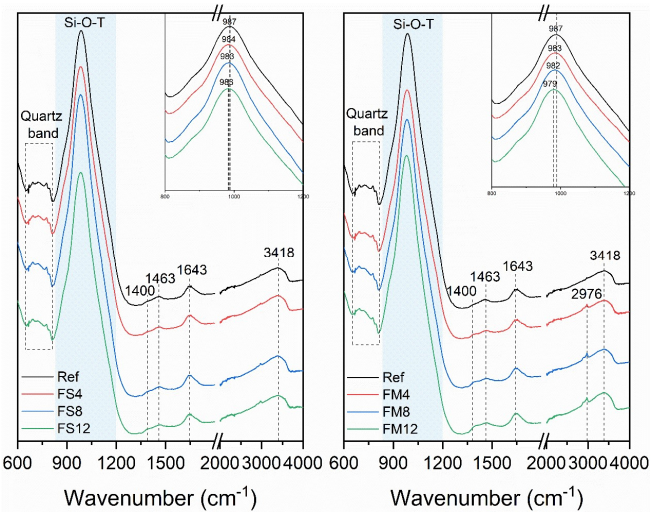

Fig. 5.14 FT-IR spectra of the 28 days paste samples.

Table 5.4 Assignment and interpretation of FTIR spectra.

Wavenumber (cm^{-1})	Assignment	Interpretation	Reference
670-850	Si–O–Si	Quartz	235
979-987	Si-O-T	N,C-A-S-H	236
1400, 1463	C-O	Sodium/calcium carbonates	189
1643, 3418	O-H	H_2O	237

Notably, with the increased MWW incorporation, the asymmetric stretching Si-O-T bond transfers to a lower wavenumber, especially for FM samples. Here, the decrease of Si-O-T

bond wavenumber is closely related to a promoted Al uptake in geopolymeric gel [133,238], which evidences the observed Al/Si ratio variation in EDS analysis. In addition, among FS and FM with the identical MWW substitution, a lower Si-O-T wavenumber is detected in FM samples. This observation correlates well with the EDS analysis, originating from the better dissolution of MWW-m, therefore providing more readily Al into silica gel.

At this stage of the research, a consistent trend is evidenced by connecting the above results, indicating the enhancement of geopolymerization reaction through MWW incorporation, particularly with MWW-m. The influence of MWW on the gel content and composition of hybrid geopolymers has been firmly established. However, further quantitative investigation into the gel structure is still needed.

5.3.4 Bulk properties and microstructure

As shown in **Fig. 5.15**, the introduction of MWW further decreases the bulk density of hybrid geopolymer, in which the MWW-m has a more significant effect. With the MWW incorporation increases from 0 to 12 wt.%, the bulk density of FS and FM decreases from 1.55 g/cm^3 to 1.46 g/cm^3 and 1.44 g/cm^3, respectively. Here, the reduction of bulk density can be attributed to two causes. i) owing to its fibrous morphology, the introduction of MWW could impact the binder rheology and bring air bubbles, defects, and ITZ between MWW and the binder which further decreases the bulk density. ii) according to Yliniemi et al. [216], the organic resin in MWW decomposes in contact with the alkaline solution and releases ammonia. It potentially increases the porosity of the binder, and this issue should be addressed regarding the reutilization of MWW in alkali-activated materials.

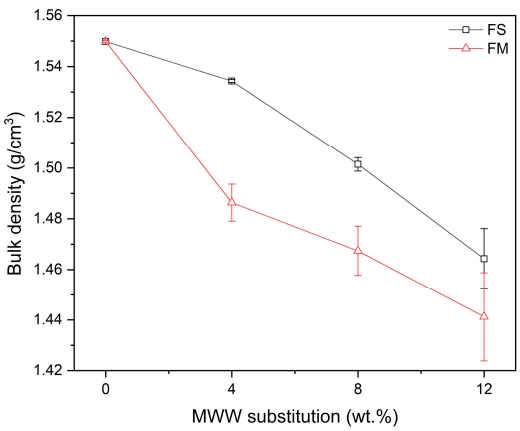

Fig. 5.15 The variation of bulk density with MWW substitution.

The microstructure of hybrid geopolymers with MWW substitution is compared with plain geopolymer in **Fig. 5.16**. The unreacted FA is distinguished by its spheric shape, the

cylindrical fibers in **Fig. 5.16b** and **c** indicate MWW, the gray region in between denotes binder gel, and the dark regions represent pores and voids. In FS12, MWW fiber with different lengths can be observed, and notably, the distribution of MWW in geopolymeric binder is anisotropic. In comparison, only short MWW particles are noticed in FM12, referring to a limited fibrous effect of MWW-m. In the enlarged image, a rough texture with surface precipitates is noticed on the surface of MWW, which is consistent with previous work [224]. It further implies the dissolution and reaction of MWW under the applied alkaline environment. Additionally, an obvious interfacial transition zone (ITZ) between MWW fiber and binder gel is observed in both FM and FS samples, which might be due to the autogenous shrinkage of the geopolymeric binder.

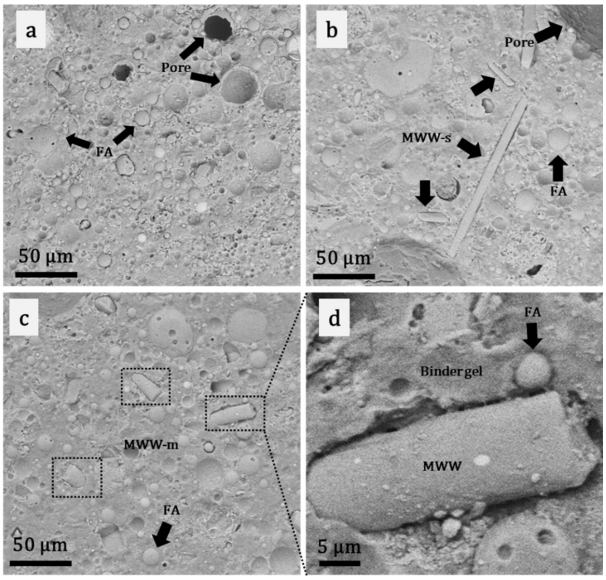

Fig. 5.16 SEM micrographs of (a) Ref, (b) FS12, (c) FM12, and (d) enlarged image of FM12.

To learn the pore structure development of the specimens, microtomography analysis is performed on the geopolymers with different MWW substitutions. By applying IPLFE v1.16 software (Scanco Medical AG, Switzerland), the pores are extracted and colored differently according to the pore diameter, and the 3D pore visualization is presented in **Fig. 5.17**. According to the 3D geopolymer rendering, the introduction of MWW not only increases the total pore volume but also enlarges the pore diameter when comparing with Ref sample. Furthermore, a higher MWW substitution further leads to a more compact pore distribution.

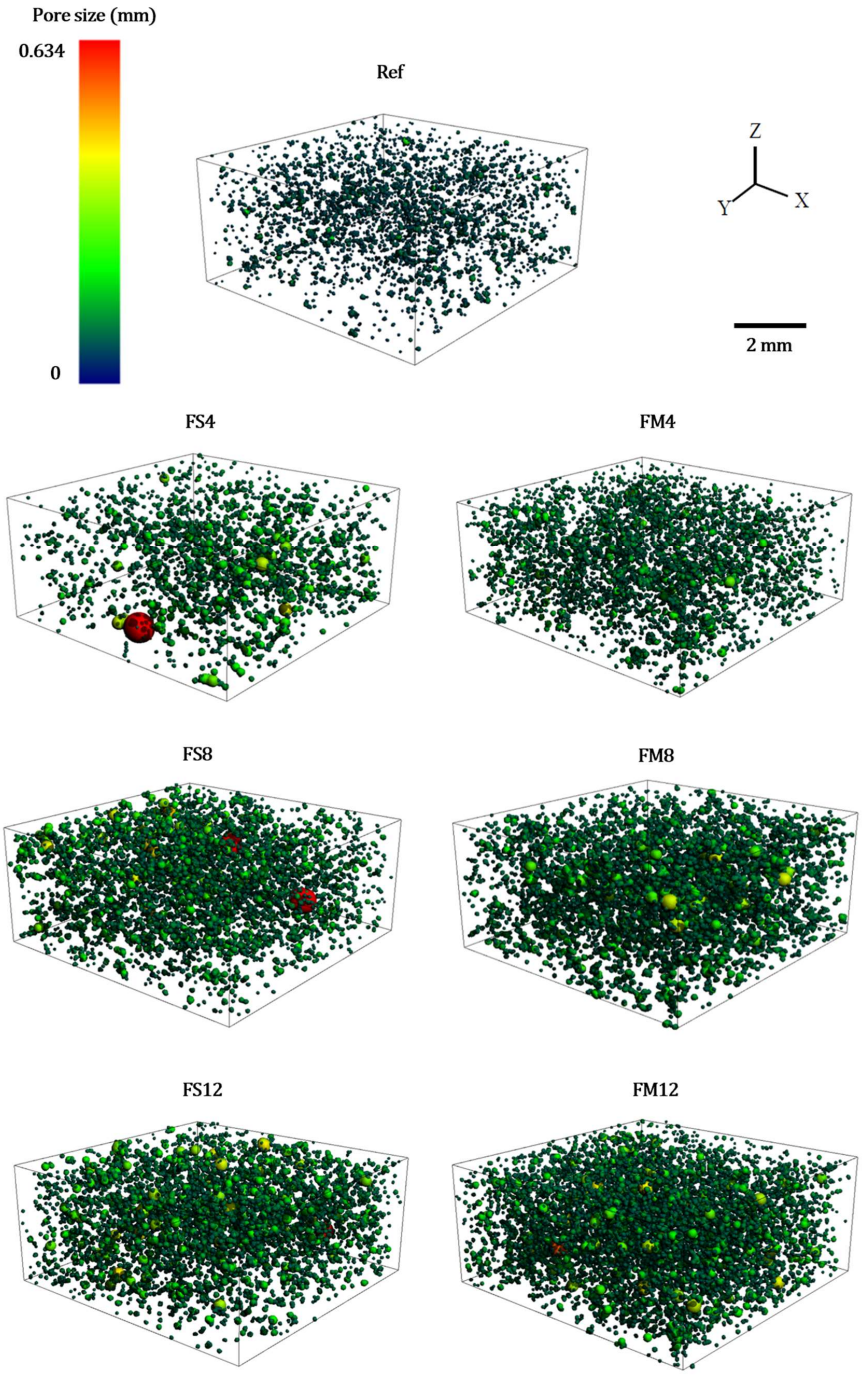

Fig. 5.17 The 3D rendering of pore distribution of the investigated specimens according to μ-CT.

The pore size distribution is further calculated based on the microtomography analysis. It should be noted that due to the measurement limitation, the μ-CT only covers a pore range above 6.6 μm. Thus, the pore size distribution of the investigated samples is further retrieved by comparing the calculated total porosity and porosity from μ-CT. As presented in **Table 5.5**, it is noticed that the majority of porosity in the investigated samples is below 10 μm. With a higher substitution of MWW, the fraction of pores below 10 μm is reduced, while the proportion of pores exceeding 10 μm has increased steadily, resulting in a coarser pore size distribution. Noteworthy, when comparing the hybrid geopolymers with the same substitution of MWW-s and MWW-m, there is a higher pore fraction in the range of 10 to 100 μm whereas a lower fraction above 100 μm in FM samples. As mentioned above, the increased pore proportion above 100 μm in the FS sample can be related to its fibrous effect, which impacts the binder homogeneity with the formation of air bubbles and macro defects. In comparison, the milled MWW is mainly composed of finer particles below 100 μm, which largely avoids the fibrous impact but increases the pores between 10-100 μm because of ITZ (See **Fig. 5.16**).

Table 5.5 Pore size distribution retrieved by μ-CT.

Sample code	Total porosity (%)	Pore volume in the range (μm)				
		<10	[10,50]	[50,100]	[100,500]	>500
Ref	34.19	25.82	7.70	0.51	0.15	-
FS4	34.79	23.88	8.83	0.95	1.00	0.13
FS8	37.01	21.84	10.95	1.78	2.24	0.20
FS12	38.10	21.27	12.15	1.95	2.69	0.05
FM4	36.66	22.98	11.02	1.69	0.97	-
FM8	37.82	16.96	15.68	2.77	2.42	-
FM12	38.66	17.44	15.54	2.98	2.67	0.03

The majority of pores in the samples are below 10 μm, and cannot be well detected by micro-CT. Thus, MIP analysis is further carried out as shown in **Fig. 5.18**. All samples show a pore size distribution below 1000 nm, with the main peak centered at around 15 nm. The FS samples have a very similar pore size distribution as Ref, especially the pores of 20-1000 nm. With the increasing MWW-s dosage, a discernible reduction in the primary peak fraction is observed, along with a growing minor hump within the 5 to 10 nm range. Notably, this pore fraction shifting is more significant in FM samples. The main peak is decreased constantly and shifted towards a smaller size approximately 10 nm with higher MWW-m content, and the emergence of a secondary peak becomes increasingly evident. Here, the pore size fraction serves as an indicator of the reaction degree, where a promoted sample shows a higher fraction of the denser gel [98]. It further proves the promoting effect of MWW on the geopolymerization reaction. And in line with the dissolution, reaction kinetics, and

phase assemblage results, MWW-m shows a greater contribution as compared to MWW-s.

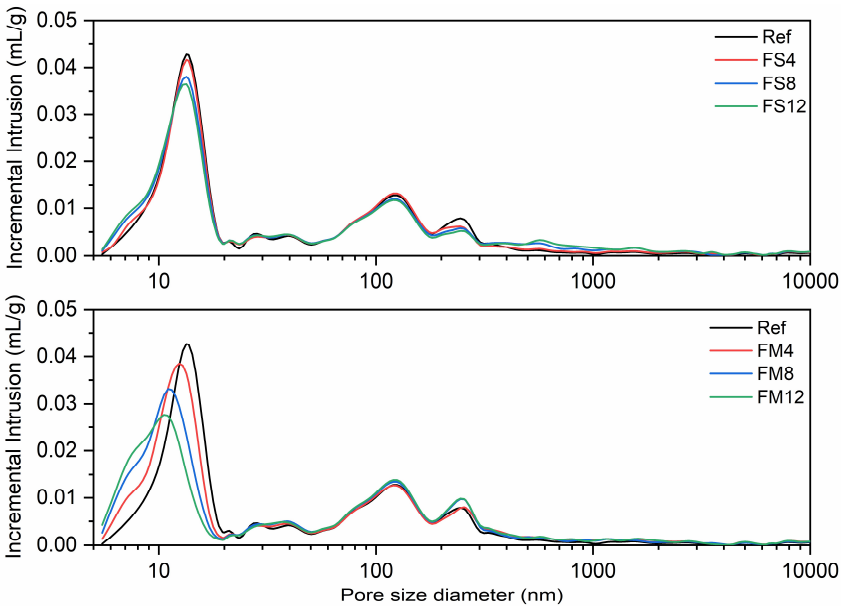

Fig. 5.18 The pore size distribution of specimens based on MIP.

5.3.5 Drying shrinkage

The mass loss of the investigated samples under free drying conditions is measured up to 63 days as shown in **Fig. 5.19a** and **b**. For both FM and FS, a higher MWW substitution leads to a lower mass loss as compared to the Ref sample. This should be attributed to the higher amount of MWW that facilitates reaction degree with more tightly bound water as evidenced by TGA, hence less water evaporation is observed. Accordingly, the lowest mass loss is observed in the MWW-m incorporated sample. It further proves that mass loss is closely related to the reaction degree. The shrinkage behavior of the hybrid geopolymers during the drying process is presented in **Fig. 5.19c** and **d**. The FM samples exhibit a clear reduction in drying shrinkage as compared to plain geopolymer, following the drying mass loss. The drying shrinkage is reduced with higher MWW-m content at an early age, and a similar linear shrinkage is noticed up to 63 days. It is widely accepted that the drying shrinkage process of alkaline activated materials is not only related to the quantity of water loss over time but also the characteristics of the binder material, reaction kinetics, and microstructure [228,239]. Firstly, in line with reaction kinetics, the promoted reaction with increasing MWW-m addition reduces the free water in FM samples, thus a lower internal relative humidity with reduced drying mass loss is expected, which directly eases the drying shrinkage. Moreover, as observed by MIP analysis, a higher MWW-m addition leads to the

formation of a denser gel structure below 10 nm. This pore refinement not only reduces the moisture loss rate but potentially delays the meniscus invasion to generate capillary pressure [240]. It explains the increased shrinkage at a late age in FM12. Moreover, according to pore size distribution results from MIP and Micro-CT, the incorporation of MWW-m further decreases capillary pores (10-50 nm) but introduces more macropores (>10 μm). According to the Young-Laplace equation:

$$P = \frac{2\gamma_{LV}\cos\theta}{r} \tag{5.4}$$

Where P_c is the capillary pressure, γ_{LV} is the surface tension of the pore fluid, θ is the equilibrium water contact angle, and r is the radius of the pore. The pores with a larger diameter generate a much lower capillary pressure than smaller pores. Above all, the FM sample would endure a lower shrinkage strain with increasing MWW-m substitution.

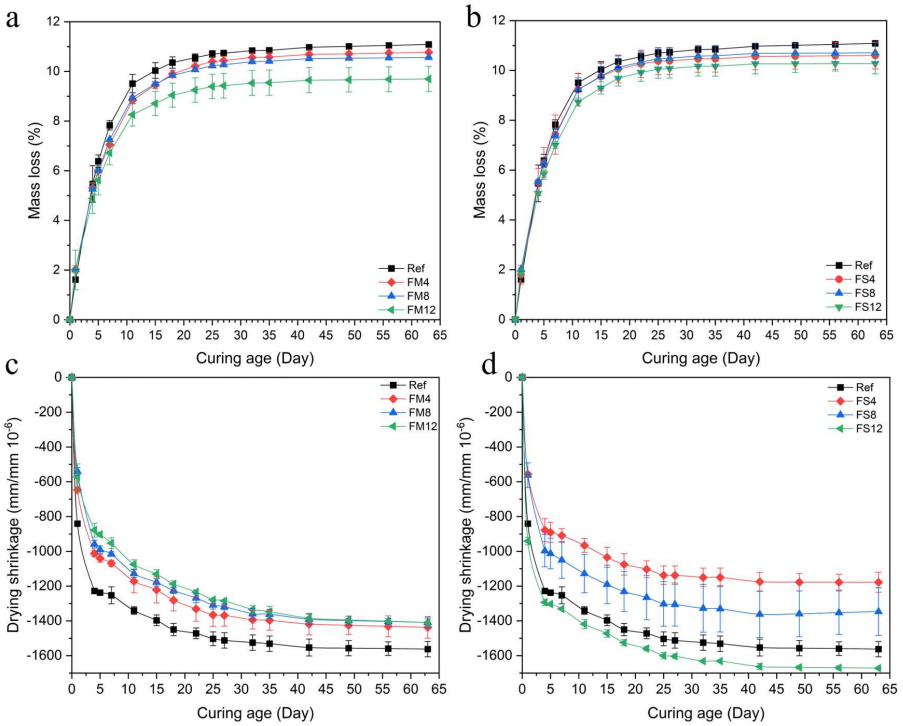

Fig. 5.19 The mass loss and drying shrinkage of samples during the drying process.

The inclusion of MWW-s with long fibers further complicates the shrinkage process. In particular, the lowest drying shrinkage is obtained with 4 wt.% of MWW-s, achieving a drying shrinkage of 1178.1 mm/mm 10^6, as compared to 1562.5 mm/mm 10^6 in the Ref

sample. Whilst the effectiveness of MWW-s on drying shrinkage is lessened with increasing MWW-s, the FS12 exhibits the largest drying shrinkage among all samples. In comparison with MWW-m, with a low MWW-s substitution, the well-distributed fibers serve as passive internal restraints to decrease the shrinkage strain and resist the free drying deformation, showing the optimum volumetric stability in FS4. Nevertheless, the increasing MWW-s substitution further introduces defects, which are likely to cause an uneven gradient of shrinkage stress and consequently give rise to severe shrinking during free drying [241]. In addition, as reported by Zhang et al. [242] and Si et al. [240], the inadequate packing of particles with large wetting surface area can generate high shrinkage strain in the matrix. Herein, the excessive MWW-s fibers will inevitably agglomerate, which can be another trigger for the observed phenomenon. To encapsulate, the lowest drying shrinkage of 1178.1 mm/mm 10^6 is achieved in hybrid geopolymer with 4 wt.% MWW-s, showing a 24.6% shrinkage reduction to plain geopolymer paste at the age of 63 days.

5.3.6 Mechanical strength

Compressive strength

The 28 days compressive strength of geopolymers with different MWW substitutions are plotted in **Fig. 5.20**. As compared to Ref (28.35 MPa), the compressive strength in overall ranges from 27.03 to 21.14 MPa, and 24.97 to 23.11 MPa for FS and FM respectively, along with higher MWW substitution. The strength variation of the hybrid geopolymers is in line with the observed porosity change, yielding a lower compressive strength with a higher porosity. It indicates the pore structure plays a dominant role in determining the compressive strength despite the promoted reaction degree by the MWW introduction. Interestingly, the FM samples have a higher porosity than FS samples at the same substitution amount, while a larger compressive strength is obtained in FM with MWW substitution from 8 to 12 wt.%. This might be due to the discrepancy in the hydration degree and pore size distribution between FS and FM specimens. According to micro-CT and MIP analyses, FM samples possess a high content of dense gel, which strengthens the structure. On the other hand, given the heterogeneity of fibers, increasing the MWW-s substitution introduces a higher volume fraction of defects/air bubbles larger than 100 μm, which is believed to pose a more destructive impact on compressive strength.

Flexural properties

To provide an insight into the fibrous effect of MWW, the flexural properties of the hybrid geopolymers are characterized via a three-point bending method. **In Fig. 5.21a**, all samples exhibit an increasing stage reaching the peak load, followed by an abrupt failure without strain softening process. It implies the post-peak load performance is not promoted by

MWW, which is due primarily to the limited fiber length of MWW. For FM specimens with MWW substitution from 0 to 12 wt.%, the slope of the load to displacement curve exhibits

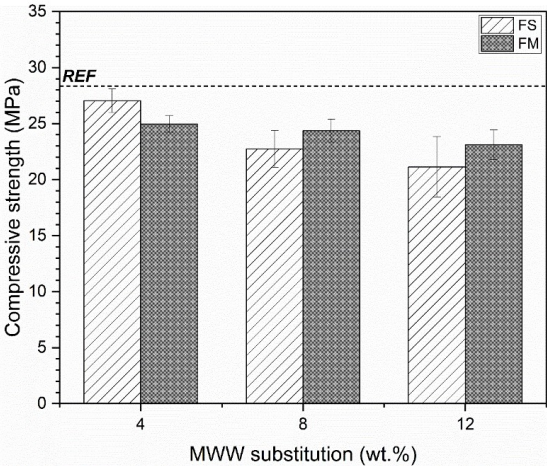

Fig. 5.20 The compressive strength of the specimens at 28 days.

a decreasing trend, indicating a reduced stiffness. Moreover, the displacement at fracture is significantly increased as compared to Ref, with a 90.8 % improvement in FM12, which refers to a promoted flexibility. In consequence, the flexural energy is enhanced with the increased MWW-m inclusion. A similar phenomenon is noticed in the FS samples, but the displacement at break is narrowed in a range between 0.36 and 0.41 mm with MWW-s from 4 to 12 wt.%, and the flexural energy exhibits a non-linear relationship with the substitution content.

By comparing the fracture surface shown in **Fig. 5.21 b-d**, the Ref sample exhibits a smooth fracture surface, indicating the brittleness of the geopolymer gel. In contrast, both FM and FS exhibit a relatively rough fracture surface, with discernible MWW particles of diverse dimensions. It indicates the promoted flexibility and flexural energy are highly related to the bonding effect of MWW filler/fibers on the matrix. Besides, the mechanical properties of geopolymers are strongly dependent on the gel formation. It is reported that the overall Young's modulus and stiffness are decreased along with the Si/Al ratio in the observed range [197,243], which is in line with the gel composition analysis in the present study. In comparison with FM, the flexural reinforcement of FS samples is more significant with a low substitution, while this effect is lessened with a higher MWW-s content. It infers that the efficiency of MWW-s on flexibility improvement is synergistically influenced by the fibrous effect and microstructure. As seen in **Fig. 5.21d**, fiber agglomeration is inevitable in FS samples due to the heterogeneity of the long fibers. Therefore, the excessive MWW-s

addition would negatively impact the flexural performance with a more pronounced impact observed in flexural strength development below.

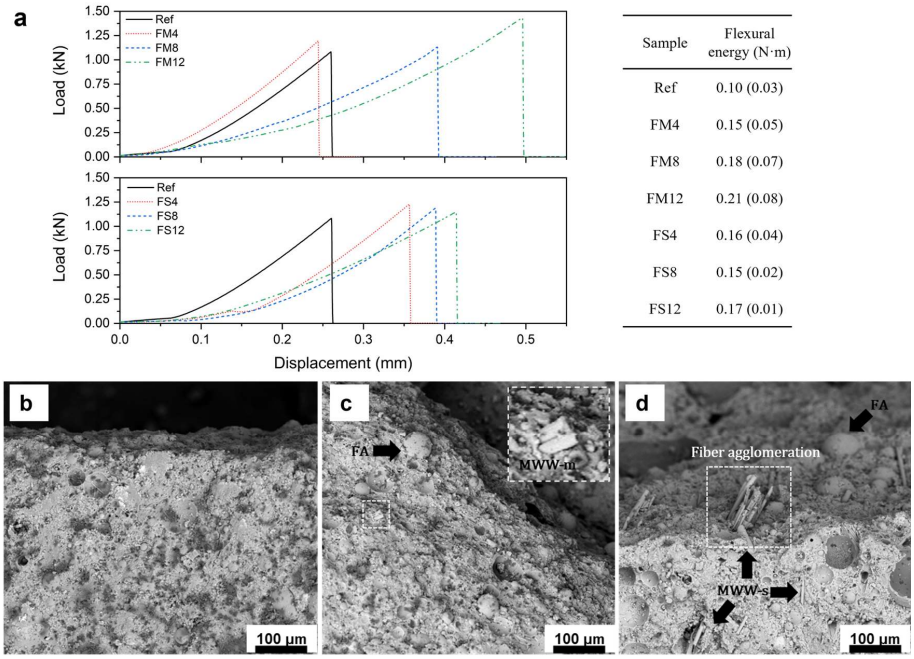

Sample	Flexural energy (N·m)
Ref	0.10 (0.03)
FM4	0.15 (0.05)
FM8	0.18 (0.07)
FM12	0.21 (0.08)
FS4	0.16 (0.04)
FS8	0.15 (0.02)
FS12	0.17 (0.01)

Fig. 5.21 The flexural properties of samples at the age of 28 days: (a)The load-displacement response, and the facture surface of (b) Ref, (c) FM, and (d) FS sample.

The flexural strength results are plotted in **Fig. 5.22**. Contrary to the deterioration in the compressive strength, all hybrid geopolymers achieve higher flexural strength than the Ref sample due to the fibrous reinforcement effect of MWW discussed above. The fracture behavior of the investigated samples is asymmetric with a discrete distribution of flexural strength; the average value variation is observed to exhibit a distinguishable trend. Among these, the flexural strength of FM is increased with a higher MWW-m substitution. In terms of FS samples, FS4 achieves the highest flexural strength, while a higher MWW-s substitution only poses a limited strength reinforcement. Given the fine particle size, the MWW-m addition efficiently promotes the bonding between particles, thus enabling better flexural strength. For FS samples, as discussed above, a low MWW-s addition shows a good bridging effect, enabling high flexural toughness and flexural strength. However, when there is an excess of MWW-s, the defects and voids arising from fiber agglomeration further restrict flexural development.

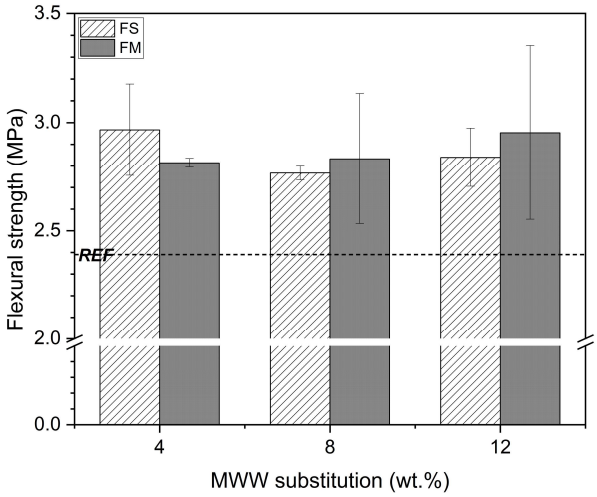

Fig. 5.22 The flexural strength of samples at the age of 28 days.

5.3.7. High-temperature behavior

Given the promising heat resistance performance of mineral wool up to 1000 °C, the possible improvement of MWW on hybrid geopolymers under elevated temperature is characterized via a high-temperature exposure test. The morphology of samples after exposure to 800 °C is presented in **Fig. 5.23**. As compared to the microstructure before heat treatment, a disordered matrix with widened voids and pores can be detected due to the thermal deterioration and viscous sintering of the binder gel. In **Fig. 5.23b** and **c**, it is observed that the MWW undergoes a partial melting, resulting in the loss of its fiber shape. Especially in FM, it is difficult to differentiate the MWW particles from the binder gel since the melt MWW further fills the pores/voids. The reason behind the partial melting of MWW at 800 °C is not entirely clear. It is possibly due to the chemical attack during alkali activation that degrades the thermal stability of MWW and reduces the melting point.

The crystalline patterns of the samples after thermal exposure are further compared in **Fig. 5.24**, in which FS12 and FM12 are selected as the representative samples, and other results are given in **Appendix C** (**Fig. C2**). When compared with initial XRD patterns (**Fig. 5.11**), new phases including nepheline ((Na, K)$AlSiO_4$, PDF# 01-085-1487) and diopside ($CaMgSi_2O_6$, PDF# 01-086-0932) are noticed in all samples. Among these, nepheline primarily arises from the partial decomposition and recrystallization of the geopolymeric gel, while the presence of diopside indicates the formation of a glass-ceramic phase [244]. Notably, the hybrid geopolymer with increasing MWW exhibits increased intensity of nepheline and diopside phases, especially for FM12, indicating that MWW incorporation further enhances the re-crystallization of geopolymers under high temperatures. This is

because, in geopolymers, the finer particle with higher specific surface area and energy implies low sintering temperature and high crystalline phase content [245].

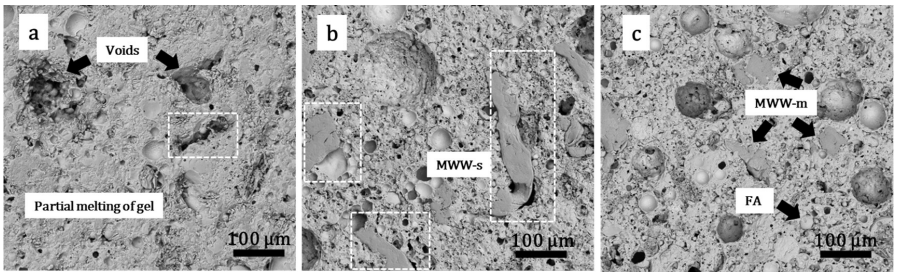

Fig. 5.23 The microstructural evolution of (a) Ref, (b) FS, and (c) FM samples after 800 ˚C.

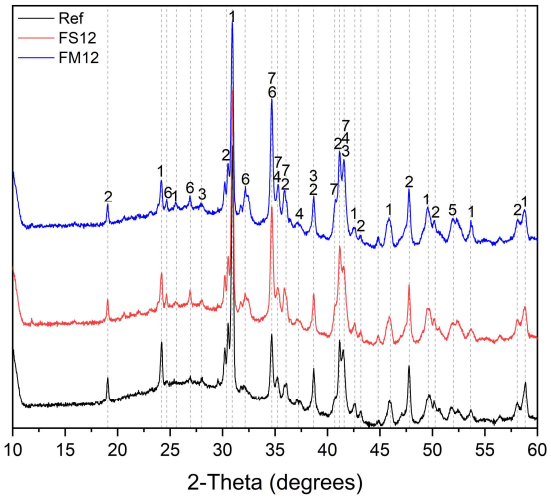

Fig. 5.24 XRD patterns of the investigated pastes after 800 ˚C exposure (1-Quartz, 2-Mullite, 3-Hematite, 4-Magnetite, 5-Iron, 6-Nepheline, 7-Diopside).

Table 5.6 The mass loss and thermal shrinkage of samples exposed to 800 ˚C.

Sample code	Mass loss (%)	Linear shrinkage (%)
Ref	7.79 (0.05)	4.78 (0.03)
FS4	7.93 (0.03)	5.46 (0.07)
FS8	8.09 (0.04)	5.39 (0.16)
FS12	8.24 (0.02)	5.35 (0.03)
FM4	8.34 (0.04)	5.42 (0.08)
FM8	8.82 (0.03)	5.89 (0.13)
FM12	9.03 (0.01)	6.20 (0.09)

The mass loss and thermal shrinkage of samples at 800 ˚C are shown in **Table 5.6**. With increasing MWW substitution, there is a notable rise in mass loss at 800 ˚C, which is attributed to the dehydration of the gel phases. Consistent with the TG and XRD analysis,

FM samples with higher gel phase proportion exhibit severe dehydration after thermal exposure, resulting in the highest mass loss among others. In terms of linear shrinkage, there is no positive effect observed with the incorporation of MWW. As generally acknowledged, the thermal shrinkage of geopolymer is synergistically influenced by capillary strain, gel dehydration, and viscous sintering [205,246]. In hybrid geopolymers incorporating MWW, the high mass loss aggravates the capillary strain during heating. Besides, the pronounced gel decomposition and recrystallization pose a negative impact on volumetric stability. Moreover, the observed partial melting of MWW also leads to thermal shrinkage. Consequently, hybrid geopolymers exhibit more pronounced thermal shrinkage compared to the reference, with the shrinkage further increasing with greater MWW-m substitution. Contrary to FM, the thermal shrinkage of FS samples is slightly reduced with higher MWW-s substitution. This phenomenon implies the limited resistance of MWW-s fiber to matrix deformation at elevated temperatures.

As for the residual mechanical performance, all samples exhibit a flexural strength reduction due to the thermally induced cracking in **Fig. 5.25a**. Notably, with increasing MWW substitution, higher flexural strength is retained for the hybrid geopolymers in **Fig. 5.25b**, which can be an indication of the promoted microstructural stability by introducing MWW. This phenomenon is mainly related to the pore structure and toughness/flexibility of the hybrid geopolymers. On the one hand, the high porosity with increasing MWW incorporation facilitates water removal and alleviates crack formation. On the other hand, as learned from the initial flexural properties, the increased MWW dosage enhances the toughness and flexibility of the hybrid matrix. It enables a superior ability to accommodate the inner thermal incompatibility and thus mitigates the thermally induced microstructural destruction [68]. As a result, larger flexural strength retention is achieved in the FM sample owing to its highly porous matrix with higher toughness.

The residual compression properties of samples are presented in **Fig. 5.25c** and **d**. After 800 °C exposure, FS samples obtain a similar residual compressive strength to Ref samples, while that of FM samples is significantly increased along with higher MWW-m substitution, achieving the highest residual strength of 45.88 MPa as compared to Ref of 29.16 MPa. As shown in **Fig. 5.25d**, for both FS and FM, the higher residual strength gain with increasing MWW substitution is proportionally related to the observed thermal shrinkage variation. Here, the matrix densification induced by thermal shrinkage favours the compressive strength gain upon heating [203]. Besides, according to the microstructure evolution, the MWW shows a healing effect on the matrix due to the partial melting. It further explains the different strength gain rates in FM and FS samples. The MWW-m with a larger specific surface area potentially enhances the healing effect and induces a robust bonding with binder gel during viscus sintering and partial melting, resulting in a remarkable strength gain as

compared to the FS sample.

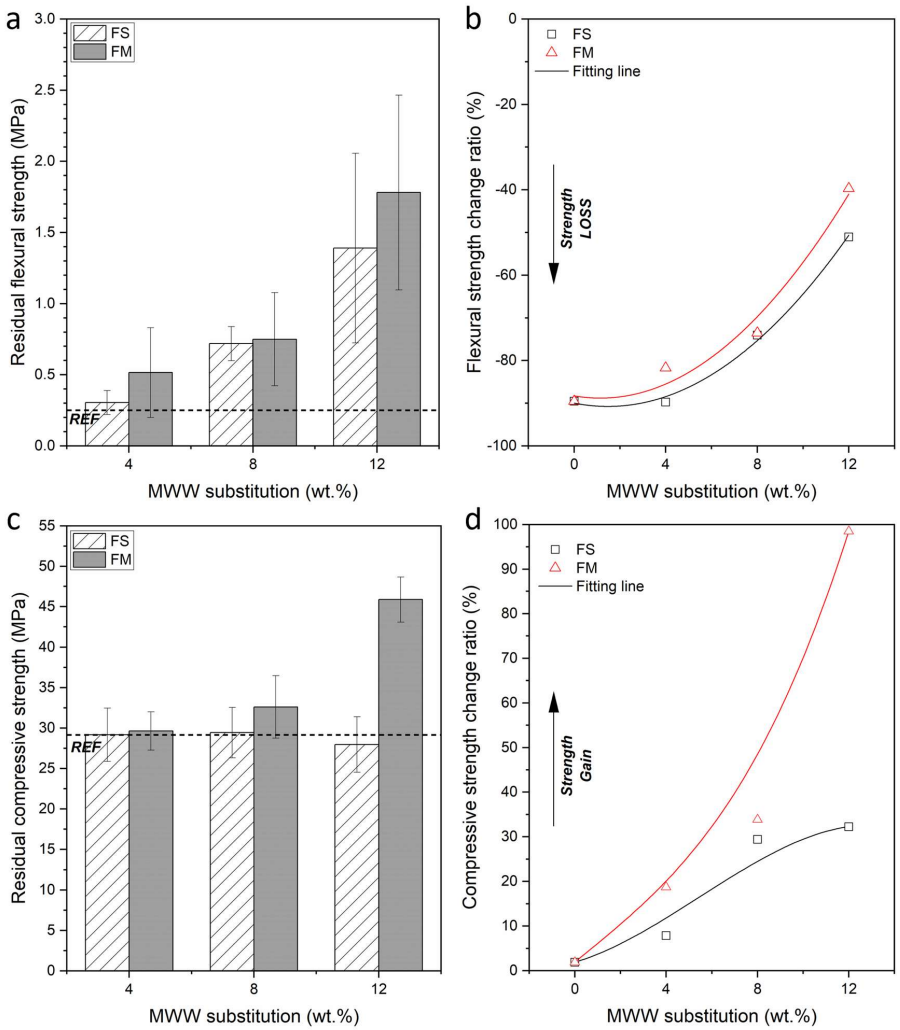

Fig. 5.25 Residual mechanical properties of samples, (a) Residual flexural strength, (b) Flexural strength change ratio, (c) Residual compressive strength, and (d) Compressive strength change ratio.

However, it should be noted that this chapter provides a preliminary insight into the potential use of MWW as filler/fiber in hybrid geopolymers for high-temperature applications. Further investigation is required to understand the progressive development of the designed geopolymer at various temperatures.

5.4 Conclusions

This chapter investigates the potential of reutilizing mineral wool waste (MWW) as both co-precursor and fiber reinforcement in the production of class F fly ash (FA) based hybrid geopolymers. Two different pre-treatments, namely sieving and milling, are applied to recycle MWW, and the potential geopolymerization reactivity of the treated MWW is determined. The roles of reactivity and dimension of MWW on the hybrid geopolymers are systematically revealed by reaction kinetics and products, microstructure, drying shrinkage, mechanical strength, and thermal behavior study. The results lead to the following conclusions:

(1) MWW shows specific geopolymerization reactivity under the alkaline environment. In comparison to FA, MWW exhibits 2-3 times higher levels of Si and Al dissolution, with the formation of new hydrates such as hydrogarnet and hydrotalcite. Among these, the milled MWW with a larger surface area exhibits the highest reactivity with higher reactive content dissolution and reaction products.

(2) The substitution of FA by MWW largely enhances the geopolymerization process with an improved reaction degree, as evidenced by a higher cumulative heat release. Moreover, the MWW incorporation not only promotes the gel formation but alters the gel composition, especially for MWW-m. The hybrid geopolymer remains a N-A-S-H dominated binder, whereas the Al uptake by N-A-S-H is stimulated by MWW, showing a higher Al/Si ratio with the increased MWW replacement.

(3) The alkali reaction of MWW as well as its fiber dimension has a synergetic effect on the microstructure and drying shrinkage behavior of the hybrid geopolymer. With increased MWW substitution, a denser gel is formed, while a higher porosity is observed due to the formation of more macropores. The obtained matrix with optimum MWW fibers largely mitigates the shrinkage strain, enabling a drying shrinkage as low as 1178.1 mm/mm 10^6 up to 63 days (with 4 wt.% MWW-s), in comparison to 1562.5 mm/mm 10^6 in the plain FA geopolymer.

(4) The effects of MWW incorporation on flexural strength are inversely proportional to the compressive strength. The MWW substitution in geopolymers results in a reduced compressive strength since the pore structure plays a major role in determining the compressive strength. However, the incorporation of MWW improves the flexural performance with the highest flexural strength of 2.97 MPa achieved in hybrid geopolymer with 4 wt.% MWW-s. This is not only attributed to the bridging effect of MWW but also to the modified gel composition. Nevertheless, the excessive MWW-s inclusion further limits

the flexural improvement due to fiber agglomeration and matrix defection.

(5) At elevated temperatures, on the one hand, the severe mass loss and re-crystallization with higher MWW substitution further aggravate thermal shrinkage. On the other hand, the highly porous matrix with enhanced flexibility mitigates the thermally induced structural destruction, which retains the flexural strength to a certain extent. Meanwhile, the partial melting of MWW poses a healing effect on the matrix. More specifically, the finer MWW-m with a larger specific surface area potentially induces a robust bonding with binder gel during viscus sintering and partial melting, enabling a 98.5% compressive strength gain after 800 °C.

In this chapter, the MWW incorporation demonstrates notable contributions to the geopolymer system, particularly for the key ion dissolution, reaction degree, mitigating drying shrinkage, and enhancing flexural strength development. However, with a limited addition, the advantageous impact of MWW as a co-precursor may be compromised by its fibrous characteristics, resulting in matrix defects and compressive strength deterioration. In general, the results presented herein pave the way for incorporating MWW into geopolymer-based materials at elevated dosages. Forthcoming research should explore the utilization of MWW at increased dosages while ensuring matrix homogeneity.

CHAPTER 6

Understanding the thermal behavior of geopolymeric composites designed by packing model

The interaction between geopolymer binder and aggregates has a significant impact on thermal performance, which however still lacks sufficient understanding. In this chapter, a novel approach for designing high temperature resistant geopolymer composites is introduced. The microstructural-thermophysical properties and heat transfer pattern of the developed geopolymer composites are investigated and further linked to the progressive evolution up to 800 °C. Results reveal that the optimized packing contributes to a significantly high porosity from 48.6% to 52.8% and large moisture permeability in lightweight aggregate incorporated geopolymer (LWAG). A much lower thermal conductivity but comparable mechanical strength is achieved in LWAG as compared to sand aggregate incorporated geopolymer (SAG). At elevated temperatures, sand incorporation results in a fast heat transfer, and lightweight aggregates lead to a large temperature gradient within geopolymer composites. Compared to SAG, LWAGs show a lessened microstructural degradation with noticeable strength gain at 800 °C. Increasing the distribution modulus from 0.2 to 0.3 eases the thermal deterioration thanks to the decreased temperature gain rate and thermal diffusivity, resulting in low thermal shrinkage and high residual strength.

This chapter has been published in the following article:

Y. Luo, C.H. Koh, S.H. Li, H.J.H. Brouwers, Q.L. Yu, Understanding the thermal behavior of geopolymeric composites designed by packing model, Cement and Concrete Composites 143 (2023), 105265

6.1 Introduction

Geopolymer has emerged as an environmentally sustainable binder material in the last few years, which is recognized as a promising alternative to ordinary Portland cement (OPC), especially for applications requiring thermal stability [10,17]. Generally, geopolymer is mainly derived from pozzolanic or aluminosilicate sources, which involve in the alkali activation or acidic activation process [10,160,247,248]. Among these, the common geopolymer is produced by alkaline activating Class F fly ash (FA), resulting in a three-dimensional aluminosilicate structure. It enables a superior level of mechanical property and structural integrity after exposure to high temperatures, as compared to OPC concrete [54,52]. Since the excellent thermal behavior of geopolymer binders has been extensively verified, there is a growing research interest in designing high temperature resistant geopolymeric composites for large-scale applications.

Zhang et al. [249] compared geopolymer and OPC-based mortar/concrete with sand aggregates and reduced thermal degradation of compressive strength is observed in geopolymer composites due to the superior thermal stability of geopolymeric gel. Çelikten et al. [67] studied the microstructural properties of geopolymer mortar exposed to high temperatures and found that the interfacial transition zone between the geopolymeric binder and sand is weakened with temperature increase. Kong et al. [49,80] and Rickard et al. [50] investigated geopolymer composites with sand, basalt, slag, and lightweight aggregates (LWA), and concluded that the thermal expansion incompatibility between binder and aggregates significantly impacts the structural and strength deterioration of geopolymer composites at elevated temperatures. According to previous works, the interaction between geopolymer binder and aggregates plays an important role in determining the thermal performance of geopolymer composites. The incorporation of aggregates with different characteristics, such as inert property, density, and particle size, varies the pore structure as well as the total porosity of composites. Besides, it not only alters the thermophysical properties such as thermal conductivity and thermal diffusivity but also affects the thermal stress and bonding mechanism within geopolymer composites on exposure to elevated temperatures [51,250,251]. Ultimately, it both influences and potentially complicates the thermal behavior of the resultant geopolymer composites. However, limited attention has been devoted to exploring the correlation between geopolymeric binder-aggregate interaction and initial properties, including microstructure and thermophysical characteristics. Consequently, the subsequent impact of these factors on the thermal behavior of geopolymer composites remains unexplored.

On the other hand, it is widely accepted that the durability of cementitious composites is strongly linked to the packing of granular ingredients. Brouwers and Radix [252] first applied a modified Andreasen and Andersen (A&A) particle packing model to design concrete mixture ingredients, including powders, fine aggregate, and coarse aggregate. The rheology and mechanical properties of the concrete mixture were optimized by achieving a high packing density and homogeneity. Based on that, self-compacting concrete (SCC) [252,253], ultra-high-performance concrete (UHPC) [254,255], earth-moist concrete [256,257], and ultra-

lightweight concrete (ULWC) [258–260] were developed. Nevertheless, limited attention has been given to applying the packing model to design composites for thermal application. Yu et al. [261] applied the modified A&A model to optimize the packing of LWA in gypsum-based composite and obtained a good balance between thermal conductivity and mechanical properties. Superior thermal stability was testified as compared to traditional gypsum board. It refers that the packing of ingredients alters the thermophysical properties and further influences the thermal behavior of the resultant composites. In particular, when applying LWA with high inert porosity, the modified A&A model can be used to design the porosity and pore size distribution of the component, hence tailoring the thermophysical properties. It is possible that, by optimizing the particle packing of geopolymer-based composite, better thermal performance can be achieved. However, in the realm of designing geopolymer-based materials for thermal applications, existing studies have predominantly focused on raw materials, alkali activators, and the selection of fibers or aggregates. To the best knowledge of the authors, no studies have been reported concerning the role of aggregate packing in determining the thermal performance of geopolymers.

In light of the above research gaps, a packing theory is introduced to develop geopolymer composites with normal quartz sand and LWA. The effect of geopolymeric binder-aggregate interaction on the initial properties, such as microstructural formation, thermophysical properties, and mechanical strength, are systematically characterized. Based on the acquired properties, a simulation study is carried out to numerically explore the heat transfer pattern within geopolymer composites. Ultimately, the initial properties and heat transfer patterns of geopolymer composites are further linked to the high temperature behavior, including post-heating thermal conductivity, microstructure/volumetric stability, and residual strength. The novelty of this chapter lies in clarifying the interrelationships among microstructural-thermophysical properties, heat transfer patterns, and the high temperature behavior of geopolymer composites. Additionally, it provides a comprehensive understanding of the progressive evolution of geopolymer composites under high temperatures, which is essential for revealing the thermal degradation mechanism of geopolymer-based mortar and concrete.

6.2 Experimental program

6.2.1 Materials

In this study, low calcium (class F) fly ash (FA) and ladle slag (LS) were applied as binder materials. The same FA and LS were utilized as mentioned in Chapters 3 and 4. Before using, LS was ground using a disk mill to obtain a suitable particle size distribution. The average particle size (d_{50}) of FA and LS are around 16.00 μm and 13.99 μm respectively as determined by a laser particle size analyzer (Mastersizer 2000, Malvern Instruments, UK). The detailed particle size distributions (PSD) of all applied solid materials are shown in **Fig. 6.1**. The chemical composition of FA and LS are given in **Table 6.1**, as determined by X-ray fluorescence spectrometry (XRF) (PANalytical Epsilon 3). The loss on ignition has been measured from 105 °C to 1000 °C. Commercially available sodium hydroxide

(NaOH) pellets (analytical level) and sodium silicate (Na_2SiO_3) solution (27.69 wt.% SiO_2, 8.39 wt.% Na_2O, and 63.9 wt.% H_2O) were used.

Table 6.1 Chemical composition and loss on ignition.

Oxide (wt.%)	SiO_2	Al_2O_3	CaO	Fe_2O_3	MgO	SO_3	K_2O	Others	LOI (1000 °)
Fly ash	54.57	21.60	6.12	9.04	1.17	0.41	2.85	2.13	2.11
Ladle slag	2.1	24.6	56.75	3.12	2.24	0.61	-	1.16	9.42

Commercially available mineral granulates, ROTOCELL PLUS® is applied in this work as lightweight aggregate (LWA) with five different size fractions of 0.1-0.3 mm, 0.25-0.5 mm, 0.5-1 mm, 1-2 mm, and 2-4 mm. The PSDs of LWA in different size fractions are presented in **Fig. 6.1**. The physical and chemical properties given by the producer are listed in **Table 6.2**. The applied LWA is produced from highly porous expanded silicate as shown in **Fig. 6.2**, exhibiting ultra-low bulk density and good thermal stability up to 1000 °C. In addition, normal sand with different size fractions of 0.1-0.3 mm, 0.3-0.5 mm, 0.5-1 mm, 1-2 mm, and 2-4 mm was used as normal weight aggregate compared to LWA. The specific density of normal sand is around 2575 kg/m^3.

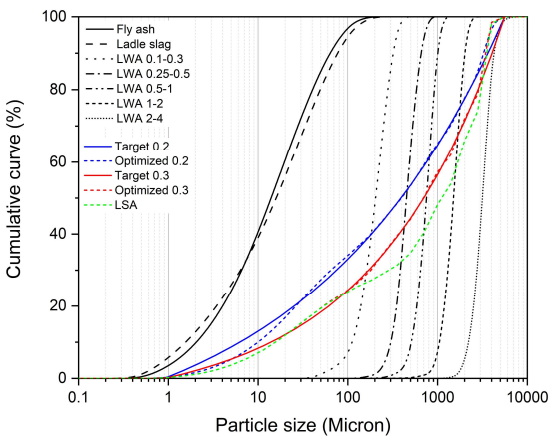

Fig. 6.1 PSDs of the solid materials, the target lines, and the resulting integral grading lines of mixtures with different distribution modulus.

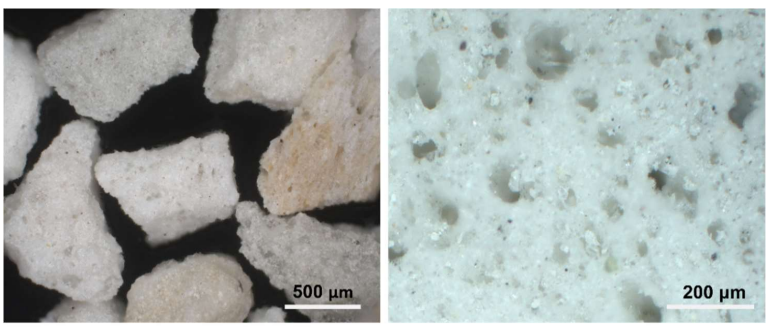

Fig. 6.2 Structure of LWA: (a) surface and (b) pore structure.

Table 6.2 The physical-chemical properties of applied lightweight aggregates.

Type	0.1-0.3 mm	0.25-0.5 mm	0.5-1 mm	1-2 mm	2-4 mm
Physical properties					
Bulk density (kg/m^3)	400±15%	365±15%	330±15%	310±15%	300±15%
Particle density (kg/m^3)	700	700	600	550	500
Average grain strength (N/mm^2)	22	18	18	18	12
Melting point in °C	1000				
Chemical composition					
SiO_2	55.0%				
Al_2O_3	22.0%				
K_2O+Na_2O	12.0%				
Fe_2O_3	3.0%				
CaO	2.0%				
MgO	1.0%				
TiO_2	0.5%				
LOI (1000 °C)	4.0%				

6.2.2 Mix design methodology

For room temperature applications, for instance, a high mechanical strength matrix always requires a dense structure with low porosity. Nevertheless, under high temperatures, the dense structure with low permeability impedes thermally induced water evaporation, resulting in high thermal stress and severe structural deterioration [205]. Herein, the design target is to develop a geopolymer composite with a good balance between room temperature properties and elevated temperature performance. A packing design is proposed to optimize the accumulation of solid particles including solid precursors and aggregates, and hence obtain a dense matrix with good packing of particles. By applying a highly porous LWA into the packing model, a porous matrix with high permeability but less flaw or closed pores can be designed.

In the present study, the target integral grading curve was determined following the modified Andreasen and Andersen (A&A) model [262], reading:

$$P(D) = \frac{D^q - D_{min}^q}{D_{max}^q - D_{min}^q} \tag{6.1}$$

Where *P(D)* is referred to the cumulative fraction of total particles being smaller than size *D*, *D* is the particle size (μm), D_{min} and D_{max} are the minimum and maximum particle size (μm) respectively, and q represents the distribution modulus. Based on that, the mix proportion was calculated following:

$$RSS = \sum_{i=1}^{n} \left[P_{mix}\left(D_i^{i+1}\right) - P_{tar}\left(D_i^{i+1}\right) \right]^2 \rightarrow min \tag{6.2}$$

The RSS represents the sum of the squares of the residuals, P_{mix} is the composed mix, P_{tar} is the target grading curve obtained from Eq. (6.1). To optimally approach the target

particle grading curve, an optimization algorithm namely, the Least Squares Method (LSM) was applied to adjust the proportion of each solid material until the RSS is minimal. The optimization algorithm was fulfilled by applying the solver tool in Microsoft Excel@. In the applied packing model, the distribution modulus determines the relative proportion of fine particles and coarse particles. According to Hüsken and Brouwers [256], a coarser mixture can be obtained with a higher distribution modulus and vice versa. For the geopolymeric system, Borges et al. [263] and Gao et al. [264] proposed an optimum q value of around 0.23, accounting for factors such as packing density and mechanical strength. In the present study, to investigate the effect of packing patterns on the high temperature behavior of geopolymer-based concrete, two distribution moduli (0.2 and 0.3) were adopted. The target particle grading curve and optimized grading curve with two distribution moduli were calculated respectively as depicted in **Fig. 6.1**, and the accordant solid materials proportion of the mixtures (named L-2 and L-3) is shown in **Table 6.3**. Moreover, to study the effect of the packing principle as well as aggregate size distribution, a mixture with un-optimized packing (denoted as L-L) was designed based on L-3 by manually adjusting the aggregate size distribution towards a higher fraction of big aggregates while keeping aggregate vol.% as constant, as also presented in **Fig. 6.1**. An optimized mixture (denoted as S-3) with normal sand as aggregate was prepared to compare with L-3.

Table 6.3 The proportion of mix designed applying packing model (per m^3).

Material		L-2	L-3	L-L	S-3
Binder	Total	605.3	462.5	462.7	462.5
	FA (85 wt.%)	514.5	393.1	393.3	393.1
	LS (15 wt.%)	90.8	69.4	69.4	69.4
Aggregate	0.1-0.3	28.4	36.6	13.0	244.3
	0.25-0.5	22.8	22.9	16.9	166.6
	0.5-1	22.1	27.1	29.9	211.4
	1-2	28.8	35.7	43.0	298.6
	2-4	46.7	64.6	81.3	569.9
Activator		337.2	257.6	257.7	257.6
Si modulus		1.5	1.5	1.5	1.5
Na_2O%		6.0	6.0	6.0	6.0
w/c		0.4	0.4	0.4	0.4
Distribution modulus		0.2	0.3	-	0.3
Aggregate vol.%		45.9	57.9	57.9	57.9

In terms of the geopolymeric binder design, a by-product of steel manufacturing, ladle slag (LS), is incorporated to regulate the workability in avoiding the sedimentation/floatation of aggregates. Besides, the incorporation of LS is clarified to promote the thermal performance of geopolymer binders according to Chapter 3 and 4. In all mixtures, the binder was blended by FA and LS at a mass ratio of 85 to 15, and the silicate modulus (SiO_2/Na_2O mol. ratio), as well as equivalent Na_2O wt.%, were set as 1.5 and 6 wt.% respectively according to Ref. [174]. To ensure acceptable workability without the addition of superplasticizer, a fixed w/c ratio of 0.4 was adopted. The water content included the water in sodium silicate solution and extra distilled water.

6.2.3 Sample preparation

The activator was prepared by mixing sodium hydroxide pellets, sodium silicate solution, and distilled water. The mass ratio of 0.14 between NaOH pellets and sodium silicate solution was used to achieve the desired silicate modulus, equivalent Na_2O wt.%. Distilled water was applied to tailor the water/binder ratio. The activator was cooled at ambient temperature for 24 h before use.

A 5L Hobart mixer was applied to prepare geopolymer composites. Firstly, the solid precursors and aggregates smaller than 2 mm were added in a mixer and mixed for 1 min until a homogeneous state has been reached. Then, the activator was slowly added while stirring at a low speed for 30 s. Afterward, the aggregate fraction between 2-4 mm was added slowly, following another 60 s at a high-speed stirring. After mixing, the fresh mixtures were immediately poured into 40×40×160 mm^3 molds and slightly vibrated for 30 s. The samples were sealed with plastic foil and stored at room temperature (20 ± 2 ˚C) for 24 h before another 24 h of 60 ˚C curing. Subsequently, the samples were demoulded and cured at room temperature under sealed conditions for 26 days until characterization.

6.2.4 Test methods

For the measurement of density, porosity, Micro-computed tomography (Micro-CT), scanning electron microscopy (SEM), thermal transport properties, and water vapor properties, the tested samples were cut from the core part of specimens at 28 days of curing and immersed in isopropanol for 72 h to cease the hydration, following a 24 h 40 ˚C drying.

Basic properties

The microstructure was observed by applying Phenom Pro (The Netherlands). The tested samples were cut from the center of prisms and impregnated with epoxy resin. Subsequently, the samples were polished and coated with Au by using a Quorum 150TS plus sputter coater. The observation was performed in a Backscattered electron (BSE) mode with an accelerating voltage of 15 kV. The bulk density, skeleton density, and porosity, φ were determined as per **Section 2.2.3**. Micro-CT was performed following the description in **Section 4.2.3**. The data were combined and visualized as shown in **Fig. 6.3**, and then the pores were extracted to calculate the pore size distribution. The volume of 140 mm^3 was tested for different samples, and the pore size between 6.6 to 660 μm was detected.

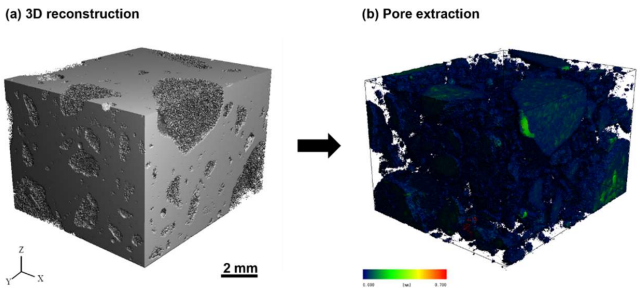

Fig. 6.3 The reconstruction and visualization of the 3D structure by Micro-CT.

The thermal transport parameters including thermal conductivity λ, thermal diffusion α, and volumetric heat capacity $C_{p,v}$ were measured by a Hot Disk thermal constants analyzer (TPS 2500 S, Sweden) at room temperature (20 ± 2 °C), following ISO 22007-2 [265]. Before measurement, the samples (40×40×20 mm^3) are dried at 40 °C until a constant weight is reached. A transiently heated plane sensor (Hot Disk 8563 F2 Kapton sensor, capable of operating up to 300 °C) was placed in between two slices of the identical sample with a smooth surface or directly inserted into aggregates, acting as the heat source and dynamic temperature sensor. The measurement time was set as 80 s and the heating power was 70 mW. Three measurements were carried out on each sample and the average data was recorded. The apparatus accuracy is ±2% for thermal conductivity measurement and ±7% for specific heat measurement.

To determine the water vapor transmission within specimens, the dry cup method was performed according to standard ASTM E96 [266]. The specimens in size of 40×40×40 mm^3 were applied. Before the measurement, the edges of specimens were thoroughly sealed with plastic film and wax to prevent vapor through the edges. The sealed samples were attached to the cups filled with anhydrous calcium chloride and then placed in a humidity chamber at 20 °C, 50% RH. The change of weight (Δm) at a successive time (Δt) is collected by weighing the cups over a specific period. Six consecutive weighings were recorded when the weight change rate of specimens reached a steady state. The water vapor transmission rate (WVTR) was calculated according to:

$$WVTR = \frac{\Delta m}{A \cdot \Delta t} \tag{6.3}$$

where A is the test area, used as 0.0016 m^2. The permeability, δ was calculated following:

$$\delta = \frac{WVTR}{\Delta p} \cdot Th \tag{6.4}$$

where Δp represents the vapor pressure difference, used as 8.77 mm Hg at 20 °C, 50% RH, and thickness, Th is 0.04 m.

The compressive strength test was carried out on 7 and 28 days cured samples, following EN 196-1 [86], and the detailed procedure was given in **Section 2.2.3**.

Heat transfer study

Two modeling setups are incorporated in the heat transfer study, refer to **Fig. 6.4**. The aggregates and binder are modeled separately in the component's setup (denoted as 'CS') model; the properties of the aggregates (denoted as 'agg') are measured, while the properties of the geopolymer binder (denoted as 'bind') are calculated. The 'bulk setup (denoted as 'BS') model depicts the composite as a single bulk body, where its material properties are measured directly from the overall composite (denoted as 'comp'). The CS model is used to study the influence of aggregates in the composite, while the BS model is used to validate the CS model. The comparison of modeling output between 'CS' model and 'BS' model is given in **Appendix D (Fig. D1)**.

(1) Set up of Geometry

To set up the composite geometry for CS study, models are represented two-dimensionally. The aggregate is portrayed as a sphere with a diameter d_{agg} after averaging out their irregular shapes and represented as a circle in two dimensions, refer to **Fig. 6.4b**. In addition, the volume fraction of aggregates in the composite $\%V_{agg}$ is converted into area fraction $\%A_{agg}$ in two-dimension. The aggregates are represented by their mean diameter d_{agg}, with five different categories of aggregate size included in the model. The overall geometry setup is presented in **Fig. 6.5**, it should be noted that identical geometry is applied for L-3 and S-3 due to their same packing design. The geometries are generated with MATLAB codes and imported into Comsol Multiphysics for further simulation.

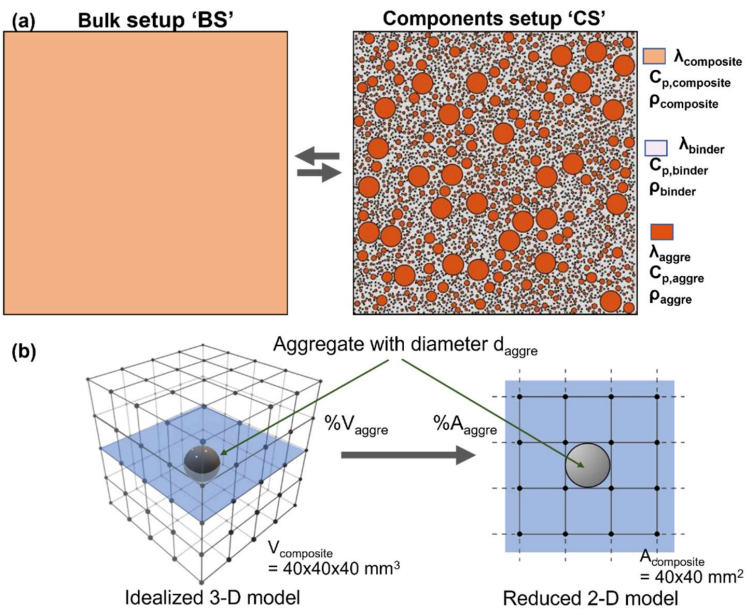

Fig. 6.4 (a) Model setups and (b) aggregate modeling in the 'CS' model.

Range (mm)	d_{aggre} (mm)	L-2				L-3 and S-3				L-L			
		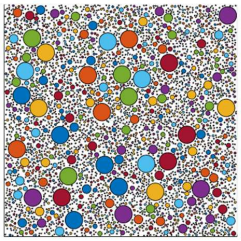				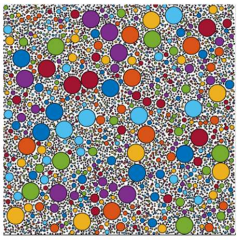				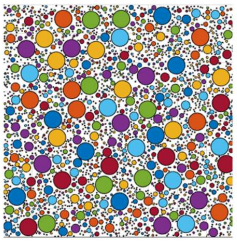			
		$\%V_{aggre}$	$n_{V,aggre}$	$n_{A,aggre}$	$\%A_{aggre}$	$\%V_{aggre}$	$n_{V,aggre}$	$n_{A,aggre}$	$\%A_{aggre}$	$\%V_{aggre}$	$n_{V,aggre}$	$n_{A,aggre}$	$\%A_{aggre}$
2 – 4	3.000	16.1	730	29	12.7	22.2	1007	40	17.5	27.1	1227	48	21.3
1 – 2	1.500	9.3	3363	66	7.3	11.5	4173	82	9.0	13.8	5015	98	10.9
0.5 – 1	0.750	6.7	19422	191	5.3	8.2	23813	234	6.5	9.1	26268	258	7.1
0.25 – 0.5	0.375	6.5	150726	740	5.1	6.5	151318	743	5.1	4.6	107389	527	3.6
0.1 – 0.3	0.200	7.3	1113893	2916	5.7	9.4	1434229	3755	7.4	3.3	496883	1301	2.6
	Total	**45.9**			**36.0**	**57.9**			**45.5**	**57.9**			**45.5**
Mesh elements				993679 (triangles)				1042778 (triangles)				640919 (triangles)	

Fig. 6.5 Two dimensions geometry setup.

(2) Heat transfer modeling

The influence of different packing models on the heat transfer process within the composites is studied using the Comsol Multiphysics 5.6 software. The model is solved using the following heat transport equation [267]:

$$\frac{C_{p,v}}{\rho}\frac{\partial T}{\partial t} - \lambda\left(\frac{\partial^2 T}{\partial^2 x} + \frac{\partial^2 T}{\partial^2 y}\right) = Q \tag{6.5}$$

where λ is the effective bulk thermal conductivity, $C_{p,v}$ is the measured volumetric heat capacity under constant pressure, ϱ is the bulk density, Q is the heat source, and T is the temperature profile to be solved. For practical reasons, λ is assumed to remain constant at the average value. The main input parameters, namely bulk density, thermal conductivity, and volumetric heat capacity for the modeling are determined as follows:

The bulk density of the standalone binder ϱ_{bind} is calculated according to:

$$\rho_{bind} = \frac{m_{comp} - m_{agg}}{(1 - \%V_{agg})} \tag{6.6}$$

where m_{comp} and m_{agg} are the mass of the composite and aggregate respectively, and $\%V_{agg}$ is the volume fraction of aggregates in the composite.

The thermal conductivity λ_{bind} is obtained by treating the solid and pores in the binder as thermal resistors in parallel [268] with the following equation:

$$\lambda_{bind} = (1 - \varphi)\lambda_{solid} + \varphi\lambda_{air} \tag{6.7}$$

in which, φ is the volume fraction of the air pores (porosity) in the binder, λ_{solid} is calculated from the approximate thermal conductivity of the solid skeleton of a plain FA/LS geopolymer as 0.5480 W/mK, and λ_{air} is the thermal conductivity of air at 0.026 W/mK.

The volumetric heat capacity of binder $C_{p,v,bind}$ is obtained by using a weighted average equation [269]:

$$\frac{C_{p,v,comp}}{\rho_{comp}} = \%wt._{agg}\frac{C_{p,v,agg}}{\rho_{agg}} + \%wt._{bind}\frac{C_{p,v,bind}}{\rho_{bind}} \quad (6.8)$$

where $\%wt._{agg}$ and $\%wt._{bind}$ represent the weight percentage of binder and aggregate respectively.

(3) External thermal load and output results

Both models are set up with heat transfer from the heat source through their perimeter into the body. Similar to the laboratory setup, heat is transferred from the heating source in an oven to the body by convection and radiation, which can be described by an equivalent heat transfer coefficient (h), and the heat source Q_{in} can be described:

$$Q_{in} = h(T_{ext} - T) \quad (6.9)$$

where T_{ext} is the temperature in the oven, and h is set at 10. The heating temperature T_{ext} profile is set as the boundary conditions:

$$\begin{matrix} T_{ext}(x = 0{,}0 \le y \le L, t) \\ T_{ext}(x = L, 0 \le y \le L, t) \\ T_{ext}(0 \le x \le L, y = 0, t) \\ T_{ext}(0 \le x \le L, y = L, t) \end{matrix} = \begin{cases} 20 & t = 0 \\ 20 + 10t & 0 < t \le 78\,min \\ 800 & 78 < t \le 138\,min \end{cases} \quad (6.10)$$

Namely, the sample is heated at a rate of 10 °C/min from 20 °C to 800 °C, and subsequently held at 800 °C for another 60 minutes to reach the thermal equilibrium. The initial condition of the body is set at 20 °C. A time-dependent solver is used, with a total simulation time of 138 minutes with a 1-minute time-step. The T profiles from six data points are extracted for study: 0 (on the surface), 4, 8, 12, 16, and 20 cm (center) from the surface. The temperature graphical profiles at 10 minutes intervals are exported to supplement the result analysis.

High temperature behavior

The high temperature exposure test was performed according to the procedure described in **Section 2.2.3**. The prismatic samples (40×40×160 mm^3) at 28 curing days were heated from room temperature to different temperatures of 100, 200, 400, 600, and 800 °C. Then the specimens were naturally cooled down to ambient temperature (20 ± 2 °C) in the furnace and sealed with plastic foil until further characterization. For each composite, three samples were tested under the same condition. The thermally induced linear shrinkage of samples was determined by comparing the length of the longest side of the prismatic samples before and after thermal exposure. For the residual compressive strength, an identical protocol was conducted on cooled prismatic samples as mentioned above. The average value of six replicates was recorded as residual compressive strength.

6.3 Results

6.3.1 Basic characteristics

Appearance observation and microstructure

The cross-section of samples with different aggregates and packing models are presented in **Fig. 6.6**. The highlighted white particles and crystalline-like particles represent LWA and sand, respectively, and the dark regions around the particles indicate the binder gel and the black regions denote pores and voids. The aggregates distribute homogeneously in all matrices, indicating the proper workability to avoid aggregate segregation. Notably, a wide range of particle sizes can be observed in developed L-2, L-3, and L-L samples. From L-2 to L-3, with an increasing q value, more LWAs are detected. A coarser packing pattern with a larger proportion of big size aggregates but fewer small size aggregates is obtained in unoptimized sample L-L. The S-3 sample with sand aggregates shows a similar packing pattern as L-3 because of the same q value in the mix design. Moreover, pores and voids are formed in all specimens caused by air entrainment during the mixing.

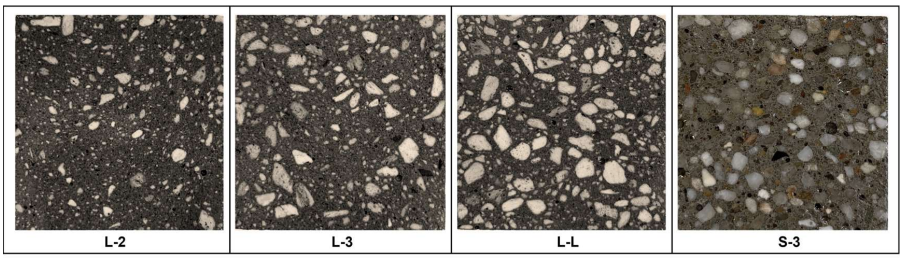

Fig. 6.6 The cross-section of samples with LWA and sand aggregates.

The interface between binder gel and aggregates is presented in **Fig. 6.7**. In **Fig. 6.7a** and **b**, the dense regions with spherical FA particles are identified as geopolymer binder whilst the extremely porous structures are referred to as LWAs. A well-connected interfacial transition zone (ITZ) between paste and LWAs is observed, which should be attributed to the impregnation of binder gel into the porous surface of LWAs that forms an interlocked bonding. While a poorer connection is noticed between binder and sand aggregates in **Fig. 6.7c and d**.

Density and porosity

Fig. 6.8 depicts the bulk density and porosity of the geopolymer composites. In general, the SAG sample has a significantly high density of 1.99 g/cm^3 and low porosity of 24.55% as compared to LWAGs. The incorporation of LWA largely decreases the density to 1.21 g/cm^3 and increases the porosity to 48.63% in L-2. In addition, when increasing the q value from 0.2 to 0.3, the density is further decreased with higher porosity. This is because the

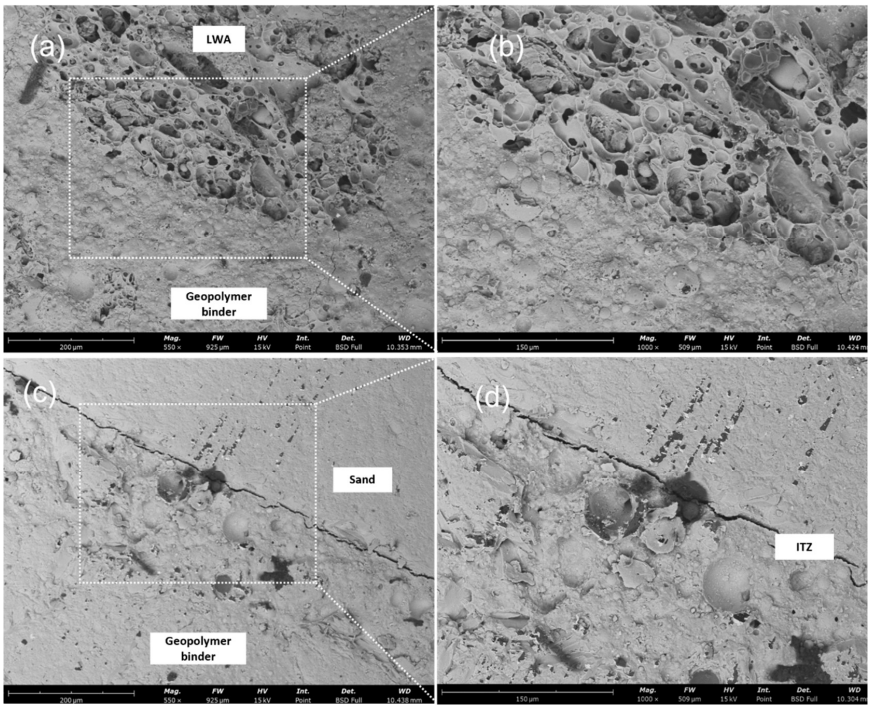

Fig. 6.7 SEM image of geopolymer binder and aggregate interface.

increased q value leads to a higher LWA amount while a reduction in binder content as can be known from **Table. 6.3**. Notably, a lower density with higher porosity is obtained in unoptimized sample L-L as compared to L-3, despite the aggregate vol.% being kept the same as L-3. This can be attributed to both the poor packing quality in L-L and the higher fraction of big aggregates in L-L as compared to L-3, which potentially introduces more pores. The porosity from the binder and aggregate are further calculated and summarized in **Table 6.4**. It is clear that a higher q value leads to a lower binder porosity but a higher aggregate porosity, and the unoptimized L-L samples have higher aggregate porosity. Moreover, it should be noted that the highest binder porosity of 20.44% is resulted in S-3. It is ascribed to the poor workability in SAG due to the water absorption from the sand.

Table 6.4 Calculated porosity of binder and aggregate in different mixes.

Sample code	φ_{Bind}	φ_{Agg}	φ_{Total}
L-2	8.06	40.57	48.63
L-3	2.49	50.3	52.79
L-L	2.8	51.22	54.02
S-3	20.44	4.11	24.55

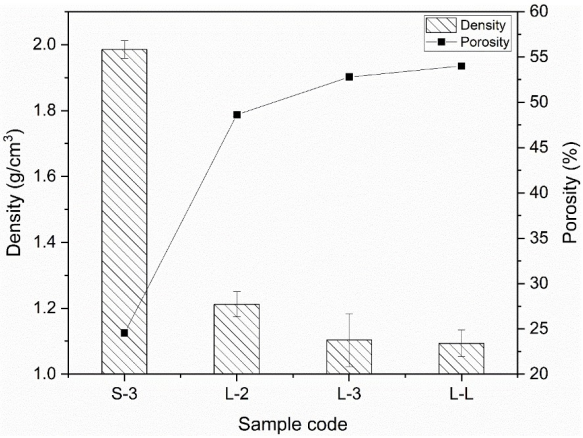

Fig. 6.8 The density and porosity of samples.

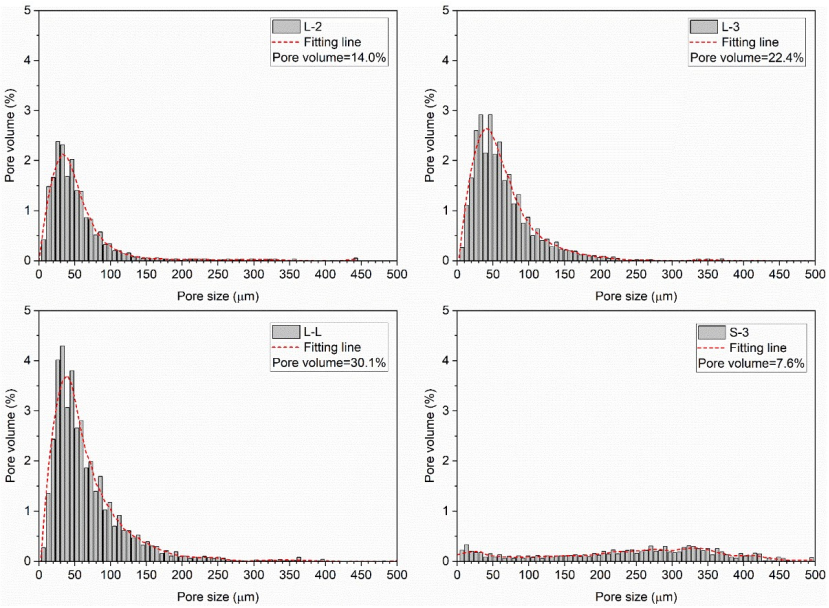

Fig. 6.9 Pore size distribution of geopolymer composites from Micro-CT scanning.

The detailed pore structure of geopolymer composite is investigated by microtomography technology (Micro-CT) as presented in **Fig. 6.9**. The calculated porosity is 14.0%, 22.4%, 30.1%, and 7.6% for L-2, L-3, L-L, and S-3 respectively. Here, the calculated porosity is lower than the total porosity, resulting from the limited pore size detected range (>6.6 μm) of Micro-CT. In general, the variation trend correlates well with that of total porosity in different composites, and the calculated results can be used as an indicator for understanding the influence of different aggregates and packing designs on pore structure. The pore size distribution in LWAG shows a parabolic shape with the main peak, while the SAG has a widely distributed size of pores. The pores detected in S-3 are mainly from the binder, which is related to the poor workability. In LWAG, with the q value change

from 0.2 to 0.3, the main peak shifts from 34.6 to 40.9 μm with an increased peak intensity and wider pore size range, resulting in a coarser pore structure. As compared to L-3, the L-L sample shows higher main peak intensity and higher fraction of big pores/defects (larger than 100 μm), which explains its higher porosity as compared to L-3.

Water vapor properties

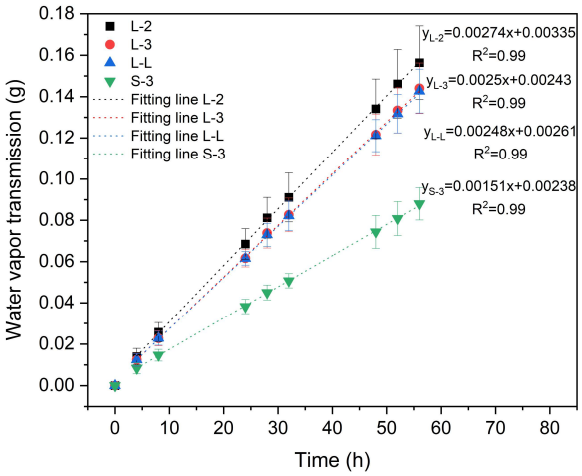

Fig. 6.10 Water vapor transport in different samples as a function of time duration.

Table 6.5 Water transport properties, water vapor transmission rate (WVTR), permeability (δ).

Code	Slope (g/h)	WVTR (g/h m²)	δ (m/s)
L-2	0.00274	1.71	0.0078
L-3	0.0025	1.56	0.0071
L-L	0.00248	1.55	0.0071
S-3	0.00151	0.94	0.0043

Water vapor transport plays an important role in determining the thermal stability of building materials since it represents the ability to transfer water vapor from the body at high temperatures. The water vapor transmission along with time is shown in **Fig. 6.10**, and the transport properties are calculated and summarized in **Table. 6.5**. It can be seen that the introduction of LWAs results in a much higher water vapor transport and permeability than that of SAG owing to the higher porosity and pore openness. However, among LWAGs, it is interesting to notice that the water vapor transport, as well as permeability, are negatively related to the total porosity of the composites. The L-3 and L-L with the highest porosity show the lowest water vapor transmission and permeability. Because water vapor transport is mainly determined by pore connectivity, it is most likely the LWAs are largely composed of closed/isolated pores. Thus, despite the high porosity, the higher incorporation of LWAs has a minor or even negative influence on pore connectivity. In this case, a higher binder porosity with lower aggregate porosity in L-2 results in better water transport properties as compared to L-3 and L-L. On the other hand,

the pore size distribution within samples also plays a vital role in determining water vapor transport. Huang et al. [270] concluded that large capillaries and microcracks have a greater impact on moisture transport rates than other pore components. As learned from **Fig. 6.9**, L-2 exhibits the highest percentage of pore below 10 μm among LWAGs, which can be another cause for the promoted water transport property. Here, the superior water transport performance observed in LWAGs can offer better thermal stability over sand geopolymer composites by facilitating the thermally induced water vapor, and thus reducing the inner thermal stress, which will be discussed below.

Mechanical strength

The compressive strength of designed samples is determined at the age of 7 and 28 days, and the results are shown in **Fig. 6.11**. As expected, the SAG exhibits the highest compressive strength from 7 to 28 days owing to its dense structure. For the LWAG, the optimized mixtures, namely L-2 and L-3, have a higher strength as compared to the unoptimized mixture. This is mainly due to the poor packing in L-L as evidenced by pore size distribution, proving the advantage of packing design for LWAGs considering the mechanical strength. Moreover, L-2 shows a lower early compressive strength at 7 days while a higher compressive strength at a later age when compared to L-3. This should be due to the slow strength development of the geopolymer binder, which is initially weaker than LWA. Therefore, the increasing content of LWAs in L-3 further strengthens the matrix at an early age. While the binder gel takes the dominant role in the compressive behavior at a later age, thus L-2 sample shows the highest strength gain from 7 to 28 days.

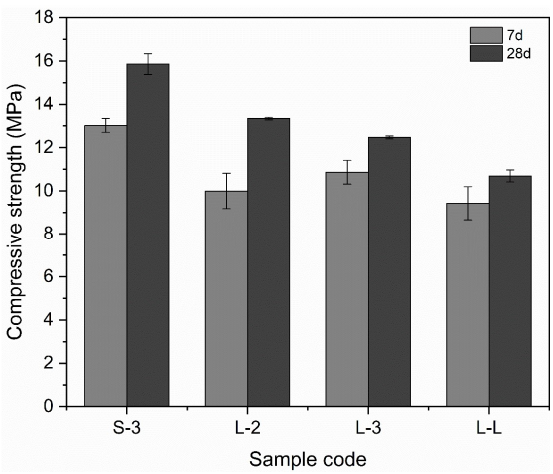

Fig. 6.11 Compressive strength of sample at 7 and 28 days of curing.

6.3.2 Heat transfer study

Thermo-physical properties

The thermal-physical properties, including thermal conductivity, thermal diffusion, and volumetric heat capacity are summarized in **Table 6.6**. All parameters are measured under constant pressure and volume. The volumetric heat capacity considers the role of bulk density, which is preferable to differentiate the effect of lightweight aggregates and normal sand on the heat gain within the composites. For simplification, the volumetric heat capacity is represented as heat capacity in the following discussion.

Table 6.6 The thermal conductivity (λ), thermal diffusion (α), and volumetric heat capacity ($C_{p,v}$) of samples.

	λ (W/mK)	St dev	α (mm^2/s)	St dev	$C_{p,v}$ (MJ/m^3K)	St dev
L-2	0.2866	0.0036	0.2874	0.0148	0.9986	0.0375
L-3	0.2769	0.0018	0.2443	0.0045	1.1337	0.0133
L-L	0.2498	0.0036	0.2496	0.0072	1.0011	0.0147
S-3	1.4010	0.0151	0.9332	0.0511	1.5043	0.0650

The thermal conductivity of prepared geopolymer composites with sand is significantly increased as compared to LWAs. This is primarily due to the high thermal conductivity of regular sand, which largely amplifies the overall thermal conductivity of the geopolymer composite. For LWAG, it is noticed that a higher q value contributes to lower thermal conductivity. In addition, the unoptimized sample L-L exhibits a lower thermal conductivity as compared to L-3. It is because the poor packing in L-L introduces more large pores/voids in the matrix, further reducing the thermal conductivity. In addition to thermal conductivity, SAG also exhibits the highest thermal diffusion and volumetric heat capacity among all the developed composites due to its dense structure. Moreover, among LWAGs, it is noticed that the variation of heat capacity and thermal diffusion is not linearly related to thermal conductivity or bulk density. This discrepancy might be because of the specific pore structure by introducing LWAs. Hence, the obtained thermos-physical properties with specific pore structures are expected to impact the high temperature behavior of geopolymer composites, which will be discussed below.

Lastly, the thermal conductivity versus compressive strength is compared with previous literature in **Fig. 6.12**. In accordance with previous studies, the compressive strength of designed LWAGs is found to reduce along with the thermal conductivity. Moreover, it is noted that a higher mechanical strength is obtained in this study as compared to other lightweight geopolymers with similar thermal conductivity. It further proves that the optimized packing model contributes to a compact mixture with homogenously distributed LWAs, enabling a low thermal conductivity with decent compressive strength.

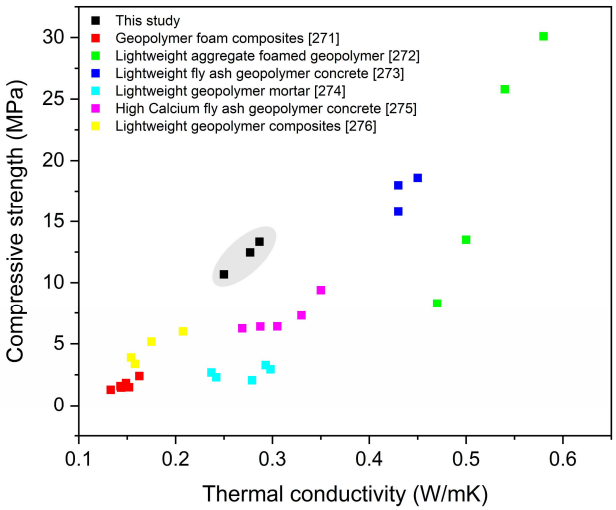

Fig. 6.12 The relationship between compressive strength and thermal conductivity as compared to other geopolymer-based lightweight materials [271–276].

Temperature contour

Numerical simulation is employed to study the heat transfer process within different composites as a function of packing design and aggregate type. In the 'CS' model, the binder and aggregates are assigned individual main parameters, including bulk density, thermal conductivity, and heat capacity which are determined as mentioned in the testing method section and summarized in **Table 6.7**.

Table 6.7 Main parameters of the heat transfer simulation.

Sample	Component	ϱ_b kg/m^3	λ W/mK	$C_{p,v}$ MJ/m^{3}K
L-2	Composite	1210.0	0.2866	0.9986
	Aggregate	324.2	0.0698	0.2884
	Binder	1961.6	0.4702	1.6011
L-3	Composite	1100.0	0.2769	1.1337
	Aggregate	322.8	0.0698	0.2860
	Binder	2168.9	0.5171	2.2995
L-L	Composite	1090.0	0.2498	1.0011
	Aggregate	318.0	0.0698	0.2735
	Binder	2151.8	0.5133	2.0018
S-3	Composite	1990.0	1.4010	1.5043
	Aggregate	2082.0	0.2024	1.7281
	Binder	1758.0	0.4241	1.1966

The simulated heat transfer through the L-2 composite as a function of exposure time is extracted and shown as an example in **Fig. 6.13a**, and the temperature maps of different composites at 100 min are compared in **Fig. 6.13b**. The external heating load is imposed on the perimeters of the simulated models as per experimental setup corresponds to the Eq. (6.10), and a cyclic-shaped temperature distribution can be observed within all composites. In LWAG, the isothermal lines are unevenly distributed, and the isotherms are denser in the area close to the heating source than that in the core area. As compared to L-2, denser isothermal lines are presented in L-3 and L-L, indicating a higher LWA proportion leads to a larger temperature gradient within the matrix, while a slower temperature gain rate has resulted. Between L-3 and L-L, the isothermal lines in L-L appear relatively more irregular. This is due to the unoptimized packing of L-L, causing a significant difference in thermal conductivity between the binder and aggregates (**See Table 6.7**). In comparison, the smaller difference in thermal conductivity between sand and geopolymer binder leads to a more evenly distributed isotherm line in S-3.

Temperature variation

The temperature gradients within different composites are compared in **Fig. 6.14**, and the simulated temperature change on the surface and at the core of samples is provided in **Appendix D (Fig. D2)**. For all samples, the temperature gradient increases first and then decreases while the heating temperature is constant. In general, the geopolymers with aggregates diffuse heat slower and show a higher temperature gradient than the standalone binder (Ref) under the same heating conditions. In terms of the packing modulus, L-3 shows the best thermal insulation performance. The dense binder with a relatively low LWA proportion in L-2 leads to a high thermal diffusivity with a small temperature gradient. As for the effect of packing, despite its lower thermal conductivity, L-L exhibits a lower temperature difference as compared to L-3. It is because, the denser matrix obtained in L-3 contributes to a higher heat capacity with a lower thermal diffusivity, meaning a higher thermal inertia to be overcome in L-3 than in L-L. Moreover, it is expected that S-3 shows a smaller temperature gradient than L-3, because of the higher thermal conductivity and faster heat diffusion of sand than that of LWAs.

In summary, the types and packing of aggregates have a combined effect on thermophysical parameters, which have a direct impact on the heat transfer properties of geopolymer composites. The high thermal conductivity and heat capacity of sand result in a more even heat distribution with a small temperature gradient in SAG as compared to LWAGs. In terms of LWAGs, the optimized packing contributes to a high heat capacity and low thermal conductivity, resulting in a low thermal diffusivity with a large temperature gradient. These observed heat transfer properties further influence the high temperature behaviors of geopolymer composites, which is discussed in the next section.

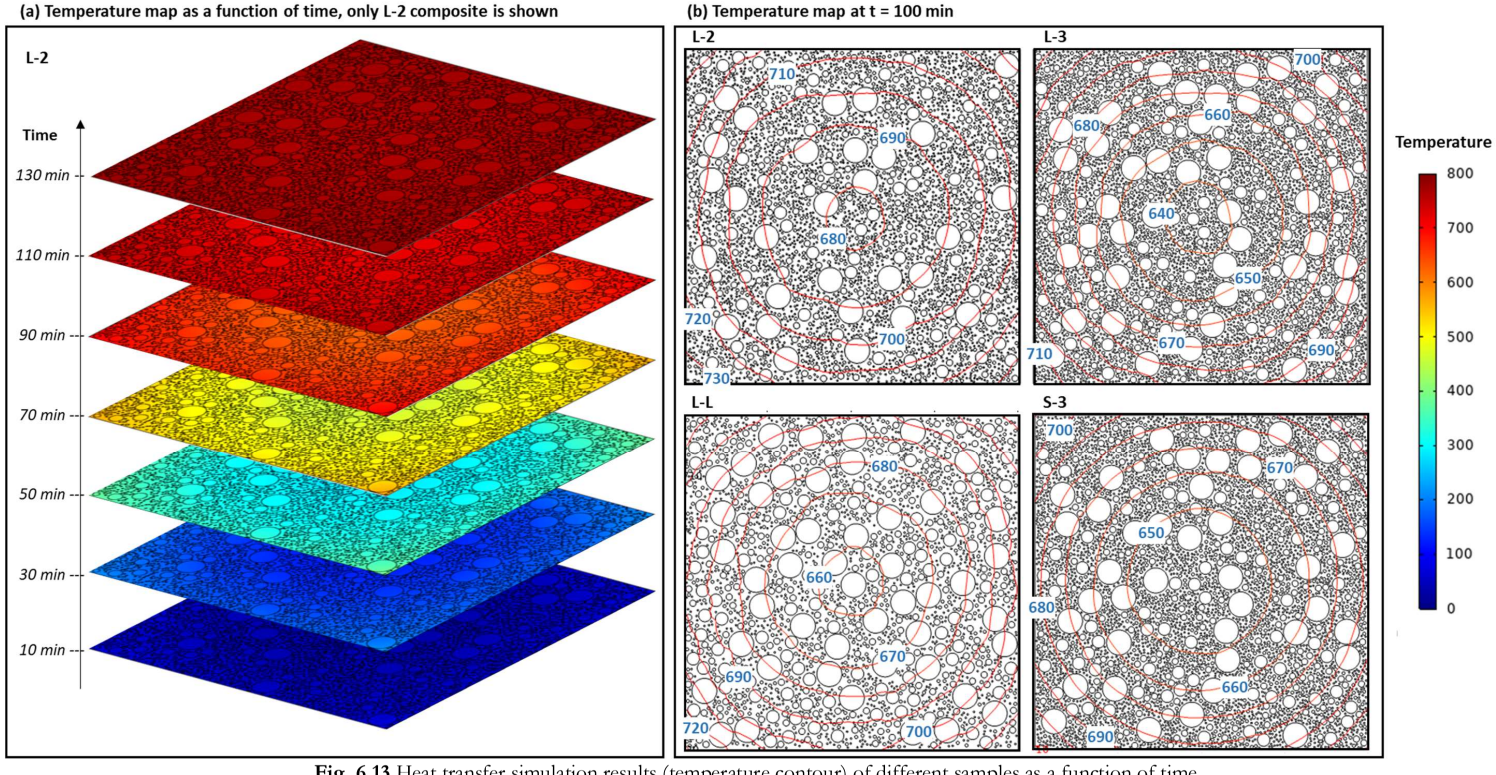

Fig. 6.13 Heat transfer simulation results (temperature contour) of different samples as a function of time.

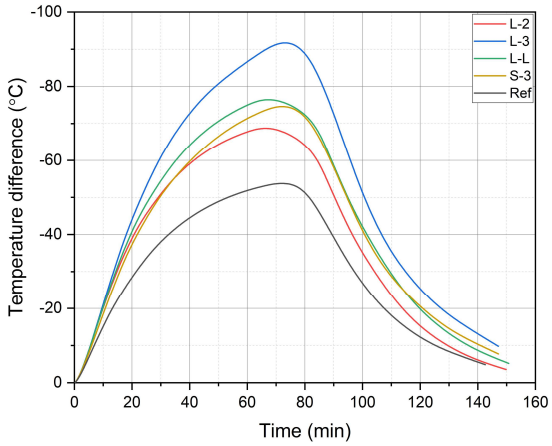

Fig. 6.14 The temperature gradient within samples between the surface and core.

6.3.3. High temperature behavior

It has been well studied that the thermal behavior of geopolymer binder under elevated temperatures is governed by major factors including further geopolymerization, gel dehydration, re-crystallization, and viscous sintering [20,22,277]. Hence, this section mainly focuses on the interaction between aggregates and geopolymer binder under elevated temperatures, and its further influence on high temperature performance, such as thermal transport properties, microstructural change, volumetric stability, and thermal mechanical evolution.

Thermal conductivity and microstructural transformation

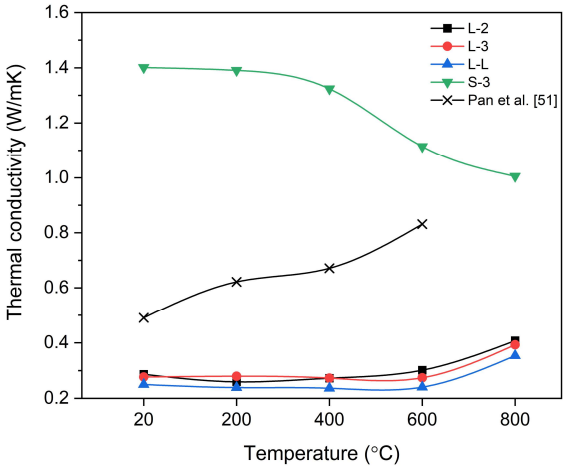

Fig. 6.15 Thermal conductivity after exposure to elevated temperatures.

The thermal conductivity of the geopolymer composites after high temperature exposure is depicted in **Fig. 6.15**. The thermal conductivity of the SAG sample keeps decreasing from 1.401 to 1.005 W/mK. LWAGs show a stable thermal conductivity before 600 °C, following a slightly increase up to 800 °C. The difference in thermal conductivity among LWAGs is insignificant, and the thermal conductivity after 800 ℃ exposure is proportional to the initial thermal conductivity. Pan et al. [51] reported the thermal conductivity of FA based geopolymer paste during high temperature exposure as summarized in **Fig. 6.15**. In comparison, the initial thermal conductivity of LWAGs is lower than FA based geopolymer paste, while that of SAG is much higher, owing to the thermophysical properties of different aggregates as discussed in **Section 6.3.2**. Moreover, the thermal conductivity of LWAGs shows a similar but more stable tendency to FA geopolymer paste at high temperatures. Here, the difference between the presented and previous study should mainly result from the aggregate incorporation. The incorporation of LWAs promotes the microstructural stability and subsequently, minimizes the thermal conductivity variation at high temperatures. While the sand incorporation further intensifies the thermally induced microcracking, resulting in a continuous reduction in thermal conductivity. On the other hand, this discrepancy may be raised by the measurement technique. The thermal conductivity at high temperatures might be higher than that of exposed geopolymer due to the presence of thermal radiation upon exposure to heat [268].

The thermally induced microstructure transformation between SAG and LWAG (L-3 and S-3) is compared in **Fig. 6.16**. Before being exposed to high temperature, spherical particles can be observed in both L-3 and S-3, representing the unreacted FA. A weak bond between sand and binder gel is noticed in S-3, while it is difficult to identify the ITZ between LWA and gel. At 200 °C, both samples are relatively stable with minor cracks. Noteworthy, owing to the further geopolymerization of the binder, the ITZ in S-3 is refined and becoming insignificant. From 200 to 600 °C, varying degrees of microstructure degradation are detected due to the decomposition of geopolymeric gel as well as the physical interaction between binder gel and aggregates. Two deterioration patterns are differentiated in L-3 and S-3: i) In S-3, drastic structural deterioration is noticed in geopolymer binder along sand aggregates, especially at 600 °C. It is known the sand experiences a volumetric expansion owing to α-β quartz transformation at around 573 °C [278]. Simultaneously, the geopolymeric gel is prone to dehydrate and shrink at elevated temperatures [174]. With the significant thermal incompatibility between geopolymer binder and sand, numerous cracks and voids are formed as observed in **Fig. 6.16h**. Moreover, sand and unreacted FA particles are increasingly separated from the binder gel, which further weakens the matrix bonding. ii) As for LWAGs, only minor cracks occur to the LWA body along the interface. Interestingly, as compared to S-3, the negative effect of gel shrinkage is mitigated in L-3. This is due to the intrinsic weak mechanical property of LWA. The aggregate body is inevitably damaged

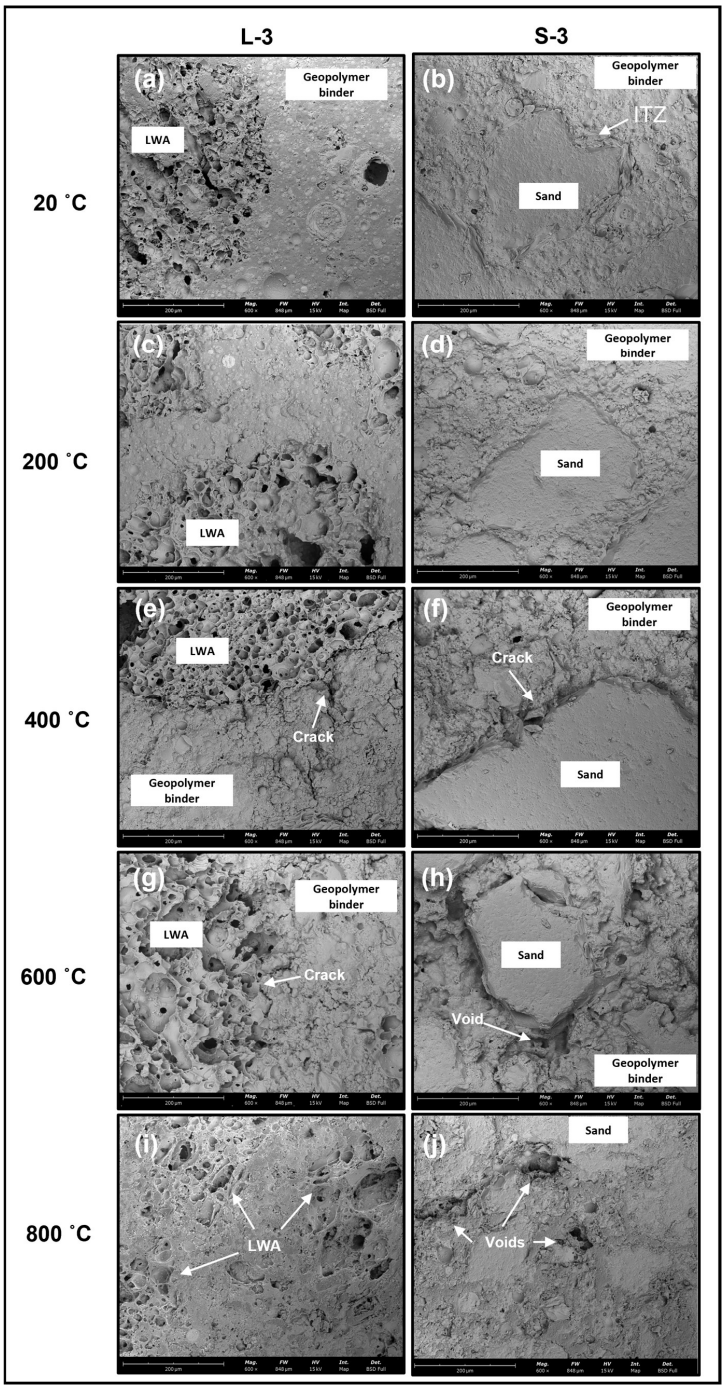

Fig. 6.16 The microstructure of geopolymer composites exposed to high temperatures.

during the gel shrinking, while the thermal strain between binder gel and aggregates is reduced, thus largely retaining the binder's structural integrity. At 800 °C, owing to the viscous sintering and re-crystallization of geopolymeric binder [234], the pores of LWAs and cracks in L-3 are partially filled with gel, and the matrix is largely healed and densified. It further explains the rise in thermal conductivity at 800 °C as observed in **Fig. 6.15**. While voids between sand and binder gel are still visible in S-3 due to the severe structural deterioration.

Volumetric stability

The linear shrinkage, bulk density, and porosity transformation of samples as a function of temperature are presented in **Fig. 6.17**. In general, the thermal evolution of volumetric properties in mixtures with different aggregate type exhibit varied trends. The SAG exhibits a minor linear shrinkage of 0.35% at 800 °C. Kong et al. [80] and Zhang et al. [249] reported that geopolymer mortars with sand or basalt aggregates experience thermal expansion up to 800 °C, attributed to the thermal incompatibility between geopolymer binder and aggregates. Here, the observed good thermal volumetric stability can be assigned to the optimized sand aggregate packing, which serves as a reinforcing skeleton that can resist thermal deformation. In comparison, LWAGs undergo different degree of thermal shrinkage with the sharpest shrinkage occurs from 600 to 800 °C. This is because, on the one hand, the LWAs are relatively weak, and the thermal shrinkage of binder gel plays a dominate role before 600 °C. On the other hand, as observed in **Fig. 6.16i**, the partial melting and viscous sintering of binder at 800 °C fill the pores of LWAs, which is the main cause of the drastic shrinkage. More specifically, it is noticed that unoptimized LWAG as well as LWAG with a higher q value experiences less linear shrinkage. It can be deduced that a coarse pore structure with high porosity or large LWAs fraction is beneficial to alleviate the matrix thermal shrinkage.

As shown in **Fig. 6.17b** and **c**, the evolution of bulk density and porosity can be an indicator of thermally induced microstructural change, such as crack formation and matrix densification. As compared to LWAGs, despite SAG showing the lowest linear shrinkage up to 800 °C, significant variations in bulk density as well as porosity are observed. The S-3 shows an obvious reduction in bulk density with increased porosity at 100 °C. A similar trend was reported in geopolymer composites with fine pegmatite aggregates [279], indicating the crack formation induced by the drastic water evaporation. From 400 to 600 °C, there is a remarkable drop in bulk density accompanied by increased porosity in S-3. This can be attributed to the sand expansion, which is consistent with SEM results. Then, insignificant matrix densification is noticed at 800 °C, suggesting a diminished healing effect during viscous sintering. The LWAGs exhibit similar trends in bulk density as well

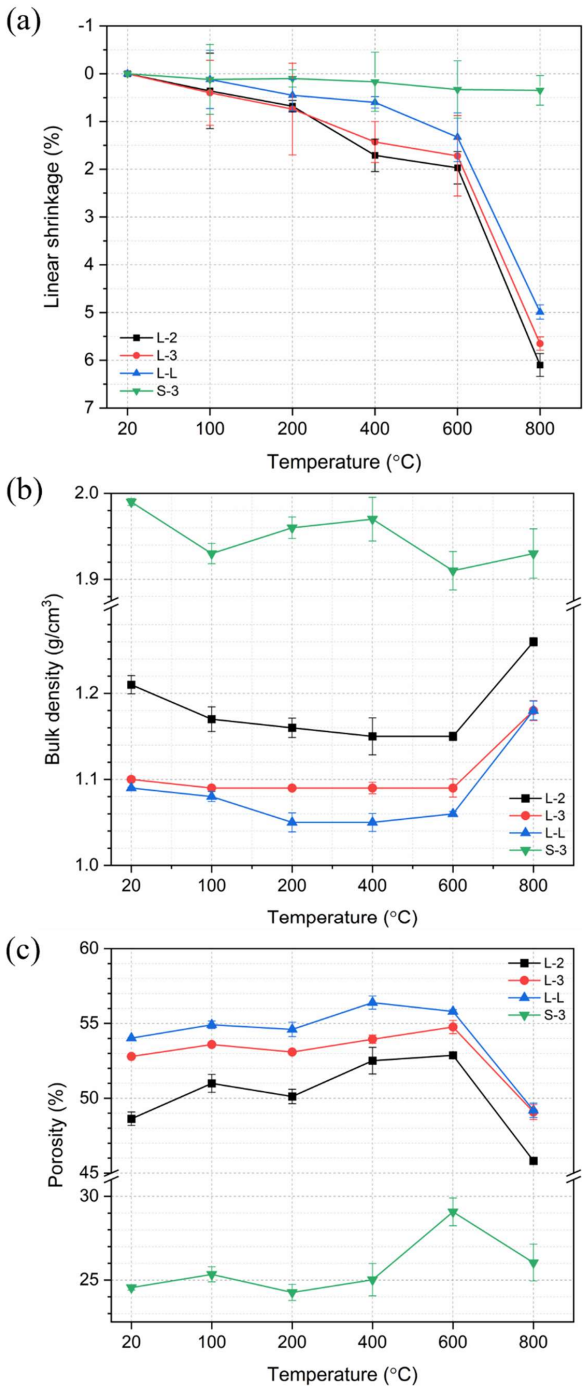

Fig. 6.17 The variation of (a) linear shrinkage, (b) density, and (c) porosity of geopolymer composites at different temperatures.

as porosity from 20 to 800 ˚C. Among these, the optimized mixture with a q value of 0.3 shows the best stability before 600 ˚C. After 600 ˚C, all the LWAGs undergo significant matrix densification with reduced porosity, further proving the filling effect of viscous gels.

In general, the high stiffness of sand with optimized packing provides decent macro stability at high temperatures. However, at the microstructural level, the conflicting thermal behavior among geopolymer binder and sand aggregates leads to severe microstructural deterioration. On the other hand, the incorporation of LWAs helps to alleviate the thermal mismatch between paste and aggregates thanks to its high permeability and mechanical weakness, resulting in reduced microstructural deterioration.

Residual compressive strength

The mechanical strength variation as a function of temperature is depicted in **Fig. 6.18a**. A noticeable difference in mechanical strength evolution is observed between SAG and LWAG. All composites show a different degree of strength gain at 100 ˚C. Then, LWAGs exhibit a strength reduction till 600 ˚C, following a strength rise at 800 ˚C. While the compressive strength of S-3 keeps dropping from 100 to 800 ˚C. Above all, the SAG sample shows the highest mechanical strength before 600 ˚C, while LWAGs have superior mechanical strength at 800 ˚C, especially for L-3.

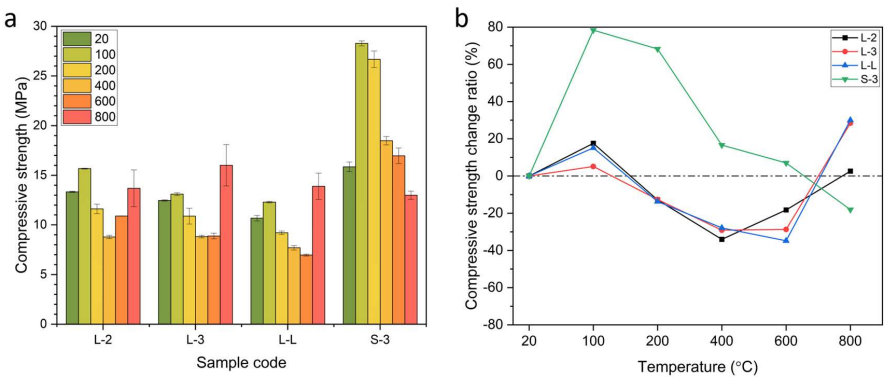

Fig. 6.18 (a) The compressive strength and (b) strength change ratio of composites at different temperatures.

The thermal mechanical strength change ratio in different composites is further compared in **Fig. 6.18b**. It is known that the strength gain of geopolymer binder at 100 ˚C is mainly because of the further geopolymerization [206]. As compared to the remarkable strength gain of 78.4% in SAG, LWAGs only exhibit a slight compressive strength gain. This is because in LWAGs, despite the further geopolymerization that refines the ITZ between binder and

aggregates, the poor mechanical property of LWAs largely hinders the strength gain effect. It explains the higher strength gain in L-2 than L-3 due to its higher binder content. Whilst given the high stiffness of sand aggregates, the positive effect of further geopolymerization is more significant in SAG. After 100 °C, the strength evolution in geopolymers is mainly affected by two mechanisms, namely the dehydration/decomposition of binder gel and the thermal interaction between binder gel and aggregates. In general, SAG experiences a more drastic strength deterioration compared to LWAGs from 100 to 800 °C. This is because, on the one hand, the dense matrix with low permeability (see **Table 6.6**) gives rise to thermal stress during water evaporation [68]. On the other hand, as detected in SEM, the thermal mismatch among binder shrinkage and sand expansion after 400 °C remarkably damages the matrix with serious cracking and voids formation. In comparison, LWAGs undergo a moderate strength loss till 400 °C, following a strength gain. As discussed above, the decreased strength loss in LWAGs is mainly thanks to the reduced thermal incompatibilities between binder gel and LWAs. In addition, the high permeability in LWAGs contributes to a lower water vapor pressure, hence weakening the matrix damage. Moreover, it is interesting that a higher q value enables a reduced strength loss rate, whilst a prolonged compressive strength loss period till 600 °C (L-3). This likely corresponds to the different heat transfer processes in L-2 and L-3. As discussed in **Section 3.2**, during the heating process, L-3 exhibits a lower temperature gain rate than L-2, which would certainly alleviate the thermally induced damage. However, the large thermal gradient in L-3 might prolong the effects of thermal deterioration. Beyond 600 °C, strength gains of 2.6%, 28.4%, and 30.0% are noticed in L-2, L-3, and L-L, respectively, attributed to the viscous sintering. The sample with a larger q value exhibits a higher strength gain, which is contributed by the reduced matrix degradation that allows a superior healing effect. The L-3 and L-L show a relatively similar strength gain ratio due to the same gel/aggregate proportion, whilst the optimized matrix exhibits a higher residual strength. In S-3, the strength gain is hindered due to the drastic structural deterioration.

In conclusion, the geopolymer composites with different aggregate types experience a varied strength evolution under elevated temperatures. As compared to SAG, a reduced strength loss from 100 to 400 °C and an obvious strength gain at 800 °C is observed in LWAGs, owing to the higher permeability, and lessened thermal incompatibility. In addition, a higher q value not only contributes to lower thermal-induced damage but also slows down the development of strength deterioration. It should be related to its low binder gel/aggregate ratio and specific heat transfer properties during heating.

6.4 Conclusions

This chapter introduces a novel theoretical approach toward the design of high temperature resistant geopolymer composites based on packing optimization. The microstructural formation, as well as thermophysical properties of the designed lightweight aggregate incorporated geopolymer (LWAG), are examined to compare with sand aggregate incorporated geopolymer (SAG). The role of aggregate characteristics in determining the heat transfer process is numerically explored via heat transfer simulation. Ultimately, the interrelationships between the microstructural-thermophysical properties, heat transfer pattern, and high temperature performance are clarified. The following findings can be summarized:

(1) By applying an optimized packing model, the incorporation of lightweight aggregates (LWA) into geopolymer achieves a significantly high porosity ranging from 48.6% to 54.0% as compared to SAG of 24.6%. Among LWAGs, a higher distribution modulus results in a coarser pore structure. Accordingly, a high moisture permeability of around 0.0078 m/s is obtained in LWAG as compared to SAG of 0.0043 m/s. Owing to the rough surface of LWA, the mechanical interlocking effect between LWA and geopolymeric binder contributes to a good binding and compact matrix, resulting in a comparable mechanical strength to that of SAG.

(2) The type and packing design of aggregates significantly affect the thermophysical parameters of geopolymer composites, especially for thermal conductivity and heat capacity. The incorporation of sand into geopolymer composite leads to a high thermal conductivity and heat capacity. In contrast, LWA enables a promising thermal insulation performance. The optimized packing further contributes to a well-packed matrix with high porosity, resulting in a high heat capacity and low thermal diffusivity. When decreasing the distribution modulus from 0.3 to 0.2, higher thermal conductivity and lower heat capacity are resulted due to the reduced aggregate proportion.

(3) The thermal progression development of geopolymer composites is largely influenced by the intrinsic property of aggregates. The optimized packing of sand in geopolymer largely resists the macro-deformation up to 800 °C. But severe microstructural deterioration and strength loss is noticed in SAG due to the drastic matrix incompatibility. In contrast, the incorporation of LWAs results in less thermal destruction with better mechanical stability. However, it ultimately leads to significant shrinkage. Increasing the distribution modulus further alleviates the strength deterioration in LWAGs, attributed to the resulting microstructure and heat transfer pattern.

(4) The distinct thermophysical properties of LWAs and sand significantly vary the heat transfer pattern in geopolymer composites. Sand incorporation results in a fast heat transfer with even temperature distribution in geopolymer composite upon heating. In contrast, the low thermal conductivity of LWAs impedes the inner heat transfer, hence generating a large temperature gradient within the composites. In addition, increasing the distribution modulus reduces the thermal diffusivity and temperature gain rate. It potentially slows down the development of strength deterioration and eases the mechanical degradation in LWAGs at elevated temperatures.

The results from this chapter build a picture of the progressive evolution of geopolymer composites under elevated temperatures, which offers new insights into the thermal degradation mechanism of geopolymer-based mortar/concrete. The introduced design approach can serve as a framework for advancing high temperature resistant geopolymer composites. It shows potential for using geopolymers in large-scale applications like structural elements and tunnel linings that require heat/fire resistance. Nevertheless, this study primarily focuses on the post-heating behavior of geopolymer composites. Future research concerning the in-situ thermal behavior characterization is imperative to achieve a more comprehensive grasp of the thermal performance of geopolymer composites.

CHAPTER 7

Conclusions and recommendations

This thesis focuses on high temperature-resistant geopolymer-based materials, with the objective of achieving economically and environmentally sustainable solutions. As the starting point, the thermal degradation mechanism of geopolymer-based materials is thoroughly revealed by investigating the synergetic effect of chemical transformation and physical change at elevated temperatures. Followingly, the thermal performance of geopolymer-based materials is effectively enhanced through the strategic integration of industrial by-products and waste materials. The major findings and corresponding recommendations for future research are shown below.

7.1 Conclusions

7.1.1 Thermal degradation mechanism of geopolymer-based materials

In an effort to clarify the thermal degradation mechanism of geopolymer-based materials, the interaction between physical change and chemical transformation at elevated temperatures is investigated. From room temperature to 800 ˚C, two different cracking patterns are detected in geopolymer-based materials: a) Long and narrow cracks formed along the interfacial transition zone at low temperatures because of water evaporation. b) Evenly distributed and widened cracks occur at elevated temperatures owing to the dehydration and decomposition of geopolymeric gel. In terms of thermally induced chemical transformation, further geopolymerization before 200 ˚C strengthens the gel skeleton and protects the matrix from spalling. From 200 to 600 ˚C, the decomposition of geopolymer gel accounts for the main inducer of strength deterioration. After 600 ˚C, the viscous sintering and partial melting of gel largely fill the pores and cracks. The mechanical strength evolution of geopolymer-based material under elevated temperatures is not only influenced by crack formation but also by chemical transformation. In particular, further geopolymerization could compensate for the microstructural deterioration and enable a strength gain in the early stage, and the viscous sintering further densifies the matrix at 800 ˚C.

As compared to plain fly ash-based geopolymer, the dense matrix of hybrid fly ash/GGBS geopolymer results in higher capillary pressure and poorer ability to accommodate thermal stress at high temperatures. On the other hand, the GGBS addition not only lessens the positive effect of further geopolymerization but also negatively impacts the gel thermal stability. As a result, from 20 to 800 ˚C, a 41.04% strength loss is detected in hybrid fly ash/GGBS geopolymer as compared to a 150.25% strength gain in sole fly ash based-geopolymer. The GGBS addition enables a superior mechanical strength in hybrid geopolymer without high temperature curing, while poor thermal stability is resulted due to the intrinsic properties of GGBS.

7.1.2 Gel development by precursor tailoring

With the aim to improve both the initial properties and high-temperature stability of geopolymer-based materials, the composition and structure of geopolymeric gel are purposefully modified by introducing ladle slag into Class F fly ash geopolymer. As a by-product from the steelmaking industry, ladle slag promotes alkali activation degree, resulting in a higher content of aluminosilicate hydrates. Within an alkaline system rich in soluble Si, the initially hydrated CAH phases from ladle slag absorb Si to form a more stable C-A-S-H gel, which hinders the conversion reaction between metastable and stable CAH phases. With the rapid reaction of ladle slag, the product layer (C-A-(S)-H) largely limits Ca dissolution and diffusion. Hence, the geopolymerization is retained, with the formation of a partial Ca uptake N-A-S-H gel. As a result, a co-existence of C-(N)-A-(S)-H and N-(C)-A-S-H is obtained in hybrid ladle slag/fly ash geopolymer, and the compressive strength increases with ladle slag substitution from 0 to 15 wt.%. When exposed to elevated temperatures, the hybrid gel exhibits good thermal stability due to the retained geopolymeric gel. On the other hand, the specific pore system in hybrid ladle slag/fly ash geopolymer reduces the thermal stress and thus contributes to better pore stability. As a result, the residual compressive strength, as well as strength gain rate after 800 ˚C is increased along with ladle slag substitution. Nevertheless, increasing the ladle slag substitution leads to a higher mass loss and volumetric shrinkage due to severe dehydration and recrystallization of hybrid binders at high temperatures.

Furthermore, the compatibility between C-(N)-A-(S)-H and N-(C)-A-S-H gel plays a vital role in determining the initial properties and thermal performance of hybrid ladle slag/fly ash geopolymer, which can be tailored by adjusting activator parameters. A high Na content promotes the development of two isolated gels, achieving a low porosity and high mechanical strength as compared to a geopolymer gel-dominated system. Under elevated temperatures, the further geopolymerization and viscous sintering of N-(C)-A-S-H gel densifies the matrix by healing the cracks and pores, posing a tendency for shrinking. While

the dense C-(N)-A-(S)-H gel with thermally induced crystalline phases exhibits certain resistance to thermal shrinkage. Ultimately, the competition between the two gels results in crack formation, low linear shrinkage, and insignificant compressive strength change after 800 ℃.

7.1.3 Structure optimization by physical design

Structural optimization, such as fiber or aggregate incorporation, is proposed as an efficient approach to optimize the thermal performance of cementitious materials. In this thesis, the potential of reutilizing mineral wool waste (MWW) as both co-precursor and fiber reinforcement in the production of geopolymer composites is investigated. Under an alkaline environment, MWW shows certain geopolymerization reactivity, with 2-3 times higher Si and Al dissolution than Class F fly ash. The substitution of Class F fly ash by MWW, especially in fine particle form, not only enhances the geopolymerization degree but also stimulates the Al uptake by N-A-S-H gel. As MWW dosage increases (0 to 12 wt.%), it densifies the gel pores but simultaneously increases porosity and lowers compressive strength due to greater macropore formation. The matrix with optimum MWW distribution largely mitigates the drying shrinkage and improves flexural performance. At elevated temperatures, the highly porous matrix with promoted flexibility effectively minimizes the matrix damage caused by thermal stress. Meanwhile, the partial melting of mineral wool waste poses a healing effect on the matrix, resulting in a 98.5% increase in compressive strength after 800 ˚C. However, this process also leads to substantial thermal shrinkage after high temperature exposure.

To reach a good balance between room temperature property and high temperature stability, lightweight aggregate is incorporated into ladle slag/fly ash geopolymer following a packing model. The optimized packing contributes to a compact matrix with well-packed lightweight aggregates, enabling a high porosity from 48.6% to 54.0% and comparable mechanical strength to normal sand-incorporated geopolymer (SAG). Moreover, the thermophysical parameters of composites are significantly influenced by both aggregates' properties and the packing pattern. As upon high temperature, the optimized lightweight aggregate incorporated geopolymer (LWAG) capacitates a low thermal diffusivity with a slow temperature gain rate. At the same time, the thermal mismatch within LWAG is alleviated thanks to the high permeability and mechanical weakness of lightweight aggregates. Thus, a reduced microstructural deterioration with better mechanical stability is achieved in LWAG as compared to SAG. Nevertheless, it ultimately results in a significant volumetric shrinkage after 800 ˚C. Herein, increasing the distribution modulus to 0.3 in LWAG potentially decelerates the progression of mechanical degradation and mitigates thermal-induced shrinkage, owing to the low binder gel/aggregate ratio and specific heat transfer pattern.

7.2 Recommendations

Alkali-activated materials are identified as sustainable candidates to substitute traditional Portland cement, offering superior performance in many aspects. In this dissertation, several interrelated topics are explored, including thermal degradation mechanism, gel development, and structural optimization on high temperature resistant geopolymers. Nevertheless, as a promising component in the future construction industry, the practicability, economic advantages, and environmental impact of geopolymer binders remain a topic of ongoing examination. For future research, some general recommendations have surfaced during the course of this dissertation:

- To achieve an adequate activation, the production of geopolymers typically necessitates an external heat curing. This thermal accommodation substantially impedes the widespread use and on-site applications of geopolymers due to technical constraints and production expenses. Thus, innovative technologies are essential to avoid this process. One possible solution involves incorporating calcium sources to accelerate the rate of geopolymerization. Nevertheless, the Ca inclusion can impact the desired geopolymer properties, such as thermal stability, warranting careful consideration.

- The usage of alkaline activators represents another technological barrier to the large-scale application of geopolymer-based materials when taking environmental implications and production costs into consideration. Even though the applied activator alkalinity in the presented research is carefully regulated at a low level, further attempts are encouraged to explore more sustainable solutions that either utilize low/non-alkali activators or waste-based activators. An alternative approach is suggested to re-utilize mineral wool waste, as the silicate source for alkali activator synthesis.

- The developed admixtures comprise industrial wastes and by-products, which potentially contain toxic/heavy metals, and organic compounds. It is imperative to conduct further research to ascertain their long-term environmental implications, for instance, the leaching behavior. Moreover, the manufacturing process of Alkali-activated materials is more intricate when compared to traditional cementitious materials, which encompasses raw material processing, chemical additives, curing, etc. It is urgently needed to conduct a comprehensive life-cycle assessment of the designed products, considering factors such as carbon emissions, energy consumption, and overall costs.

Specific recommendations pertaining to this thesis are outlined below.

7.2.1 Thermal degradation mechanism of geopolymer-based materials

- In this thesis, the conceptual models are proposed to reveal the thermal degradation mechanism of geopolymer-based materials. Notably, the proposed degradation model and mechanism can be robust as applied to a low slag-contained geopolymer ((C,N)-A-S-H gel dominated) system, while the thermal degradation pattern may vary with high slag addition. The increasing slag addition in geopolymer would alter the phase composition and microstructure, hence influencing the thermal behavior, which deserves further investigation.

- To optimize the thermal performance of geopolymers, this thesis examines chemical tailoring and physical design to improve the gel stability and strengthen the structure at elevated temperatures. An alternative effort can be devoted to postponing the adverse impact of degradation of geopolymer-based materials, by enhancing the self-healing effect of geopolymeric gel, such as further geopolymerization reaction.

- In general, the thermal assessment for alkali-activated materials remains diverse, without a universally accepted protocol, in particular the applied heating rate varying from 1 to 10 °C/min in previous studies. Hence, it is essential to establish a standardized protocol for thermal exposure tests, encompassing aspects like pre-treatment, sample size, heating rate, dwelling time, etc., to ensure generality and comparability of the assessments.

7.2.2 Gel development by precursor tailoring

- Weathered ladle slag is applied due to the fact that the majority of ladle slag production in Europe is typically disposed of in landfills or stored in yards. Material consistency can present challenges owing to the complexity of the disposal environment, for instance, the season, weather, humidity, stacking age, etc. For widespread application, it is imperative to establish a standardized protocol for ladle slag processing to ensure consistent quality. On the other hand, there is abundant room for further improving the reactivity of ladle slag by adjusting the processing procedure, such as the cooling method, and environmental humidity. With improved reactivity, the joint activation of ladle slag with Class F fly ash holds the potential to eliminate the need for thermal curing.

- The proposed thermal degradation model offers a comprehensive overview of how gel compatibility affects the thermal behavior of geopolymers. Followingly, the temperature-induced progressive evolution among co-existing geopolymeric gel and Ca-enriched gel needs to be further understood.

- This research proposes a promising route to design a hybrid geopolymer by modifying the compatibility of geopolymeric gel and Ca-enriched gel. Strategies focused on

controlling the co-existence of gels, such as precisely tailoring relative gel content and gel distribution, are encouraged to achieve a desired performance.

7.2.3 Structure optimization by physical design

- The potential of reutilizing mineral wool waste as a co-precursor in the production of hybrid geopolymers is examined at low dosages. To maximize the valorization of mineral wool waste in alkali-activated materials, forthcoming research should explore its incorporation at increased dosages while ensuring matrix homogeneity. It is suggested to either optimize the mixing technology by using an ultra-sonic blender or further adjust the rheology of the mixtures.

- The thermophysical parameters of the designed composites are determined before and after thermal exposure in this thesis. Further exploration into the evolution of thermophysical parameters with increasing temperature is warranted to enhance the comprehensive understanding of heat transfer within geopolymer composites.

- Commercially available lightweight aggregates have demonstrated the capacity to enhance the thermal stability of geopolymer-based material. To attain optimal economic and environmental value, it is recommended to substitute commercial lightweight aggregates with waste-based artificial aggregates, for instance, mineral wool waste-based aggregates.

Bibliography

1. International Association of Fire Services. *World Fire Statistics Report № 27*. https://ctif.org/news/ctif-world-fire-statistics-report-no-27 (2020).
2. McNamee, R. Fire Spalling of Concrete: Theoretical and Experimental Studies. (2013).
3. Kodur, V. Properties of Concrete at Elevated Temperatures. *ISRN Civil Engineering* **2014**, 1–15 (2014).
4. Kodur, V., Kumar, P. & Rafi, M.M. Fire hazard in buildings: review, assessment and strategies for improving fire safety. *PSU Research Review* **4**, 1–23 (2019).
5. Khoury, G.A. Passive fire protection of concrete structures. *Proceedings of the Institution of Civil Engineers - Structures and Buildings* **161**, 135–145 (2008).
6. Alonso, C. & Fernandez, L. Dehydration and rehydration processes of cement paste exposed to high temperature environments. *Journal of Materials Science* **39**, 3015–3024 (2004).
7. Rostásy, F.S., Weiβ, R. & Wiedemann, G. Changes of pore structure of cement mortars due to temperature. *Cement and Concrete Research* **10**, 157–164 (1980).
8. Klima, K.M. *High-temperature resistant geopolymers: composition, microstructure and performance.* (PhD Thesis, Eindhoven University of Technology, 2023).
9. Duxson, P. & Provis, J.L. Designing Precursors for Geopolymer Cements. *Journal of the American Ceramic Society* **91**, 3864–3869 (2008).
10. Provis, J.L. & Bernal, S.A. Geopolymers and Related Alkali-Activated Materials. *Annu. Rev. Mater. Res.* **44**, 299–327 (2014).
11. Sousa, V. & Bogas, J.A. Comparison of energy consumption and carbon emissions from clinker and recycled cement production. *Journal of Cleaner Production* **306**, 127277 (2021).
12. Zhao, J., Tong, L.Y., Li, B., Chen, T.H., Wang, C.P., Yang, G.Q., Zheng, Y. Eco-friendly geopolymer materials: A review of performance improvement, potential application and sustainability assessment. *Journal of Cleaner Production* **307**, 127085 (2021).
13. Provis, J.L. Geopolymers and other alkali activated materials: why, how, and what? *Mater Struct* **47**, 11–25 (2014).
14. Davidovits, J. Properties of Geopolymer Cements (1994).
15. Provis, J.L. Alkali-activated materials. *Cement and Concrete Research* **114**, 40–48 (2018).
16. Davidovits, J. Geopolymers: Inorganic Polymeric New Materials (1991).
17. Duxson, P., Fernández-Jiménez, A., Provis, J.L., Lukey, G.C., Palomo, A., van Deventer, J.S.J. Geopolymer technology: the current state of the art. *Journal of Materials Science* **42**, 2917–2933 (2007).
18. Shi, C., Jiménez, A.F. & Palomo, A. New cements for the 21st century: The pursuit of an alternative to Portland cement. *Cement and Concrete Research* **41**, 750–763 (2011).
19. Bakharev, T. Resistance of geopolymer materials to acid attack. *Cement and Concrete Research* **35**, 658–670 (2005).
20. Tu, W. & Zhang, M. Behaviour of alkali-activated concrete at elevated temperatures: A critical review. *Cement and Concrete Composites* **138**, 104961 (2023).

21. Zhang, J., Provis, J.L., Feng, D. & van Deventer, J.S.J. Geopolymers for immobilization of Cr^{6+}, Cd^{2+}, and Pb^{2+}. *Journal of Hazardous Materials* **157**, 587–598 (2008).
22. Lahoti, M., Tan, K.H. & Yang, E.-H. A critical review of geopolymer properties for structural fire-resistance applications. *Construction and Building Materials* **221**, 514–526 (2019).
23. Rivera, O.G., Long, W.R., Weiss Jr, C.A., Moser, R.D., Williams, B.A., Torres-Cancel, K., Gore, E.R., Allison, P.G. Effect of elevated temperature on alkali-activated geopolymeric binders compared to portland cement-based binders. *Cement and Concrete Research* **90**, 43–51 (2016).
24. Park, S.M., Jang, J.G., Lee, N.K. & Lee, H.K. Physicochemical properties of binder gel in alkali-activated fly ash/slag exposed to high temperatures. *Cement and Concrete Research* **89**, 72–79 (2016).
25. Palomo, A., Krivenko, P., Kavalerova, E., Maltseva, O., Fernández-Jiménez, A. A review on alkaline activation: new analytical perspectives. *Materiales de Construcción* **64**, e022–e022 (2014).
26. Si, R., Guo, S. & Dai, Q. Influence of calcium content on the atomic structure and phase formation of alkali-activated cement binder. *Journal of the American Ceramic Society* **102**, 1479–1494 (2019).
27. Schilling, P.J., Butler, L.G., Roy, A. & Eaton, H.C. ^{29}Si and ^{27}Al MAS-NMR of NaOH-Activated Blast-Furnace Slag. *J American Ceramic Society* **77**, 2363–2368 (1994).
28. Rafeet, A., Vinai, R., Soutsos, M. & Sha, W. Effects of slag substitution on physical and mechanical properties of fly ash-based alkali activated binders (AABs). *Cement and Concrete Research* **122**, 118–135 (2019).
29. Kaja, A.M., Lazaro, A. & Yu, Q.L. Effects of Portland cement on activation mechanism of class F fly ash geopolymer cured under ambient conditions. *Construction and Building Materials* **189**, 1113–1123 (2018).
30. Pan, Z., Tao, Z., Cao, Y.F., Wuhrer, R. & Murphy, T. Compressive strength and microstructure of alkali-activated fly ash/slag binders at high temperature. *Cement and Concrete Composites* **86**, 9–18 (2018).
31. Lee, N.K., Koh, K.T., An, G.H. & Ryu., G.S. Influence of binder composition on the gel structure in alkali activated fly ash/slag pastes exposed to elevated temperatures. *Ceramics International* **43**, 2471–2480 (2017).
32. Luo, Y., Li, S.H., Klima, K.M., Brouwers, H.J.H. & Yu, Q.L. Degradation mechanism of hybrid fly ash/slag based geopolymers exposed to elevated temperatures. *Cement and Concrete Research* **151**, 106649 (2022).
33. Natali Murri, A., Rickard, W.D.A., Bignozzi, M.C. & van Riessen, A. High temperature behaviour of ambient cured alkali-activated materials based on ladle slag. *Cement and Concrete Research* **43**, 51–61 (2013).
34. Adediran, A., Yliniemi, J., Moukannaa, S., Ramteke, D.D., Perumal, P., Illikainen, M. Enhancing the thermal stability of alkali-activated Fe-rich fayalite slag-based mortars by incorporating ladle and blast furnace slags: Physical, mechanical and structural changes. *Cement and Concrete Research* **166**, 107098 (2023).
35. Jiang, X., Xiao, R., Ma, Y.T., Zhang, M.M., Bai, Y., Huang, B.S. Influence of waste glass powder on the physico-mechanical properties and microstructures of fly ash-based geopolymer paste after exposure to high temperatures. *Construction and Building Materials* **262**, 120579 (2020).
36. Adesanya, E., Ohenoja, K., Kinnunen, P. & Illikainen, M. Alkali Activation of Ladle Slag from Steel-Making Process. *J. Sustain. Metall.* **3**, 300–310 (2017).
37. Adolfsson, D., Robinson, R., Engström, F. & Björkman, B. Influence of mineralogy on the hydraulic

properties of ladle slag. *Cement and Concrete Research* **41**, 865–871 (2011).

38. Serjun, V.Z., Mirti, B. & Mladenovi, A. Evaluation of ladle slag as a potential material for building and civil engineering. *Materiali in tehnologije* 8 (2013).
39. Bignozzi, M.C., Manzi, S., Lancellotti, L., Kamseu, E., Barbieri, L., Leonelli, C. Mix-design and characterization of alkali activated materials based on metakaolin and ladle slag. *Applied Clay Science* **73**, 78–85 (2013).
40. Papayianni, I., Konopisi, S. & Kesikidou, F. Physico-Mechanical Properties and Durability Aspects of Alkali-Activated Calcareous Fly Ash/Slag Mortars. *Key Engineering Materials* **761**, 87-91 (2018).
41. Ducman, V. & Mladenovič, A. The potential use of steel slag in refractory concrete. *Materials Characterization* **62**, 716–723 (2011).
42. Ranjbar, N. Fiber-reinforced geopolymer composites: A review. *Cement and Concrete Composites* 19 (2020).
43. Bangi, M.R. & Horiguchi, T. Pore pressure development in hybrid fibre-reinforced high strength concrete at elevated temperatures. *Cement and Concrete Research* **41**, 1150–1156 (2011).
44. Ríos, J.D., Leiva, C., Ariza, M.P., Seitl, S. & Cifuentes, H. Analysis of the tensile fracture properties of ultra-high-strength fiber-reinforced concrete with different types of steel fibers by X-ray tomography. *Materials & Design* **165**, 107582 (2019).
45. Wu, H., Lin, X. & Zhou, A. A review of mechanical properties of fibre reinforced concrete at elevated temperatures. *Cement and Concrete Research* **135**, 106117 (2020).
46. Zhang, P., Kang, L.Y., Wang, K., Guo, J.J., Hu, S.W., Ling, Y.F. Mechanical Properties and Explosive Spalling Behavior of Steel-Fiber-Reinforced Concrete Exposed to High Temperature—A Review. *Applied Sciences* **10**, 2324 (2020).
47. Ranjbar, N., Mehrali, M., Behnia, A., Javadi Pordsari, A., Mehrali, A. A Comprehensive Study of the Polypropylene Fiber Reinforced Fly Ash Based Geopolymer. *PLoS ONE* **11**, e0147546 (2016).
48. Kong, D.L.Y. & Sanjayan, J.G. Effect of elevated temperatures on geopolymer paste, mortar and concrete. *Cement and Concrete Research* **40**, 334–339 (2010).
49. Kong, D.L.Y. & Sanjayan, J.G. Damage behavior of geopolymer composites exposed to elevated temperatures. *Cement and Concrete Composites* **30**, 986–991 (2008).
50. Rickard, W.D.A., Gluth, G.J.G. & Pistol, K. In-situ thermo-mechanical testing of fly ash geopolymer concretes made with quartz and expanded clay aggregates. *Cement and Concrete Research* **80**, 33–43 (2016).
51. Pan, Z., Tao, Z., Cao, Y.-F. & Wuhrer, R. Measurement and prediction of thermal properties of alkali-activated fly ash/slag binders at elevated temperatures. *Mater Struct* **51**, 108 (2018).
52. Fernández-Jiménez, A., Palomo, A., Pastor, J.Y. & Martín, A. New Cementitious Materials Based on Alkali-Activated Fly Ash: Performance at High Temperatures. *Journal of the American Ceramic Society* **91**, 3308–3314 (2008).
53. Aziz, I.H., Al Bakri Abdullah, M., Yong, H.C., Ming, L.Y., Hussin, K., Surleva, A., Azimi, E.A. Manufacturing parameters influencing fire resistance of geopolymers: A review. *Proceedings of the IMechE* **233**, 721–733 (2019).
54. Kong, D.L.Y., Sanjayan, J.G. & Sagoe-Crentsil, K. Comparative performance of geopolymers made with metakaolin and fly ash after exposure to elevated temperatures. *Cement and Concrete Research* **37**, 1583–1589

(2007).

55. Luukkonen, T., Abdollahnejad, Z., Yliniemi, J., Kinnunen, P. & Illikainen, M. One-part alkali-activated materials: A review. *Cement and Concrete Research* **103**, 21–34 (2018).
56. Davidovits, J. Geopolymers and geopolymeric materials. *Journal of Thermal Analysis* **35**, 429–441 (1989).
57. Büchler, C. Fire safety in industrial buildings and nuclear power plants with air-filters made of geopolymer composite. *Second International Conference Geopolymere* 181–188 (1999).
58. Cheng, T.W. & Chiu, J.P. Fire-resistant geopolymer produced by granulated blast furnace slag. *Minerals Engineering* **16**, 205–210 (2003).
59. Buchwald, A., Hohmann, M., Kaps, Ch., Bettzieche, H. & Kühnert, J.-Th. Stabilised foam clay material with high performance thermal insulation properties. *CFI Ceramic Forum International* **81**, E39–E42 (2004).
60. Rickard, W.D.A. & Van Riessen, A. Performance of solid and cellular structured fly ash geopolymers exposed to a simulated fire. *Cement and Concrete Composites* **48**, 75–82 (2014).
61. García, J.I.E., Campos-Venegas, K., Gorokhovsky, A. & Fernández, A. Cementitious composites of pulverised fuel ash and blast furnace slag activated by sodium silicate: effect of Na_2O concentration and modulus. *Advances in Applied Ceramics* **105**, 201–208 (2006).
62. Gao, X., Yu, Q.L. & Brouwers, H.J.H. Reaction kinetics, gel character and strength of ambient temperature cured alkali activated slag–fly ash blends. *Construction and Building Materials* **80**, 105–115 (2015).
63. Samantasinghar, S. & Singh, S. Effects of curing environment on strength and microstructure of alkali-activated fly ash-slag binder. *Construction and Building Materials* **235**, 117481 (2020).
64. Ismail, I., Bernal, S.A., Provis, J.L., San Nicolas, R., Hamdan, S., van Deventer, J.S.J. Modification of phase evolution in alkali-activated blast furnace slag by the incorporation of fly ash. *Cement and Concrete Composites* **45**, 125–135 (2014).
65. Gao, X., Yu, Q.L. & Brouwers, H.J.H. Apply ^{29}Si, ^{27}Al MAS NMR and selective dissolution in identifying the reaction degree of alkali activated slag-fly ash composites. *Ceramics International* **43**, 12408–12419 (2017).
66. Ye, H. & Radlińska, A. Fly ash-slag interaction during alkaline activation: Influence of activators on phase assemblage and microstructure formation. *Construction and Building Materials* **122**, 594–606 (2016).
67. Çelikten, S., Sarıdemir, M. & Özgür Deneme, İ. Mechanical and microstructural properties of alkali-activated slag and slag + fly ash mortars exposed to high temperature. *Construction and Building Materials* **217**, 50–61 (2019).
68. Guerrieri, M. & Sanjayan, J.G. Behavior of combined fly ash/slag-based geopolymers when exposed to high temperatures. *Fire and Materials* **34**, 163–175 (2010).
69. Lahoti, M., Wong, K.K., Tan, K.H. & Yang, E.-H. Effect of alkali cation type on strength endurance of fly ash geopolymers subject to high temperature exposure. *Materials & Design* **154**, 8–19 (2018).
70. Lahoti, M., Wijaya, S.F., Tan, K.H. & Yang, E.-H. Tailoring sodium-based fly ash geopolymers with variegated thermal performance. *Cement and Concrete Composites* **107**, 103507 (2020).
71. Sabbatini, A., Vidal, L., Pettinari, C., Sobrados, I. & Rossignol, S. Control of shaping and thermal resistance of metakaolin-based geopolymers. *Materials & Design* **116**, 374–385 (2017).

72. Rickard, W.D.A., Kealley, C.S. & Riessen, A. van. Thermally Induced Microstructural Changes in Fly Ash Geopolymers: Experimental Results and Proposed Model. *Journal of the American Ceramic Society* **98**, 929–939 (2015).
73. Dudek, M. & Sitarz, M. Analysis of Changes in the Microstructure of Geopolymer Mortar after Exposure to High Temperatures. *Materials* **13**, 4263 (2020).
74. Gao, X., Yu, Q.L., Lazaro, A. & Brouwers, H.J.H. Investigation on a green olivine nano-silica source based activator in alkali activated slag-fly ash blends: Reaction kinetics, gel structure and carbon footprint. *Cement and Concrete Research* **100**, 129–139 (2017).
75. Zhuang, X.Y., Chen, L., Komarneni, S., Zhou, C.H., Tong, D.S. Fly ash-based geopolymer: clean production, properties and applications. *Journal of Cleaner Production* **125**, 253–267 (2016).
76. Qu, F., Li, W., Tao, Z., Castel, A. & Wang, K. High temperature resistance of fly ash/GGBFS-based geopolymer mortar with load-induced damage. *Mater Struct* **53**, 111 (2020).
77. Fan, F., Liu, Z., Xu, G., Peng, H. & Cai, C.S. Mechanical and thermal properties of fly ash based geopolymers. *Construction and Building Materials* **160**, 66–81 (2018).
78. Cai, R. & Ye, H. Clinkerless ultra-high strength concrete based on alkali-activated slag at high temperatures. *Cement and Concrete Research* **145**, 106465 (2021).
79. Bakharev, T. Thermal behaviour of geopolymers prepared using class F fly ash and elevated temperature curing. *Cement and Concrete Research* **36**, 1134–1147 (2006).
80. Kong, D.L.Y. & Sanjayan, J.G. Effect of elevated temperatures on geopolymer paste, mortar and concrete. *Cement and Concrete Research* **40**, 334–339 (2010).
81. Griffiths, L., Heap, M.J., Baud, P. & Schmittbuhl, J. Quantification of microcrack characteristics and implications for stiffness and strength of granite. *International Journal of Rock Mechanics and Mining Sciences* **100**, 138–150 (2017).
82. Arena, A., Delle Piane, C. & Sarout, J. A new computational approach to cracks quantification from 2D image analysis: Application to micro-cracks description in rocks. *Computers & Geosciences* **66**, 106–120 (2014).
83. Delle Piane, C., Arena, A., Sarout, J., Esteban, L. & Cazes, E. Micro-crack enhanced permeability in tight rocks: An experimental and microstructural study. *Tectonophysics* **665**, 149–156 (2015).
84. Etter, D.M. *Introduction to MATLAB*. (Prentice Hall, 2011).
85. ASTM C597-16. *Test Method for Pulse Velocity Through Concrete*. Book of Standards Volume: 04.02: Developed by Subcommittee C09.64 (2016)
86. British Standards Institution: London. *Methods of testing cement. Part 1, Part 1*. (2016).
87. Yip, C.K., Lukey, G.C. & van Deventer, J.S.J. The coexistence of geopolymeric gel and calcium silicate hydrate at the early stage of alkaline activation. *Cement and Concrete Research* **35**, 1688–1697 (2005).
88. Nasr, D., Pakshir, A.H. & Ghayour, H. The influence of curing conditions and alkaline activator concentration on elevated temperature behavior of alkali activated slag (AAS) mortars. *Construction and Building Materials* **190**, 108–119 (2018).
89. Glover, P.W.J., Baud, P., Darot, M., Meredith, P.G., Boon, S.A., LeRavalec, M., Zoussi, S., Reuschlé, T. α/β phase transition in quartz monitored using acoustic emissions. *Geophys J Int* **120**, 775–782 (1995).

90. Bernal, S.A., de Gutierrez, R.M., Provis, J.L. & Rose, V. Effect of silicate modulus and metakaolin incorporation on the carbonation of alkali silicate-activated slags. *Cement and Concrete Research* **40**, 898–907 (2010).
91. Gao, X., Yu, Q.L. & Brouwers, H.J.H. Reaction kinetics, gel character and strength of ambient temperature cured alkali activated slag–fly ash blends. *Construction and Building Materials* **80**, 105–115 (2015).
92. Rovnaník, P., Bayer, P. & Rovnaníková, P. Characterization of alkali activated slag paste after exposure to high temperatures. *Construction and Building Materials* **47**, 1479–1487 (2013).
93. Rickard, W.D.A., Temuujin, J. & van Riessen, A. Thermal analysis of geopolymer pastes synthesised from five fly ashes of variable composition. *Journal of Non-Crystalline Solids* **358**, 1830–1839 (2012).
94. Anovitz, L.M. & Cole, D.R. Characterization and Analysis of Porosity and Pore Structures. *Reviews in Mineralogy and Geochemistry* **80**, 61–164 (2015).
95. Diamond, S. Mercury porosimetry: An inappropriate method for the measurement of pore size distributions in cement-based materials. *Cement and Concrete Research* **30**, 1517–1525 (2000).
96. Ma, H. Mercury intrusion porosimetry in concrete technology: tips in measurement, pore structure parameter acquisition and application. *J Porous Mater* **21**, 207–215 (2014).
97. Zeng, Q., Li, K., Fen-chong, T. & Dangla, P. Pore structure characterization of cement pastes blended with high-volume fly-ash. *Cement and Concrete Research* **42**, 194–204 (2012).
98. Aligizaki, K.K. *Pore Structure of Cement-Based Materials: Testing, Interpretation and Requirements*. (CRC Press, 2005).
99. Everett, D.H. Manual of Symbols and Terminology for Physicochemical Quantities and Units, Appendix II: Definitions, Terminology and Symbols in Colloid and Surface Chemistry. *Pure and Applied Chemistry* **31**, 577–638 (1972).
100. Lee, N.K., Jang, J.G. & Lee, H.K. Shrinkage characteristics of alkali-activated fly ash/slag paste and mortar at early ages. *Cement and Concrete Composites* **53**, 239–248 (2014).
101. Qu, Z.Y., Yu, Q., Ji, Y.D., Gauvin, F. & Voets, I.K. Mitigating shrinkage of alkali activated slag with biofilm. *Cement and Concrete Research* **138**, 106234 (2020).
102. Ye, H., Cartwright, C., Rajabipour, F. & Radlińska, A. Understanding the drying shrinkage performance of alkali-activated slag mortars. *Cement and Concrete Composites* **76**, 13–24 (2017).
103. Fernández-Jiménez, A., Pastor, J.Y., Martín, A. & Palomo, A. High-Temperature Resistance in Alkali-Activated Cement. *Journal of the American Ceramic Society* **93**, 3411–3417 (2010).
104. Behfarnia, K. & Shahbaz, M. The effect of elevated temperature on the residual tensile strength and physical properties of the alkali-activated slag concrete. *Journal of Building Engineering* **20**, 442–454 (2018).
105. Hertz, K.D. Limits of spalling of fire-exposed concrete. *Fire Safety Journal* **38**, 103–116 (2003).
106. Gao, X., Yu, Q.L. & Brouwers, H.J.H. Apply ^{29}Si, ^{27}Al MAS NMR and selective dissolution in identifying the reaction degree of alkali activated slag-fly ash composites. *Ceramics International* **43**, 12408–12419 (2017).
107. Kourounis, S., Tsivilis, S., Tsakiridis, P.E., Papadimitriou, G.D. & Tsibouki, Z. Properties and hydration of blended cements with steelmaking slag. *Cement and Concrete Research* **37**, 815–822 (2007).
108. Midgley, H.G. & Midgley, A. The conversion of high alumina cement. *Magazine of Concrete Research* (2015)

doi:10.1680/macr.1975.27.91.59.

109. Matusinović, T., Šipušić, J. & Vrbos, N. Porosity–strength relation in calcium aluminate cement pastes. *Cement and Concrete Research* **33**, 1801–1806 (2003).
110. Torréns-Martín, D., Fernández-Carrasco, L. & Martínez-Ramírez, S. Hydration of calcium aluminates and calcium sulfoaluminate studied by Raman spectroscopy. *Cement and Concrete Research* **47**, 43–50 (2013).
111. Scrivener, K.L., Cabiron, J.-L. & Letourneux, R. High-performance concretes from calcium aluminate cements. *Cement and Concrete Research* **29**, 1215–1223 (1999).
112. Adesanya, E., Karhu, M., Ismailov, A., Ohenoja, K., Kinnunen, P., Illikainen, M. Thermal behaviour of ladle slag mortars containing ferrochrome slag aggregates. *Advances in Cement Research* **33**, 168–182 (2021).
113. British Standards Institution: London. BS EN 1015-3 : Methods of test for mortar for masonry - Part 3: Determination of consistence of fresh mortar (by flow table). (1999).
114. Williamson, T. & Juenger, M.C.G. The role of activating solution concentration on alkali–silica reaction in alkali-activated fly ash concrete. *Cement and Concrete Research* **83**, 124–130 (2016).
115. Fernández-Jiménez, A., Palomo, A., Vazquez, T., Vallepu, R., Terai, T., Ikeda, K. Alkaline Activation of Blends of Metakaolin and Calcium Aluminate. *Journal of the American Ceramic Society* **91**, 1231–1236 (2008).
116. Pommersheim, J. & Chang, J. Kinetics of hydration of tricalcium aluminate. *Cement and Concrete Research* **16**, 440–450 (1986).
117. Majumbar, A.J., Singh, B. & Edmonds, R.N. Hydration of mixtures of $C_{12}A_7$ and granulated blastfurnace slag. *Cement and Concrete Research* **19**, 848–856 (1989).
118. Corstanje, W.A., Stein, H.N. & Stevels, J.M. Hydration reactions in pastes $C_3S+C_3A+CaSO_4.2aq+H_2O$ at 25°C. *Cement and Concrete Research* **3**, 791–806 (1973).
119. Setién, J., Hernández, D. & González, J.J. Characterization of ladle furnace basic slag for use as a construction material. *Construction and Building Materials* **23**, 1788–1794 (2009).
120. Adesanya, E., Sreenivasan, H., Kantola, A.M., Telkki, V.V., Ohenoja, K., Kinnunen, P., Illikainen, M. Ladle slag cement – Characterization of hydration and conversion. *Construction and Building Materials* **193**, 128–134 (2018).
121. Ukrainczyk, N., Matusinovic, T., Kurajica, S., Zimmermann, B. & Sipusic, J. Dehydration of a layered double hydroxide—C_2AH_8. *Thermochimica Acta* **464**, 7–15 (2007).
122. Bushnell-Watson, S.M. & Sharp, J.H. The application of thermal analysis to the hydration and conversión Reactions of calcium alumínate Cements. *materconstrucc* **42**, 13–32 (1992).
123. Nonnet, E., Lequeux, N. & Boch, P. Elastic properties of high alumina cement castables from room temperature to 1600°C. *Journal of the European Ceramic Society* **19**, 1575–1583 (1999).
124. Yuan, B., Yu, Q.L. & Brouwers, H.J.H. Assessing the chemical involvement of limestone powder in sodium carbonate activated slag. *Mater Struct* **50**, 136 (2017).
125. Rozov, K., Berner, U., Taviot-Gueho, C., Leroux, F., Renaudin, G., Kulik, D., Diamond, L.W. Synthesis and characterization of the LDH hydrotalcite–pyroaurite solid-solution series. *Cement and Concrete Research* **40**, 1248–1254 (2010).
126. Ukrainczyk, N., Matusinovic, T., Kurajica, S., Zimmermann, B. & Sipusic, J. Dehydration of a layered double hydroxide—C_2AH_8. *Thermochimica Acta* **464**, 7–15 (2007).

127. Fernández-Carrasco, L. Blanco-Varela, M.T. Puertas, F. Vázquez, T. Glasser, F.P. Lachowski, E. Hydration of high alumina cement in the presence of alkalis. *Advances in Cement Research* **12**, 143–152 (2000).

128. Pastor, C., Fernández-Jiménez, A., Vázquez, T. & Palomo, Á. Calcium aluminate cement hydration in a high alkalinity environment. *Materiales de Construcción* **59**, 21–34 (2009).

129. Bernal, S.A., Provis, J.L., Rose, V. & Mejía de Gutierrez, R. Evolution of binder structure in sodium silicate-activated slag-metakaolin blends. *Cement and Concrete Composites* **33**, 46–54 (2011).

130. Sun, Z. & Vollpracht, A. Isothermal calorimetry and in-situ XRD study of the NaOH activated fly ash, metakaolin and slag. *Cement and Concrete Research* **103**, 110–122 (2018).

131. Chithiraputhiran, S. & Neithalath, N. Isothermal reaction kinetics and temperature dependence of alkali activation of slag, fly ash and their blends. *Construction and Building Materials* **45**, 233–242 (2013).

132. Jiang, C., Wang, A., Bao, X., Ni, T. & Ling, J. A review on geopolymer in potential coating application: Materials, preparation and basic properties. *Journal of Building Engineering* **32**, 101734 (2020).

133. Fernández-Jiménez, A. & Palomo, A. Mid-infrared spectroscopic studies of alkali-activated fly ash structure. *Microporous and Mesoporous Materials* **86**, 207–214 (2005).

134. Ashrit, S., Chatti, R.V., Sarkar, S., Venugopal, R. & Nair, U.G. An infrared spectroscopic study of non-metallic portion of Linz-Donawitz slag fines generated at Tata Steel, Jamshedpur. *Metall. Res. Technol.* **115**, 608 (2018).

135. Schroeder, R.A. & Lyons, L.L. Infra-red spectra of the crystalline inorganic aluminates. *Journal of Inorganic and Nuclear Chemistry* **28**, 1155–1163 (1966).

136. Zapata, J.F., Gomez, M. & Colorado, H.A. Structure-property relation and Weibull analysis of calcium aluminate cement pastes. *Materials Characterization* **134**, 9–17 (2017).

137. Maitra, S., Bose, S., Bandyopadhyay, N. & Roychoudhury, A. Dehydration kinetics of calcium aluminate cement hydrate under non-isothermal conditions. *Ceramics International* **31**, 371–374 (2005).

138. Soleimani, M.A., Naghizadeh, R., Mirhabibi, A. & Golestanifard, F. The influence of phosphorus slag addition on microstructure and mechanical properties of metakaolin-based geopolymer pastes. *Ceramics - Silikaty* **57**, 33–38 (2013).

139. Kani, E.N. & Mehdizadeh, H. Investigating Gel Molecular Structure and Its Relation with Mechanical Strength in Geopolymer Cement Based on Natural Pozzolan Using In Situ ATR-FTIR Spectroscopy. *Journal of Materials in Civil Engineering* **29**, 04017078 (2017).

140. Alarcon-Ruiz, L., Platret, G., Massieu, E. & Ehrlacher, A. The use of thermal analysis in assessing the effect of temperature on a cement paste. *Cement and Concrete Research* **35**, 609–613 (2005).

141. Payá, J., Monzó, J., Borrachero, M.V., Perris, E. & Amahjour, F. Thermogravimetric Methods for Determining Carbon Content in Fly Ashes. *Cement and Concrete Research* **28**, 675–686 (1998).

142. Fernández-Jiménez, A., Vázquez, T. & Palomo, A. Effect of Sodium Silicate on Calcium Aluminate Cement Hydration in Highly Alkaline Media: A Microstructural Characterization. *Journal of the American Ceramic Society* **94**, 1297–1303 (2011).

143. Li, L., Liu, W.F., You, Q.X., Chen, M.C., Zeng, Q., Zhou, C.S., Zhang, M.Z. Relationships between microstructure and transport properties in mortar containing recycled ceramic powder. *Journal of Cleaner Production* **263**, 121384 (2020).

144. Choi, S., Kim, J.-M., Han, D. & Kim, J.-H. Hydration properties of ladle furnace slag powder rapidly cooled by air. *Construction and Building Materials* **113**, 682–690 (2016).

145. Mehta, P.K., Monteiro, P.J.M. *Concrete: Microstructure, Properties, and Materials*. (McGraw-Hill Professional., 2014).

146. Adesanya, E., Ohenoja, K., Kinnunen, P. & Illikainen, M. Properties and durability of alkali-activated ladle slag. *Mater Struct* **50**, 255 (2017).

147. Kaja, A.M., Schollbach, K., Melzer, S., van der Laan, S.R., Brouwers, H.J.H., Yu, Q.L. Hydration of potassium citrate-activated BOF slag. *Cement and Concrete Research* **140**, 106291 (2021).

148. Van Riessen, A., Rickard, W. & Sanjayan, J. 15 - Thermal properties of geopolymers. in *Geopolymers* (eds. Provis, J.L. & van Deventer, J.S.J.) 315–342 (Woodhead Publishing, 2009).

149. Dombrowski, K., Buchwald, A. & Weil, M. The influence of calcium content on the structure and thermal performance of fly ash based geopolymers. *J Mater Sci* **42**, 3033–3043 (2007).

150. Wang, W.-C., Wang, H.-Y. & Tsai, H.-C. Study on engineering properties of alkali-activated ladle furnace slag geopolymer. *Construction and Building Materials* **123**, 800–805 (2016).

151. Mostafa, N.Y., Zaki, Z.I. & Abd Elkader, O.H. Chemical activation of calcium aluminate cement composites cured at elevated temperature. *Cement and Concrete Composites* **34**, 1187–1193 (2012).

152. Ding, J., Fu, Y. & Beaudoin, J.J. Study of hydration mechanisms in the high alumina cement - sodium silicate system. *Cement and Concrete Research* **26**, 799–804 (1996).

153. Rivas Mercury, J.M., Turrillas, X., de Aza, A.H. & Pena, P. Calcium aluminates hydration in presence of amorphous SiO_2 at temperatures below 90°C. *Journal of Solid State Chemistry* **179**, 2988–2997 (2006).

154. Shi, C., Roy, D. & Krivenko, P. *Alkali-Activated Cements and Concretes*. (CRC Press, 2014).

155. Frías, M. & Cabrera, J. Influence of MK on the reaction kinetics in MK/lime and MK-blended cement systems at 20°C. *Cement and Concrete Research* **31**, 519–527 (2001).

156. Ul Haq, E., Kunjalukkal Padmanabhan, S. & Licciulli, A. Synthesis and characteristics of fly ash and bottom ash based geopolymers–A comparative study. *Ceramics International* **40**, 2965–2971 (2014).

157. Alonso, S. & Palomo, A. Calorimetric study of alkaline activation of calcium hydroxide–metakaolin solid mixtures. *Cement and Concrete Research* **31**, 25–30 (2001).

158. Cabrera, J. & Rojas, M.F. Mechanism of hydration of the metakaolin–lime–water system. *Cement and Concrete Research* **31**, 177–182 (2001).

159. Provis, J.L. Alkali-activated materials. *Cement and Concrete Research* **114**, 40–48 (2018).

160. Provis, J.L., Palomo, A. & Shi, C. Advances in understanding alkali-activated materials. *Cement and Concrete Research* **78**, 110–125 (2015).

161. Duxson, P., Fernández-Jiménez, A., Provis, J.L., Lukey, G.C., Palomo, A., van Deventer, J.S.J. Geopolymer technology: the current state of the art. *Journal of Materials Science* **42**, 2917–2933 (2007).

162. Van Jaarsveld, J.G.S., Van Deventer, J.S.J. & Schwartzman, A. The potential use of geopolymeric materials to immobilise toxic metals: Part II. Material and leaching characteristics. *Minerals Engineering* **12**, 75–91 (1999).

163. Li, C., Sun, H. & Li, L. A review: The comparison between alkali-activated slag (Si+Ca) and metakaolin (Si+Al) cements. *Cement and Concrete Research* **40**, 1341–1349 (2010).

164. García-Lodeiro, I., Fernández-Jiménez, A. & Palomo, A. Variation in hybrid cements over time. Alkaline activation of fly ash–portland cement blends. *Cement and Concrete Research* **52**, 112–122 (2013).

165. Granizo, M.L., Alonso, S., Blanco-Varela, M.T. & Palomo, A. Alkaline Activation of Metakaolin: Effect of Calcium Hydroxide in the Products of Reaction. *Journal of the American Ceramic Society* **85**, 225–231 (2002).

166. Yip, C.K., Lukey, G.C., Provis, J.L. & van Deventer, J.S.J. Effect of calcium silicate sources on geopolymerisation. *Cement and Concrete Research* **38**, 554–564 (2008).

167. García-Lodeiro, I., Fernández-Jiménez, A., Palomo, A. & Macphee, D.E. Effect of Calcium Additions on N–A–S–H Cementitious Gels. *Journal of the American Ceramic Society* **93**, 1934–1940 (2010).

168. Bernal, S.A., Gutiérrez, R.M. de, Ruiz, F., Quiñones, H. & Provis, J.L. High-temperature performance of mortars and concretes based on alkali-activated slag/metakaolin blends. *Materiales de Construcción* **62**, 471–488 (2012).

169. Bernal, S.A., Rodríguez, E.D., Mejía de Gutiérrez, R., Gordillo, M. & Provis, J.L. Mechanical and thermal characterisation of geopolymers based on silicate-activated metakaolin/slag blends. *Journal of Materials Science* **46**, 5477–5486 (2011).

170. Najm, O., El-Hassan, H. & El-Dieb, A. Ladle slag characteristics and use in mortar and concrete: A comprehensive review. *Journal of Cleaner Production* **288**, 125584 (2021).

171. Adolfsson, D., Robinson, R., Engström, F. & Björkman, B. Influence of mineralogy on the hydraulic properties of ladle slag. *Cement and Concrete Research* **41**, 865–871 (2011).

172. Shi, C. Characteristics and cementitious properties of ladle slag fines from steel production. *Cement and Concrete Research* **32**, 459–462 (2002).

173. Fernández-Jiménez, A., Vázquez, T. & Palomo, A. Effect of Sodium Silicate on Calcium Aluminate Cement Hydration in Highly Alkaline Media: A Microstructural Characterization. *Journal of the American Ceramic Society* **94**, 1297–1303 (2011).

174. Luo, Y., Klima, K.M., Brouwers, H.J.H. & Yu, Q.L. Effects of ladle slag on Class F fly ash geopolymer: Reaction mechanism and high temperature behavior. *Cement and Concrete Composites* **129**, 104468 (2022).

175. British Standards Institution: London. *Methods of testing cement. Part 1, Part 3*. (2016).

176. van Hoek, C., Small, J. & van der Laan, S. Large-Area Phase Mapping Using PhAse Recognition and Characterization (PARC) Software. *Microscopy Today* **24**, 12–21 (2016).

177. Scrivener, K., Snellings, R., Lothenbach, B. *A Practical Guide to Microstructural Analysis of Cementitious Materials*. (CRC Press, 2018).

178. Zhang, P., Zheng, Y., Wang, K. & Zhang, J. A review on properties of fresh and hardened geopolymer mortar. *Composites Part B: Engineering* **152**, 79–95 (2018).

179. Sun, B., Sun, Y., Ye, G. & De Schutter, G. A mix design methodology of slag and fly ash-based alkali-activated paste. *Cement and Concrete Composites* **126**, 104368 (2022).

180. Kaja, A.M., Lazaro, A. & Yu, Q.L. Effects of Portland cement on activation mechanism of class F fly ash geopolymer cured under ambient conditions. *Construction and Building Materials* **189**, 1113–1123 (2018).

181. Dron, R. & Brivot, F. Thermodynamic and kinetic approach to the alkali-silica reaction. Part 1: Concepts. *Cement and Concrete Research* **22**, 941–948 (1992).

182. Adolfsson, D., Robinson, R., Engström, F. & Björkman, B. Influence of mineralogy on the hydraulic properties of ladle slag. *Cement and Concrete Research* **41**, 865–871 (2011).

183. Bernal, S.A., Provis, J.L., Rose, V. & Mejía de Gutierrez, R. Evolution of binder structure in sodium silicate-activated slag-metakaolin blends. *Cement and Concrete Composites* **33**, 46–54 (2011).

184. Zhang, S., Li, Z., Ghiassi, B., Yin, S. & Ye, G. Fracture properties and microstructure formation of hardened alkali-activated slag/fly ash pastes. *Cement and Concrete Research* **144**, 106447 (2021).

185. Ye, N., Yang, J.K., Ke, X.Y., Zhu, J., Li, Y.L., Xiang, C., Wang, H.B., Li, L. Synthesis and Characterization of Geopolymer from Bayer Red Mud with Thermal Pretreatment. *Journal of the American Ceramic Society* **97**, 1652–1660 (2014).

186. Thiery, M., Villain, G., Dangla, P. & Platret, G. Investigation of the carbonation front shape on cementitious materials: Effects of the chemical kinetics. *Cement and Concrete Research* **37**, 1047–1058 (2007).

187. Abdalqader, A.F., Jin, F. & Al-Tabbaa, A. Characterisation of reactive magnesia and sodium carbonate-activated fly ash/slag paste blends. *Construction and Building Materials* **93**, 506–513 (2015).

188. Hajimohammadi, A., Provis, J.L. & van Deventer, J.S.J. The effect of silica availability on the mechanism of geopolymerisation. *Cement and Concrete Research* **41**, 210–216 (2011).

189. Reig, F. FTIR quantitative analysis of calcium carbonate (calcite) and silica (quartz) mixtures using the constant ratio method. Application to geological samples. *Talanta* **58**, 811–821 (2002).

190. Rađenović, A., Malina, J. & Sofilić, T. Characterization of Ladle Furnace Slag from Carbon Steel Production as a Potential Adsorbent. *Advances in Materials Science and Engineering* vol. 2013.

191. Wang, J., Hu, Z.L., Chen, Y., Huang, J.L., Ma, Y.F., Zhu, W.W., Liu, J.P. Effect of Ca/Si and Al/Si on micromechanical properties of C(-A)-S-H. *Cement and Concrete Research* **157**, 106811 (2022).

192. García Lodeiro, I., Macphee, D.E., Palomo, A. & Fernández-Jiménez, A. Effect of alkalis on fresh C–S–H gels. FTIR analysis. *Cement and Concrete Research* **39**, 147–153 (2009).

193. Puligilla, S. & Mondal, P. Co-existence of aluminosilicate and calcium silicate gel characterized through selective dissolution and FTIR spectral subtraction. *Cement and Concrete Research* **70**, 39–49 (2015).

194. Walkley, B., San Nicolas, R., Sani, M.C., Rees, G.J., Hanna, J.V., van Deventer, J.S.J., Provis, J.L. Phase evolution of C-(N)-A-S-H/N-A-S-H gel blends investigated via alkali-activation of synthetic calcium aluminosilicate precursors. *Cement and Concrete Research* **89**, 120–135 (2016).

195. Garcia-Lodeiro, I., Palomo, A., Fernández-Jiménez, A. & Macphee, D.E. Compatibility studies between N-A-S-H and C-A-S-H gels. Study in the ternary diagram Na_2O–CaO–Al_2O_3–SiO_2–H_2O. *Cement and Concrete Research* **41**, 923–931 (2011).

196. Ma, Y. & Ye, G. The shrinkage of alkali activated fly ash. *Cement and Concrete Research* **68**, 75–82 (2015).

197. Duxson, P., Provis, J.L., Lukey, G.C., Mallicoat, S.H., Kriven, W.M., van Deventer, J.S.J. Understanding the relationship between geopolymer composition, microstructure and mechanical properties. *Colloids and Surfaces A: Physicochemical and Engineering Aspects* **269**, 47–58 (2005).

198. Zheng, L., Wang, W. & Shi, Y. The effects of alkaline dosage and Si/Al ratio on the immobilization of heavy metals in municipal solid waste incineration fly ash-based geopolymer. *Chemosphere* **79**, 665–671 (2010).

199. Sun, B., Ye, G. & de Schutter, G. A review: Reaction mechanism and strength of slag and fly ash-based

alkali-activated materials. *Construction and Building Materials* **326**, 126843 (2022).

200. Klima, K.M., Schollbach, K., Brouwers, H.J.H. & Yu, Q.L. Enhancing the thermal performance of Class F fly ash-based geopolymer by sodalite. *Construction and Building Materials* **314**, 125574 (2022).
201. Klima, K.M., Schollbach, K., Brouwers, H.J.H. & Yu, Q.L. Thermal and fire resistance of Class F fly ash based geopolymers – A review. *Construction and Building Materials* **323**, 126529 (2022).
202. Pan, Z. & Sanjayan, J.G. Factors influencing softening temperature and hot-strength of geopolymers. *Cement and Concrete Composites* **34**, 261–264 (2012).
203. Lahoti, M., Wong, K.K., Yang, E.-H. & Tan, K.H. Effects of Si/Al molar ratio on strength endurance and volume stability of metakaolin geopolymers subject to elevated temperature. *Ceramics International* **44**, 5726–5734 (2018).
204. Yan, D., Zhang, Y.J., Chen, S.K., Fazli, H., Liu, Y., Ao, Y. Effect of Silica Moduli on the Thermal Degradation Mechanisms of Fly Ash–Based Geopolymer Mortars. *J. Mater. Civ. Eng.* **33**, 04021059 (2021).
205. Luo, Y., Li, S.H., Klima, K.M., Brouwers, H.J.H. & Yu, Q.L. Degradation mechanism of hybrid fly ash/slag based geopolymers exposed to elevated temperatures. *Cement and Concrete Research* **151**, 106649 (2022).
206. Pan, Z., Sanjayan, J.G. & Rangan, B.V. An investigation of the mechanisms for strength gain or loss of geopolymer mortar after exposure to elevated temperature. *J Mater Sci* **44**, 1873–1880 (2009).
207. Liu, X., Feng, P., Lyu, C. & Ye, S. The role of sulfate ions in tricalcium aluminate hydration: New insights. *Cement and Concrete Research* **130**, 105973 (2020).
208. Havlica, J., Roztocká, D. & Sahu, S. Hydration kinetics of calciumaluminate phases in the presence of various ratios of Ca^{2+} and SO_4^{2-} ions in liquid phase. *Cement and Concrete Research* **23**, 294–300 (1993).
209. Ding, J., Fu, Y. & Beaudoin, J.J. Strätlingite formation in high-alumina cement-zeolite systems. *Advances in Cement Research* **7**, 171–178 (1995).
210. Le Saoût, G., Lothenbach, B., Hori, A., Higuchi, T. & Winnefeld, F. Hydration of Portland cement with additions of calcium sulfoaluminates. *Cement and Concrete Research* **43**, 81–94 (2013).
211. Dombrowski, K., Buchwald, A. & Weil, M. The influence of calcium content on the structure and thermal performance of fly ash based geopolymers. *J Mater Sci* **42**, 3033–3043 (2007).
212. Garcia-Lodeiro, I., Palomo, A. & Fernández-Jiménez, A. 2 - An overview of the chemistry of alkali-activated cement-based binders. in *Handbook of Alkali-Activated Cements, Mortars and Concretes* (eds. Pacheco-Torgal, F., Labrincha, J.A., Leonelli, C., Palomo, A. & Chindaprasirt, P.) 19–47 (Woodhead Publishing, 2015).
213. Duxson, P., Provis, J.L., Lukey, G.C. & van Deventer, J.S.J. The role of inorganic polymer technology in the development of 'green concrete'. *Cement and Concrete Research* **37**, 1590–1597 (2007).
214. Lee, W.K.W. & van Deventer, J.S.J. The effect of ionic contaminants on the early-age properties of alkali-activated fly ash-based cements. *Cement and Concrete Research* **32**, 577–584 (2002).
215. Väntsi, O. & Kärki, T. Mineral wool waste in Europe: a review of mineral wool waste quantity, quality, and current recycling methods. *J Mater Cycles Waste Manag* **16**, 62–72 (2014).
216. Yliniemi, J., Ramaswamy, R., Luukkonen, T., Laitinen, O., de Sousa, A.N., Huuhtanen, M., Illikainen, M. Characterization of mineral wool waste chemical composition, organic resin content and fiber dimensions:

Aspects for valorization. *Waste Management* **131**, 323–330 (2021).

217. Cheng, A., Lin, W.-T. & Huang, R. Application of rock wool waste in cement-based composites. *Materials & Design* **32**, 636–642 (2011).
218. Lin, W.-T., Cheng, A., Huang, R. & Zou, S.-Y. Improved microstructure of cement-based composites through the addition of rock wool particles. *Materials Characterization* **84**, 1–9 (2013).
219. Piña Ramírez, C., Atanes Sánchez, E., del Río Merino, M., Viñas Arrebola, C. & Vidales Barriguete, A. Feasibility of the use of mineral wool fibres recovered from CDW for the reinforcement of conglomerates by study of their porosity. *Construction and Building Materials* **191**, 460–468 (2018).
220. Yliniemi, J., Walkley, B., Provis, J.L., Kinnunen, P. & Illikainen, M. Nanostructural evolution of alkali-activated mineral wools. *Cement and Concrete Composites* **106**, 103472 (2020).
221. Yliniemi, J., Kinnunen, P., Karinkanta, P. & Illikainen, M. Utilization of Mineral Wools as Alkali-Activated Material Precursor. *Materials* **9**, 312 (2016).
222. Lemougna, P.N., Adediran, A., Yliniemi, J., Luukkonen, T. & Illikainen, M. Effect of organic resin in glass wool waste and curing temperature on the synthesis and properties of alkali-activated pastes. *Materials & Design* **212**, 110287 (2021).
223. Pavlin, M., Horvat, B., Frankovič, A. & Ducman, V. Mechanical, microstructural and mineralogical evaluation of alkali-activated waste glass and stone wool. *Ceramics International* **47**, 15102–15113 (2021).
224. Ramaswamy, R., Yliniemi, J. & Illikainen, M. Dissolution-precipitation reactions of silicate mineral fibers at alkaline pH. *Cement and Concrete Research* **160**, 106922 (2022).
225. Lee, B., Kim, G., Kim, R., Cho, B., Lee, S., Chon, C. Strength development properties of geopolymer paste and mortar with respect to amorphous Si/Al ratio of fly ash. *Construction and Building Materials* **151**, 512–519 (2017).
226. Kinnunen, P., Yliniemi, J., Talling, B. & Illikainen, M. Rockwool waste in fly ash geopolymer composites. *J Mater Cycles Waste Manag* **19**, 1220–1227 (2017).
227. Mastali, M., Zahra, A., Hugo, K. & Faraz, R. Utilization of mineral wools in production of alkali activated materials. *Construction and Building Materials* **283**, 122790 (2021).
228. Ma, Y. & Ye, G. The shrinkage of alkali activated fly ash. *Cement and Concrete Research* **68**, 75–82 (2015).
229. Li, Z., Alfredo Flores Beltran, I., Chen, Y., Šavija, B. & Ye, G. Early-age properties of alkali-activated slag and glass wool paste. *Construction and Building Materials* **291**, 123326 (2021).
230. Ambikakumari Sanalkumar, K.U., Lahoti, M. & Yang, E.-H. Investigating the potential reactivity of fly ash for geopolymerization. *Construction and Building Materials* **225**, 283–291 (2019).
231. Utton, C.A., Hand, R.J., Bingham, P.A., Hyatt, N.C., Swanton, S.W., Williams, S.J. Dissolution of vitrified wastes in a high-pH calcium-rich solution. *Journal of Nuclear Materials* **435**, 112–122 (2013).
232. Cao, Y.Y.Y., Li, P.P., Brouwers, H.J.H., Sluijsmans, M. & Yu, Q.L. Enhancing flexural performance of ultra-high performance concrete by an optimized layered-structure concept. *Composites Part B: Engineering* **171**, 154–165 (2019).
233. Shi, C., Jiménez, A.F. & Palomo, A. New cements for the 21st century: The pursuit of an alternative to Portland cement. *Cement and Concrete Research* **41**, 750–763 (2011).
234. Luo, Y., Brouwers, H.J.H. & Yu, Q.L. Understanding the gel compatibility and thermal behavior of alkali

activated Class F fly ash/ladle slag: The underlying role of Ca availability. *Cement and Concrete Research* **170**, 107198 (2023).

235. Tuchman, D.P. *Research Toward Direct Analysis of Quartz Dust on Filters Using FTIR Spectroscopy*. (U.S. Department of the Interior, Bureau of Mines, 1992).
236. García-Lodeiro, I., Fernández-Jiménez, A., Blanco, M.T. & Palomo, A. FTIR study of the sol–gel synthesis of cementitious gels: C–S–H and N–A–S–H. *J Sol-Gel Sci Technol* **45**, 63–72 (2008).
237. Yu, P., Kirkpatrick, R.J., Poe, B., McMillan, P.F. & Cong, X. Structure of Calcium Silicate Hydrate (C-S-H): Near-, Mid-, and Far-Infrared Spectroscopy. *Journal of the American Ceramic Society* **82**, 742–748 (1999).
238. García Lodeiro, I., Macphee, D.E., Palomo, A. & Fernández-Jiménez, A. Effect of alkalis on fresh C–S–H gels. FTIR analysis. *Cement and Concrete Research* **39**, 147–153 (2009).
239. Ling, Y., Wang, K. & Fu, C. Shrinkage behavior of fly ash based geopolymer pastes with and without shrinkage reducing admixture. *Cement and Concrete Composites* **98**, 74–82 (2019).
240. Si, R., Dai, Q., Guo, S. & Wang, J. Mechanical property, nanopore structure and drying shrinkage of metakaolin-based geopolymer with waste glass powder. *Journal of Cleaner Production* **242**, 118502 (2020).
241. Soliman, A.M. & Nehdi, M.L. Effects of shrinkage reducing admixture and wollastonite microfiber on early-age behavior of ultra-high performance concrete. *Cement and Concrete Composites* **46**, 81–89 (2014).
242. Zuhua, Z., Xiao, Y., Huajun, Z. & Yue, C. Role of water in the synthesis of calcined kaolin-based geopolymer. *Applied Clay Science* **43**, 218–223 (2009).
243. Duxson, P., Mallicoat, S.W., Lukey, G.C., Kriven, W.M. & van Deventer, J.S.J. The effect of alkali and Si/Al ratio on the development of mechanical properties of metakaolin-based geopolymers. *Colloids and Surfaces A: Physicochemical and Engineering Aspects* **292**, 8–20 (2007).
244. Yoon, S.-D. & Yun, Y.-H. Waste glass and fly ash derived glass-ceramic. *J Mater Sci* **41**, 4315–4319 (2006).
245. Zeng, L., Sun, H., Peng, T. & Zheng, W. The sintering kinetics and properties of sintered glass-ceramics from coal fly ash of different particle size. *Results in Physics* **15**, 102774 (2019).
246. Duxson, P., Lukey, G.C. & van Deventer, J.S.J. Physical evolution of Na-geopolymer derived from metakaolin up to 1000 °C. *J Mater Sci* **42**, 3044–3054 (2007).
247. Kaze, C.R., Lecomte-Nana, G.L., Kamseu, E., Camacho, P.S., Yorkshire, A.S., Provis, J.L., Duttine, M., Wattiaux, A., Melo, U.C. Mechanical and physical properties of inorganic polymer cement made of iron-rich laterite and lateritic clay: A comparative study. *Cement and Concrete Research* **140**, 106320 (2021).
248. Lin, H., Liu, H., Li, Y. & Kong, X. Properties and reaction mechanism of phosphoric acid activated metakaolin geopolymer at varied curing temperatures. *Cement and Concrete Research* **144**, 106425 (2021).
249. Zhang, H.Y., Kodur, V., Wu, B., Cao, L. & Wang, F. Thermal behavior and mechanical properties of geopolymer mortar after exposure to elevated temperatures. *Construction and Building Materials* **109**, 17–24 (2016).
250. Jaya, N.A. Correlation between pore structure, compressive strength and thermal conductivity of porous metakaolin geopolymer. *Construction and Building Materials* 12 (2020).
251. Deutou Nemaleu, J.G., Kaze, C.R., Belela, E.A., Lecomte-Nana, G.L., Kamseu, E., Sglavo, V.M., Leonelli, C. Refractory ceramics bonds from potassium-based inorganic polymer for advanced applications: Crystalline phase changes and descriptive microstructure. *Ceramics International* **48**, 21579–21588 (2022).

252. Brouwers, H.J.H. & Radix, H.J. Self-Compacting Concrete: Theoretical and experimental study. *Cement and Concrete Research* **35**, 2116–2136 (2005).

253. Hunger, M. *An integral design concept for ecological self-compacting concrete*. (PhD Thesis, Eindhoven University of Technology, 2010).

254. Yu, R., Spiesz, P. & Brouwers, H.J.H. Development of an eco-friendly Ultra-High Performance Concrete (UHPC) with efficient cement and mineral admixtures uses. *Cement and Concrete Composites* **55**, 383–394 (2015).

255. Yu, R., Spiesz, P. & Brouwers, H.J.H. Mix design and properties assessment of Ultra-High Performance Fibre Reinforced Concrete (UHPFRC). *Cement and Concrete Research* **56**, 29–39 (2014).

256. Hüsken, G. & Brouwers, H.J.H. A new mix design concept for earth-moist concrete: A theoretical and experimental study. *Cement and Concrete Research* **38**, 1246–1259 (2008).

257. Hüsken, G. *A multifunctional design approach for sustainable concrete: with application to concrete mass products*. (PhD Thesis, Eindhoven University of Technology, 2010).

258. Yu, Q.L., Spiesz, P. & Brouwers, H.J.H. Ultra-lightweight concrete: Conceptual design and performance evaluation. *Cement and Concrete Composites* **61**, 18–28 (2015).

259. Yu, Q.L., Spiesz, P. & Brouwers, H.J.H. Development of cement-based lightweight composites – Part 1: Mix design methodology and hardened properties. *Cement and Concrete Composites* **44**, 17–29 (2013).

260. Spiesz, P., Yu, Q.L. & Brouwers, H.J.H. Development of cement-based lightweight composites – Part 2: Durability-related properties. *Cement and Concrete Composites* **44**, 30–40 (2013).

261. Yu, Q.L. & Brouwers, H.J.H. Development of a self-compacting gypsum-based lightweight composite. *Cement and Concrete Composites* **34**, 1033–1043 (2012).

262. Funk, J.E. & Dinger, D.R. *Predictive Process Control of Crowded Particulate Suspensions: Applied to Ceramic Manufacturing*. (Kluwer Academic Publishers, 1994).

263. Borges, P.H.R., Fonseca, L.F., Nunes, V.A., Panzera, T.H. & Martuscelli, C.C. Andreasen Particle Packing Method on the Development of Geopolymer Concrete for Civil Engineering. *Journal of Materials in Civil Engineering* **26**, 692–697 (2014).

264. Gao, X., Yu, Q.L. & Brouwers, H.J.H. Assessing the porosity and shrinkage of alkali activated slag-fly ash composites designed applying a packing model. *Construction and Building Materials* **119**, 175–184 (2016).

265. ISO/DIS22007-2. Determination of thermal conductivity and thermal diffusivity, Part 2: Transient Plane Heat Source (Hot Disc) Method. *International Organization for Standardization* (2008).

266. ASTM E96/E96M-21. *Standard test methods for water vapor transmission of materials Standard Test Methods for Gravimetric Determination of Water Vapor Transmission Rate of Materials*.

267. COMSOL 5.6. *COMSOL Multiphysics Reference Manual*. (2020).

268. Smith, D.S., Alzina, A., Bourret, J., Nait-Ali, B., Pennec, F., Tessier-Doyen, N., Otsu, K., Matsubara, H., Elser, P., Gonzenbach, U.T. Thermal conductivity of porous materials. *J. Mater. Res.* **28**, 2260–2272 (2013).

269. Budiansky, B. Thermal and Thermoelastic Properties of Isotropic Composites. *Journal of Composite Materials* **4**, 286–295 (1970).

270. Huang, Q., Jiang, Z., Gu, X., Zhang, W. & Guo, B. Numerical simulation of moisture transport in concrete based on a pore size distribution model. *Cement and Concrete Research* **67**, 31–43 (2015).

271. Chen, Y.X., Klima, K.M., Brouwers, H.J.H. & Yu, Q. Effect of silica aerogel on thermal insulation and acoustic absorption of geopolymer foam composites: The role of aerogel particle size. *Composites Part B: Engineering* **242**, 110048 (2022).

272. Liu, M.Y.J., Alengaram, U.J., Jumaat, M.Z. & Mo, K.H. Evaluation of thermal conductivity, mechanical and transport properties of lightweight aggregate foamed geopolymer concrete. *Energy and Buildings* **72**, 238–245 (2014).

273. Wongsa, A., Zaetang, Y., Sata, V. & Chindaprasirt, P. Properties of lightweight fly ash geopolymer concrete containing bottom ash as aggregates. *Construction and Building Materials* **111**, 637–643 (2016).

274. Wongsa, A., Sata, V., Nematollahi, B., Sanjayan, J. & Chindaprasirt, P. Mechanical and thermal properties of lightweight geopolymer mortar incorporating crumb rubber. *Journal of Cleaner Production* **195**, 1069–1080 (2018).

275. Posi, P., Ridtirud, C., Ekvong, C., Chammanee, D., Janthowong, K., Chindaprasirt, P. Properties of lightweight high calcium fly ash geopolymer concretes containing recycled packaging foam. *Construction and Building Materials* **94**, 408–413 (2015).

276. Colangelo, F., Roviello, G., Ricciotti, L., Ferrándiz-Mas, V., Messina, F., Ferone, C., Tarallo, O., Cioffi, R., Cheeseman, C.R. Mechanical and thermal properties of lightweight geopolymer composites. *Cement and Concrete Composites* **86**, 266–272 (2018).

277. Hager, I., Sitarz, M. & Mróz, K. Fly-ash based geopolymer mortar for high-temperature application – Effect of slag addition. *Journal of Cleaner Production* **316**, 128168 (2021).

278. Axe, J.D. & Shirane, G. Study of the α-β Quartz Phase Transformation by Inelastic Neutron Scattering. *Phys. Rev. B* **1**, 342–348 (1970).

279. Nana, A., Cyriaque Kaze, R., Salman Alomayri, T., Suliman Assaedi, H., Nemaleu Deutou, J.G., Ngouné, J., Kouamo Tchakouté, H., Kamseu, E., Leonelli, C. Innovative porous ceramic matrices from inorganic polymer composites (IPCs): Microstructure and mechanical properties. *Construction and Building Materials* **273**, 122032 (2021).

Appendix A

Table A1 The phase composition of the hydrated pastes at different temperatures in wt.%, determined by XRD-Rietveld analysis.

Phase	20 °C				400 °C				800 °C			
	Ref.	FL5	FL15	FL25	Ref.	FL5	FL15	FL25	Ref.	FL5	FL15	FL25
Quartz	6.0	5.6	5.2	4.4	5.4	5.0	4.6	4.2	8.1	7.3	6.3	5.0
Mullite	8.5	7.6	7.0	5.9	9.1	8.9	8.2	7.3	8.6	8.6	8.1	6.3
Hydrogarnet	0.0	0.3	1.4	2.3	0.0	0.0	0.0	0.0	0.0	0.0	0.0	0.0
C_3A	0.0	0.5	1.3	1.8	0.0	0.8	2.0	3.6	0.0	0.0	0.6	2.1
Calcium Sodium Cyclo-Hexaaluminate		-				-			0.0	0.9	1.1	0.9
Mayenite		-			0.0	0.1	0.1	0.4	0.0	1.1	1.1	2.5
Hematite	1.3	1.1	0.9	0.6	1.1	0.8	0.9	0.6	1.8	0.6	1.3	0.9
Magnetite	0.7	0.6	0.5	0.3	0.7	0.7	0.8	0.5	0.0	0.0	0.0	0.0
Calcite	0.4	0.5	0.5	0.6	0.2	0.3	0.5	0.6	0.2	0.3	0.4	0.7
Periclase	0.4	0.2	0.4	0.4	0.4	0.3	0.1	0.6	0.8	0.9	0.8	1.0
Pyrrhotite	0.3	0.3	0.4	0.5	0.3	0.2	0.2	0.3	0.0	0.4	0.4	0.2
Rutile	0.2	0.1	0.1	0.1	0.2	0.2	0.1	0.1	0.7	0.2	0.6	0.7
Nepheline		-				-			0.9	2.1	4.5	5.6
Dolomite		-				-			0.9	0.0	0.0	0.0
Albite		-				-			0.5	0.7	0.7	0.3
AlFe3		-				-			0.2	0.2	0.2	0.2
Silicone Carbide		-				-			0.2	0.0	0.0	0.0
Wollastonite		-			0.0	0.6	0.2	0.6	0.0	3.4	3.1	4.5
Gehlenite		-				-			0.0	0.7	1.3	2.4
Akermanite		-				-			0.0	0.1	0.5	0.5
Tricalcium Cyclo-trisilicate		-				-			0.0	1.7	2.7	1.5
Amorphous	82.2	83.2	82.4	83.1	76.6	75.4	74.5	72.9	69.0	62.4	57.0	54.3

Appendix B

Table B1 The average chemical composition of phases calculated by PARC.

Phase	Oxide											
	Na_2O	MgO	Al_2O_3	SiO_2	P_2O_5	SO_3	K_2O	CaO	TiO_2	MnO	Fe_xO_y	NiO
C-(N)-A-S-H	2.21	1.06	22.10	22.79	1.66	1.43	0.39	44.63	-	0.83	1.59	1.30
N-(C)-A-S-H	13.16	0.50	13.84	51.92	1.64	2.22	1.37	11.46	-	-	3.90	-
Mullite	2.19	1.05	29.33	53.72	1.46	1.43	2.59	1.82	1.36	-	5.05	-
Quartz	1.73	0.19	2.07	88.97	1.95	2.47	-	0.43	0.30	-	1.89	-
CAs, CAH	0.37	0.65	34.14	1.52	0.99	1.12	-	59.52	-	0.70	0.98	-
FexOy	-	1.24	2.62	1.47	1.05	0.19	0.06	0.49	0.20	1.31	91.38	-
Periclase	1.22	79.18	6.42	2.47	0.00	0.00	0.85	0.85	0.03	2.58	6.39	-
C_2S	1.74	-	3.92	25.38	2.34	0.59	0.10	43.00	0.70	0.04	21.25	0.94

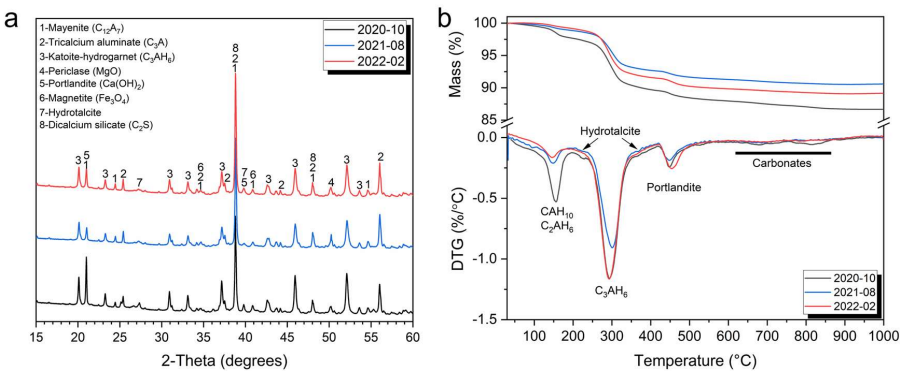

Fig. B1 The variability between raw ladle slag collection from 2020 to 2022, (a) XRD patterns and (b) TGA-DTG results.

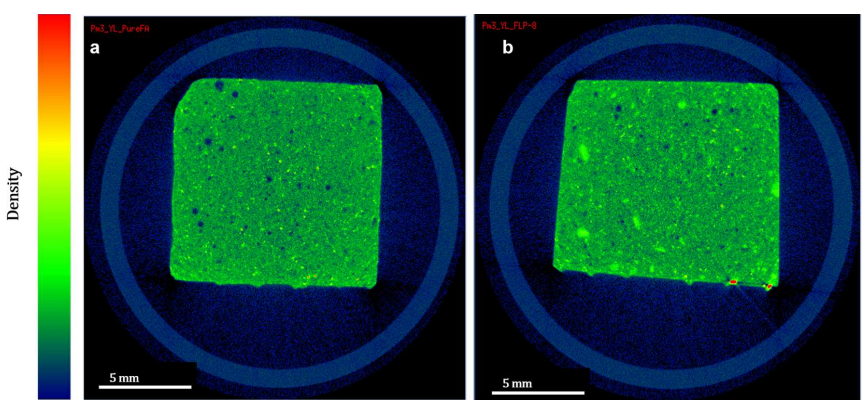

Fig. B2 Comparison between Micro-CT 2D images depending on density, a) Plain FA based geopolymer, b) LS/FA hybrid geopolymer.

Appendix C

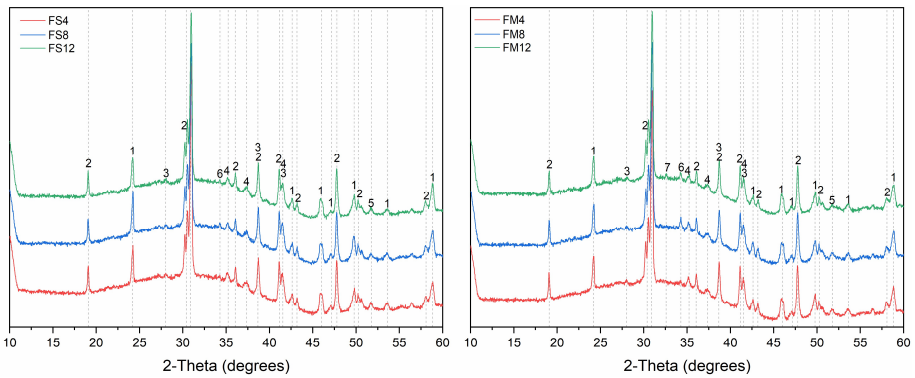

Fig. C1 XRD patterns of the specimens with different MWW substitutions (1-Quartz, 2-Mullite, 3-Hematite, 4-Magnetite, 5-Iron, 6-C-S-H, 7-Rutile).

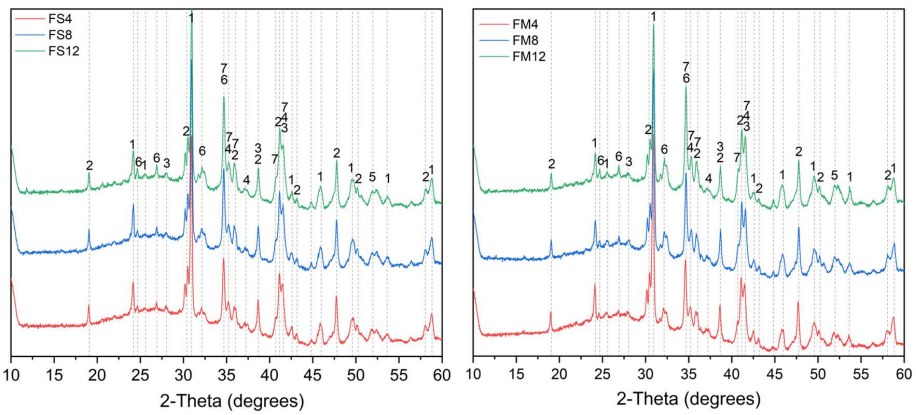

Fig. C2 XRD patterns of the specimens with different MWW substitutions after 800 ˚C exposure (1-Quartz, 2-Mullite, 3-Hematite, 4-Magnetite, 5-Iron, 6-Nepheline, 7-Diopside).

Appendix D

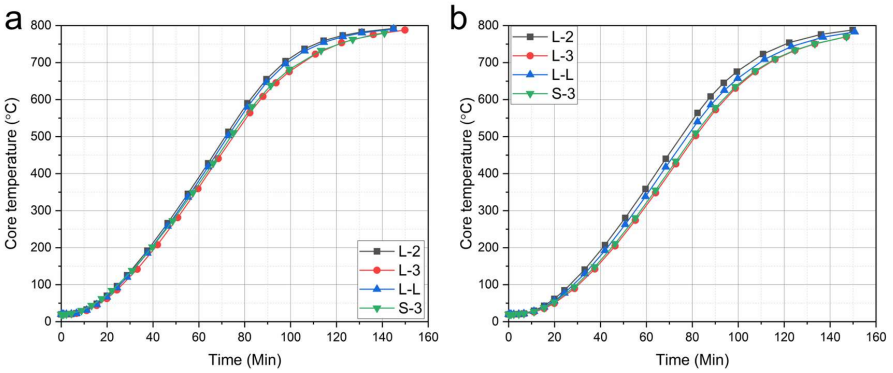

Fig. D1 Validation of heat transfer simulation (a: BS model, b: CS model).

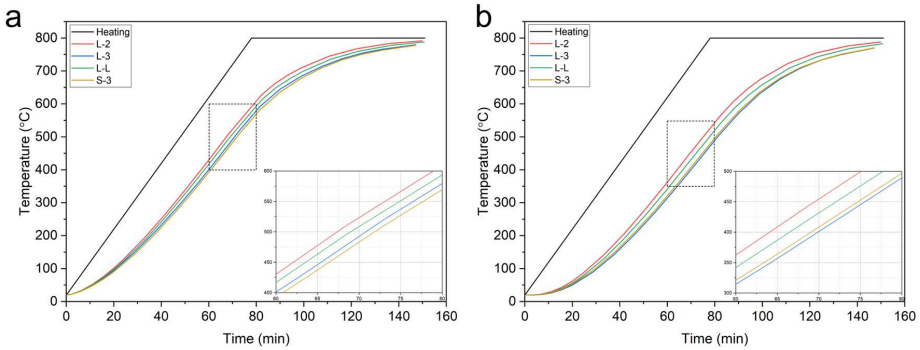

Fig. D2 The temperature change of (a) the surface (0 mm) and (b) the core (20 mm) for different samples.

List of notations

Abbreviations	
A&A	Andreasen and Andersen
AAF	Alkali-activated fly ash
AAFL	Alkali-activated fly ash/ladle slag
AAFS	Alkali-activated fly ash/GGBS
AAM	Alkali-activated material
BET	Brunauer-Emmett-Teller
BOFS	Basic oxygen furnace slag
BSE	Backscattered electron
C&D	Construction and demolition
C-(A)-S-H	Calcium (aluminate) silicate hydrate
CA	Calcium aluminate
CAC	Calcium aluminate cement
C-S-H	Calcium silicate hydrate
DSC	Differential scanning calorimetry
DTG	Differential thermogravimetry
EDS	Energy-dispersive spectroscopy
FA	Class F fly ash
FTIR	Fourier transform infrared
GGBS	Ground granulated blast furnace slag
GW	Glass wool
ICP-OES	Inductively coupled plasma-optical emission spectrometry
ITZ	Interfacial transition zone
LOI	Loss on ignition
LS	Ladle slag
LSM	Least Squares Method
LWA	Lightweight aggregate
LWAG	Lightweight aggregate incorporated geopolymer
Micro-CT	Micro-computed tomography
MIP	Mercury intrusion porosimetry
MWW	Mineral wool waste
N,C-A-S-H	Sodium/calcium aluminosilicate hydrate
N-A-S-H	Sodium aluminate silicate hydrate
NMR	Nuclear Magnetic Resonance
OPC	Ordinary Portland Cement
PARC	PhAse Recognition and Characterization
PP	Polypropylene
PSD	Particle size distribution

PVA	Polyvinyl alcohol
RH	Relative humidity
RSS	The sum of the squares of the residuals
SAG	Sand aggregate incorporated geopolymer
SCC	Self-compacting concrete
SCM	Supplementary cementitious materials
SEM	Scanning electron microscopy
SW	Stone wool
TG	Thermogravimetry
TGA	Thermal gravimetric analysis
UHPC	Ultra-high-performance concrete
ULWC	Ultra-lightweight concrete
UPV	Ultrasonic pulse velocity
WVTR	Water vapor transmission rate
XRD	X-ray diffractometry
XRF	X-ray fluorescence spectrometry

Nomenclatures		SI Unit	Chapter
ρ_s	Specific density	g/cm^3	2 & 3 & 4 & 5
SSA	Specific surface area	m^2/g	2 & 3 & 4 & 5
L_A	Crack density	$\mu m/\mu m^2$	2
L	Cumulative crack length	μm	2
A	Area	μm^2	2 & 6
ρ_b	Bulk density	g/cm^3	2 & 3 & 4 & 5
v	Velocity	m/s	2
d	Distance	m	2
t	Time	s	2 & 6
d_{50}	Average particle size	μm	2 & 3 & 4 & 5
Ms	Silicate modulus	-	2 & 3 & 4 & 5
ϕ	Porosity	%	2 & 3 & 4 & 5
L_{50}	Mean fiber length	μm	5
Ø	Diameter	mm	5
H	Height	mm	5
D_i	Dissolution degree	mg/g	5
E_i	Normalized dissolution extent	%	5
C_i	Element concentration	mg/L	5
V	Volume	L, cm^3	5 & 6
m	Mass	g	5 & 6
X_i	Element mass fraction	%	5
L_0	Initial length	mm	5
L_n	Length at specific ages	mm	5
L_i	Effective initial length	mm	5
D	Particle size	μm	6
Th	Thickness	m	6
δ	Permeability	m/s	6
Δp	Vapor pressure difference	mm Hg	6
λ	Bulk thermal conductivity	W/mK	6
$C_{p,v}$	Volumetric heat capacity	MJ/m^3K	6
wt.%	Weight percentage	%	6
h	Equivalent heat transfer coefficient	-	6
Qin	Heat source	-	6
T	Temperature	°C	6
α	Thermal diffusion	mm^2/s	6

List of publications

Peer-reviewed journal papers

[1] Y. Luo, H.J.H. Brouwers, Q.L. Yu, Understanding the gel compatibility and thermal behavior of alkali activated Class F fly ash/ladle slag: the underlying role of Ca availability, Cement and Concrete Research. 170 (2023), 107198.

[2] Y. Luo, S.H. Li, K.M. Klima, H.J.H. Brouwers, Q.L. Yu, Degradation mechanism of hybrid fly ash/slag based geopolymers exposed to elevated temperatures, Cement and Concrete Research. 151 (2022), 106649.

[3] Y. Luo, K.M. Klima, H.J.H. Brouwers, Q.L. Yu, Effects of ladle slag on Class F fly ash geopolymer: Reaction mechanism and high temperature behavior, Cement and Concrete Composites. 129 (2022), 104468.

[4] Y. Luo, C.H. Koh, S.H. Li, H.J.H. Brouwers, Q.L. Yu, Understanding the thermal behavior of geopolymeric composites designed by packing model, Cement and Concrete Composites 143 (2023), 105265

[5] Y. Luo, Q.L. Yu, Valorization of mineral wool waste in Class F fly ash geopolymer: geopolymerization, macro properties, and high temperature behavior, Cement and Concrete Composites, 145 (2024), 105318.

[6] K.M. Klima[1], **Y. Luo[1]**, H.J.H. Brouwers, Q.L. Yu, Effects of mineral wool waste in alkali activated-artificial aggregates for high-temperature applications, Construction and Building Materials. 401 (2023), 132937. (Equivalent first author).

[7] C.H. Koh, **Y. Luo**, F. Gauvin, and K. Schollbach, Wood Wool Geopolymer Boards for Sustainable Insulation: Formulation, Development, and Performance Evaluation. (Submitted).

[8] Y. Luo, K. Klima, S.R. van der Laan, H.J.H. Brouwers, Q.L. Yu, Thermal performance assessment of geopolymer based material through an in-situ high temperature study. (In preparation).

[9] Y. Luo, C.H. Koh, H.J.H. Brouwers, Q.L. Yu, High temperature performance of geopolymer mortar: An experimental and numerical modeling study. (In preparation).

Conference Proceedings

[1] Y. Luo, H.J.H. Brouwers, Q.L. Yu, The role of mineral wool waste in geopolymer: the cementing properties and environmental impact, 3rd International Conference of Sustainable Building Materials, 25-27 September. 2023, Wuhan, China. (Oral presentation).

[2] Y. Luo, Sustainable cementitious materials for high temperature application, 2023 International Young Scholars "Yueqi" Forum (China University of Mining and Technology), 24-26 October. 2023, Xuzhou, China. (Oral presentation, Online).

[3] Y. Luo, Q.L. Yu, H.J.H Brouwers. Reutilization of mineral wool waste in hybrid geopolymers. The 7th International Conference: Non-traditional Cement and Concrete (NTCC 2023), 25-28 June. 2023, Brno, Czech Republic. (Oral presentation).

[4] Y. Luo, Q.L. Yu, H.J.H. Brouwers, High-temperature resistant alkali-activated ternary fly ash-ladle slag-mineral wool waste blends, 4th International Conference on the Chemistry of Construction Materials, 26-28. September. 2022, Karlsruhe, Germany. (Poster).

Curriculum vitae

Yan Luo was born in Nanchong, Sichuan province, China, on January 3, 1994. He attended primary and secondary school in Nanchong, and obtained his bachelor's degree in Safety Engineering at the Henan University of Urban Construction in 2016, Pingdingshan. In the same year, he started his master's study in Safety Engineering at the School of Resources and Safety Engineering, Central South University, Changsha. His master project was focused on the thermal insulation and fire safety of silica aerogels-based materials, under the supervision of Prof. Xingguo Dai and Prof. Zhi Li. After receiving his master's degree in July 2019, he was awarded a scholarship from China Scholarship Council (CSC) to pursue his Ph.D. degree in the Netherlands. In October of the same year, he joined the Building Materials group at the Eindhoven University of Technology (TU/e), under the guidance of Prof. H.J.H. Brouwers and Prof. Q.L. Yu. During this period, he joined in the M2i/NWO project "Fire safety of innovative geopolymer-based building materials" and his research involved the development and optimization of geopolymer-based materials for high temperature applications. In 2022, he won the TU/e BE Research Awards: Outstanding PhD candidate.

Bouwstenen is een publicatiereeks
van de Faculteit Bouwkunde,
Technische Universiteit Eindhoven.
Zij presenteert resultaten van
onderzoek en andere activiteiten op
het vakgebied der Bouwkunde,
uitgevoerd in het kader van deze
Faculteit.

Bouwstenen en andere proefschriften van de
TU/e zijn online beschikbaar via:
https://research.tue.nl/

Reeds verschenen in de serie
Bouwstenen

nr 1
Elan: A Computer Model for Building Energy Design: Theory and Validation
Martin H. de Wit
H.H. Driessen
R.M.M. van der Velden

nr 2
Kwaliteit, Keuzevrijheid en Kosten: Evaluatie van Experiment Klarendal, Arnhem
J. Smeets
C. le Nobel
M. Broos
J. Frenken
A. v.d. Sanden

nr 3
Crooswijk: Van 'Bijzonder' naar 'Gewoon'
Vincent Smit
Kees Noort

nr 4
Staal in de Woningbouw
Edwin J.F. Delsing

nr 5
Mathematical Theory of Stressed Skin Action in Profiled Sheeting with Various Edge Conditions
Andre W.A.M.J. van den Bogaard

nr 6
Hoe Berekenbaar en Betrouwbaar is de Coëfficiënt k in x-ksigma en x-ks?
K.B. Lub
A.J. Bosch

nr 7
Het Typologisch Gereedschap: Een Verkennende Studie Omtrent Typologie en Omtrent de Aanpak van Typologisch Onderzoek
J.H. Luiten

nr 8
Informatievoorziening en Beheerprocessen
A. Nauta
Jos Smeets (red.)
Helga Fassbinder (projectleider)
Adrie Proveniers
J. v.d. Moosdijk

nr 9
Strukturering en Verwerking van Tijdgegevens voor de Uitvoering van Bouwwerken
ir. W.F. Schaefer
P.A. Erkelens

nr 10
Stedebouw en de Vorming van een Speciale Wetenschap
K. Doevendans

nr 11
Informatica en Ondersteuning van Ruimtelijke Besluitvorming
G.G. van der Meulen

nr 12
Staal in de Woningbouw, Korrosie-Bescherming van de Begane Grondvloer
Edwin J.F. Delsing

nr 13
Een Thermisch Model voor de Berekening van Staalplaatbetonvloeren onder Brandomstandigheden
A.F. Hamerlinck

nr 14
De Wijkgedachte in Nederland: Gemeenschapsstreven in een Stedebouwkundige Context
K. Doevendans
R. Stolzenburg

nr 15
Diaphragm Effect of Trapezoidally Profiled Steel Sheets: Experimental Research into the Influence of Force Application
Andre W.A.M.J. van den Bogaard

nr 16
Versterken met Spuit-Ferrocement: Het Mechanische Gedrag van met Spuit-Ferrocement Versterkte Gewapend Betonbalken
K.B. Lubir
M.C.G. van Wanroy

nr 17
De Tractaten van Jean Nicolas Louis Durand
G. van Zeyl

nr 18
Wonen onder een Plat Dak: Drie Opstellen over Enkele Vooronderstellingen van de Stedebouw
K. Doevendans

nr 19
Supporting Decision Making Processes: A Graphical and Interactive Analysis of Multivariate Data
W. Adams

nr 20
Self-Help Building Productivity: A Method for Improving House Building by Low-Income Groups Applied to Kenya 1990-2000
P. A. Erkelens

nr 21
De Verdeling van Woningen: Een Kwestie van Onderhandelen
Vincent Smit

nr 22
Flexibiliteit en Kosten in het Ontwerpproces: Een Besluitvormingondersteunend Model
M. Prins

nr 23
Spontane Nederzettingen Begeleid: Voorwaarden en Criteria in Sri Lanka
Po Hin Thung

nr 24
Fundamentals of the Design of Bamboo Structures
Oscar Arce-Villalobos

nr 25
Concepten van de Bouwkunde
M.F.Th. Bax (red.)
H.M.G.J. Trum (red.)

nr 26
Meaning of the Site
Xiaodong Li

nr 27
Het Woonmilieu op Begrip Gebracht: Een Speurtocht naar de Betekenis van het Begrip 'Woonmilieu'
Jaap Ketelaar

nr 28
Urban Environment in Developing Countries
editors: Peter A. Erkelens
George G. van der Meulen (red.)

nr 29
Stategische Plannen voor de Stad: Onderzoek en Planning in Drie Steden
prof.dr. H. Fassbinder (red.)
H. Rikhof (red.)

nr 30
Stedebouwkunde en Stadsbestuur
Piet Beekman

nr 31
De Architectuur van Djenné: Een Onderzoek naar de Historische Stad
P.C.M. Maas

nr 32
Conjoint Experiments and Retail Planning
Harmen Oppewal

nr 33
Strukturformen Indonesischer Bautechnik: Entwicklung Methodischer Grundlagen für eine 'Konstruktive Pattern Language' in Indonesien
Heinz Frick arch. SIA

nr 34
Styles of Architectural Designing: Empirical Research on Working Styles and Personality Dispositions
Anton P.M. van Bakel

nr 35
Conjoint Choice Models for Urban Tourism Planning and Marketing
Benedict Dellaert

nr 36
Stedelijke Planvorming als Co-Produktie
Helga Fassbinder (red.)

nr 37
Design Research in the Netherlands
editors: R.M. Oxman
M.F.Th. Bax
H.H. Achten

nr 38
Communication in the Building Industry
Bauke de Vries

nr 39
Optimaal Dimensioneren van Gelaste Plaatliggers
J.B.W. Stark
F. van Pelt
L.F.M. van Gorp
B.W.E.M. van Hove

nr 40
Huisvesting en Overwinning van Armoede
P.H. Thung
P. Beekman (red.)

nr 41
Urban Habitat: The Environment of Tomorrow
George G. van der Meulen
Peter A. Erkelens

nr 42
A Typology of Joints
John C.M. Olie

nr 43
Modeling Constraints-Based Choices for Leisure Mobility Planning
Marcus P. Stemerding

nr 44
Activity-Based Travel Demand Modeling
Dick Ettema

nr 45
Wind-Induced Pressure Fluctuations on Building Facades
Chris Geurts

nr 46
Generic Representations
Henri Achten

nr 47
Johann Santini Aichel: Architectuur en Ambiguiteit
Dirk De Meyer

nr 48
Concrete Behaviour in Multiaxial Compression
Erik van Geel

nr 49
Modelling Site Selection
Frank Witlox

nr 50
Ecolemma Model
Ferdinand Beetstra

nr 51
Conjoint Approaches to Developing Activity-Based Models
Donggen Wang

nr 52
On the Effectiveness of Ventilation
Ad Roos

nr 53
Conjoint Modeling Approaches for Residential Group preferences
Eric Molin

nr 54
Modelling Architectural Design Information by Features
Jos van Leeuwen

nr 55
A Spatial Decision Support System for the Planning of Retail and Service Facilities
Theo Arentze

nr 56
Integrated Lighting System Assistant
Ellie de Groot

nr 57
Ontwerpend Leren, Leren Ontwerpen
J.T. Boekholt

nr 58
Temporal Aspects of Theme Park Choice Behavior
Astrid Kemperman

nr 59
Ontwerp van een Geïndustrialiseerde Funderingswijze
Faas Moonen

nr 60
Merlin: A Decision Support System for Outdoor Leisure Planning
Manon van Middelkoop

nr 61
The Aura of Modernity
Jos Bosman

nr 62
Urban Form and Activity-Travel Patterns
Daniëlle Snellen

nr 63
Design Research in the Netherlands 2000
Henri Achten

nr 64
Computer Aided Dimensional Control in Building Construction
Rui Wu

nr 65
Beyond Sustainable Building
editors: Peter A. Erkelens
Sander de Jonge
August A.M. van Vliet
co-editor: Ruth J.G. Verhagen

nr 66
Das Globalrecyclingfähige Haus
Hans Löfflad

nr 67
Cool Schools for Hot Suburbs
René J. Dierkx

nr 68
A Bamboo Building Design Decision Support Tool
Fitri Mardjono

nr 69
Driving Rain on Building Envelopes
Fabien van Mook

nr 70
Heating Monumental Churches
Henk Schellen

nr 71
Van Woningverhuurder naar Aanbieder van Woongenot
Patrick Dogge

nr 72
Moisture Transfer Properties of Coated Gypsum
Emile Goossens

nr 73
Plybamboo Wall-Panels for Housing
Guillermo E. González-Beltrán

nr 74
The Future Site-Proceedings
Ger Maas
Frans van Gassel

nr 75
Radon transport in Autoclaved Aerated Concrete
Michel van der Pal

nr 76
The Reliability and Validity of Interactive Virtual Reality Computer Experiments
Amy Tan

nr 77
Measuring Housing Preferences Using Virtual Reality and Belief Networks
Maciej A. Orzechowski

nr 78
Computational Representations of Words and Associations in Architectural Design
Nicole Segers

nr 79
Measuring and Predicting Adaptation in Multidimensional Activity-Travel Patterns
Chang-Hyeon Joh

nr 80
Strategic Briefing
Fayez Al Hassan

nr 81
Well Being in Hospitals
Simona Di Cicco

nr 82
Solares Bauen: Implementierungs- und Umsetzungs-Aspekte in der Hochschulausbildung in Österreich
Gerhard Schuster

nr 83
Supporting Strategic Design of Workplace Environments with Case-Based Reasoning
Shauna Mallory-Hill

nr 84
ACCEL: A Tool for Supporting Concept Generation in the Early Design Phase
Maxim Ivashkov

nr 85
Brick-Mortar Interaction in Masonry under Compression
Ad Vermeltfoort

nr 86
Zelfredzaam Wonen
Guus van Vliet

nr 87
Een Ensemble met Grootstedelijke Allure
Jos Bosman
Hans Schippers

nr 88
On the Computation of Well-Structured Graphic Representations in Architectural Design
Henri Achten

nr 89
De Evolutie van een West-Afrikaanse Vernaculaire Architectuur
Wolf Schijns

nr 90
ROMBO Tactiek
Christoph Maria Ravesloot

nr 91
External Coupling between Building Energy Simulation and Computational Fluid Dynamics
Ery Djunaedy

nr 92
Design Research in the Netherlands 2005
editors: Henri Achten
Kees Dorst
Pieter Jan Stappers
Bauke de Vries

nr 93
Ein Modell zur Baulichen Transformation
Jalil H. Saber Zaimian

nr 94
Human Lighting Demands: Healthy Lighting in an Office Environment
Myriam Aries

nr 95
A Spatial Decision Support System for the Provision and Monitoring of Urban Greenspace
Claudia Pelizaro

nr 96
Leren Creëren
Adri Proveniers

nr 97
Simlandscape
Rob de Waard

nr 98
Design Team Communication
Ad den Otter

nr 99
Humaan-Ecologisch Georiënteerde Woningbouw
Juri Czabanowski

nr 100
Hambase
Martin de Wit

nr 101
Sound Transmission through Pipe Systems and into Building Structures
Susanne Bron-van der Jagt

nr 102
Het Bouwkundig Contrapunt
Jan Francis Boelen

nr 103
A Framework for a Multi-Agent Planning Support System
Dick Saarloos

nr 104
Bracing Steel Frames with Calcium Silicate Element Walls
Bright Mweene Ng'andu

nr 105
Naar een Nieuwe Houtskeletbouw
F.N.G. De Medts

nr 106 and 107
Niet gepubliceerd

nr 108
Geborgenheid
T.E.L. van Pinxteren

nr 109
Modelling Strategic Behaviour in Anticipation of Congestion
Qi Han

nr 110
Reflecties op het Woondomein
Fred Sanders

nr 111
On Assessment of Wind Comfort by Sand Erosion
Gábor Dezsö

nr 112
Bench Heating in Monumental Churches
Dionne Limpens-Neilen

nr 113
RE. Architecture
Ana Pereira Roders

nr 114
Toward Applicable Green Architecture
Usama El Fiky

nr 115
Knowledge Representation under Inherent Uncertainty in a Multi-Agent System for Land Use Planning
Liying Ma

nr 116
Integrated Heat Air and Moisture Modeling and Simulation
Jos van Schijndel

nr 117
Concrete Behaviour in Multiaxial Compression
J.P.W. Bongers

nr 118
The Image of the Urban Landscape
Ana Moya Pellitero

nr 119
The Self-Organizing City in Vietnam
Stephanie Geertman

nr 120
A Multi-Agent Planning Support System for Assessing Externalities of Urban Form Scenarios
Rachel Katoshevski-Cavari

nr 121
Den Schulbau Neu Denken, Fühlen und Wollen
Urs Christian Maurer-Dietrich

nr 122
Peter Eisenman Theories and Practices
Bernhard Kormoss

nr 123
User Simulation of Space Utilisation
Vincent Tabak

nr 125
In Search of a Complex System Model
Oswald Devisch

nr 126
Lighting at Work: Environmental Study of Direct Effects of Lighting Level and Spectrum on Psycho-Physiological Variables
Grazyna Górnicka

nr 127
Flanking Sound Transmission through Lightweight Framed Double Leaf Walls
Stefan Schoenwald

nr 128
Bounded Rationality and Spatio-Temporal Pedestrian Shopping Behavior
Wei Zhu

nr 129
Travel Information: Impact on Activity Travel Pattern
Zhongwei Sun

nr 130
Co-Simulation for Performance Prediction of Innovative Integrated Mechanical Energy Systems in Buildings
Marija Trčka

nr 131
Niet gepubliceerd

nr 132
Architectural Cue Model in Evacuation Simulation for Underground Space Design
Chengyu Sun

nr 133
Uncertainty and Sensitivity Analysis in Building Performance Simulation for Decision Support and Design Optimization
Christina Hopfe

nr 134
Facilitating Distributed Collaboration in the AEC/FM Sector Using Semantic Web Technologies
Jacob Beetz

nr 135
Circumferentially Adhesive Bonded Glass Panes for Bracing Steel Frame in Façades
Edwin Huveners

nr 136
Influence of Temperature on Concrete Beams Strengthened in Flexure with CFRP
Ernst-Lucas Klamer

nr 137
Sturen op Klantwaarde
Jos Smeets

nr 139
Lateral Behavior of Steel Frames with Discretely Connected Precast Concrete Infill Panels
Paul Teewen

nr 140
Integral Design Method in the Context of Sustainable Building Design
Perica Savanović

nr 141
Household Activity-Travel Behavior: Implementation of Within-Household Interactions
Renni Anggraini

nr 142
Design Research in the Netherlands 2010
Henri Achten

nr 143
Modelling Life Trajectories and Transport Mode Choice Using Bayesian Belief Networks
Marloes Verhoeven

nr 144
Assessing Construction Project Performance in Ghana
William Gyadu-Asiedu

nr 145
Empowering Seniors through Domotic Homes
Masi Mohammadi

nr 146
An Integral Design Concept for Ecological Self-Compacting Concrete
Martin Hunger

nr 147
Governing Multi-Actor Decision Processes in Dutch Industrial Area Redevelopment
Erik Blokhuis

nr 148
A Multifunctional Design Approach for Sustainable Concrete
Götz Hüsken

nr 149
Quality Monitoring in Infrastructural Design-Build Projects
Ruben Favié

nr 150
Assessment Matrix for Conservation of Valuable Timber Structures
Michael Abels

nr 151
Co-simulation of Building Energy Simulation and Computational Fluid Dynamics for Whole-Building Heat, Air and Moisture Engineering
Mohammad Mirsadeghi

nr 152
External Coupling of Building Energy Simulation and Building Element Heat, Air and Moisture Simulation
Daniel Cóstola

nr 153
Adaptive Decision Making In Multi-Stakeholder Retail Planning
Ingrid Janssen

nr 154
Landscape Generator
Kymo Slager

nr 155
Constraint Specification in Architecture
Remco Niemeijer

nr 156
A Need-Based Approach to Dynamic Activity Generation
Linda Nijland

nr 157
Modeling Office Firm Dynamics in an Agent-Based Micro Simulation Framework
Gustavo Garcia Manzato

nr 158
Lightweight Floor System for Vibration Comfort
Sander Zegers

nr 159
Aanpasbaarheid van de Draagstructuur
Roel Gijsbers

nr 160
'Village in the City' in Guangzhou, China
Yanliu Lin

nr 161
Climate Risk Assessment in Museums
Marco Martens

nr 162
Social Activity-Travel Patterns
Pauline van den Berg

nr 163
Sound Concentration Caused by Curved Surfaces
Martijn Vercammen

nr 164
Design of Environmentally Friendly Calcium Sulfate-Based Building Materials: Towards an Improved Indoor Air Quality
Qingliang Yu

nr 165
Beyond Uniform Thermal Comfort on the Effects of Non-Uniformity and Individual Physiology
Lisje Schellen

nr 166
Sustainable Residential Districts
Gaby Abdalla

nr 167
Towards a Performance Assessment Methodology using Computational Simulation for Air Distribution System Designs in Operating Rooms
Mônica do Amaral Melhado

nr 168
Strategic Decision Modeling in Brownfield Redevelopment
Brano Glumac

nr 169
Pamela: A Parking Analysis Model for Predicting Effects in Local Areas
Peter van der Waerden

nr 170
A Vision Driven Wayfinding Simulation-System Based on the Architectural Features Perceived in the Office Environment
Qunli Chen

nr 171
Measuring Mental Representations Underlying Activity-Travel Choices
Oliver Horeni

nr 172
Modelling the Effects of Social Networks on Activity and Travel Behaviour
Nicole Ronald

nr 173
Uncertainty Propagation and Sensitivity Analysis Techniques in Building Performance Simulation to Support Conceptual Building and System Design
Christian Struck

nr 174
Numerical Modeling of Micro-Scale Wind-Induced Pollutant Dispersion in the Built Environment
Pierre Gousseau

nr 175
Modeling Recreation Choices over the Family Lifecycle
Anna Beatriz Grigolon

nr 176
Experimental and Numerical Analysis of Mixing Ventilation at Laminar, Transitional and Turbulent Slot Reynolds Numbers
Twan van Hooff

nr 177
Collaborative Design Support: Workshops to Stimulate Interaction and Knowledge Exchange Between Practitioners
Emile M.C.J. Quanjel

nr 178
Future-Proof Platforms for Aging-in-Place
Michiel Brink

nr 179
Motivate: A Context-Aware Mobile Application for Physical Activity Promotion
Yuzhong Lin

nr 180
Experience the City: Analysis of Space-Time Behaviour and Spatial Learning
Anastasia Moiseeva

nr 181
Unbonded Post-Tensioned Shear Walls of Calcium Silicate Element Masonry
Lex van der Meer

nr 182
Construction and Demolition Waste Recycling into Innovative Building Materials for Sustainable Construction in Tanzania
Mwita M. Sabai

nr 183
Durability of Concrete with Emphasis on Chloride Migration
Przemysław Spiesz

nr 184
Computational Modeling of Urban Wind Flow and Natural Ventilation Potential of Buildings
Rubina Ramponi

nr 185
A Distributed Dynamic Simulation Mechanism for Buildings Automation and Control Systems
Azzedine Yahiaoui

nr 186
Modeling Cognitive Learning of Urban Networks in Daily Activity-Travel Behavior
Şehnaz Cenani Durmazoğlu

nr 187
Functionality and Adaptability of Design Solutions for Public Apartment Buildings in Ghana
Stephen Agyefi-Mensah

nr 188
A Construction Waste Generation Model for Developing Countries
Lilliana Abarca-Guerrero

nr 189
Synchronizing Networks: The Modeling of Supernetworks for Activity-Travel Behavior
Feixiong Liao

nr 190
Time and Money Allocation Decisions in Out-of-Home Leisure Activity Choices
Gamze Zeynep Dane

nr 191
How to Measure Added Value of CRE and Building Design
Rianne Appel-Meulenbroek

nr 192
Secondary Materials in Cement-Based Products: Treatment, Modeling and Environmental Interaction
Miruna Florea

nr 193
Concepts for the Robustness Improvement of Self-Compacting Concrete: Effects of Admixtures and Mixture Components on the Rheology and Early Hydration at Varying Temperatures
Wolfram Schmidt

nr 194
Modelling and Simulation of Virtual Natural Lighting Solutions in Buildings
Rizki A. Mangkuto

nr 195
Nano-Silica Production at Low Temperatures from the Dissolution of Olivine - Synthesis, Tailoring and Modelling
Alberto Lazaro Garcia

nr 196
Building Energy Simulation Based Assessment of Industrial Halls for Design Support
Bruno Lee

nr 197
Computational Performance Prediction of the Potential of Hybrid Adaptable Thermal Storage Concepts for Lightweight Low-Energy Houses
Pieter-Jan Hoes

nr 198
Application of Nano-Silica in Concrete
George Quercia Bianchi

nr 199
Dynamics of Social Networks and Activity Travel Behaviour
Fariya Sharmeen

nr 200
Building Structural Design Generation and Optimisation including Spatial Modification
Juan Manuel Davila Delgado

nr 201
Hydration and Thermal Decomposition of Cement/Calcium-Sulphate Based Materials
Ariën de Korte

nr 202
Republiek van Beelden:
De Politieke Werkingen van het Ontwerp in Regionale Planvorming
Bart de Zwart

nr 203
Effects of Energy Price Increases on Individual Activity-Travel Repertoires and Energy Consumption
Dujuan Yang

nr 204
Geometry and Ventilation:
Evaluation of the Leeward Sawtooth Roof Potential in the Natural Ventilation of Buildings
Jorge Isaac Perén Montero

nr 205
Computational Modelling of Evaporative Cooling as a Climate Change Adaptation Measure at the Spatial Scale of Buildings and Streets
Hamid Montazeri

nr 206
Local Buckling of Aluminium Beams in Fire Conditions
Ronald van der Meulen

nr 207
Historic Urban Landscapes:
Framing the Integration of Urban and Heritage Planning in Multilevel Governance
Loes Veldpaus

nr 208
Sustainable Transformation of the Cities:
Urban Design Pragmatics to Achieve a Sustainable City
Ernesto Antonio Zumelzu Scheel

nr 209
Development of Sustainable Protective Ultra-High Performance Fibre Reinforced Concrete (UHPFRC):
Design, Assessment and Modeling
Rui Yu

nr 210
Uncertainty in Modeling Activity-Travel Demand in Complex Uban Systems
Soora Rasouli

nr 211
Simulation-based Performance Assessment of Climate Adaptive Greenhouse Shells
Chul-sung Lee

nr 212
Green Cities:
Modelling the Spatial Transformation of the Urban Environment using Renewable Energy Technologies
Saleh Mohammadi

nr 213
A Bounded Rationality Model of Short and Long-Term Dynamics of Activity-Travel Behavior
Ifigeneia Psarra

nr 214
Effects of Pricing Strategies on Dynamic Repertoires of Activity-Travel Behaviour
Elaheh Khademi

nr 215
Handstorm Principles for Creative and Collaborative Working
Frans van Gassel

nr 216
Light Conditions in Nursing Homes: Visual Comfort and Visual Functioning of Residents
Marianne M. Sinoo

nr 217
Woonsporen: De Sociale en Ruimtelijke Biografie van een Stedelijk Bouwblok in de Amsterdamse Transvaalbuurt
Hüseyin Hüsnü Yegenoglu

nr 218
Studies on User Control in Ambient Intelligent Systems
Berent Willem Meerbeek

nr 219
Daily Livings in a Smart Home: Users' Living Preference Modeling of Smart Homes
Erfaneh Allameh

nr 220
Smart Home Design: Spatial Preference Modeling of Smart Homes
Mohammadali Heidari Jozam

nr 221
Wonen: Discoursen, Praktijken, Perspectieven
Jos Smeets

nr 222
Personal Control over Indoor Climate in Offices: Impact on Comfort, Health and Productivity
Atze Christiaan Boerstra

nr 223
Personalized Route Finding in Multimodal Transportation Networks
Jianwe Zhang

nr 224
The Design of an Adaptive Healing Room for Stroke Patients
Elke Daemen

nr 225
Experimental and Numerical Analysis of Climate Change Induced Risks to Historic Buildings and Collections
Zara Huijbregts

nr 226
Wind Flow Modeling in Urban Areas Through Experimental and Numerical Techniques
Alessio Ricci

nr 227
Clever Climate Control for Culture: Energy Efficient Indoor Climate Control Strategies for Museums Respecting Collection Preservation and Thermal Comfort of Visitors
Rick Kramer

nr 228
Fatigue Life Estimation of Metal Structures Based on Damage Modeling
Sarmediran Silitonga

nr 229
A multi-agents and occupancy based strategy for energy management and process control on the room-level
Timilehin Moses Labeodan

nr 230
Environmental assessment of Building Integrated Photovoltaics: Numerical and Experimental Carrying Capacity Based Approach
Michiel Ritzen

nr 231
Performance of Admixture and Secondary Minerals in Alkali Activated Concrete: Sustaining a Concrete Future
Arno Keulen

nr 232
World Heritage Cities and Sustainable Urban Development:
Bridging Global and Local Levels in Monitoring the Sustainable Urban Development of World Heritage Cities
Paloma C. Guzman Molina

nr 233
Stage Acoustics and Sound Exposure in Performance and Rehearsal Spaces for Orchestras:
Methods for Physical Measurements
Remy Wenmaekers

nr 234
Municipal Solid Waste Incineration (MSWI) Bottom Ash:
From Waste to Value Characterization, Treatments and Application
Pei Tang

nr 235
Large Eddy Simulations Applied to Wind Loading and Pollutant Dispersion
Mattia Ricci

nr 236
Alkali Activated Slag-Fly Ash Binders: Design, Modeling and Application
Xu Gao

nr 237
Sodium Carbonate Activated Slag: Reaction Analysis, Microstructural Modification & Engineering Application
Bo Yuan

nr 238
Shopping Behavior in Malls
Widiyani

nr 239
Smart Grid-Building Energy Interactions: Demand Side Power Flexibility in Office Buildings
Kennedy Otieno Aduda

nr 240
Modeling Taxis Dynamic Behavior in Uncertain Urban Environments
Zheng Zhong

nr 241
Gap-Theoretical Analyses of Residential Satisfaction and Intention to Move
Wen Jiang

nr 242
Travel Satisfaction and Subjective Well-Being: A Behavioral Modeling Perspective
Yanan Gao

nr 243
Building Energy Modelling to Support the Commissioning of Holistic Data Centre Operation
Vojtech Zavrel

nr 244
Regret-Based Travel Behavior Modeling: An Extended Framework
Sunghoon Jang

nr 245
Towards Robust Low-Energy Houses: A Computational Approach for Performance Robustness Assessment using Scenario Analysis
Rajesh Reddy Kotireddy

nr 246
Development of sustainable and functionalized inorganic binder-biofiber composites
Guillaume Doudart de la Grée

nr 247
A Multiscale Analysis of the Urban Heat Island Effect: From City Averaged Temperatures to the Energy Demand of Individual Buildings
Yasin Toparlar

nr 248
Design Method for Adaptive Daylight Systems for buildings covered by large (span) roofs
Florian Heinzelmann

nr 249
Hardening, high-temperature resistance and acid resistance of one-part geopolymers
Patrick Sturm

nr 250
Effects of the built environment on dynamic repertoires of activity-travel behaviour
Aida Pontes de Aquino

nr 251
Modeling for auralization of urban environments: Incorporation of directivity in sound propagation and analysis of a framework for auralizing a car pass-by
Fotis Georgiou

nr 252
Wind Loads on Heliostats and Photovoltaic Trackers
Andreas Pfahl

nr 253
Approaches for computational performance optimization of innovative adaptive façade concepts
Roel Loonen

nr 254
Multi-scale FEM-DEM Model for Granular Materials: Micro-scale boundary conditions, Statics, and Dynamics
Jiadun Liu

nr 255
Bending Moment - Shear Force Interaction of Rolled I-Shaped Steel Sections
Rianne Willie Adriana Dekker

nr 256
Paralympic tandem cycling and handcycling: Computational and wind tunnel analysis of aerodynamic performance
Paul Fionn Mannion

nr 257
Experimental characterization and numerical modelling of 3D printed concrete: Controlling structural behaviour in the fresh and hardened state
Robert Johannes Maria Wolfs

nr 258
Requirement checking in the building industry: Enabling modularized and extensible requirement checking systems based on semantic web technologies
Chi Zhang

nr 259
A Sustainable Industrial Site Redevelopment Planning Support System
Tong Wang

nr 260
Efficient storage and retrieval of detailed building models: Multi-disciplinary and long-term use of geometric and semantic construction information
Thomas Ferdinand Krijnen

nr 261
The users' value of business center concepts for knowledge sharing and networking behavior within and between organizations
Minou Weijs-Perrée

nr 262
Characterization and improvement of aerodynamic performance of vertical axis wind turbines using computational fluid dynamics (CFD)
Abdolrahim Rezaeiha

nr 263
In-situ characterization of the acoustic impedance of vegetated roofs
Chang Liu

nr 264
Occupancy-based lighting control: Developing an energy saving strategy that ensures office workers' comfort
Christel de Bakker

nr 265
Stakeholders-Oriented Spatial Decision Support System
Cahyono Susetyo

nr 266
Climate-induced damage in oak museum objects
Rianne Aleida Luimes

nr 267
Towards individual thermal comfort: Model predictive personalized control of heating systems
Katarina Katic

nr 268
Modelling and Measuring Quality of Urban Life: Housing, Neighborhood, Transport and Job
Lida Aminian

nr 269
Optimization of an aquifer thermal energy storage system through integrated modelling of aquifer, HVAC systems and building
Basar Bozkaya

nr 270
Numerical modeling for urban sound propagation: developments in wave-based and energy-based methods
Raúl Pagán Muñoz

nr 271
Lighting in multi-user office environments: improving employee wellbeing through personal control
Sanae van der Vleuten-Chraibi

nr 272
A strategy for fit-for-purpose occupant behavior modelling in building energy and comfort performance simulation
Isabella I. Gaetani dell'Aquila d'Aragona

nr 273
Een architectuurhistorische waardestelling van naoorlogse woonwijken in Nederland: Het voorbeeld van de Westelijke Tuinsteden in Amsterdam
Eleonore Henriette Marie Mens

nr 274
Job-Housing Co-Dependent Mobility Decisions in Life Trajectories
Jia Guo

nr 275
A user-oriented focus to create healthcare facilities: decision making on strategic values
Emilia Rosalia Catharina Maria Huisman

nr 276
Dynamics of plane impinging jets at moderate Reynolds numbers – with applications to air curtains
Adelya Khayrullina

nr 277
Valorization of Municipal Solid Waste Incineration Bottom Ash - Chemical Nature, Leachability and Treatments of Hazardous Elements
Qadeer Alam

nr 278
Treatments and valorization of MSWI bottom ash - application in cement-based materials
Veronica Caprai

nr 279
Personal lighting conditions of office workers - input for intelligent systems to optimize subjective alertness
Juliëtte van Duijnhoven

nr 280
Social influence effects in tourism travel: air trip itinerary and destination choices
Xiaofeng Pan

nr 281
Advancing Post-War Housing: Integrating Heritage Impact, Environmental Impact, Hygrothermal Risk and Costs in Renovation Design Decisions
Lisanne Claartje Havinga

nr 282
Impact resistant ultra-high performance fibre reinforced concrete: materials, components and properties
Peipeng Li

nr 283
Demand-driven Science Parks: The Perceived Benefits and Trade-offs of Tenant Firms with regard to Science Park Attributes
Wei Keat Benny Ng

nr 284
Raise the lantern; how light can help to maintain a healthy and safe hospital environment focusing on nurses
Maria Petronella Johanna Aarts

nr 285
Modelling Learning and Dynamic Route and Parking Choice Behaviour under Uncertainty
Elaine Cristina Schneider de Carvalho

nr 286
Identifying indoor local microclimates for safekeeping of cultural heritage
Karin Kompatscher

nr 287
Probabilistic modeling of fatigue resistance for welded and riveted bridge details. Resistance models and estimation of uncertainty.
Davide Leonetti

nr 288
Performance of Layered UHPFRC under Static and Dynamic Loads: Effects of steel fibers, coarse aggregates and layered structures
Yangyueye Cao

nr 289
Photocatalytic abatement of the nitrogen oxide pollution: synthesis, application and long-term evaluation of titania-silica composites
Yuri Hendrix

nr 290
Assessing knowledge adoption in post-disaster reconstruction: Understanding the impact of hazard-resistant construction knowledge on reconstruction processes of self-recovering communities in Nepal and the Philippines
Eefje Hendriks

nr 291
Locating electric vehicle charging stations: A multi-agent based dynamic simulation
Seheon Kim

nr 292
De invloed van Lean Management op de beheersing van het bouwproces
Wim van den Bouwhuijsen

nr 293
Neighborhood Environment and Physical Activity of Older Adults
Zhengying Liu

nr 294
Practical and continuous luminance distribution measurements for lighting quality
Thijs Willem Kruisselbrink

nr 295
Auditory Distraction in Open-Plan Study Environments in Higher Education
Pieternella Elizabeth Braat-Eggen

nr 296
Exploring the effect of the sound environment on nurses' task performance: an applied approach focusing on prospective memory
Jikke Reinten

nr 297
Design and performance of water resistant cementitious materials– Mechanisms, evaluation and applications
Zhengyao Qu

nr 298
Design Optimization of Seasonal Thermal Energy Storage Integrated District Heating and Cooling System: A Modeling and Simulation Approach
Luyi Xu

nr 299
Land use and transport: Integrated approaches for planning and management
Zhongqi Wang

nr 300
Multi-disciplinary optimization of building spatial designs: co-evolutionary design process simulations, evolutionary algorithms, hybrid approaches
Sjonnie Boonstra

nr 301
Modeling the spatial and temporal relation between urban land use, temperature, and energy demand
Hung-Chu Chen

nr 302
Seismic retrofitting of masonry walls with flexible deep mounted CFRP strips
Ömer Serhat Türkmen

nr 303
Coupled Aerostructural Shape and Topology Optimization of Horizontal-Axis Wind Turbine Rotor Blades
Zhijun Wang

nr 304
Valorization of Recycled Waste Glass and Converter Steel Slag as Ingredients for Building Materials: Hydration and Carbonation Studies
Gang Liu

nr 305
Low-Carbon City Development based on Land Use Planning
Gengzhe Wang

nr 306
Sustainable energy transition scenario analysis for buildings and neighborhoods - Data driven optimization
Shalika Saubhagya Wickramarachchi Walker

nr 307
In-between living and manufactured: an exploratory study on biobuilding components for building design
Berrak Kirbas Akyurek

nr 308
Development of alternative cementitious binders and functionalized materials: design, performance and durability
Anna Monika Kaja

nr 309
Development a morphological approach for interactive kinetic façade design: Improving multiple occupants' visual comfort
Seyed Morteza Hosseini

nr 310
PV in urban context: modeling and simulation strategies for analyzing the performance of shaded PV systems
Ádám Bognár

nr 311
Life Trajectory, Household Car Ownership Dynamics and Home Renewable Energy Equipment Adoption
Gaofeng Gu

nr 312
Impact of Street-Scale Built Environment on Walking/Cycling around Metro Stations
Yanan Liu

nr 313
Advances in Urban Traffic Network Equilibrium Models and Algorithms
Dong Wang

nr 314
Development of an uncertainty analysis framework for model-based consequential life cycle assessment: application to activity-based modelling and life cycle assessment of multimodal mobility
Paul Martin Baustert

nr 315
Variable stiffness and damping structural joints for semi-active vibration control
Qinyu Wang

nr 316
Understanding Carsharing-Facilitating Neighborhood Preferences
Juan Wang

nr 317
Dynamic alignment of Corporate Real Estate to business strategies: An empirical analysis using historical data and in-depth modelling of decision making
Howard Cooke

nr 318
Local People Matter: Towards participatory governance of cultural heritage in China
Ji Li

nr 319
Walkability and Walkable Healthy Neighborhoods
Bojing Liao

nr 320
Light directionality in design of healthy offices: exploration of two methods
Parisa Khademagha

nr 321
Room acoustic modeling with the time-domain discontinuous Galerkin method
Huiqing Wang

nr 322
Sustainable insulating lightweight materials for enhancing indoor building performance: miscanthus, aerogel and nano-silica
Yuxuan Chen

nr 323
Computational analysis of the impact of façade geometrical details on wind flow and pollutant dispersion
Xing Zheng

nr 324
Analysis of urban wind energy potential around high-rise buildings in close proximity using computational fluid dynamics
Yu-Hsuan Jang

nr 325
A new approach to automated energy performance and fault detection and diagnosis of HVAC systems: Development of the 4S3F method
Arie Taal

nr 326
Innovative Admixtures for Modifying Viscosity and Volume Change of Cement Composites
Hossein Karimi

nr 327
Towards houses with low grid dependency: A simulation-based design optimization approach
Zahra Mohammadi

nr 328
Activation of demand flexibility for heating systems in buildings: Real-life demonstration of optimal control for power-to-heat and thermal energy storage
Christian Finck

nr 329
A computational framework for analysis and optimisation of automated solar shading systems
Samuel B. de Vries

nr 330
Challenges and potential solutions for cultural heritage adaptive reuse: a comparative study employing the Historic Urban Landscape approach
Nadia Pintossi

nr 331
Shared control in office lighting systems
Tatiana Aleksandrovna Lashina

nr 332
Comfort in Urban Public Spaces
You Peng

nr 333
Numerical modelling of metal soap formation in historical oil paintings
Gerardus Johannes Anna Maria Eumelen

nr 334
A transdisciplinary decision-making approach to food-water-energy nexus: A guide towards sustainable development
Maryam Ghodsvali

nr 335
Numerical modelling of transient low-frequency sound propagation and vibration in buildings
Indra Sihar

nr 336
Characterization of impact sound from lightweight joist floors
Yi Qin

nr 337
Cities for Children: Supporting Children and Caregivers in Participatory Urban Planning
Özlemnur Ataol

nr 338
Engaging the unengaged: Exploring citizen participation in nature-based solutions in China
Li Dai

nr 339
Municipal Solid Waste Incineration Residues: analysis, treatments, and applications
Ekaterina Loginova

nr 340
Enhancing the Uptake of Nature-Based Solutions in Urban Settings: An Information Systems Approach
Shahryar Ershad Sarabi

nr 341
Work Schedule Arrangements in Two-Adult Households with Children
Bilin Han

nr 342
Increasing awareness of urban cultural heritage using digital technologies: empirical design and analysis of a new multi-media web platform
Benshuo Wang

nr 343
Mechanical and physical properties of fibre-cement composites using alternative natural fibres
Katerina Kochova

nr 344
Numerical and experimental investigation of urban microclimate in a real compact heterogeneous urban area
Nestoras Antoniou

nr 345
Examining in-class activities to facilitate academic achievement in higher education: A framework for optimal indoor environmental conditions
Henk W. Brink

nr 346
High-temperature resistant geopolymers: composition, microstructure and performance
Kinga Malgorzata Klima

nr 347
Individual and household decision-making in shared parking
Qianqian Yan

nr 348
In-situ formation of LDHs in Alkali activated binders
Tao Liu

nr 349
Condition assessment of concrete sewer pipes through an integrated experimental-numerical approach
Irene C. Scheperboer

nr 350
In situ PU-based characterization of sound absorbing materials for room acoustic modeling purposes
Baltazar Briere de La Hosseraye

nr 351
Uncertainty analysis and management in building energy data mining: A bottom-up approach considering the temporal and spatial aspect of data
Waqas Khan

nr 352
Personalized Heating Control Systems to improve thermal comfort and reduce energy consumption
Michal Veselý

nr 353
Restorative value of the urban greenscape: Urban residential streets as restorative environments
Robert P. van Dongen

nr 354
Urban ventilation and the compact Mediterranean city: numerical investigations of the dynamic relationships between density, morphology and wind flow
Olga Palusci

nr 355
Data science for buildings: a multi-scale approach bridging occupants to smart-city energy planning
Julien Leprince

nr 356
Class Association Rule Models for Predicting Transportation Mode Choice
Jiajia Zhang

nr 357
Acceptance and use of autonomous vehicles
Zhihui Tian

nr 358
Consumer Acceptance of Crowdshipping Services
Chenyu Wang

nr 359
Determinants of habitual participation in leisure-time physical activity and active travel in life trajectories
Xiaoyue Chen

nr 360
Analysis of Citizens' Motivation and Intention Using Modern Information Technology in Urban Planning Public Participation
Wenshu Li

nr 361
Linking smart and physical port cities. Port-city interface areas: from obsolete/isolated to smart environments.
Mercè de Miguel Capdevila

nr 362
Assessment and improvement of indoor thermal comfort and energy demand of Chinese heritage apartment buildings under climate change
Muxi Lei

nr 363
Indoor airflow and heat transfer in a cross-ventilated generic building: wind tunnel experiments and computational fluid dynamics analyses
Katarina Kosutova

nr 364
A Robotic Construction Simulation Platform for Light-weight Prefabricated Structures. Lifetime prediction of vertical-axis wind turbines based on CFD simulations and high-cycle fatigue modeling
Aiyu Zhu

nr 365
Lifetime prediction of vertical-axis wind turbines based on CFD simulations and high-cycle fatigue modeling
Feiyu Geng

nr 366
Computational modeling of convective heat transfer at building surfaces
Samy Iousef

nr 367
Numerical simulation of the atmospheric boundary layer with application to natural ventilation
Raffaele Vasaturo

nr 368
Bouwen zonder scrupules. De Nederlandse bouwnijverheid tijdens de bezetting en de eerste jaren van wederopbouw (1940-1950)
Geert-Jan Mellink

nr 369
Factors Promoting a Positive Experienced Neighborhood Public Space--A Virtual Environment-based analysis.
Yuwen Zhao

nr 370
Place quality making in high-speed railway station areas: Devising place quality indicators for urban design, beyond the transport-land use divide
Jinglun Du

nr 371
Sustainable Bio-based Adsorptive Concrete for Phosphorus Removal
Fan Wu

nr 372
The physical workplace as a resource for mental health: A salutogenic approach to a mentally healthy workplace design at home and at the office
Lisanne Bergefurt

nr 373
High-end application of basic oxygen furnace steel slag as sustainable building materials
Muhammad Jawad Ahmed

nr 374
Energy-Efficient Urban Rail Transit Operations: Models, Algorithms, and Applications
Kang Huang

nr 375
Household Energy Efficiency Adoption: Influencing Factors and Diffusion Interventions
Hua Du

Fire hazards in buildings constitute a substantial risk to both occupants and property, highlighting the significance of fire safety measures in construction practices. The poor high-temperature stability and negative environmental impact of ordinary Portland cement have spurred the research on thermal-resistant building materials for the future sustainable construction industry. In the past decades, geopolymers have received significant attention owing to their potential to serve as sustainable alternatives to traditional cementitious materials for high-temperature applications. While geopolymers exhibit promising thermal stability, major concerns arise due to issues such as resource competition, unsatisfactory mechanical performance, and limited applicability, greatly impeding their broader application.

This dissertation focuses on geopolymer-based materials for high-temperature applications. The aim is to improve the performance of geopolymers by incorporating industrial residuals, achieving economically and environmentally sustainable solutions. Three interrelated topics are explored, evolving from mechanism understanding (Chapter 2) to gel development (Chapters 3-4) and performance optimization (Chapters 5-6).

DEPARTMENT OF THE BUILT ENVIRONMENT

TU/e EINDHOVEN UNIVERSITY OF TECHNOLOGY